Systematic Management of Traffic Signal Timing with Vehicle Trajectory Data

by

Zachary Jerome

A dissertation submitted in partial fulfillment
of the requirements for the degree of
Doctor of Philosophy
(Civil Engineering)
in the University of Michigan
2025

Doctoral Committee:

Professor Henry Liu, Chair
Associate Professor Neda Masoud
Professor Gabor Orosz
Professor Yafeng Yin

Journey before Destination

Zachary Jerome
zjerome@umich.edu
ORCID iD: 0000-0002-7455-8387

© Zachary Jerome 2025

DEDICATION

To my parents, Aaron and Jennie, and my brother Andrew— thank you for your unwavering support, encouragement, and love. You gave me the foundation to pursue this journey, and the strength to see it through.

And to my wife, Nicole, who believes in me more than I believe in myself and gives me the courage to face every new challenge. I pray that our children will grow with the confidence to chase their dreams as fearlessly as you've encouraged me to chase mine.

ACKNOWLEDGEMENTS

During my time as a Ph.D. student at the University of Michigan, I have greatly valued the collaborative environment that my advisor, Professor Henry Liu, has fostered in the Mobility Transformation Lab (MTL). Under his leadership, I have been able to grow not only as a researcher, but also as a colleague, mentor, and supporter through the relationships I have formed with my labmates. More than any other experience at the university, I will treasure the opportunity to work in such a dynamic and well-rounded research group.

I am especially grateful to Professor Liu for granting me the flexibility to pursue my research interests and for shaping them through his thoughtful guidance. He always made time to meet when I needed support, listened genuinely to my ideas, and included my perspectives in his decision-making. Thank you, Professor Liu, for welcoming me as a valued member of your research team.

A special thanks to my primary collaborators in MTL, Dr. Xingmin Wang and Zihao Wang. This dissertation would not have been possible without your contributions. I deeply appreciate your dedication, teamwork, and commitment to the research we pursued together, and I greatly value the collaborative spirit we cultivated as a team. Another special thanks to Dr. Xintao Yan, who recruited me to join the group and helped me integrate during my first year in the program. I would also like to thank my former and current lab mates in MTL, Shengyin Shen, Dr. Zhen Yang, Dr. Rusheng Zhang, Dr. Ran Sun, Dr. Haowei Sun, Dr. Jiawei Wang, Dr. Haojie Zhu, Dr. Ronan Keane, Dr. Depu Meng, Dr. Shuo Feng, Dr. Xiaowei Shi, Dr.. Zhengxia Zou, Dr. Yukun Zuo, Dr. Yuanxin Zhong, Dr. Boqi Li, Dr. Zhong Cao, Dr. Tinghan Wang, Zhijie Qiao, and Xingpeng Xia.

Many thanks to my committee members, Professor Yafeng Yin, Professor Neda Masoud, and Professor Gabor Orosz, for their guidance and encouragement throughout my doctoral studies. I am grateful for the opportunities to collaborate and learn from them through classes, seminars, and projects, and I deeply appreciate the insight and support they have shared along the way.

I would also like to express my heartfelt gratitude to my current and former collaborators at the Road Commission for Oakland County—Gary Piotrowicz, Danielle Deneau, Rachel Jones, Jeffrey Wood, and Ahmad Jawad—for their continued support and their willingness

to implement this research in the field. My than also to my collaborators at General Motors Research and Development, Vivek Vijaya Kumar, Dr. Fan Bai, Donald Grimm, and Dr. Paul Krajewski.

Thank you to Michigan Engineering, the National Science Foundation, the Rackham Graduate School, the Michigan Department of Transportation, the Road Commission for Oakland County, General Motors, the United States Department of Transportation, Dr. J. Robert and Betty Beyster, and the Center for Connected and Automated Transportation for funding this research.

On a personal note, I would like to thank my parents, Aaron and Jennie, for giving me the foundation and flexibility to pursue my interests; my brother, Andrew, for being my lifelong friend and unwavering presence; and the Grace Churches Community for shaping my growth as a person. Through Grace Church, I met my wife, Nicole, to whom I owe my deepest gratitude for her confidence in me and her steadfast support throughout this journey. Nicole, thank you for your commitment to living life together; you give me the courage to overcome every challenge.

PREFACE

One of the unique aspects of being a researcher in transportation engineering is that nearly everyone I encounter has some direct experience with my field. The immediate, practical relevance of transportation engineering is what first drew me to this discipline. Of course, the question I am most often asked when I say I am a transportation engineer is, *"What do you think about roundabouts?"* While that is not the focus of this dissertation (for the record, I believe roundabouts have many benefits in the right context, particularly for traffic calming), it has been rewarding to explain my research on traffic signal timing and, in doing so, spark engaging conversations with people from a wide variety of technical backgrounds. With that in mind, although this dissertation represents the culmination of my doctoral research at the University of Michigan, my hope is that readers of all backgrounds will be able to take something valuable from it.

The main reason I chose to pursue my Ph.D. research at the University of Michigan with Professor Henry Liu was the opportunity to engage in real-world implementations. My experience here has shaped my interest in working at the intersection of research and practice. During this time, I have had the chance to explore the potential of vehicle trajectory data to transform traffic signal management. My goal throughout this work has been to bridge the gap between theory and practice by developing methods that are not only rigorous, but also applicable in real-world settings.

While this dissertation marks the completion of my Ph.D. studies and I am eager for the next stage of my career, I want to express how deeply I have appreciated and enjoyed the past five years. Graduate school can be difficult to fully appreciate, as its very structure emphasizes progress toward completion and preparation for what comes next. Yet I will never take for granted the freedom that a Ph.D. at the University of Michigan provided—the opportunity to explore a topic at the highest level. For me, that experience in itself has been a destination, and one that represents a life well lived.

Over the past few weeks, as I have reflected on my Ph.D. experience, I have found myself asking what led me to pursue one topic at the highest level. Where does this drive for knowledge come from? My faith tradition teaches that at the origins of human existence, God gave us the mandate to "fill the earth and subdue it" (Genesis 1:28). One way to

understand this directive is as a call to bring order out of the natural chaos of the world. In this light, I believe that pursuing a Ph.D. has given me the opportunity to live out an innate desire placed within my soul by my Creator. It is my hope that the contributions of this dissertation will serve, in some small way, to advance the human experience and offer a glimpse of God's eternal kingdom. It is with this desire to glimpse God's kingdom in mind that I leave you with a quote that has inspired me at many points throughout my studies:

> "If you want to build a ship, don't drum up people to collect wood and don't assign them tasks and work, but rather teach them to long for the endless immensity of the sea."
>
> - Antoine de Saint-Exupéry

TABLE OF CONTENTS

DEDICATION ii

ACKNOWLEDGEMENTS iii

PREFACE v

LIST OF FIGURES x

LIST OF TABLES xiii

LIST OF ACRONYMS xv

LIST OF SYMBOLS xvii

ABSTRACT xx

CHAPTER

1 Introduction 1

1.1 Background 1
1.1.1 Current signal timing management strategies 2
1.1.2 Vehicle trajectory data 4
1.1.3 Opportunity for scalable systematic management 7
1.2 Dissertation overview 8
1.2.1 Research scope 8
1.2.2 Data 11
1.2.3 Contributions 11
1.2.4 Organization 12

2 Evaluating Yellow Change and Red Clearance Intervals 14

2.1 Introduction 14
2.1.1 Background 14
2.1.2 Related works 16
2.1.3 Contributions and organization of the chapter 17
2.2 Current kinematic models 18
2.2.1 Yellow change interval 19
2.2.2 Red clearance interval 22

2.3 Vehicle trajectory preprocessing for yellow change and red clearance interval analysis . . . 23
2.4 New kinematic model for left-turn movements . . . 25
2.4.1 Vehicle trajectory speed profile observations . . . 26
2.4.2 Proposed kinematic equations . . . 33
2.4.3 Numerical comparisons with the current kinematic models . . . 34
2.4.4 Conclusions . . . 36
2.5 Determining minimum change intervals from vehicle trajectory data . . . 37
2.5.1 Methodology . . . 38
2.5.2 Case study . . . 41
2.5.3 Conclusions . . . 46
2.6 Conclusion . . . 47
2.6.1 Summary . . . 47
2.6.2 Integration into the traffic signal timing management system) . . . 48

3 A Signalized Intersection Performance Diagram (SIPD) . . . 49

3.1 Introduction . . . 49
3.1.1 Background and related works . . . 49
3.1.2 Contributions and organization of this chapter . . . 51
3.2 Analytical derivation of the SIPD . . . 52
3.2.1 Newellian Coordinates . . . 52
3.2.2 SIPD boundaries and zones . . . 54
3.3 Red light and blockage performance measures . . . 57
3.4 SIPD construction using vehicle trajectory data . . . 61
3.4.1 Modifications for real-time systems . . . 64
3.5 Case studies . . . 64
3.5.1 Evaluating blockage impacts of permissive movements . . . 65
3.5.2 Evaluating blockage impacts of spillover . . . 72
3.6 Conclusion . . . 76
3.6.1 Summary . . . 76
3.6.2 Integration into the traffic signal timing management system) . . . 77

4 Detecting Opportunities for Improving Signal Coordination without Signal Timing Data . . . 78

4.1 Introduction . . . 78
4.1.1 Background . . . 79
4.1.2 Contributions and organization of the chapter . . . 79
4.2 Estimating intersection cycle lengths . . . 79
4.2.1 Background and related works . . . 80
4.2.2 Contributions . . . 81
4.2.3 Vehicle trajectory preprocessing for cycle length estimation . . . 81
4.2.4 Cycle length estimation . . . 82
4.2.5 Case studies . . . 89
4.3 Winter conditions . . . 93
4.3.1 Background . . . 93

4.3.2 Related works . . . 94
4.3.3 Contributions . . . 98
4.3.4 Data and study area . . . 98
4.3.5 Results and discussion . . . 103
4.3.6 Summary . . . 109
4.4 Conclusion . . . 111
4.4.1 Summary . . . 111
4.4.2 Integration into the traffic signal timing management system . . . 112
5 Iterative Traffic Signal Timing Optimization to Alleviate Traffic Congestion 113
5.1 Introduction . . . 113
5.1.1 Background and related works . . . 113
5.1.2 Contributions and organization of this chapter . . . 115
5.2 Theoretical foundations . . . 115
5.2.1 The probabilistic time-space probabilistic time-space (PTS) model . 116
5.2.2 Modifications for coordinated-actuated control . . . 119
5.3 Case study . . . 121
5.3.1 Study area and data . . . 121
5.3.2 Procedures for before and after studies . . . 123
5.3.3 Optimization procedures . . . 123
5.3.4 Results and discussion . . . 127
5.3.5 Summary . . . 132
5.4 Conclusion . . . 134
5.4.1 Summary . . . 134
5.4.2 Integration into the traffic signal timing management system) . . . 135
6 Summary and Future Directions . . . 136
6.1 Summary . . . 136
6.2 Future Directions . . . 137
BIBLIOGRAPHY . . . 139

LIST OF FIGURES

FIGURE

1.1 Illustration of typical traffic signal timing parameters . . . 2
1.2 Expected benefits of more iterative retiming . . . 3
1.3 Global Navigation Satellite System (GNSS) points from observed vehicles in Birmingham, MI . . . 5
1.4 Leveraging temporal-spatial information of observed vehicle trajectories to infer the presence of other vehicles. . . . 6
1.5 Illustration of vehicle trajectory on time-space diagram . . . 7
1.6 Systematic traffic signal timing management with vehicle trajectory data . . . 9
1.7 Applications . . . 10
1.8 Integrated online signal retiming process . . . 13

2.1 Original Gazis, Herman, and Maradudin (GHM) kinematic model for determining yellow change intervals . . . 19
2.2 Extended kinematic model for determining yellow change intervals . . . 21
2.3 Free-flowing vehicle speed profiles for original GHM and extended kinematic models when determining clearance intervals . . . 23
2.4 Critical distance identification for individual trajectory. . . . 24
2.5 Plymouth Rd corridor and intersections of interest . . . 26
2.6 Free-flowing vehicle speed profile from left-turning vehicle trajectory observations 28
2.7 Comparison between the current recommended speed profile model and the observed speed profile. . . . 29
2.8 Critical distance for vehicles preparing for a left turn . . . 30
2.9 Free-flowing vehicle speed profiles for the extended kinematic equation and the proposed equation . . . 31
2.10 Speed profile for a left-turning vehicle traversing an intersection . . . 32
2.11 Change interval performance evaluation for a left-turning movement . . . 40
2.12 Birmingham, MI intersection locations and trajectory point GNSS scatters (Wang et al., 2024a). . . . 41
2.13 Percentage of critical distance travel times less than the current change interval vs. 85th percentile critical distance speed for each movement. . . . 44
2.14 85th percentile intersection entry speed vs. 85th percentile critical distance along with respective speed limits for each movement. . . . 45
2.15 85th percentile critical distance travel time histograms for straight movements at different speed limits. . . . 46

2.16 85th percentile critical distance travel time histograms for left-turning movements at different speed limits. 47

3.1 Demonstrations of Newellian Coordinates 53
3.2 Signalized Intersection Performance Code (SIPD) 55
3.3 Flow chart for calculating proposed performance measures from trajectories plotted on the Signalized Intersection Performance Diagram (SIPD) 58
3.4 Example trajectories plotted on the SIPD 59
3.5 Departure time t_b after green start vs. stop position plot for stopped vehicles with expected departure regression line for a straight movement sharing a lane with a left-turn movement 62
3.6 Stop end time (t_{se}) scatter plot on SIPD with example trajectory for a straight movement sharing a lane with a left-turn movement 63
3.7 Stop end time (t_{se}) scatter plot on SIPD for the left-Turn movement that shares a lane with the straight movement in Figure 3.5 64
3.8 Intersection geometries and traffic control phase sequences for case studies examining blockage impacts from permissive movements 65
3.9 Example trajectories from Lincoln St and Pierce St 66
3.10 Example trajectories with ted light split failures missed by state-of-the-practice 69
3.11 Example trajectories from Telegraph Rd and Elizabeth Lake Rd 70
3.12 Geometric Layout for Corridor Case Study Examining Blockage Impacts from Spillover (West Maple Road from Bates St. to Old Woodward Ave) 73
3.13 SIPD Aggregated time-space Diagram for Old Woodward Ave 73
3.14 SIPD Aggregated time-space Diagrams for Henrietta St and Bates St 74

4.1 Green start estimation from vehicle trajectory 82
4.2 Extract green start time difference $\Delta\tau_j^m$ from observed vehicle trajectories . . . 84
4.3 For each movement m, $n^m(k)$ is the frequency of h_j^m, which is expected to follow a geometric distribution 86
4.4 Probabilistic model of the green start difference. 87
4.5 Identification of cycle length variation 88
4.6 Examples of cycle length estimation: fixed (Telegraph Rd and Huron St) vs. variable (Fuller St and Maiden Ln). 90
4.7 Validation of the geometric distribution of h_j^m in Section 4.2.4.2 (Telegraph Rd and Huron St). 91
4.8 Detected suboptimal coordination caused by inconsistent cycle length 92
4.9 Before and after time-space diagrams for 8 Mile Rd 92
4.10 Study area in southeast Oakland County, MI 99
4.11 Hourly snowfall and snow depth prediction in each High-Resolution Rapid-Refresh (HRRR) prediction cell 100
4.12 Performance calculations for vehicle traveling between two intersections 101
4.13 Hourly number of intersection pair observations during snow and no snow conditions 102
4.14 Travel time distributions for E. Lincoln St. to Bowers St on Woodward Ave NB 103
4.15 Regression lines at different snow depths 105
4.16 Selected arterial and collector sections 106

4.17 Aggregated time space diagrams for NB Woodward Ave. in normal and snowy conditions . . . 108
4.18 Histograms of travel times for vehicles traveling the entire NB Woodward Corridor section in normal and snow conditions . . . 108
4.19 Aggregated time-space diagrams for Adams Rd. in normal and snow conditions 109

5.1 Building the aggregated time-space diagram . . . 116
5.2 Difference Between the current practice and the proposed vehicle trajectory-based method . . . 117
5.3 Demonstration of PTS model. (a) Newellian coordinate system; (b) Arrival rate profile $A(t)$; (c) Signal state $S(t)$; (c) PTS diagram given arrival rate and signal state, drawn in the Newellian coordinates; . . . 118
5.4 Before (left) and after (right) comparison of implemented offsets in morning peak of northbound Adams Rd corridor . . . 118
5.5 Estimating green start time distribution in coordinated actuated settings. . . . 120
5.6 Telegraph road study segment in Pontiac, MI . . . 122
5.7 Implementation schedule . . . 122
5.8 Corridor travel times using crowdsourced vehicle trajectory Data . . . 124
5.9 Trajectory histograms for northbound and southbound movements along corridor segment across 24-hour period with timing plan schedule changes . . . 124
5.10 Observed and modeled time-space diagrams (TSDs) of Telegraph Road during the AM time period before and after vehicle trajectory-based optimization . . . 126
5.11 Green split adjustment methodology . . . 128
5.12 Time-space diagrams before and after trajectory-based optimizations for each movement at Telegraph Rd and Huron St for the MD time period . . . 133

LIST OF TABLES

TABLE

2.1 Number of free-flowing trajectories for each Plymouth Rd intersection by phase movement . . . 27
2.2 Average mean absolute percentage error (MAPE) for speed estimation through the critical distance for intersections along Plymouth Rd. . . . 31
2.3 MAPE for speed estimation through the intersection for intersections along Plymouth Rd . . . 32
2.4 Comparison of yellow change and red clearance intervals calculated by the original (O), extended (E), and proposed (P) kinematic equations for each phase (Ph) based on 85th percentile measurements . . . 35
2.5 Proposed minimum yellow change intervals vs. $t_{c,85}$ for intersections and phases along Plymouth Rd . . . 40
2.6 Number of movements by direction and change interval . . . 42
2.7 Number of movements by direction and speed limit . . . 42
2.8 Movement performance table (top ten worst performing movements) . . . 43

3.1 Diagnosing intersection movement congestion conditions using the SIPD . . . 56
3.2 Proposed performance measure comparison with state-of-the-practice . . . 57
3.3 Performance measures from trajectories in Figure 3.9 . . . 67
3.4 Aggregated delay and stop performance measures for Lincoln St and Pierce St in the PM peak period (3 - 7 PM) . . . 67
3.5 Aggregated split failure performance measures for Lincoln St and Pierce St in the PM peak period (3 - 7 PM) . . . 68
3.6 Aggregated delay and stop measures for Adams Rd and Derby Rd in the AM (7 - 10 AM) and PM2 (3:15 - 3:40 PM) peak periods . . . 69
3.7 Performance measures from trajectories in Figure 3.11 . . . 71
3.8 Aggregated delay and stop performance measures for Telegraph Rd and Elizabeth Lake Rd in the AM (6 - 10 AM) and PM (3 - 7 PM) peak periods . . . 71
3.9 Aggregated split failure performance measures for Telegraph Rd and Elizabeth Lake Rd in the PM (3 - 7 PM) peak period . . . 72
3.10 Aggregated delay and stop performance measures for Maple Rd eastbound in the MD (10 AM - 3 PM) and PM (3 - 7 PM) peak periods . . . 75
3.11 Aggregated split failure performance measures for Maple Rd eastbound in the MD (10 AM - 3 PM) and PM (3 - 7 PM) peak periods . . . 75

4.1 Average number of observations per intersection pair for different snow depths . 102

4.2 Descriptive statistics of key variables at different snow depths and time ranges for each intersection pair 104
4.3 Percent changes in average number of stops and control delay (per intersection per vehicle) for selected corridors 106
4.4 Woodward Ave. NB results at each intersection 110
4.5 Adams Rd. SB results at each intersection 110

5.1 Prediction of average control delay per movement (s) along coordinated movements for different cycle lengths during the MD time period 127
5.2 Summary of timing plan schedule changes and cycle lengths 127
5.3 Average corridor travel time (s) by time range before and after trajectory-based and traditional optimizations (weekdays) 129
5.4 Average control delay per movements (s) along coordinated movements by time range before and after trajectory-based and traditional optimizations (weekdays) 129
5.5 Average control delay per movement along coordinated movements for different time periods: observations vs. model calibration and optimization 130
5.6 Average control delay and number of stops per movement for all movements by time range before and after trajectory-based and traditional optimizations (weekdays) 131

LIST OF ACRONYMS

AACVTE Ann Arbor Connected Vehicle Test Environment

AOG arrival on green

API application programming interface

ATSC adaptive traffic control systems

ATSPM automated traffic signal performance measures

BSM Basic Safety Message

CV connected vehicle

CV2X Cellular Vehicle-to-Everything

ERG early return to green

FFS free-flow speed

FHWA Federal Highway Administration

GHM Gazis, Herman, and Maradudin

GNSS Global Navigation Satellite System

HCM Highway Capacity Manual

HRRR High-Resolution Rapid-Refresh

IMU inertial measurement unit

INDOT Indiana Department of Transportation

ITE Institute of Transportation Engineers

LOS level of service

LWR Lighthill-Whitham-Richards

MAPE mean absolute percentage error

MDOT Michigan Department of Transportation

MUTCD Manual on Uniform Traffic Control Devices

NACTO National Association of City Transportation Officials

NCHRP National Cooperative Highway Research Program

NOAA National Oceanic Atmospheric Administration

OEM original equipment manufacturer

PCD Purdue Coordination Diagram

PPD Purdue Probe Diagram

PR perception-reaction

PTS probabilistic time-space

RCOC Road Commission for Oakland County

RSU Roadside Unit

RWMP Roadway Weather Management Program

SAE Society of Automotive Engineers

SIPD Signalized Intersection Performance Diagram

SPaT Signal Phase and Timing

SPM signal performance measures

SSD stopping sight distance

WRTM Weather Responsive Traffic Management

LIST OF SYMBOLS

a^*	maximum safe and comfortable deceleration rate
a_{apr}	approach deceleration in preparation for left-turn
$A(t)$	arrival at time t
α	probability of observing at least one stopped trajectory in a cycle
C	cycle length
d_a	downstream free-flow arrival time
δ	perception-reaction time
g	green split
g^1	first available departure green split where $g_e > t_a$
g_s	green split start time
$g^*_{s,i}$	time where trajectory i begins to move after green split start
$g'_{s,i}$	estimated green split start time for trajectory i
g_e	green split end time
h	number of cycles in $\Delta\tau$
j	cycle index for observed cycles
k	number of cycles
l	vehicle length
m	phase movement index
M	maximum number of cycle lengths between adjacent trajectories
n	vehicle stop position (number in queue)
n_c	capacity boundary (number of vehicles)

$n(k)$	frequency of h_j for number of cycles k where $j = k$
N	number of observed cycles
p	trajectory point
q_s	saturation flow rate
R	red clearance interval
$S(t)$	traffic signal state at time t
t	time
t_a	free-flow arrival time
t_b	departure time
t_c	travel time through critical distance
$t_{c,85}$	85th percentile critical distance travel time
t_e	expected departure time
t_s	conflicting vehicular movement start up delay
t_{se}	trajectory stop end time
t_{ud}	free-flow travel time between two intersections
t_{wl}	travel time to clear intersection after crossing the stop bar
τ_j	cycle j start time
$\Delta\tau$	time difference between two observed cycles
u	unit flow
u_d	upstream departure time
x	distance to stop bar
x_c	critical distance
x_i^*	distance to stop bar when trajectory i begins to move after green split start
x_s	stopping distance
x^i	trajectory i
v_0	original approach speed
v_c	critical distance speed

v_d	intersection departure speed
v_e	intersection entrance speed
v_f	free-flow speed
v_i	speed at trajectory point i
v_m	minimum speed reach by vehicle during turning maneuver
v_r	perception-reaction time speed
$v_{\cdot,85}$	85th percentile speed under free-flow conditions
w	intersection width
w_d	departure shockwave speed
Y	yellow change interval
Y_{min}	minimum yellow change interval

ABSTRACT

Each year, drivers in the United States incur tens of billions of dollars in congestion-related costs at intersections controlled by traffic signals. In addition, thousands of people are killed—and hundreds of thousands more are injured—in crashes occurring at these locations. Signal retiming, which adjusts when and for how long green, yellow, and red time is given to each direction, is a cost-effective way to reduce congestion and improve safety as it does not require any changes to the physical infrastructure. However, it is very difficult to monitor traffic dynamics across the more than 330,000 signalized intersections in the United States. Due to the high costs of installing and maintaining permanent detection infrastructure, agencies often rely on temporary detection methods to support signal retiming projects. These efforts are typically conducted on a 3- to 5-year fixed rotation or in response to major land use changes. As a result, agencies may miss key opportunities where retiming could have the greatest impact—or may direct resources toward locations that are not in urgent need of adjustment. Without reliable widespread data coverage, the process can resemble performing surgery without first understanding the symptoms or confirming the diagnosis.

Recently, Global Navigation Satellite System (GNSS) data from vehicles equipped with cloud or cellular services has become increasingly accessible through navigation, ride-hailing, and roadside assistance applications. This data offers detailed insights into travel paths—such as delays, stops, and travel times—across entire traffic networks. These capabilities create unprecedented opportunities to manage signalized intersections more systematically, rapidly, and cost-effectively, without the need for additional roadside sensors. However, few comprehensive solutions currently exist that fully leverage these advantages to detect performance issues at signalized intersections, diagnose their root causes, and implement the targeted interventions needed to improve their operation.

This dissertation presents one of the world's first traffic signal timing management systems that relies solely on currently available vehicle trajectory data, even at low penetration rates, and represents a major milestone in this research group's ten years of groundbreaking theoretical work—culminating in a deployable system with demonstrated impact in real-world transportation engineering practice. The system is built around three core functions: performance monitoring, diagnostics, and targeted retiming interventions—forming a closed-loop

framework that offers a comprehensive, systematic solution. Key technical contributions of this dissertation include a method for determining minimum yellow change and all-red clearance intervals that reduce the risk of red-light running; the development of the Signalized Intersection Performance Diagram (SIPD), which integrates signal timing data with advanced performance analytics to identify the root causes of congestion; and rule-based approaches for diagnosing signal coordination deficiencies without requiring signal timing data from the agency. In addition, the system includes procedures for iteratively optimizing timing plan schedules, cycle lengths, offsets, and green splits every few weeks in response to evolving traffic demand patterns.

The system's technical readiness for deployment is demonstrated through multiple real-world implementations, including a direct comparison with a traditional optimization. In that deployment, the proposed system outperformed the conventional approach, reducing overall control delay by 17.4% and the number of stops by 20.4%, compared to 13.7% and 14.9% reductions, respectively, from the traditional method. By leveraging trajectory data as the sole input and requiring no additional infrastructure, this system offers a scalable and cost-effective solution that can be applied to signalized intersections around the world.

CHAPTER 1

Introduction

1.1 Background

Drivers in the United States experience $22.9 billion in congestion costs at signalized intersections each year (National Operations Center of Excellence, 2019), spending over 18 seconds idling at each intersection resulting in the annual release of nearly 28 million metric tons of CO_2 equivalent (Schuman, 2022). These intersections also present significant safety challenges. Every year, more than 10,000 people are killed in crashes involving one, and hundreds of thousands more are injured (National Center for Statistics and Analysis, 2022; U.S.DOT FHWA, 2024).

Much of these costs at signalized intersections are the result of outdated or improper traffic signal operations, which the 2019 National Traffic Signal Report Card gave a C+ grade (National Operations Center of Excellence, 2019). Signal retiming, which adjusts when and for how long green, yellow, and red time is given to each direction, is a cost-effective way to reduce congestion and improve safety as it does not require any changes to the physical infrastructure. In terms of congestion, large benefit-to-cost ratios (ranging from 20:1 to 83:1) have been reported by traffic agencies across the country (Chien et al., 2006; Denney Jr et al., 2012; Boston Transportation Department and Howard/Stein-Hudson Associates, Inc, 2010; Sunkari, 2004). A study by INRIX found that just a one second reduction in delay at every intersection in the United States would save 1.5 million tons of CO_2 equivalent annually (Schuman, 2022). Additionally, the National Cooperative Highway Research Program (NCHRP) Report 731: Guidelines for Timing Yellow and All-Red Intervals at Signalized Intersections found that properly timed yellow change intervals can reduce red-light violations by about 36% to 50%. The report also found that these intervals can reduce total crashes by about 8% to 14%, and injury crashes by about 12% (Transportation Research Board, 2012).

1.1.1 Current signal timing management strategies

Traffic signal retiming requires knowledge of current traffic dynamics including traffic volumes, free-flow speeds, and signal performance measures (SPM) such as delay. The most commonly practiced methods for collecting this information involve fixed-point roadside detections systems such as video cameras and inductive loop detectors, which have high installation and maintenance costs. As a result, many signalized intersections in the United States lack detection infrastructure and continue to operate under fixed-time (pre-timed) control schemes (National Operations Center of Excellence, 2019; Zhao and Tian, 2012). Figure 1.1 illustrates the typical timing parameters programmed for this type of control. Signal controllers use a schedule of timing plans that vary by period of the day, such as the morning and evening peaks. Within each plan, the cycle length defines the total time required for the controller to allocate right-of-way to all movements. The offset specifies the point at which the cycle begins, enabling coordination among adjacent intersections. The green splits determine the portion of green time assigned to each movement. In addition, although not shown in this figure, the yellow change and clearance intervals must also be specified to ensure the safe transfer of right-of-way between conflicting vehicular movements.

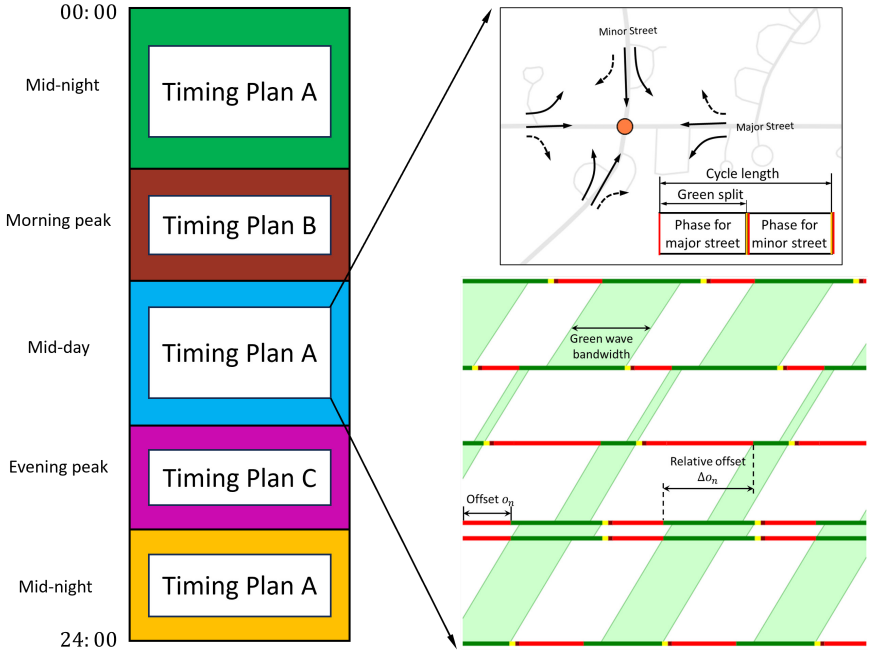

Figure 1.1: Illustration of typical traffic signal timing parameters

Signal retiming projects which adjust these parameters are usually only executed every 3-5 years in practice (Transportation Research Board and National Academies of Sciences, Engineering, and Medicine, 2010), and rely on temporary detection methods to collect cur-

rent traffic dynamics. These measurements inform a variety of models that help engineers design new signal timing plans and enable before-and-after performance evaluations of those plans. However, narrow observation windows limit potential traffic signal improvements and evaluation capabilities. Such "one-shot" optimizations can quickly become outdated as traffic demand undergoes natural changes or growth, which can increase congestion and energy costs. As shown in Figure 1.2, more responsive signal retiming that decreases the time between each iteration could recover lost opportunities as traffic dynamics change over time (difference between the blue and green shaded areas).

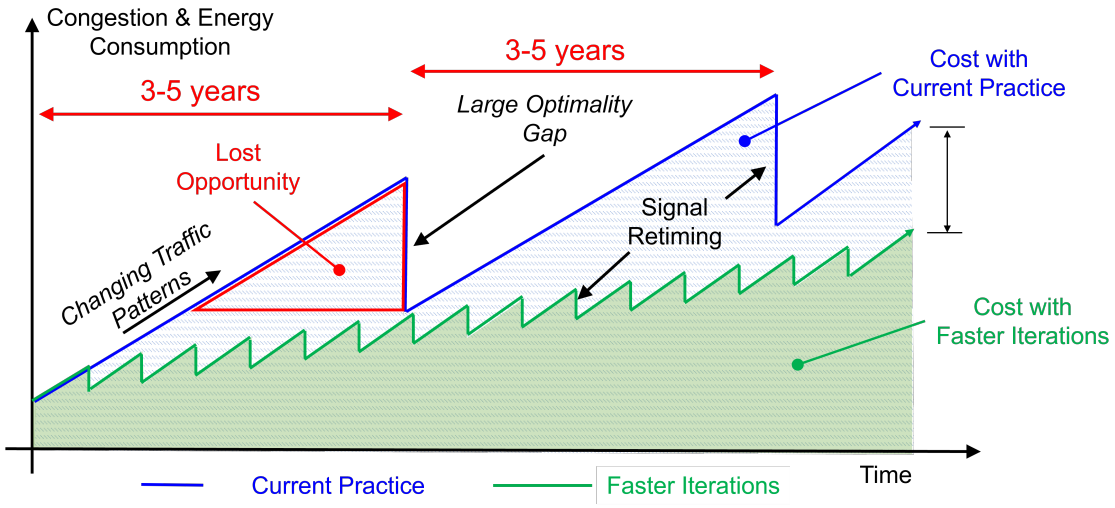

Figure 1.2: Expected benefits of more iterative retiming

Some intersections with detection capability use vehicle-actuated control, traffic responsive control. or adaptive traffic control systems (ATSC), which are more responsive to the time-varying traffic demand compared to fixed-time traffic signals. While in many cases traffic responsive control and ATSC has proven to be effective, sometimes improving travel times by up to 50% or more, their widespread implementation has been prevented by high installation, maintenance, and software licensing costs (Dobrota et al., 2020). In addition, actuated signal control has also been discouraged by the National Association of City Transportation Officials (NACTO) because of the maintenance requirements and detection upkeep on streets (National Association of City Transportation Officials (NACTO), 2012). Since a single unreliable detector can jeopardize the effectiveness of an entire ATSC or actuated system, these detectors require frequent monitoring and maintenance. Many agencies have also discovered that ATSC cannot simply be installed and left alone for long periods of time. Some, especially those who are not knowledgeable of the inner workings of ATSC, have been forced to switch back to traditional fixed-timed plans after the original ATSC settings are

unable to handle long-term changes in traffic patterns (Dobrota et al., 2022). As a result, although the first ATSC systems were developed in the early 1970s, only a small percentage of signalized intersections in the U.S. ($2-5\%$) have been outfitted with this technology (Zhao and Tian, 2012).

While many agencies have struggled to implement the "black-box" control strategies associated with ATSC for managing signal timing, fixed-point roadside detection systems can still offer valuable capabilities for monitoring current traffic dynamics and collecting SPMs. High resolution signal controller data (e.g., detector actuations and phase changes) provided by data logging controllers every tenth of a second can be converted into a variety of performance measurements known as automated traffic signal performance measures (ATSPM). ATSPMs such as volumes, turning movement counts, arrival on green (AOG) percentages, which evaluate the percentage of vehicles that have to stop before clearing the intersection, make it easier to identify signal timing issues (Smaglik et al., 2007; Brennan Jr et al., 2011). Rather than just providing a temporary observation window, these performance measures collect data continuously, including weekends and off-peak times when performance is typically not assessed (Day et al., 2010). However, physical infrastructure costs of around $50,000 for installation and $2,000 per year in maintenance have again prevented the widespread adoption of ATSPMs (Remias et al., 2018).

The prohibitive cost and ongoing maintenance of fixed-point roadside detection systems make it nearly impossible to monitor traffic dynamics at the more than 320,000 signalized intersections in the United States. As a result, data collection, performance monitoring, and diagnostics remain as the chief bottlenecks to implementing responsive, large-scale traffic signal timing management. Today, most intersections lack any monitoring capability, preventing timely performance evaluations and retiming efforts.

1.1.2 Vehicle trajectory data

Recently, Global Navigation Satellite System (GNSS) data from vehicles equipped with cloud or cellular services has become increasingly accessible through crowdsourced applications, including navigation tools, ride-hailing services, and roadside assistance platforms. Vehicle trajectory data—also known as probe or telematics data—from these vehicles has the potential to bring dynamic and responsive signal control solutions to millions of traffic signals around the world without the need for additional roadside sensors. It provides detailed travel-path information 24/7 across entire traffic networks, acting as mobile sensors enabling scalable performance monitoring capabilities. Even at limited vehicle observation rates, the temporal-spatial properties of vehicle trajectory data can give insights into the

overall traffic performance Figure 1.3 plots GNSS points from observed vehicles in Birmingham, MI. The color of each point represents the speed, as indicated by the color bar on the right. Even at just the estimated 7% penetration (observation) rate of the total number of vehicles (Wang et al., 2024a), the figure demonstrates how the speed information can give us a general understanding of the traffic dynamics across an entire network. As automation and connectivity increase on our traffic networks, there will be greater opportunity for vehicle trajectory-based traffic signal control.

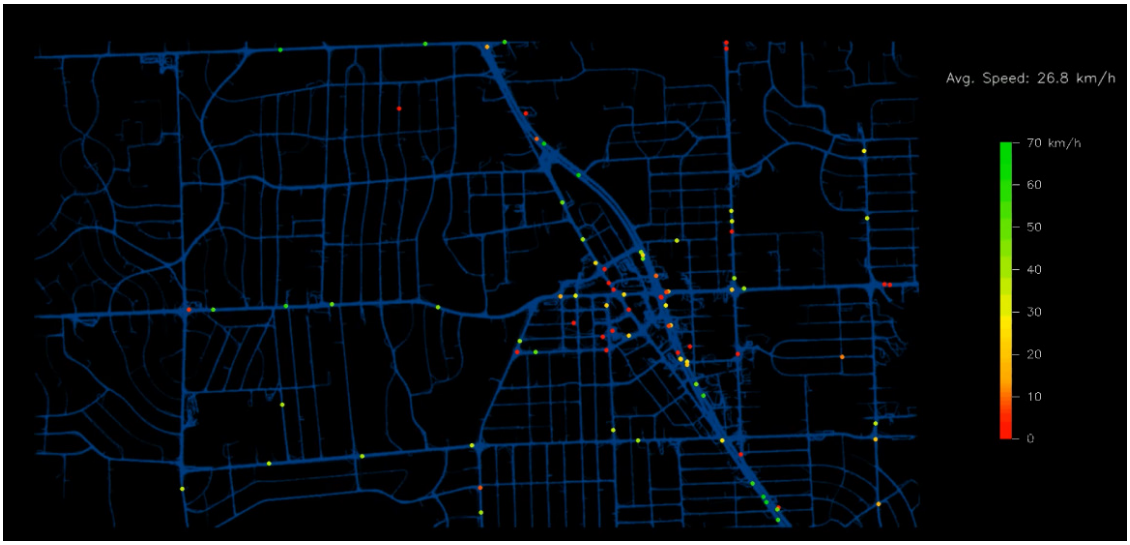

Figure 1.3: GNSS points from observed vehicles in Birmingham, MI

Vehicle trajectory data provides traces of vehicle paths through time and space that can be leveraged to infer other traffic dynamics. Figure 1.4 illustrates two examples of observed vehicles approaching an intersection on time-space diagrams. First, consider a vehicle trajectory that exhibits a stop some distance before the stop bar. Based on the stopping location, we can infer the number of vehicles queued ahead. Alternative, Figure 1.4 (b) illustrates how if we do not observe a stop in a vehicle trajectory, it indicates that a vehicle queue at the intersection did not impact that trajectory's path. Therefore, low observation rates can be overcome by leveraging the temporal-spatial information embedded in vehicle trajectory data.

The increasing availability of this data has bolstered the development of the next generation of traffic SPMs that expand upon the existing ATSPMs. Monitoring traffic through vehicle trajectory data is highly scalable due to its large coverage area, offering many advantages over fixed point detection methods used for ATSPMs (Waddell et al., 2020; Saldivar-Carranza et al., 2023; Wang et al., 2023; Wolf et al., 2019; INRIX, 2024). It has a much larger coverage area than detector data because it is available at almost every intersection,

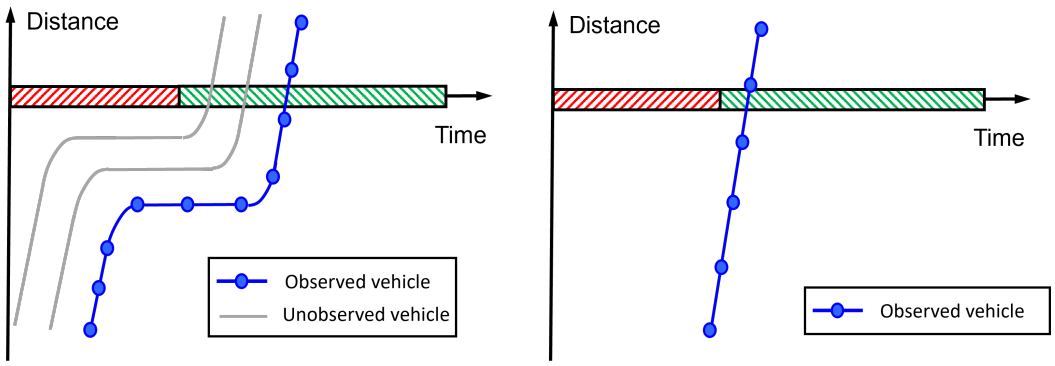

(a) Unobserved vehicles queued ahead of observed vehicle

(b) No unobserved vehicles queued ahead of observed vehicle

Figure 1.4: Leveraging temporal-spatial information of observed vehicle trajectories to infer the presence of other vehicles.

especially those with higher traffic volumes. While detector data can only provide traffic counts and estimated speeds at certain locations, vehicle trajectory data spans the entire spatial-temporal space and provides more enriched SPMs such as control delay, number of stops, and travel path. Figure 1.5 plots a vehicle trajectory on a time-space diagram and illustrates how these SPMs are extracted. These measures can be aggregated for operational performance evaluations such as AOG percentages and level of service (LOS). A performance monitoring system built on trajectory-based performance measures does not require any additional roadside detection technology, and is more resilient to equipment failure as it will not completely lose traffic monitoring capability at any specific location if one vehicle's transponder malfunctions.

Existing performance monitoring systems with vehicle trajectory data offer valuable insights into existing congestion levels. However, while these tools help us understand where delays are occurring, they have not yet enabled agencies to efficiently identify where signal retiming would be most effective or feasible. In many cases, agencies are already aware of intersections experiencing significant delays through citizen complaints or personal experience, but further timing improvements are constrained by physical or operational limitations. Additionally, these platforms lack robust modeling capabilities to forecast how traffic patterns would respond to different signal timing strategies. As a result, agencies are unable to fully leverage vehicle trajectory data in a predictive or optimization context, limiting its utility for proactive signal management.

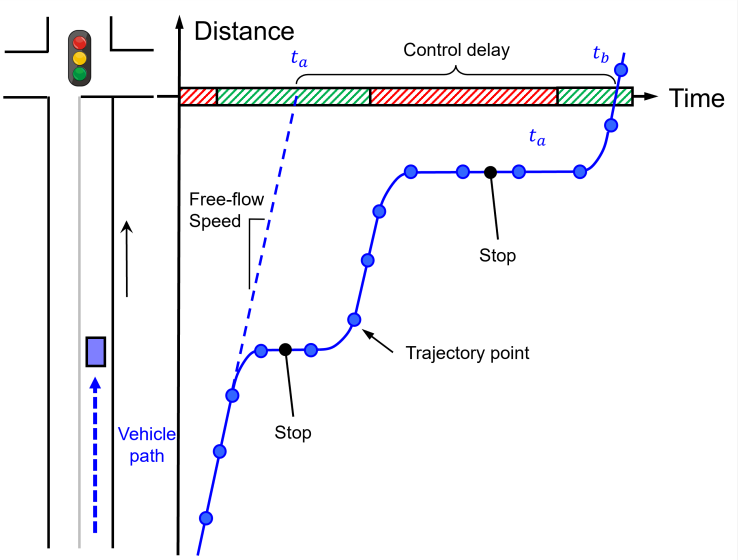

Figure 1.5: Illustration of vehicle trajectory on time-space diagram

1.1.3 Opportunity for scalable systematic management

Typically, signal retiming efforts are conducted on a 3- to 5-year fixed rotation or in response to major land use changes. This timeline is in large part dictated by the need to collect information about the traffic dynamics as part of the project. Without reliable, continuous, and widespread data coverage, the process can resemble performing surgery without first understanding the symptoms or confirming the diagnosis. As a result, agencies may miss key opportunities to retime signals where optimization could have the greatest impact—or may direct resources toward locations that are not in urgent need of adjustment. Improved data sources would also facilitate a transition from infrequent, periodic adjustments to more continuous and responsive optimization as traffic patterns evolve.

Vehicle trajectory data offers a unique opportunity to enable more systematic, large-scale signal timing management by delivering continuous and widespread insights into current traffic dynamics. However, few comprehensive solutions currently exist that fully leverage the advantages of this data to 1.) detect performance issues at signalized intersections, 2.) diagnose their root causes, and 3.) implement the targeted interventions needed to improve their operation. Such a solution would offer a more scalable, efficient, iterative, and cost-effective solution that could be applied to signalized intersections around the world.

1.2 Dissertation overview

1.2.1 Research scope

This dissertation presents one of the world's first traffic signal timing management systems that relies solely on currently available vehicle trajectory data, even at low penetration rates, and represents a major milestone in this research group's ten years of groundbreaking theoretical work—culminating in a deployable system with demonstrated impact in real-world transportation engineering practice. The system is built around three core functions: performance monitoring, diagnostics, and targeted retiming interventions—forming a closed-loop framework that offers a comprehensive, systematic solution. Key technical contributions of this dissertation include a method for determining minimum yellow change and all-red clearance intervals that reduce the risk of red-light running by eliminating dilemma zones; the development of the Signalized Intersection Performance Diagram (SIPD), which integrates signal timing data with advanced performance analytics to identify the root causes of congestion by diagnosing inefficient right-of-way control; and rule-based approaches for diagnosing signal coordination deficiencies without requiring signal timing data from the agency. In addition, the system includes procedures for iteratively optimizing timing plan schedules, cycle lengths, offsets, and green splits every few weeks to alleviate traffic congestion caused by evolving traffic demand patterns.

Figure 1.6 charts how the traffic signal timing management system presented in this dissertation supports these four applications (represented by the blue boxes on the far right side of the figure). Each procedure in the system is designed to be implemented in a microservice manner on the cloud. Therefore, the system is highly maintainable, scalable, and robust. Moreover, the architecture has been deliberately structured to support future scalability, enabling the incorporation of new applications with minimal modification.

The system utilizes vehicle trajectory data as the exclusive input for inferring and analyzing prevailing traffic dynamics. It is compatible with any data source that supplies a unique trip ID, timestamp, and GNSS coordinates within every 5 seconds. The accuracy of the GNSS coordinates should not be larger than 10 meters. The trajectory data is preprocessed through data archiving, matching the points to compatible map data, and traffic performance calculations (e.g., SPMs). All of these procedures are available in Wang et al. (2023). In addition to the SPMs described in that work, this system utilizes new performance measures introduced in this dissertation. The database includes all of the processed map, trajectory, and signal timing data. The signal timing data is provided by a local traffic agency, but is not required for all applications.

Each application retrieves the requisite data from the database to execute the corre-

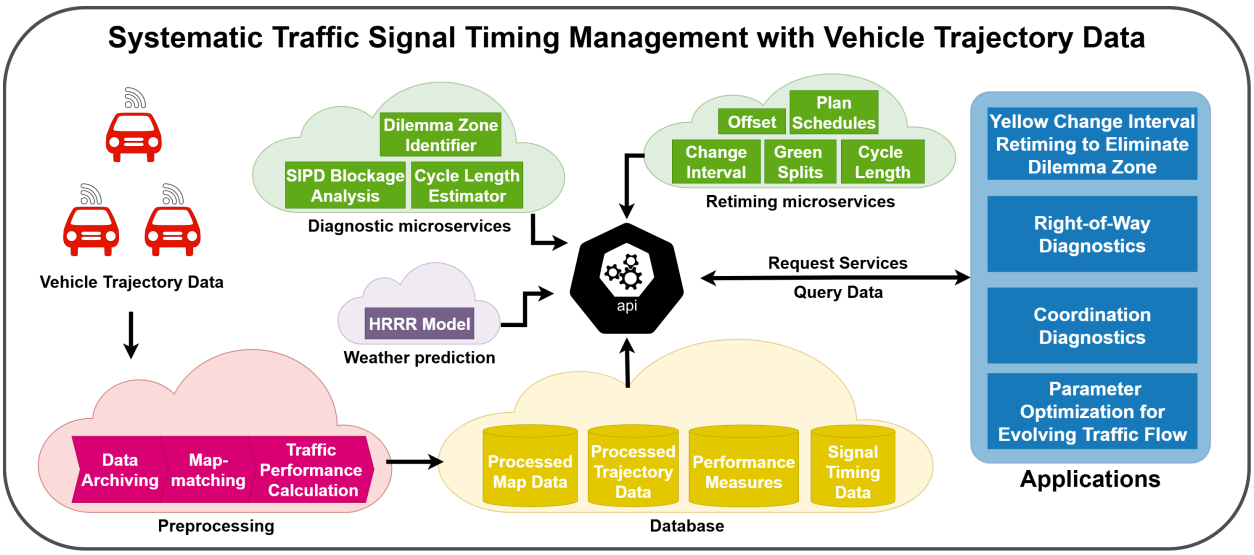

Figure 1.6: Systematic traffic signal timing management with vehicle trajectory data

sponding microservices, which are modularly organized into diagnostic and retiming functionalities. The retiming microservices can address key parameters associated with traffic signal timing for fixed-time and coordinated-actuated signal control, including timing plan schedules, cycle lengths, offsets, green splits, and yellow change intervals. The system does not currently adjust flash schedules, phase modes (e.g., recall mode), left-turn operations (e.g., permissive/protected or leading/lagging), and pedestrian clearance intervals. For now, these parameters are treated as constraints. The right-of-way diagnostics application does provide insight into the performance of left-turn permissive movements, but the system does not have any modules for changing operations. However, as mentioned before, the system is designed in a way that will allow for the smooth incorporation of microservices targeting these parameters in the future.

While performance measures can provide help us measure congestion levels, the diagnostic microservices are designed to identify signal retiming opportunities by measuring inefficiencies. Figure 1.7 differentiates performance measures from diagnostics for each application. First, let us consider the yellow change interval retiming application. A key performance measure that may indicate the need for retiming of yellow change interval is red light running. However, a red light violation alone can not differentiate between an improperly timed interval or driver error. Therefore, our system includes a "dilemma zone identifier" to first diagnose if the signal timing is properly deigned to allow drivers enough time to cross the stop bar if they can no longer stop once the yellow light is shown.

The right-of-way diagnostic application identifies where there may be inefficient right-of-way allocations. This could refer to both protected and permissive right-of-way. Through

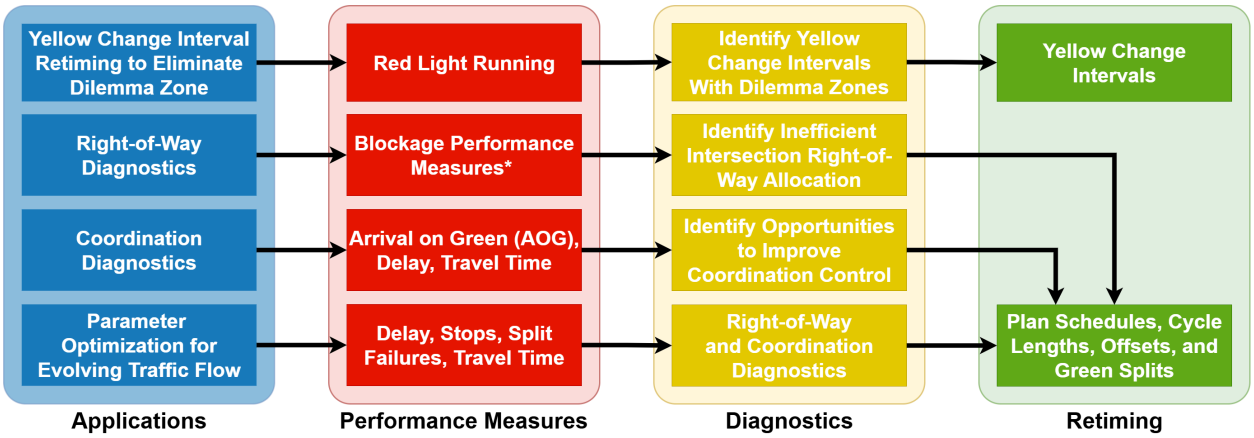

Figure 1.7: Applications

the development of the SIPD, we introduce new performance measures that determine if the traditional SPMs were caused by blockage (such as when waiting for acceptable gap during the permissive phase) or queues formed during the red light phase. These are the only new performance measure introduced in this dissertation. The ability to differentiate between these two types of scenarios provides new diagnostic capabilities when attempting to mitigate congestion at intersections.

Coordination diagnostics allow us to identify opportunities for improving signal coordination. While traditional measures such as percent AOG, delay, and travel time provide information about the performance of the coordination, they can't always indicate if there is an opportunity for improvement. Notably, this application does not require any knowledge of the current signal timing data. The system contains a "cycle length estimator" in the diagnostic microservices which allow us to check for inconsistent cycle lengths across corridors. In addition, this application utilizes the High-Resolution Rapid-Refresh (HRRR) model for weather prediction, enabling it to diagnose poor traffic signal coordination performance during winter conditions.

Finally, the parameter optimization for evolving traffic flow application includes procedures for iteratively optimizing timing plan schedules, cycle lengths, offsets, and green splits every few weeks to alleviate traffic congestion. It leverages both the right-of-way and coordination diagnostics to identify intersections that can be optimized and then develops the new timing plans. This dissertation builds on the foundations described in Wang et al. (2024a) to establish the full set of retiming microservices used by this application.

This dissertation aims to demonstrate a deployable system with demonstrated impact in real-world transportation engineering practice. Each chapter will describe in detail each application introduced and include real-world case studies using the data described in the next

section. Therefore, the system's technical readiness for deployment is demonstrated through multiple real-world implementations, including a direct comparison with a traditional optimization.

1.2.2 Data

Unless otherwise noted, the vehicle trajectory data used in this dissertation is from an automotive original equipment manufacturer (OEM), who equips their vehicles with GNSS receivers and inertial measurement units (IMUs) that provide accurate vehicle position and dynamics information. Approximately every 3 seconds, each vehicle sends a unique de-identified and scrambled trip ID, GNSS coordinates (latitude and longitude), timestamp, and speed measurements approximately every 3 seconds. The coordinates are accurate to roughly within 3-5 meters. The road network is re-organized from the open-source online resource OpenStreetMap (Bennett, 2010). Each vehicle trip is matched to the road network and then the raw GNSS coordinates are converted to distance information. Vehicle trips are split into trajectories at each intersection movement. More information about this process can be found in Wang et al. (2023). Data was provided at various times and locations in Oakland County, MI between March, 2022 through July, 2025. The penetration rate of equipped OEM vehicles in Oakland County is estimated to be around 7% (Wang et al., 2024a).

1.2.3 Contributions

The contributions of this dissertation are listed as the following:

1. Utilize real-world vehicle trajectory data to evaluate the current kinematic methods for determining the duration of yellow change and red clearance intervals. Based on this evaluation, we propose a new kinematic equation for determining yellow change and red clearance intervals.

2. A new framework for determining minimum yellow change intervals for eliminating dilemma zones using vehicle trajectory data. The temporal-spatial advantages of vehicle trajectory data are leveraged to extract the exact time it takes for drivers to cross the stop bar once they can no longer stop, enabling cloud-based efficient calculations of minimum yellow change intervals at scale.

3. A Signalized Intersection Performance Diagram (SIPD): a time-space diagram segmented according to the dynamics of queue formation and dissipation in response to

traffic signal control. With green split and cycle length information, this diagram is generalizable for any signalized intersection, providing a uniform method for evaluating overall intersection congestion from trajectory observations.

4. New performance measures that determine if the control delay, number of stops, and split failures are caused by blockage or queues formed during the red light phase. The ability to differentiate between these two types of scenarios will provide new diagnostic capabilities when attempting to mitigate congestion at intersections.

5. Rule-based approaches for diagnosing signal coordination deficiencies from vehicle trajectory data without requiring signal timing data from the agency. These include estimating the cycle length to identify inconsistencies along corridors and observing changes in free-flow travel times between intersections during winter weather.

6. Procedures for iteratively optimizing timing plan schedules, cycle lengths, offsets, and green splits every few weeks in response to evolving traffic demand patterns using vehicle trajectory data. The technical readiness for deployment of these procedures is demonstrated through multiple real-world implementations, including a direct comparison with a traditional optimization.

These contributions are integrated into one systematic traffic signal timing management system (Figure 1.6), providing complete signal retiming processes through three key functions: identifying congestion through performance measures, diagnosing signal optimization opportunities by measuring inefficiencies, and performing dynamic traffic signal retiming (Figure 1.8). The expected advantages of this system are two-fold: 1. It will eliminate manual signal timing procedures by advancing traffic signal systems with static parameters (i.e., fixed-time and actuated control) to automatic dynamic systems with periodical parameter updates; 2. Transportation agencies will be less reliant on infrastructure-based sensors for traffic signal timing management. By leveraging trajectory data as the sole input and requiring no additional infrastructure, this system offers a scalable and cost-effective solution that can be applied to signalized intersections around the world.

1.2.4 Organization

Each of the four applications illustrated in Figures 1.6 and 1.7 are covered in Chapters 2 through 5. While each of these chapters describe key components of the signal timing management system, they also cover unique independent functionalities and can be treated as stand-alone works. Therefore, each chapter contains detailed discussions of the background

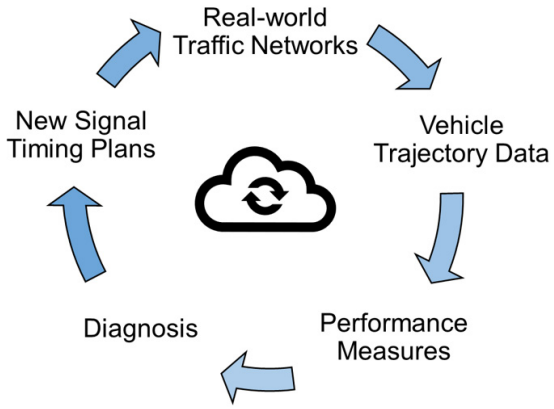

Figure 1.8: Integrated online signal retiming process

and relevant literature, descriptions of the key contributions and their respective methodology, real-world case studies to demonstrate their potential for deployment, and summaries and future directions. A short discussion on how the contributions of each chapter are integrated into the system illustrated in 1.6 is also included. A comprehensive summary of the system, along with a discussion of potential future research directions, is presented in Chapter 6.

CHAPTER 2

Evaluating Yellow Change and Red Clearance Intervals

2.1 Introduction

2.1.1 Background

Traffic signal yellow change and red clearance intervals are designed to safely transfer right-of-way between different conflicting vehicular traffic movements. These intervals are timed according to human driver behavior and vehicle kinematics. Therefore, they are typically determined using kinematic models that incorporate factors such as driver perception-reaction time, approach speed, and maximum comfortable deceleration. The yellow change interval provides a warning that the transfer of right-of-way between different phase movements at signalized intersections is beginning. The red clearance interval allows time for vehicles that entered the intersection during the yellow change interval to clear the intersection before the beginning of the next conflicting movement.

It is important that these intervals provide sufficient time for drivers to clear an intersection before conflicting traffic movements begin. For yellow change intervals, a common approach is to provide drivers that are too close to the intersection to decelerate comfortably to a stop with enough time to cross the stop bar before the yellow change interval terminates (ITE, 2020). Otherwise, there will be a "dilemma zone" where drivers can neither stop before the stop bar nor pass it before the red indication. Driver uncertainty in this zone is particularly dangerous as it can lead to unsafe behaviors such as rapid acceleration, unsafe emergency braking, or red-light running. Red clearance intervals are typically designed to provide sufficient time for vehicles that entered the intersection at the end of the yellow change interval to safely clear the intersection. This accounts for drivers who may have crossed the stop bar just as the signal changed from yellow to red (ITE, 2020; FHWA, 2023). A key difference of the yellow change interval that makes it more challenging to

design than the red clearance interval is that the stopping distance among drivers is variable depending on their approach speeds, while the distance between the stop bar and clearing the intersection is fixed.

The point at which the driver can no longer safely stop before the intersection is called the critical distance. It can be easily calculated from the stopping sight distance (SSD) equation that includes both the distance traversed during the perception-reaction time and the braking distance, with a constant approach speed as the input. In 1960, Gazis, Herman, and Maradudin (GHM) proposed a kinematic solution for the change interval that simply divided the critical distance by the constant intersection approach speed (usually free-flow speed) (Gazis et al., 1960). The red clearance interval is calculated by dividing the width of the intersection plus the length of the design vehicle by that same constant intersection approach speed. However, later studies and comments by one of the original GHM authors indicate that this solution only applies to straight through movements where vehicles are traveling at a constant speed (Beeber, 2020; Rossow, 2020; Maradudin, 2015). Traveling through the critical distance may take longer for left-turning vehicles because they need to decelerate as they approach the intersection in order to safely and comfortably execute the maneuver. Therefore, a yellow change or red clearance interval timed according to the original kinematic equation by GHM, which assumes constant speed through the critical distance and intersection, might not provide enough time for a turning vehicle to cross the stop bar or clear the intersection after the yellow indication, creating a dilemma zone.

The original GHM kinematic equations had been the recommended practice of the Institute of Transportation Engineers (ITE) since 1965 (Baerwald, 1965). However, to account for left-turning drivers decelerating before making turning maneuvers, ITE adopted an extended kinematic equation, as their recommended practice for calculating yellow change and red clearance intervals for both left-turn and straight-through movements in March 2020 (ITE, 2020). With the extended kinematic equation, the change interval for a left-turn phase is longer than that of the original GHM kinematic equation as the average speed while traversing the critical distance is lower. The clearance interval will also be longer as the entry speed into the intersection is lower than the approach speed. Because this equation is relatively new and there are some concerns over its necessity, a lot of municipalities across the United States have either not had a chance or chosen not to implement the extended kinematic equation.

2.1.2 Related works

ITE has been providing guidelines and reference material for calculating yellow change and clearance intervals since 1941 (Eccles and McGee, 2001). The GHM solution was first recommended by ITE in the 1965 Traffic Engineering Handbook (Gazis et al., 1960; Baerwald, 1965). Since then the research has developed into the well known "kinematic equation" and has become a staple for yellow change and red clearance interval timing, appearing in ITE publications in 1982, 1985, 1994, and 2001 (ITE, 2020). However, ITE failed to ratify a proposed recommended practice in 1985, and most of these publications were informational reports (ITE, 2020). Many research questions, such as the determination of approach speeds, deceleration rates, and perception-reaction times, prevented an ITE recommendation (Eccles and McGee, 2001). A lack of understanding and many incorrect interpretations of the dilemma zone introduced by GHM in 1960 resulted in improper policy solutions and a failed consensus on a uniform recommendation (Järlström, 2020; Liu et al., 1996). Additionally, there was, and still is today, a lack of uniformity in state vehicle codes regarding permissive or restrictive yellow light laws (Mohammed, 2019; Järlström, 2014).

In 1996, Gazis and Herman, together with Liu, published a paper in an attempt to clear up confusion about the dilemma zone and proposed a yellow duration that eliminated the conflict (Liu et al., 1996). The research confirmed that the dilemma can be eliminated by the GHM equation. The kinematic equation was included as a recommendation by the Federal Highway Administration (FHWA) in the Manual on Uniform Traffic Control Devices (MUTCD) and the Traffic Signal Timing Manual in 2009, but there was still uncertainty about approach speeds and the need for a clearance interval (FHWA, 2023; Transportation Research Board and National Academies of Sciences, Engineering, and Medicine, 2015). The National Cooperative Highway Research Program (NCHRP) Report 731, Guidelines for Timing Yellow and All-Red Intervals was published in 2012 (McGee Sr et al., 2012). This report summarized the findings of NCHRP Project 03-95 with the goal of developing comprehensive and uniform guidelines for yellow and red intervals. The project conducted an extensive review of the existing state of practice and published literature. It also performed a detailed investigation of driver behavior through collected field data. The report recommended the kinematic equation with the 85th percentile speed as the approach speed, and confirmed the accepted parameter values of 1 second for perception-reaction time and 10 ft/s^2 for the deceleration rate. The project also recommended universal practices for measuring intersection width and justified subtracting the conflicting movement start up delay when calculating the clearance interval.

The NCHRP report found that the 85th percentile measured approach speed for left-turning vehicles was generally slower than for vehicles traveling straight (McGee Sr et al.,

2012). However, simply inserting a slower constant speed into the kinematic equation will produce a shorter interval. Left-turning vehicles continue decelerating through the approach, so they actually require longer yellow change intervals as it takes them more time to reach the stop bar. Therefore, a modification to the kinematic equation was needed to accurately capture the deceleration behavior of left-turning vehicles since it is only designed for vehicles traveling at a constant speed (Maradudin, 2015). In 2002, Liu et al. found that the required yellow change interval for left-turn movements is generally longer than what is required for straight movements (Liu et al., 2002). They modified the kinematic equation to account for vehicle deceleration by adding a parameter for intersection entry speed, which is dependent on the average curvature of the left turn and comfortable acceleration values. The paper also introduced a new method for calculating the clearance interval based on curvature length and average speed. Yu et al. further modified the equation to include delay from low traffic signal visibility (Yu et al., 2003). In 2015, Järlström conducted research targeting red light camera enforcement abuses on right-turns that were exhibiting dilemma zones based on yellow change intervals that were too short (Järlström, 2020, 2021). The resulting "extended kinematic equation" from this work is now the current ITE recommendation for left-hand and straight-through approaches (ITE, 2020). However, very few studies have validated the assumptions made about the kinematic behavior of free-flowing left-turning vehicles in this equation.

2.1.3 Contributions and organization of the chapter

The contributions of this chapter are as follow:

1. Analysis of the kinematic behavior of free-flowing left-turning vehicles in real-world vehicle trajectory data compared to the assumptions made in the extended kinematic equation. Based on this evaluation, we propose a new kinematic equation for determining yellow change and red clearance intervals.

2. A new framework for determining minimum yellow change intervals that eliminate dilemma zones using vehicle trajectory data. The temporal-spatial advantages of vehicle trajectory data are leveraged to extract the exact time it takes for drivers to traverse the critical distance. No kinematic model is needed because the complete trajectory path is provided and hence no speed parameter inputs are required, enabling cloud-based efficient calculations of minimum yellow change intervals at scale.

Section 2.2 provides an overview of the current kinematic models for yellow change and red clearance intervals used in practice, including the newly recommended extended kinematic

equation. Section 2.3 describes the vehicle trajectory preprocessing procedures required before analysis. Section 2.4 discusses our analysis of the kinematic behavior of free-flowing left-turning vehicles, proposes a new kinematic model based on this evaluation, and provides a case study evaluation of nine left-turning movements in Ann Arbor, MI. Section 2.5 presents a new framework for determining minimum yellow change intervals that eliminate dilemma zones using vehicle trajectory data and demonstrates its capabilities through a citywide case study in Birmingham, MI. Finally, we summarize the chapter in Section 2.6.

2.2 Current kinematic models

This section discusses the current kinematic models commonly used in practice to determine minimum yellow change and red clearance intervals. The major new recommendation in the 2020 ITE guidelines was the extended kinematic equation for the calculation of yellow change intervals (ITE, 2020). Because this equation is relatively new and there are some concerns over its necessity, a lot of municipalities across the United States have either not had a chance or chosen not to implement the extended kinematic equation. Therefore, we include descriptions of both methods in this section for comparison.

ITE and MUTCD guidelines also recommend the uniform practice of the "permissive" yellow law in all 50 states. In "permissive" yellow laws, vehicles are allowed to enter the intersection during the yellow change interval, and clearance is accounted for during the red clearance interval when all phases are restricted from entering the intersection (FHWA, 2023; ITE, 2020). In "restrictive" yellow law, clearance is included in the yellow interval and drivers can neither enter nor be in the intersection on red. The permissive law has several advantages over the restrictive law. Studies have found that providing longer yellow interval times may actually encourage drivers to cross the stop bar later in the interval rather than provide intersection clearance (Benioff et al., 1980; Choupani, 2020). The NCHRP Project 03-95 findings report noted that including both the change and clearance duration in the yellow interval may confuse drivers (McGee Sr et al., 2012). There also seems to be some inconsistencies in the way state laws are communicated to drivers. A recent study found that although 74% of states follow permissive law, 72% of states cover restrictive law in their driver training manual (Mohammed, 2019). Additionally, it is not uncommon for restrictive states to still time their intersections according to permissive law (McGee Sr et al., 2012), which can lead to more driver confusion. Therefore, all the formulas and analysis in this section operate in terms of "permissive" law by separating the yellow change and clearance intervals.

2.2.1 Yellow change interval

The original kinematic equation developed by GHM estimates an approaching driver's travel time through the critical distance (Gazis et al., 1960), defined as:

$$x_c = v_0\delta + \frac{v_0^2}{2a^*} \tag{2.1}$$

where: x_c = critical distance
v_0 = original approach speed
δ = perception-reaction time; and
a^* = maximum safe and comfortable deceleration rate

As shown in Figure 2.1 (a), the critical distance is split into two sections. The first section, the perception-reaction (PR) distance, is the distance covered by the driver during the perception-reaction time δ until they activate the brake (braking point). The second section is the distance covered while the vehicle decelerates to a complete stop (braking distance). For simplicity, we ignore the term for approach grade during the braking distance.

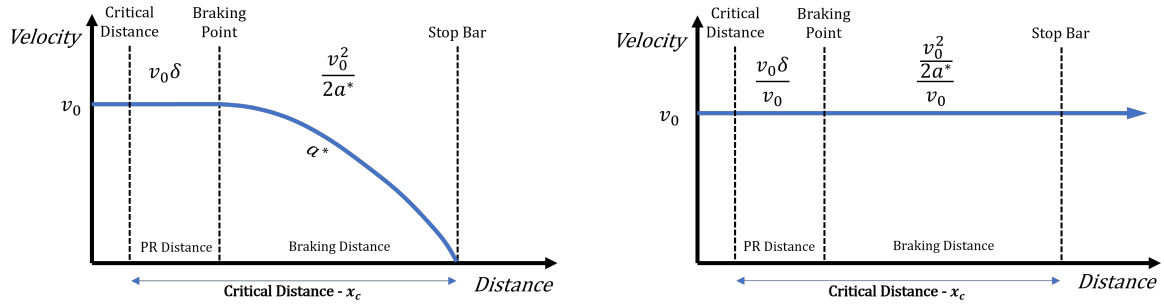

(a) Critical Distance (b) Free-Flowing Vehicle Speed Profile

Figure 2.1: Original GHM kinematic model for determining yellow change intervals

If, at the indication of the change interval, a driver's distance to the stop bar x is less than x_c, they cannot safely stop at the stop bar. Therefore, to account for all possibilities of $x \leq x_c$, the change interval duration Y must, at minimum, be equal to the driver's travel time through x_c (denoted as t_c):

$$Y_{min} = t_c \tag{2.2}$$

Otherwise, there would be a type I dilemma zone where the driver can neither safely stop before the stop bar nor pass it before the red indication. Refer to Urbanik and Koonce, *The*

Dilemma with Dilemma Zones, for more information about dilemma zone types (Urbanik and Koonce, 2007). The critical distance is independent of the actual change interval duration Y. Drivers do not require any knowledge of this duration to determine if they can safely stop before the stop bar. Therefore, using the critical distance to determine change intervals assumes that drivers, at the indication of the change interval , primarily consider if they can stop when making their stop/go decision. This assumption is debatable as many drivers may try to determine if they can pass the stop bar before the red indication (Olson and Rothery, 1972; Chang et al., 1985; Wortman and Fox, 1986), hence why the calculated Y_{min} from the kinematic equations are minimum recommended durations. At the very least, Y_{min} should be greater than or equal to the free-flow critical distance travel time t_c to prevent type I dilemma zones.

The original kinematic equation assumes constant free-flow speed through the critical distance (Figure 2.1 (b):

$$t_c = \frac{x_c}{v_0} \tag{2.3}$$

giving us:

$$Y_{min} = \frac{v_0\delta + \frac{v_0^2}{2a^*}}{v_0} = \delta + \frac{v_0}{2a^*} \tag{2.4}$$

To account for variations in speed amongst drivers, Y_{min} is calculated using the 85th percentile speed ($v_{0,85}$) under free-flow conditions (Gazis et al., 1960):

$$Y_{min} = \delta + \frac{v_{0,85}}{2a^*} \tag{2.5}$$

Later research determined that the type I dilemma zone could be eliminated according to this equation (Liu et al., 1996). It has since been recommended by ITE, the FHWA, and in NCHRP reports (ITE, 2020; FHWA, 2023; Koonce, 2008; McGee Sr et al., 2012).

The extended kinematic equation recommended by ITE in 2020 accounts for changes in intersection approach speed when preparing for turning maneuvers (ITE, 2020; Järlström, 2020; Beeber, 2020). This equation assumes that drivers slow down from the original speed to some intersection entry speed v_e at the maximum comfortable deceleration before entering the intersection and executing the maneuver:

$$t_c = \frac{x_c}{v_0 \rightarrow v_e} \tag{2.6}$$

These intervals will be longer than the original kinematic equation because the denominator in Eq. 2.6 is on average smaller than that in Eq. 2.3.

In this new equation, the calculation of the critical distance remains unchanged, but the braking distance is divided into two parts for the sake of visualizing how the speed profile of a free-flowing vehicle is modeled (Figure 2.2 (a)). This new speed profile assumes that a free-flowing vehicle will travel at v_0 through the perception-reaction time (PR distance), but then decelerate at the maximum safe and comfortable rate a^* until reaching the desired intersection entry speed v_e at the go point (deceleration distance). It will then travel at v_e past the stop bar (go distance). The extended kinematic equation is calculated by dividing the PR distance by v_0, the deceleration distance by the average of v_0 and v_e, and the go distance by v_e:

$$
\begin{aligned}
Y_{min} &= \frac{v_0\delta}{v_0} + \frac{\frac{v_0^2 - v_e^2}{2a^*}}{\frac{v_0 + v_e}{2}} + \frac{\frac{v_e^2}{2a^*}}{v_e} \\
&= \delta + \frac{v_0 - v_e}{a^*} + \frac{v_e}{2a^*} \qquad (2.7) \\
&= \delta + \frac{v_0 - \frac{v_e}{2}}{a^*} \qquad (2.8)
\end{aligned}
$$

Note that for straight through movements, v_0 and v_e are assumed to be equal and the equation reduces to the original GHM kinematic equation.

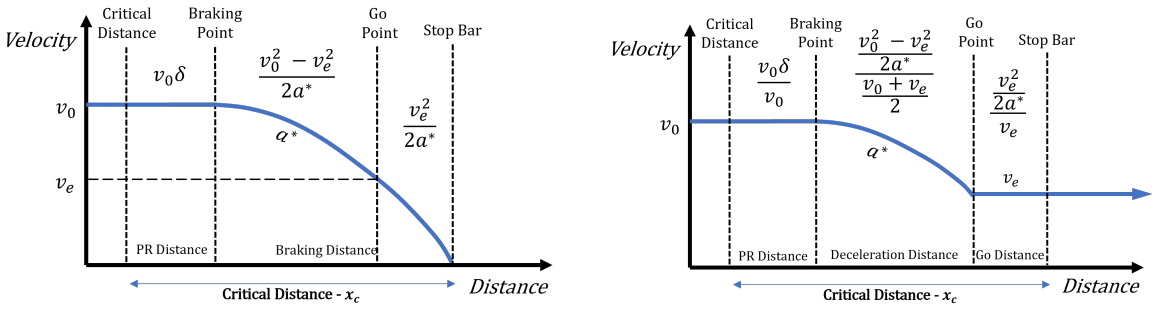

(a) Critical distance (b) Free-flowing vehicle speed profile

Figure 2.2: Extended kinematic model for determining yellow change intervals

To account for variations in speed among drivers, Y_{min} is calculated using the 85th percentile original entry speed ($v_{0,85}$) and 85th percent intersection entry speed ($v_{e,85}$) under free-flow conditions (ITE, 2020):

$$Y_{min} = \delta + \frac{v_{0,85} - \frac{v_{e,85}}{2}}{a^*} \tag{2.9}$$

2.2.2 Red clearance interval

Figure 2.3 illustrates the speed profile models for the original and extended kinematic equations when determining the red clearance interval for left-turning vehicles, assuming they decide to pass through the intersection at the yellow indication. Figure 2.3 (a) shows how the vehicle travels at v_0 through the intersection in the original model. Intersection width (w) is measured from the stop bar to the nearest "no conflict point" after the vehicle clears the intersection. The 2020 ITE guidelines define the no conflict point as the curb-line extension or outside edge of the travel lane of the farthest conflicting movement. The vehicle is not considered to be fully cleared through the intersection until it is entirely past the no conflict point. Therefore, intersection clearance does not occur until the vehicle has traversed both w and l (the length of the vehicle). The original equation uses v_0 to model speed through the clearance distance:

$$R = \frac{w + l}{v_0} - t_s \tag{2.10}$$

where t_s is the conflicting vehicular movement start up delay. Note that while the calculation for change intervals is for the minimum Y because of the differences in how drivers may interpret the yellow indication, the purpose of the red clearance interval is much more straightforward in that it must provide enough time for the driver to cross a fixed distance. Therefore, the calculation is for the absolute R rather than a minimum value.

The extended kinematic equation takes into account that turning vehicles will travel at a slower speed through the intersection. Figure 2.3 (b) depicts how a passing vehicle travels at entry speed v_e through the intersection in the extended kinematic model. Therefore, this equation uses v_e to model speed through the clearance distance:

$$R = \frac{w + l}{v_e} - t_s \tag{2.11}$$

2.2.2.1 A note on 85th percentile Speeds

As with the clearance interval, ITE recommends using the 85th intersection entry speeds when implementing these intervals. However, this recommendation creates some unintended consequences. In the calculation of Y_{min} in Equation 2.5, the 85th percentile approach speed

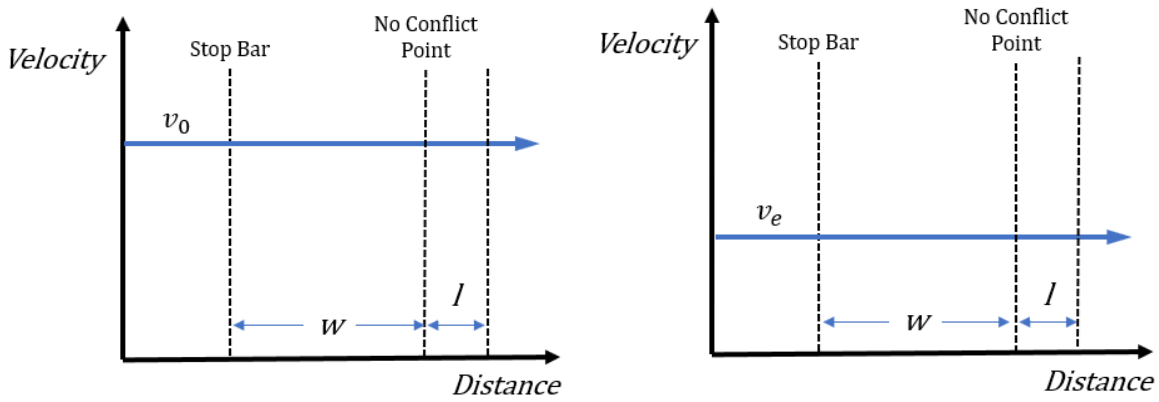

(a) Original GHM kinematic (b) Extended kinematic

Figure 2.3: Free-flowing vehicle speed profiles for original GHM and extended kinematic models when determining clearance intervals

is in the numerator of its respective term, meaning that an increase in this parameter will increase Y_{min}. However, in Equations 2.10 and 2.11, the approach and intersection entry speeds are in the denominator, so the resulting R will decrease with increases in speeds. This difference means that red clearance intervals calculated according to the recommend speed percentile are actually designed to provide enough time for the 15th percentile of drivers, rather than for the 85th percentile as intended. This works leaves the implications of this phenomena for future study as we are primarily interested in understanding the kinematic behavior of vehicles as they travel through the intersection. In this chapter, we will use the 85th percentile speeds when discussing the red clearance interval in order to give readers a more relative understanding of the differences between the common practice and our observations.

2.3 Vehicle trajectory preprocessing for yellow change and red clearance interval analysis

This section discusses how we process vehicle trajectory data before using them to evaluate change and clearance interval requirements. The analysis in this chapter is primarily focused on the speed profiles of free-flowing vehicles as they approach an intersection. We define a "free-flowing" trajectory as one that does not stop in or is not majorly influenced by the queue formed at the intersection during the red light. In other words, it is one that might conceivably have an interaction with a yellow change interval. Because the studies in this chapter use different datasets with varying resolutions, the methodology for identifying free-

flowing trajectories is different in each case and will be explained in their respective sections. While Signal Phase and Timing (SPaT) data are not necessary for identifying free-flowing trajectories, they are utilized in this chapter to identify the existing yellow change interval lengths for comparison.

Once the free-flowing trajectories are identified, the next step measures each free-flow trajectory's respective critical distance (x_c) through an iterative search procedure. At each trajectory point p, the stopping distance x_s is calculated according to the SSD:

$$x_s = v_p\delta + \frac{v_p^2}{2a^*} \tag{2.12}$$

where v_p is that point's speed (Figure 2.4). For δ and a^*, we use the standard recommended values of 1 second and 10 ft/s^2, respectively (ITE, 2020; McGee Sr et al., 2012). Once x_s equals the distance to the stop bar x, the iterative search stops, and that point is the critical distance (Eq. 2.1. In Figure 2.4, a typical speed profile for a vehicle approaching an intersection is shown in yellow. The blue dashed line represents a potential first evaluation point. The stopping distance x_s does not equal the distance to the stop bar x, so the search procedure must continue. The red dashed line represents a stopping profile where the stopping distance x_s equals the distance to the stop bar x and is therefore the critical distance x_c. Once x_c is identified, the speed profile is ready to be analyzed and other important trajectory performance measures can be extracted such as the intersection entry speed v_e.

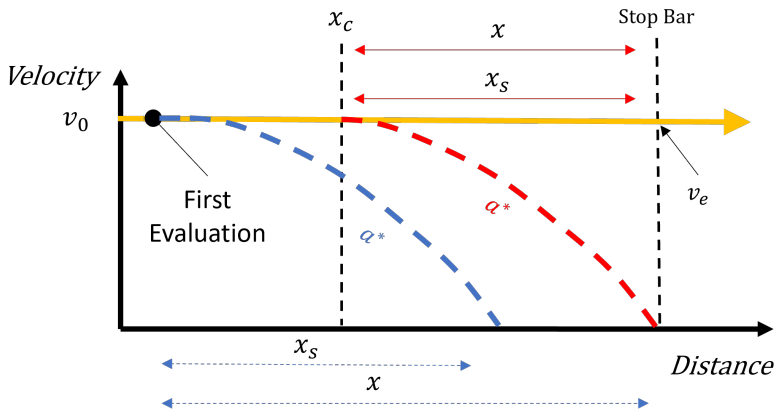

Figure 2.4: Critical distance identification for individual trajectory.

The δ and a^* parameters in Eq. 2.12 can be changed according to preferred practice. It is also important to note that the framework proposed in this chapter can be easily adjusted to account for other decision points that an engineer wishes to measure when timing the change interval. For instance, the method for calculating the critical distance could be changed to

account for variable acceleration as considered by M. Järlström in (Järlström, 2021), or a universal decision distance according to a stop/go probability could be used instead of a unique critical distance for each trajectory.

2.4 New kinematic model for left-turn movements

Traffic engineers have raised two main concerns about the appropriateness of the extended kinematic equation. First, the equation is very sensitive to the approach and entry speed parameters and in some cases generates intervals longer than the maximum duration of 6 seconds set by the MUTCD (FHWA, 2023). Second, there are unvalidated assumptions about the kinematic behavior of free-flowing left-turning vehicles (Cesme et al., 2023). For instance, the extended kinematic equation developed by M. Järlström in 2015 was developed through research that specifically targeted abuses of red-light camera enforcement on right-hand turns, not left-hand turns as recommended by ITE (Beeber, 2020; Järlström, 2020, 2021). As a result, many transportation agencies have chosen not to adopt the extended kinematic equation due to concerns about the validity of the assumptions made in the kinematic modeling of left-turning drivers (Cesme et al., 2023).

This section addresses these concerns by analyzing real-world vehicle trajectory data to model the free-flow behavior of left-turning vehicles. Vehicle trajectories from the Ann Arbor Connected Vehicle Test Environment (AACVTE) confirm that free-flowing left-turning vehicles decelerate, but deceleration usually starts at a moderate rate before reaching the critical distance and continues to the middle of the intersection. Vehicles then accelerate to a departure speed at the clearance point. Since the goal of the yellow change interval is to eliminate the dilemma zone such that a free-flowing vehicle can safely traverse the critical distance, these observations imply that the extended kinematic equation will overestimate the required duration for the following two reasons: 1.) the critical distance is shortened by the speed reduction before the braking point; 2.) the average traversing speed is higher as vehicles usually decelerate at a moderate rate instead of the maximum rate. The equation will underestimate the clearance interval as the average traversing speed through the intersection is slower than the intersection entry speed. Based on these findings, we propose a new kinematic equation for determining yellow change and red clearance intervals for left-turn movements.

2.4.1 Vehicle trajectory speed profile observations

The key to validating the extended kinematic equation is to verify its assumptions about the speed profile of free-flowing left-turning vehicles. We can then evaluate how accurately the equation calculates the time it will take for the vehicle to travel through the critical distance. These assumptions must be validated by observing the vehicle kinematics of real-world trajectories executing left turns through signalized intersections. To conduct this evaluation, this study leverages data from the AACVTE, where over 2,500 private vehicles (less than 3% penetration rate) were equipped with connected vehicle (CV) technology (Wang et al., 2020). Each vehicle broadcasts standard Basic Safety Messages (BSMs) which are received every 0.1 seconds by Roadside Units (RSUs) within communication range according to the Society of Automotive Engineers (SAE) J273 standard. Each BSM includes trajectory point information such as a unique trajectory ID, timestamp, Global Navigation Satellite System (GNSS) coordinates (e.g., latitude and longitude), and instantaneous speed and acceleration. The trajectory data was processed and matched to the road network according to the same methods used for the original equipment manufacturer (OEM) dataset described in section 1.2.2. This study analyzed four intersections on the Plymouth Road corridor from December 8th, 2020 to July 3rd, 2021 (Figure 2.5). The four intersections are located at Green Rd, Huron Pkwy, Nixon Rd, and Murfin Ave. We then obtained the vehicle trajectory data for left-turning phases at these four intersections. Overall, there were 24,460 total trajectories at the 16 left turn phase movements of interest over the study period.

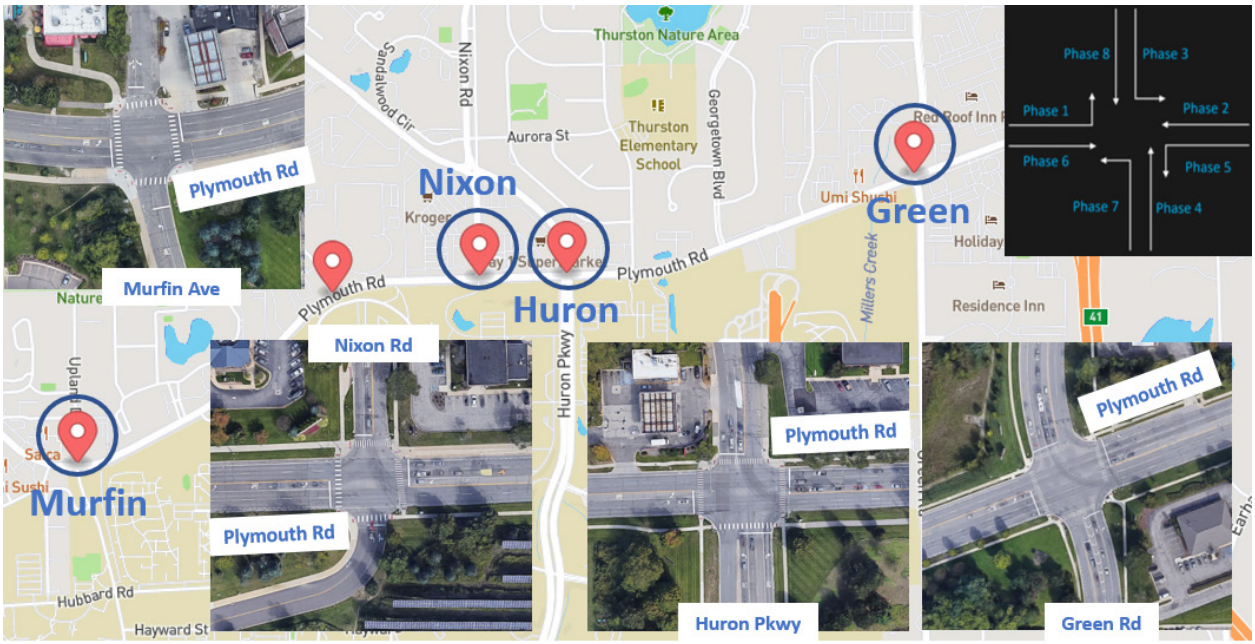

Figure 2.5: Plymouth Rd corridor and intersections of interest

As mentioned in section 2.3, a free-flowing left-turning vehicle is identified when its trajectory is not influenced by or inhibited by a queue formed by vehicles waiting at the intersection. Even though the vehicles in this study were not equipped with sensors that identify surrounding vehicles, the natural deceleration profile of a left-turning vehicle provides an easy way of identifying free-flowing vehicles. Stopped vehicles or those who slow down as they approach the end of a queue will exhibit acceleration after the left turn is given the right-of-way. Therefore, enabled by the 0.1 second frequency in the AACVTE dataset, we can eliminate vehicles that exhibit any acceleration as they approach the stop bar, and we are left with a small percentage of vehicle trajectories that are free-flowing.

Out of the 16 left turn phase movements analyzed on the Plymouth Road corridor, 9 of them provided more than 10 free-flowing trajectories for a total of 262 trajectories (Table 2.1). The cumulative speed vs. distance to stop bar profiles for 8 of these intersections are plotted in Figure 2.6. The red points represent the critical distance point for each trajectory and the vertical red line is the stop bar location at distance equals zero. The green points represent intersection clearance. Note that the distance between the stop bar and intersection clearance can be different for each trajectory depending on the turning radius of the vehicle. In the following we will analyze the results of these profiles and compare them with the extended kinematic equation.

Table 2.1: Number of free-flowing trajectories for each Plymouth Rd intersection by phase movement

Intersection	Phase 1	Phase 3	Phase 5	Phase 7
Green Road	10	98	16	15
Huron Parkway	N/A	14	N/A	11
Nixon Road	41	19	N/A	N/A
Murfin Avenue	N/A	N/A	N/A	38

We observe three unifying characteristics in the observed free-flowing vehicle speed profiles illustrated in Figure 2.6 that are different from the profile used to formulate the extended kinematic equation shown in Figure 2.2 (b). First, the vehicles start an approach deceleration in preparation for the turning maneuver before the critical distance. Second, instead of executing a maximum deceleration after the braking point, the observed passing vehicles maintain their approach deceleration all the way through the stop bar. At no point do we ever observe a free-flowing vehicle decelerating to some point and maintaining that speed constantly through the stop bar (Figure 2.6). Third, after the vehicles pass the stop bar they maintain deceleration to some minimum point in the middle of the intersection before accelerating through the clearance point. Note that in this figure the "clearance point" is

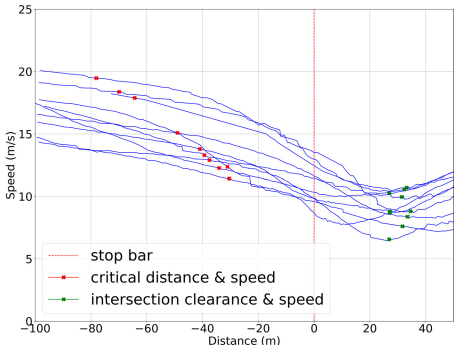

Plymouth Rd and Green Rd: Phase 1

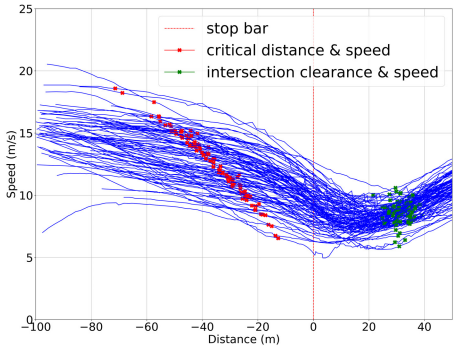

Plymouth Rd and Green Rd: Phase 3

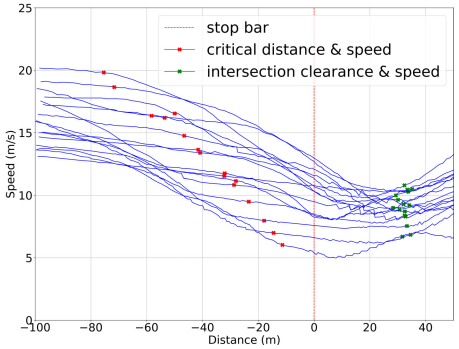

Plymouth Rd and Green Rd: Phase 5

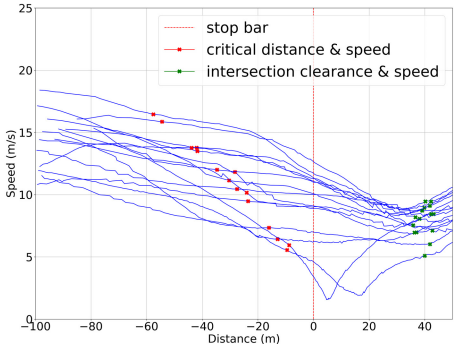

Plymouth Rd and Green Rd: Phase 7

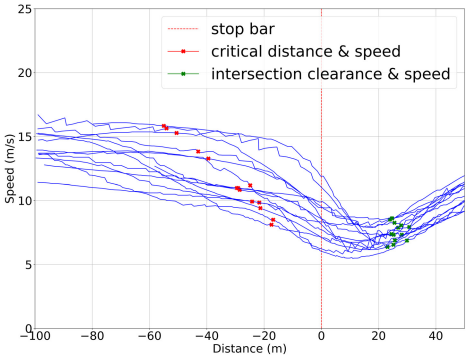

Plymouth Rd and Huron Pkwy: Phase 3

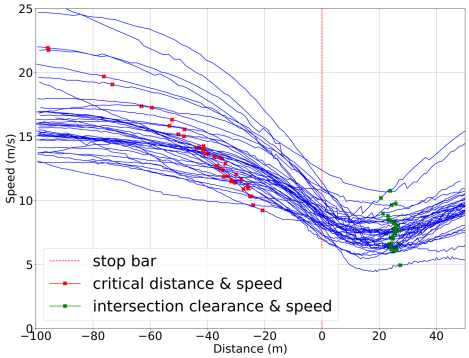

Plymouth Rd and Nixon Rd: Phase 1

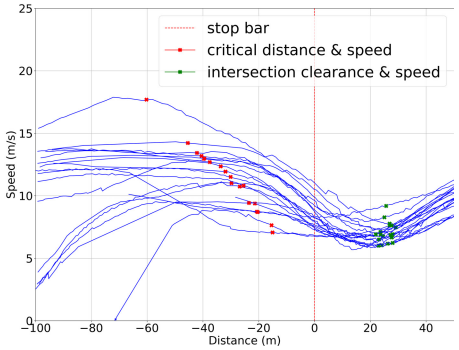

Plymouth Rd and Nixon Rd: Phase 3

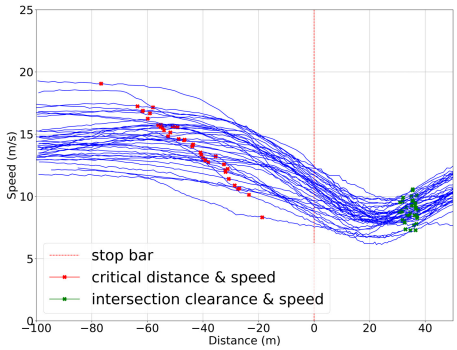

Plymouth Rd and Murfin Ave: Phase 7

Figure 2.6: Free-flowing vehicle speed profile from left-turning vehicle trajectory observations

the width of the intersection plus the length of the car $(w + l)$. Figure 2.7 illustrates these differences by comparing a typical speed profile of our observed trajectories in the bottom left corner with that of the extended kinematic equation in the top right corner. These observed differences inspired the development of new left-turn kinematic equation for yellow change and clearance intervals calculation, which will be described in the next section.

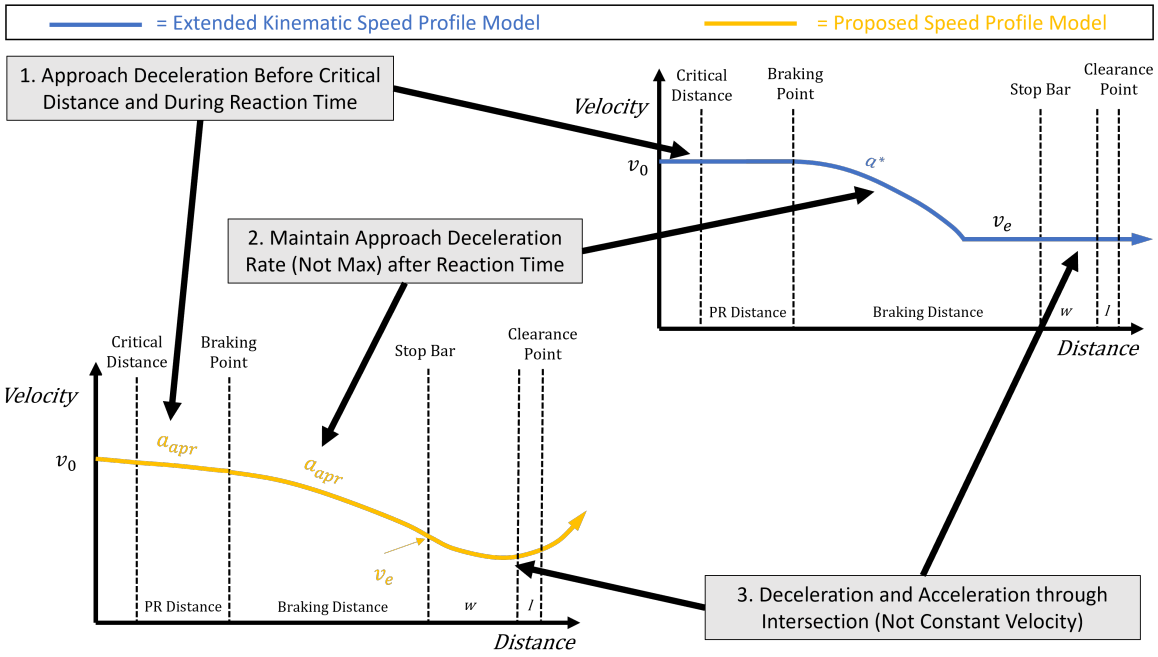

Figure 2.7: Comparison between the current recommended speed profile model and the observed speed profile.

2.4.1.1 Critical distance equation modifications

Compared to the critical distance calculated in the extended kinematic equation, the observed kinematic behavior in the last section shortens the critical distance in two ways: 1) vehicles travel at slower speeds when they reach the "point of no return" and 2) the vehicles decelerate through the PR distance, shortening the braking distance because they are traveling at an even slower speed at the braking point. Because the approach deceleration for a left-turning vehicle happens before the critical distance and through the perception reaction time, we require a new method for calculating the critical distance. Figure 2.8 compares the critical distance speed profile model for the extended kinematic equation with our proposed model. We define the "critical speed" as the speed of the vehicle at the critical distance or "point of no return," denoted as v_c. Note that v_c is slower than v_0. Next we define v_r as the speed after the perception-reaction time, which is slower than v_c. The distance traveled

through the perception-reaction time can be calculated by multiplying the average of v_c and v_r by δ. The new critical distance equation is therefore:

$$x_c = \frac{v_c + v_r}{2}\delta + \frac{v_r^2}{2a^*} \tag{2.13}$$

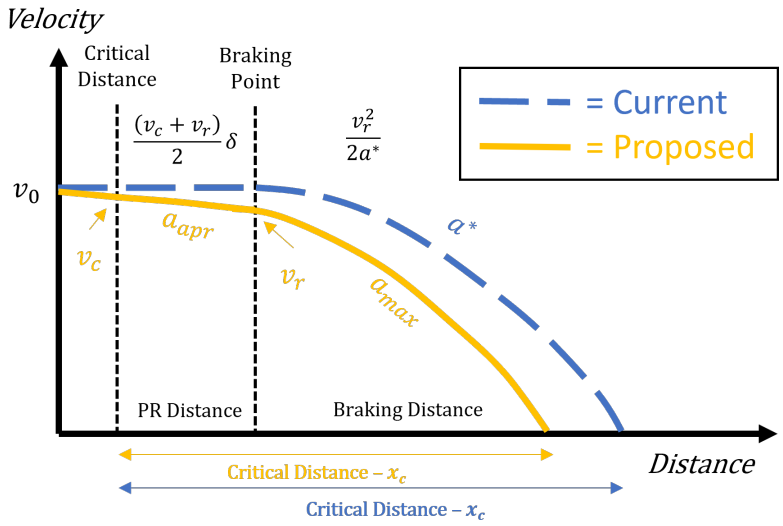

Figure 2.8: Critical distance for vehicles preparing for a left turn

This updated equation requires a simple modification to the vehicle trajectory critical distance identification process described in section 2.3. The speed at trajectory point p is set as v_c, and v_r is determined by locating the speed one second ahead of trajectory point p, assuming a perception-reaction δ of one second. We can then use the updated critical distance equation rather than the original one based on the SSD equation (Eq. 2.12) to find each trajectory's respective critical distance. Every trajectory in this study was reprocessed according to this procedure for the results in section 2.4.3

2.4.1.2 Kinematic behavior through critical distance

As shown in equation 2.2, the yellow change interval should be equivalent to the time it takes for a free-flowing vehicle to travel through the critical distance and reach the stop bar. Figure 2.9 provides a direct comparison between the speed profile assumptions in the extended kinematic equation and the proposed model. In the proposed model, vehicles maintain an approach deceleration from the time they are at the critical distance all the

way to the stop bar. Therefore, taking the average of v_c and v_e is a good way to model the kinematic behavior of the vehicle through the critical distance.

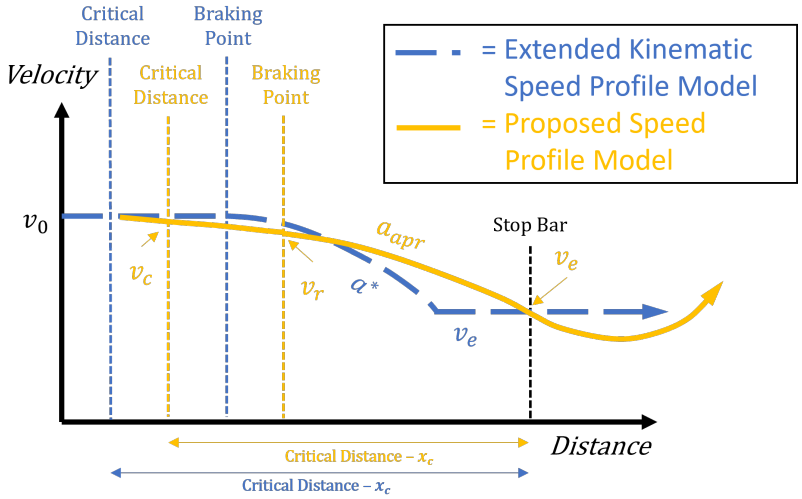

Figure 2.9: Free-flowing vehicle speed profiles for the extended kinematic equation and the proposed equation

In order to evaluate the accuracy of this method, we can compare the average of v_c and v_e for each observed trajectory (average through speed estimation) with its actual average speed. The actual average speed is calculated by dividing the trajectory's critical distance by time it took to traverse the critical distance. The inaccuracy measurement is defined according to the mean absolute percentage error (MAPE):

$$\text{MAPE} = \frac{|\text{ Estimated Average - Actual Average }|}{\text{Actual Average}} * 100\% \tag{2.14}$$

The average MAPE for each phase movement is presented in Table 2.2. In general the results fall between a 2 and 3 percent error. Therefore, taking the average of v_c and v_e is a simple and accurate method for estimating the speed through the critical distance.

Table 2.2: Average MAPE for speed estimation through the critical distance for intersections along Plymouth Rd.

Intersection	Phase 1	Phase 3	Phase 5	Phase 7
Green Road	1.98	2.30	2.18	2.26
Huron Parkway	N/A	3.10	N/A	2.76
Nixon Road	2.77	2.13	N/A	N/A
Murfin Avenue	N/A	N/A	N/A	2.82

2.4.1.3 Kinematic behavior through the intersection

Figure 2.3 (b) compares the current model speed profile used in the ITE recommendations with our proposed model speed profile based on the profiles shown in Figure 2.6. We introduce two new parameters: v_m is the minimum speed reached by the vehicle halfway through the total clearance distance $(w + l)$ and v_d is the vehicle's departure speed at complete intersection clearance. We estimate the average speed through the intersection according to:

$$\text{Average Through Speed Estimation} = \frac{\frac{v_e + v_m}{2} + \frac{v_m + v_d}{2}}{2} = \frac{1}{2}v_m + \frac{1}{4}v_e + \frac{1}{4}v_d \qquad (2.15)$$

Again, the model average can be compared to the actual average ($w + l$ divided by intersection traversal time). The results are presented in Table 2.3. The errors are low enough to support Equation 2.15 as a simple but accurate way of estimating the kinematic behavior of a vehicle making a left turn through the intersection.

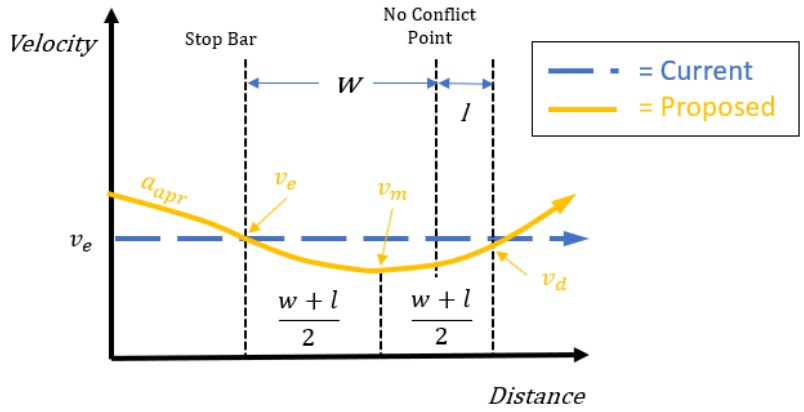

Figure 2.10: Speed profile for a left-turning vehicle traversing an intersection

Table 2.3: MAPE for speed estimation through the intersection for intersections along Plymouth Rd

Intersection	Phase 1	Phase 3	Phase 5	Phase 7
Green Road	1.62	2.58	2.33	4.20
Huron Parkway	N/A	3.24	N/A	1.95
Nixon Road	2.51	2.06	N/A	N/A
Murfin Avenue	N/A	N/A	N/A	1.62

2.4.2 Proposed kinematic equations

Based on our findings, the extended kinematic equation will overestimate the required minimum change interval duration for the following two reasons: 1.) the critical distance is shortened by the speed reduction before the braking point; 2.) the average traversing speed is higher as vehicles usually decelerate at a moderate rate instead of the maximum rate. The equation will underestimate the clearance interval as the average traversing speed through the intersection is slower than the intersection entry speed. To address these deficiencies, this section proposes new kinematic equations based on the trajectory observations.

Given the discussion above about the critical distance and the assumed free-flow vehicle speed profile, yellow change intervals for left turns can be calculated according to the following equations:

$$x_c = \frac{v_c + v_r}{2}\delta + \frac{v_r^2}{2a^*} \tag{2.16}$$

$$Y_{min} = \frac{x_c}{\frac{v_c + v_e}{2}} = \frac{\frac{v_c + v_r}{2}\delta + \frac{v_r^2}{2a^*}}{\frac{v_c + v_e}{2}} = \frac{(v_c + v_r)\delta + \frac{v_r^2}{a^*}}{v_c + v_e} \tag{2.17}$$

It is important to note that $v_c < v_0$ as the vehicle will already be decelerating from free-flow speed in preparation for the turning maneuver. A smaller critical speed and deceleration through the perception-reaction time will reduce the critical distance as compared to the one used in the current recommendations (Figure 2.8). By default, the required yellow change interval will be shorter than the extended kinematic equation because the vehicle has a shorter distance to travel.

The proposed equation for calculating the clearance interval is:

$$\begin{aligned} R &= \frac{\frac{w+l}{2}}{\frac{v_e + v_m}{2}} + \frac{\frac{w+l}{2}}{\frac{v_m + v_d}{2}} - t_s \\ &= \frac{w+l}{v_e + v_m} + \frac{w+l}{v_m + v_d} - t_s \end{aligned} \tag{2.18}$$

The clearance intervals calculated from this equation will be longer than the one calculated from the extended kinematic equation because the vehicle does not travel constantly at speed v_e through the intersection. Instead, we note how the vehicle continues to decelerate as it

passes the stop bar to some minimum speed v_m before accelerating as it clears the intersection at departure speed v_d. Therefore, it will take a vehicle a longer time to clear the intersection than what is modeled in the current ITE recommendations.

We understand that it may be difficult for agencies to obtain accurate measurements of all the parameters in the proposed left turn kinematic equation. Therefore, engineering judgment will have to be utilized during its implementation. Table 2.4 reports the field measurements values from our study and illustrates how the parameters are related. When determining v_c, practitioners should remember that v_c is less than v_0 (some of our v_c measurements are higher than the implemented design speed, indicating that some of the implemented design speeds are underestimated). In general, we note that the difference between v_0 and v_c gets gradually larger as you increase speed. A v_c speed around 5mph slower than the design speed can be used at design speeds of 45 mph. For a design speed of 35 mph, practitioners may consider a v_c speed 1-2 mph slower than the design speed. The Table also shows that v_r is consistently around 1 mph slower than v_c. For the intersection entry speed, engineers can use a speed of 25 mph for intersection width lengths around 90 feet. Engineering judgment should be used when this width is shorter and the turning radius becomes smaller. Vehicles will have to enter the intersection at slower speeds for tighter left turns.

2.4.3 Numerical comparisons with the current kinematic models

Table 2.4 compares calculates minimum yellow change and red clearance intervals for the original kinematic, extended kinematic, and the proposed left-turn kinematic equations. The minimum yellow change and red clearance intervals are calculated according to the original equations (Equations 2.5 and 2.10) where $v_{0,85}$ is calculated by taking the 85th percentile speed measured 100 meters before the stop bar from the free-flow trajectories or the first data point if the processed trajectory does not extend that far. For the extended kinematic equations (Equations 2.9 and 2.11), $v_{e,85}$ is the 85th percentile speed measured from the trajectories in this study. Finally, the proposed left-turn kinematic equations (Equations 2.17, 2.18) are calculated using the measured 85th percentile speeds of v_c, v_r, v_m, and v_d. In all three methods, we assume $t_s = 1$.

The minimum yellow change intervals calculated from the proposed kinematic equation are generally longer than the original GHM kinematic equation but shorter than the extended kinematic equation. For Green Rd phases 3, 5, and 7, the proposed yellow is equal to or shorter than the original yellow because v_c is much slower than v_0. For all other movements, the proposed yellow is always shorter than the extended yellow and slightly longer. Even

Table 2.4: Comparison of yellow change and red clearance intervals calculated by the original (O), extended (E), and proposed (P) kinematic equations for each phase (Ph) based on 85th percentile measurements

Intersection	Ph	Eq	Y_{min}	R	Total	$v_{0,85}$	$v_{e,85}$	$v_{c,85}$	$v_{r,85}$	$v_{m,85}$	$v_{d,85}$	w
Green Rd	1	O	4.1	1.3	5.4	42.0	-	-	-	-	-	120
		E	5.1	1.6	6.7	42.0	28.6	-	-	-	-	90
		P	4.4	2.1	6.5	-	28.6	40.7	39.1	22.9	23.4	90
	3	O	3.7	1.5	5.2	36.3	-	-	-	-	-	115
		E	4.6	2.1	6.7	36.3	24.3	-	-	-	-	90
		P	3.7	2.5	6.2	-	24.3	33.9	32.1	19.8	21.1	90
	5	O	4.0	1.3	5.3	41.1	-	-	-	-	-	120
		E	5.1	1.8	6.9	41.1	26.7	-	-	-	-	90
		P	4.0	2.2	6.2	-	26.7	36.9	35.4	21.7	23.3	90
	7	O	3.7	1.5	5.2	36.1	-	-	-	-	-	115
		E	4.4	2.7	7.1	36.1	25.4	-	-	-	-	120
		P	3.5	3.5	7.0	-	25.4	30.8	30.2	19.4	20.3	120
Huron Pkwy	3	O	3.6	1.1	4.7	34.9	-	-	-	-	-	90
		E	4.5	1.9	6.4	34.9	22.3	-	-	-	-	75
		P	4.0	2.4	6.4	-	22.3	34.2	33.0	17.7	19.1	75
	7	O	4.3	0.7	5.0	44.4	-	-	-	-	-	90
		E	5.9	1.8	7.7	44.4	21.97	-	-	-	-	70
		P	5.2	2.1	7.3	-	22.0	43.4	41.8	18.6	20.5	70
Nixon Rd	1	O	4.2	0.7	4.9	43.1	-	-	-	-	-	90
		E	5.7	1.6	7.3	43.1	22.6	-	-	-	-	65
		P	4.6	1.9	6.5	-	22.6	38.8	37.5	18.6	19.0	65
	3	O	3.2	1.1	4.3	30.3	-	-	-	-	-	75
		E	3.9	1.7	5.6	30.3	21.7	-	-	-	-	65
		P	3.6	2.1	5.7	-	21.7	29.7	29.1	16.6	17.2	65
Murfin Ave	7	O	3.7	1.5	5.2	37.3	-	-	-	-	-	115
		E	4.5	1.8	6.3	37.3	26.4	-	-	-	-	90
		P	4.1	2.4	6.5	-	26.4	36.8	35.8	20.2	21.6	90

*all speeds reported in mph; $l = 20$ ft; w reported in ft

though left-turning vehicles decelerate as they approach the turning maneuver, it is feasible for the required yellow to be only slightly longer than the original yellow because of the reduction in the critical distance.

The red clearance intervals calculated by the proposed kinematic equations are around a half a second longer than the ones calculated by the extended kinematic. This is reasonable as the proposed clearance calculation accounts for deceleration to a minimum speed v_m halfway through the intersection. Additionally, from the measurements shown in Table 2.4, the departure speed v_d is always smaller than entry speed v_e. Therefore, the vehicle is always

traveling at a slower speed than v_e so it will take it a longer time to clear the intersection. The required increase in the clearance interval is generally less than the allowable decrease in the yellow change interval. As a result, the total time required to transfer the right-of-way from a left-turning phase movement to a different movement is less than or equal to the current recommendations.

2.4.4 Conclusions

The extended kinematic equation has not been widely implemented by traffic engineers across the country for two main reason: 1.) the equation can sometimes generate intervals longer than the maximum duration of 6 seconds set by the MUTCD and 2.) there are unvalidated assumptions about the kinematic behavior of free-flowing left-turning vehicles. This section evaluates the equation by analyzing 262 free-flowing left turn trajectories from 9 different left turn phases at 4 intersections along the Plymouth Road corridor in Ann Arbor, MI, using real-world CV data from the Ann Arbor Connected Vehicle Test Environment (AACVTE) (Wang et al., 2020). Our observations confirm the main argument for applying the extended kinematic equation: that turning vehicles decelerate as they approach an intersection. However, there are several uniform characteristics in the speed profiles of the observed trajectories that differ from the one modeled in the extended kinematic equation. First, the free-flowing trajectories exhibited an approach deceleration before the critical distance calculated from the free-flow approach speed v_0. A new critical distance equation was developed that accounted for the critical speed v_c being less than v_0 and there being deceleration through the perception-reaction time. Second, instead of executing a maximum deceleration after the braking point, the observed passing vehicles maintain their approach deceleration all the way to stop bar. Finally, as the vehicles pass the stop bar they maintain that deceleration to some minimum point in the middle of the intersection before accelerating through the clearance point. These observations indicate that the extended kinematic equation may overestimate the required change interval and underestimate the required red clearance interval.

With the observed speed profiles for left-turning vehicles, we then propose a new left-turn kinematic equation for determining yellow change and clearance intervals. The field data in this study comes from intersections in Ann Arbor, and it is not yet clear if the results from one location can be generalized to other locations. In addition, not every jurisdiction will have access to the data necessary to measure the parameters introduced in this paper. In general, while the proposed kinematic model addresses some of the deficiencies with the extended kinematic equation, it is difficult to capture driver variability across different intersection

movements with one model. Other factors such as the impact of turning radii, approach grade, field of view, weather, and the number of turning lanes on these parameters will all have an impact on the speed profiles of left-turning vehicles. The next section will discuss a strategy for determining minimum change intervals without needing to model the kinematic behavior of vehicles traveling through the critical distance.

2.5 Determining minimum change intervals from vehicle trajectory data

In practice, kinematic models face two primary challenges when applied to eliminate the dilemma zone. First, it is difficult to get the approach and intersection entry speeds as many intersections are not equipped with the necessary detection equipment. Second, the kinematic modeling of driver behavior through the critical distance is prone to over generalization. Because of the lack of accurate speed parameters and generalized kinematic modeling, many of the implemented change intervals in practice might not be equal to or longer than the time it takes for drivers to traverse the critical distance, creating potential dilemma zones leading to unavoidable red-light running.

This section proposes a new framework for determining minimum yellow change intervals for eliminating type I dilemma zones using vehicle trajectory data. We leverage the temporal-spatial advantages of vehicle trajectory data to extract the exact time it takes for drivers to traverse the critical distance. No kinematic model is needed because the complete trajectory path is provided and hence no speed parameter inputs are required, enabling cloud-based efficient calculations of minimum yellow change intervals at scale.

It can be tricky, and in some cases controversial, to accurately model free-flow behavior at intersections with a limited number of speed parameters. Several studies, including the one presented in the previous section, have proposed models for left-turning vehicles (Jerome et al., 2022; Liu et al., 2002; Yu et al., 2003), but these all require several input parameters relating to speed and road geometry that are difficult to obtain in the field. To the best of our knowledge, no proposed mathematical model has been able to accurately capture intersection approach behavior for all drivers across different intersections. Therefore, this study proposes to measure the travel time through the critical distance directly from vehicle trajectory data.

The framework was tested in a citywide case study in Birmingham, MI of 33 intersections by aggregating two months of vehicle trajectory data (586,166 free-flowing trajectories) from the GM dataset. The study determined minimum change intervals for 207 movements based

on the 85th percentile critical distance travel time and found that the current implemented intervals at 65 movements (21 straight and 44 left-turning) did not meet this benchmark, including all movements with an 85th percentile free-flow speed at the critical distance faster than 32 mph. The study also found that retiming the yellow change intervals according to the extended kinematic equation for left-turning movements may increase the number of movements meeting the benchmark, but it would also generate intervals that are 0.4 seconds longer on average. While clearance intervals are not evaluated in this study, modifications to the proposed methodology for the clearance interval are discussed. The proposed method addresses both the parameter availability problem and the free-flow vehicle modeling problem by directly measuring driver travel times through the critical distance and can provide movement specific minimum change intervals that account for large variability in vehicle dynamics.

2.5.1 Methodology

The proposed method determines the minimum required change interval for each free-flowing trajectory without using a kinematic model by directly measuring the time it takes to travel through the critical distance. This study utilized the OEM dataset described in section 1.2.2 that provided vehicle trajectory points every 3 seconds. While the complete trajectory path within these 3 second intervals can be recovered through interpolation techniques, it was determined that the same filtering mechanism described in section 2.4.1 could not be utilized because the acceleration measurements were not sufficiently accurate. In this study, free-flowing trajectories are identified through a simple filtering mechanism that estimates if a vehicle trajectory was in or influenced by a queue by determining if the vehicle ever traveled below 20% of the speed limit within a certain distance before the stop bar. This distance is calculated using Eq. 2.1 where v_0 is the speed limit, $\delta = 1s$, and $a^* = 10ft/s^2$. Trajectories were eliminated if they met this criterion. Like traditional speed studies, the filtering mechanism can be changed to reflect an agency's preferred practices and engineering judgment. The rational for the filtering mechanism used here is that, in most cases, queued vehicles will not interact with the change interval because there should be enough green time to allow for complete queue discharge. The critical distance for each trajectory is then identified through the modified process outlined in section 2.4.1.1.

As discussed in section 2.2.1, the critical distance travel time t_c is the time it takes to traverse x_c. This study directly interprets t_c as the change interval length required for that specific trajectory. The performance evaluation for a particular movement can then take place by aggregating the results. The acceptable minimum yellow change interval can be

determined according to a target percentile of the aggregated critical distance travel times. By assuming a constant 85th percentile speed in the original kinematic equation in Eq. 2.5, the resulting Y_{min} value equals the 85th percentile of critical distance travel times ($t_{c,85}$). Put another way, Y_{min} would provide enough time for 85% of drivers to safely cross the stop bar if the change interval started right as they reached their respective critical distance. For any driver traveling slower than the 85th percentile approach speed, their critical distance travel time t_c using the original kinematic equation would be shorter than Y_{min}. Therefore, this study uses 85% as the benchmark:

$$Y_{min} = t_{c,85} \tag{2.19}$$

The critical distance travel time percentile used to determine Y_{min} can be adjusted depending on the needs of an agency's jurisdiction.

Results for an example left-turning movement are shown in Figure 2.11. The histogram in Figure 2.11 (a) reports the critical distance travel times. The current change interval Y is represented by the dashed yellow line while the 85th percentile critical distance travel time $t_{c,85}$ is the dashed red line. Any measurements to the left of the yellow line indicate critical distance travel times that would have had enough time to cross the stop bar if the change interval had started right as they hit their critical distance. In this example, 40.3% of the trajectories had enough time ($\%t_c < Y$). According to Eq. 2.19, the change interval should be greater than $t_{c,85}$, which was 1.1 seconds longer than the current change interval. Figure 2.11 (b) plots speed vs. distance. For clarity only a few trajectories are plotted. The red dots indicate the respective critical distance and critical speeds for each trajectory. The 85th percentile critical distance speed $v_{c,85}$ and intersection entry speed $v_{e,85}$ can be extracted from these measurements.

2.5.1.1 Example from AACVTE study

The ability of this methodology to evaluate how well yellow change intervals eliminate type I dilemma zones for at least 85% of drivers is demonstrated on the proposed kinematic equation presented in section 2.4.1. Table 2.5 compares the proposed Y_{min} for each phase the 85th percentile critical distance travel time $t_{c,85}$. In general, the proposed yellow change intervals from the 85th percentile speed measurements are at or slightly larger than the 85th percentile required interval for each measured trajectory. Therefore, the proposed kinematic modifications would provide enough yellow change time for 85% of the vehicles in this study at each movement.

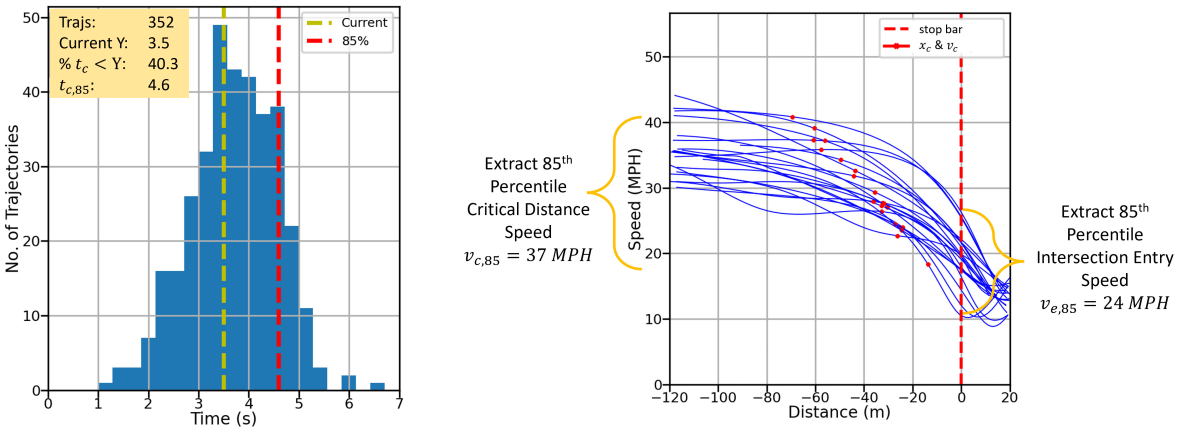

(a) t_c histogram

(b) Speed profile for selected trajectories.

Figure 2.11: Change interval performance evaluation for a left-turning movement

Table 2.5: Proposed minimum yellow change intervals vs. $t_{c,85}$ for intersections and phases along Plymouth Rd

Intersection	Phase	Proposed Y_{min}	$t_{c,85}$
Green Rd	1	4.4	4.3
Green Rd	3	3.7	3.8
Green Rd	5	4.0	4.0
Green Rd	7	3.5	3.5
Huron Pkwy	3	4.0	3.8
Huron Pkwy	7	5.2	5.1
Nixon Rd	1	4.6	4.2
Nixon Rd	3	3.6	3.5
Murfin Ave	7	4.1	4.1

2.5.1.2 Modifications for the red clearance interval

The red clearance intervals in Birmingham, MI were not evaluated in this study. However, the methodology can be easily modified for evaluating this interval. Define t_{wl} as the time is takes to clear the intersection after crossing the stop bar (width of the intersection w plus car length l). The value of R can then be determined according to some percentile of the aggregated t_{wl} measurements. Refer to section 2.2.2.1 for more discussion on choosing percentiles for red clearance intervals.

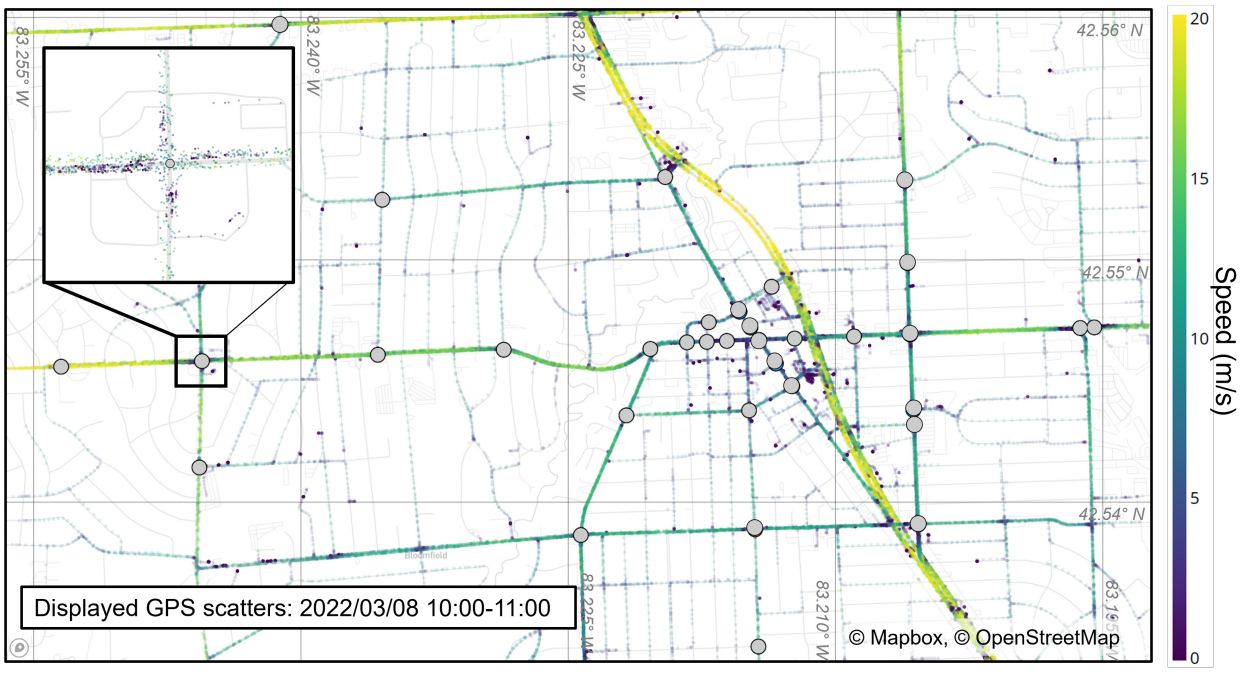

Figure 2.12: Birmingham, MI intersection locations and trajectory point GNSS scatters (Wang et al., 2024a).

2.5.2 Case study

2.5.2.1 Data and study area

Using the OEM dataset described in section 1.2.2, this study used 7 weeks of historical vehicle trajectory data from March 5th, 2022 – April 23rd, 2022, in Birmingham, MI (1.5 million trajectories). Figure 2.12 displays the intersection locations and trajectory point scatters from 10:00 – 11:00 AM on March 8th, 2022. The color bar on the right side indicates how to interpret the speed information from the plotted trajectory points.

The study area included 33 signalized intersections containing 207 straight and left-turning movements. The Road Commission for Oakland County (RCOC) provided the signal work orders. Currently, there are 3 change interval lengths implemented in Birmingham: 3.5, 3.6, and 3.9. These intervals mostly align with using the existing speed limit as the approach speed in the original kinematic equation (the extended kinematic equation is not utilized), with a minimum interval of 3.5 seconds. Tables 2.6 and 2.7 report the number of movements by direction, yellow change interval length Y, and speed limit.

Table 2.6: Number of movements by direction and change interval

Y	Straight	Left Turn	Both
3.5	92	94	186
3.6	6	3	9
3.9	6	6	12
All	104	103	207

Table 2.7: Number of movements by direction and speed limit

Speed Limit (mph)	Straight	Left Turn	Both
25	82	86	108
30	9	7	16
35	8	5	13
40	5	5	10
All	104	103	207

2.5.2.2 Results and discussion

Out of the over 1.5 million observed trajectories, 578,166 free-flowing trajectories were identified. Movements with less than 10 identified free-flowing trajectories were omitted from the analysis, leaving 192 movements. The study first evaluated the performance of the currently implemented yellow change intervals by finding the percentage of drivers whose t_c was less than the current yellow change interval. Next, the current change intervals for straight movements and a hypothetical retiming of left-turning movements according to the extended kinematic equation are compared with $t_{c,85}$. It is important to note that not all left-turning movements in the study area are serviced by protected lanes or protected movements, so the change intervals calculated through $t_{c,85}$ are hypothetical (different change intervals can't be implemented when the left-turning movement is serviced by the same signal head as the straight movement) and are meant to show the ideal change interval by quantifying potential safety risks.

Table 2.8 is a sample performance table containing the performance metrics of the top ten movements with the smallest percentage of critical distance travel times less than the currently implemented change interval ($\%t_c \leq Y$). A $\%t_c \leq Y$ less than 85% indicates that the current change interval is not sufficient. The table reports the number of free-flowing trajectory observations, Y, $t_{c,85}$, and $\%t_c \leq Y$. Because the speed limit, $v_{c,85}$, and $v_{e,85}$ are used as inputs in the kinematic equations, they are also included. As expected, most of the worst performing movements were left turns because the current implementation is based on the original kinematic equation. It is clear from the table that the intersection

Table 2.8: Movement performance table (top ten worst performing movements)

Rank	Intersection	Direction	Obs.	Y	$\%t_c \leq Y$	$t_{c,85}$	SL	$v_{c,85}$	$v_{e,85}$
1	Maple Rd & Clifton Rd	EB	22,231	3.9	27.1	4.7	40	49	49
2	Maple Rd & Clifton Rd	EBL	31	3.9	29.0	5.1	40	41	25
3	Maple Rd & Clifton Rd	WB	22,709	3.9	37.2	4.6	40	47	47
4	Cranbrook Rd & Midvale St	SBL	352	3.5	40.3	4.6	30	37	24
5	Cranbrook Rd & Midvale St	SB	5,851	3.5	45.4	4.1	30	40	40
6	Maple Rd & Clifton Rd	WBL	135	3.9	51.1	4.8	40	40	28
7	Cranbrook Rd & Quarton Rd	WBL	870	3.9	51.3	4.9	40	41	28
8	Maple Rd & Lake Park Dr	EBL	316	3.6	57.9	4.5	35	34	22
9	Cranbrook Rd & Maple Rd	EBL	664	3.9	60.4	4.9	40	39	26
10	Maple Rd & Chesterfield Ave	EBL	153	3.6	60.8	4.3	35	34	23

*Speed limit (SL), $v_{c,85}$, and $v_{e,85}$ reported in mph

entry speeds are much slower than the critical distance speeds for left-turning movements, indicating that the original kinematic equation will underestimate the required interval. It is also interesting to note that the critical distance speeds for left-turning movements are much slower than the critical distance speeds for the associated straight movement from the same direction, indicating that drivers are slowing down before the critical distance. For example, $v_{c,85}$ for the eastbound straight movement at Maple Rd & Clifton Rd is 49 mph, while the eastbound left turn $v_{c,85}$ is 41 mph. Two of the three worst performing movements, however, are straight movements because their critical distance speeds are much faster than the speed limit.

The percentage of critical distance travel times that were less than Y for each movement is reported in Figure 2.13, where straight movements are denoted by the blue circles and left-turning movements by the yellow cross marks. It is clear from the figure that left-turning movements performed worse than straight movements, with 44 left-turning movements and 21 straight movements not making the 85% benchmark (Eq. 2.19). Despite most movements making this benchmark, the city-wide percentage was short at 80.9% because most high-

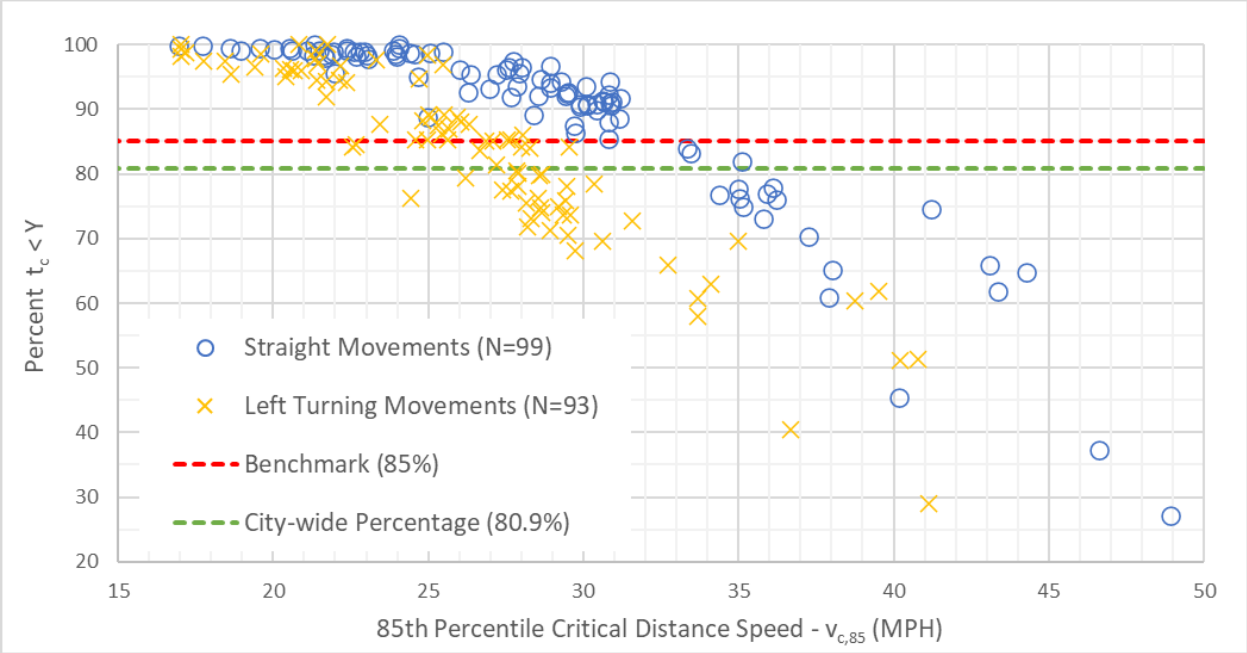

Figure 2.13: Percentage of critical distance travel times less than the current change interval vs. 85th percentile critical distance speed for each movement.

volume and high-speed roads did not make the benchmark. In fact, not a single movement with a $v_{c,85}$ speed above 32 mph had a percentage above 85%.

These phenomena can be explained for two reasons, both illustrated in Figure 2.14 which compares $v_{c,85}$ with the respective speed limit and intersection entry speed $v_{e,85}$. First, the critical distance speeds for straight movements are much faster than the speed limit, especially at higher speeds. The coloring in Figure 2.14 matches each movement with its respective speed limit. Straight movement $v_{c,85}$ (circles) are usually faster than the speed limit while left-turning movement $v_{c,85}$ (cross marks) are closer to the speed limit. Since the current change intervals were calculated with the speed limit, it will underestimate the required intervals for straight movements. Second, the intersection entry speeds are much slower than the critical distance speeds for left-turning movements, indicating that the original kinematic equation will not accurately predict vehicle behavior through the critical distance. The 1:1 line depicts locations where $v_{c,85} = v_{e,85}$. Anything below this line indicates $v_{e,85} < v_{c,85}$.

In Figure 2.14, sometimes the intersection entry speed for straight movements is faster than the critical distance speed. This can happen when there is an upstream intersection close to the intersection of interest and the approach segment is short. As vehicles depart the upstream intersection they may speed up as they approach the intersection of interest. This highlights one of the advantages of the proposed method in that it can create movement

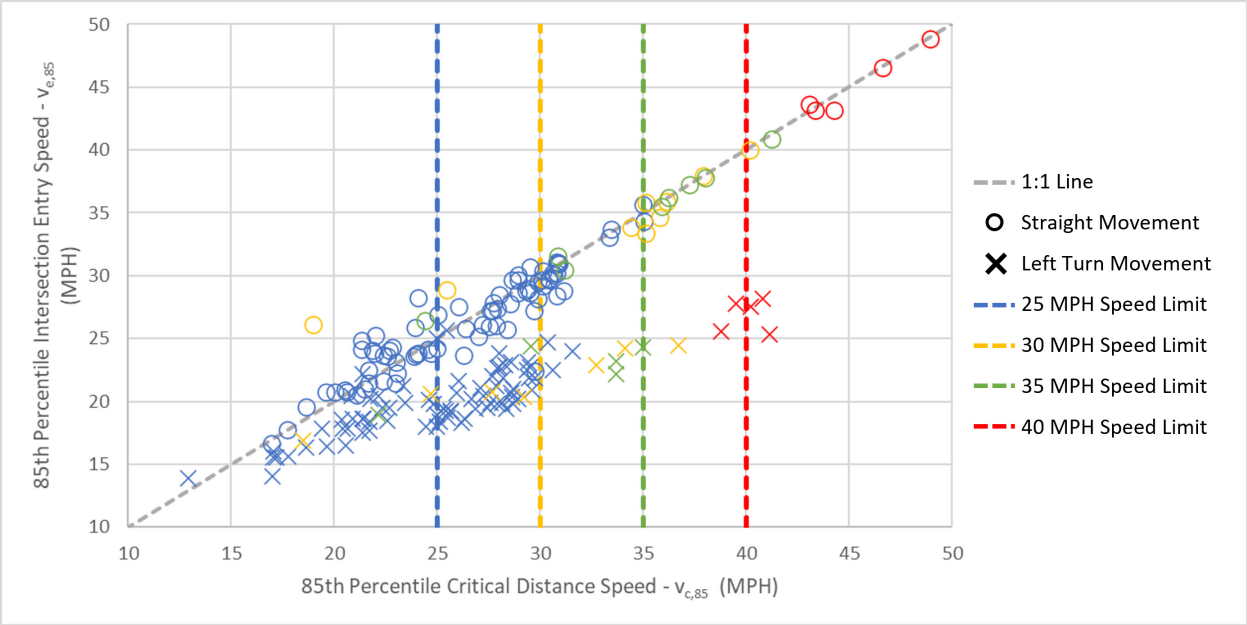

Figure 2.14: 85th percentile intersection entry speed vs. 85th percentile critical distance along with respective speed limits for each movement.

specific intervals while accounting for geometry and driver behavior.

According to Eq. 2.19, the 85th percentile critical distance travel time is the minimum recommended change interval (Y_{min}). Figure 2.15 plots the histograms of the 85th percentile critical distance travel times ($t_{c,85}$) for straight movements at different speed limits and compares them to the current change interval. Just like Figure 2.13, the performance deteriorates as the speed increases. For movements with a speed limit of 40 mph, for example, $t_{c,85}$ was on average a 0.4 seconds longer than the current interval. This can be explained by critical distance speeds that were faster than the speed limit at these movements (Figure 2.14).

Figure 2.16 plots the same histograms for left turn movements. However, instead of comparing $t_{c,85}$ to the current change interval, an interval is calculated using the extended kinematic equation with the speed limit as the approach speed and 20 mph as the entry speed (as recommended by ITE5). The extended kinematic equation reduces the number of movements not meeting $t_{c,85}$ from 44 to 33, but it greatly overestimates the minimum interval at higher speeds. For example, the interval is an average of 0.4 seconds too long for movements where the speed limit is 40 mph. As shown in Figure 2.14, $v_{c,85}$ is close to the speed limit for these movements but $v_{e,85}$ is well above 20 mph, so the extended kinematic equation should underestimate the required interval (higher average speed through critical distance). These results show how the deficiencies in the modeling of the extended kinematic equation will cause it to overestimate required yellow change intervals even with accurate

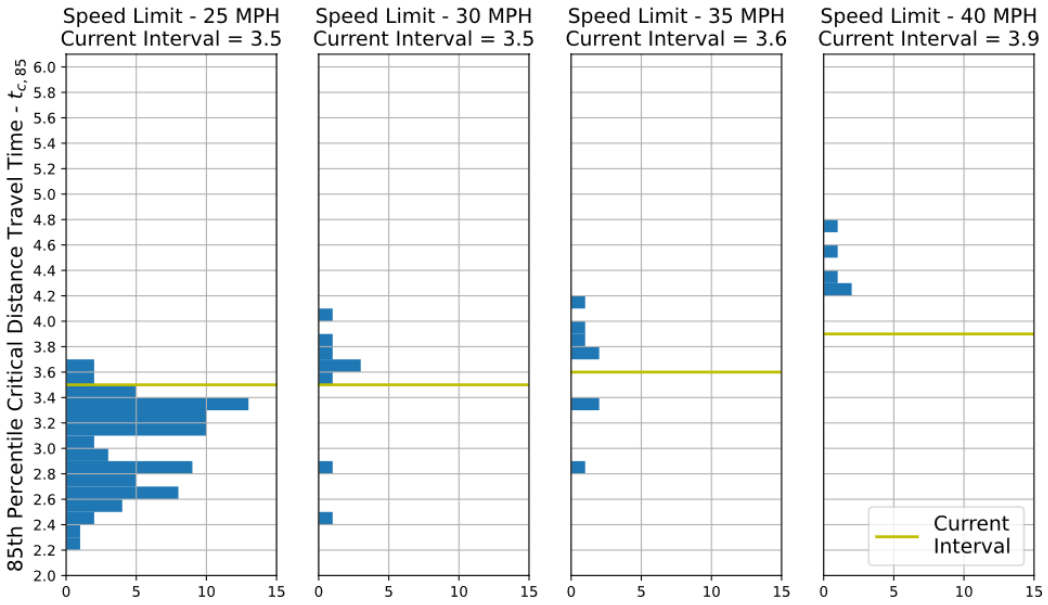

Figure 2.15: 85th percentile critical distance travel time histograms for straight movements at different speed limits.

speed parameters. The performance was worst at slower speed because $v_{c,85}$ was usually faster than the speed limit at these speeds (Figure 2.14).

2.5.3 Conclusions

This section develops a framework for determining minimum change intervals designed to eliminate type I dilemma zones using vehicle trajectory data. The method contributes to the practice by addressing two main challenges with current kinematic model approaches. First, it eliminates the need for overgeneralized assumptions about the kinematic behavior of drivers through the critical distance by directly measuring the travel time from vehicle trajectories. Second, it reduces the data collection burden by providing accurate and movement-specific speed information through increasingly available vehicle trajectory data that spans the entire spatial-temporal space. This study tested the framework by evaluating the current performance of change intervals in Birmingham, MI and found that 65 out of 192 movements (21 straight and 44 left-turning) did not have change intervals that could accommodate 85% of the critical distance travel times. Most of the poor performance for straight movements could be fixed by having accurate speed information from vehicle trajectory data. Trajectory data can also more accurately capture the free-flowing left-turning vehicle travel times through the critical distance than the extended kinematic equation and can avoid

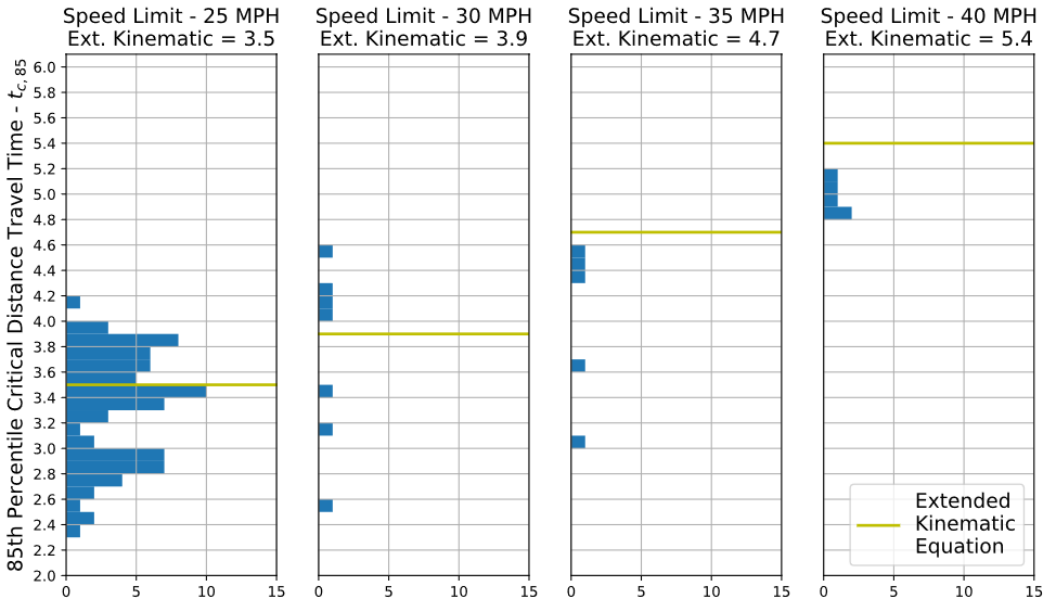

Figure 2.16: 85th percentile critical distance travel time histograms for left-turning movements at different speed limits.

overgeneralizing across intersections. By addressing both the parameter availability problem and the kinematic modeling problem, this method can provide movement specific minimum change intervals at scale in a cloud-based system, while accounting for large variability in vehicle dynamics and road geometry.

2.6 Conclusion

2.6.1 Summary

The goal of most kinematic models used to design change intervals is to determine the time it takes for free-flowing vehicles to travel the critical distance (distance to the stop bar once they pass the point at which they can no longer stop). In practice, these models have two main challenges. First, the kinematic modeling of driver behavior through the critical distance is prone to over generalization and, in some cases, is not validated. For instance, many transportation agencies have chosen not to adopt the extended kinematic equation recommended by ITE in 2020 because of unvalidated assumptions about the kinematic behavior of free-flowing left-turning drivers. Second, it is very difficult to get the 85th percentile approach and intersection entry speeds under free-flow conditions as many intersections are not

equipped with the necessary detection equipment. The extended kinematic equation recommended by ITE is very sensitive to speed parameters and in some cases generates intervals longer than the maximum duration of 6 seconds set by MUTCD. Because of generalized kinematic modeling and the lack of accurate speed parameters, many of the implemented change intervals in practice might not be equal to or longer than the time it takes for drivers to traverse the critical distance, creating potential dilemma zones leading to unavoidable red-light running.

This section first evaluates the newly recommended extended kinematic equation by analyzing left-turn trajectories from 9 different movements in Ann Arbor, MI using real-world CV data from the Ann Arbor Connected Vehicle Test Environment (AACVTE). Our observations confirm that vehicles slow down before making a left turn at intersections, but the behavior is quite different from that modeled in the extended kinematic equation. Overall we note that left-turning vehicles require a slightly longer yellow change interval than straight through vehicles, but not as long as that modeled by this equation. We also observe that left turning vehicles do not usually keep a constant speed through the clearance distance as they continue decelerating until about halfway through the turn.

We then develop a framework for determining minimum change intervals designed to eliminate type I dilemma zones using vehicle trajectory data. The method addresses the two main challenges with current kinematic model approaches by leveraging the temporal-spatial advantages of trajectory data to directly measure the vehicle travel time through the critical distance rather than relying on overgeneralized models and fixed-point speed measures. This method was tested at 34 signalized intersections in Birmingham, MI, demonstrating its ability to provide movement specific minimum change intervals at scale.

2.6.2 Integration into the traffic signal timing management system)

The methods described in this chapter integrate into the overall signal timing management system presented in Figure 1.6. First, the procedures described in Section 2.3 are included in the preprocessing model depicted in the bottom left. Next, the framework described in section 2.5 includes the dilemma zone identifier microservice, where movements with $\%t_c < Y$ less than 85% are classified as having a dilemma zone. Finally, the yellow change interval retiming microservice can determine new yellow change intervals according to $Y_{min} = t_{c,85}$.

CHAPTER 3

A Signalized Intersection Performance Diagram (SIPD)

3.1 Introduction

This chapter presents a uniform method for evaluating intersection traffic congestion from vehicle trajectory observations and traffic signal timing information through a time-space diagram segmented based on the dynamics of queue formation and dissipation in response to traffic signal control. Vehicle trajectories plotted on the proposed Signalized Intersection Performance Diagram (SIPD) can give insights into overall traffic congestion based on their behavior within each segmented zone. This chapter demonstrates how including signal timing information allows the SIPD to quantify the impacts of conflicting movement blockage on traffic signal performance measures in permissive movement and spillover scenarios. These blockages impact the normal dissipation of queues, so the trajectories influenced by such blockage can be easily identified on the SIPD. New performance measures are introduced that modify the current state-of-the-practice by determining if the control delay, number of stops, and split failures were caused by blockage or queues formed during the red light phase. The measures were collected from SIPDs plotted at six intersections with different intersection geometries and phase operations. The SIPD also makes it easy to visualize split failures, especially those caused by blockage in the first cycle and do not exhibit a second stop. Despite the limited number of vehicle trajectory observations available in practice, the SIPD helps transportation engineers visualize how these trajectory observations can give insight into the complete traffic state.

3.1.1 Background and related works

Monitoring traffic through vehicle trajectory data is highly scalable due to its large coverage area, offering many advantages over fixed point detection methods used for automated traf-

fic signal performance measures (ATSPMs). Enriched information embedded in trajectories such as delay and number of stops can be analyzed and aggregated to provide the next generation of traffic signal performance measures (Saldivar-Carranza et al., 2021, 2023; Wang et al., 2023; Waddell et al., 2020; Wolf et al., 2019; INRIX, 2024). Common performance measures extracted from each individual trajectory observations are control delay, stop delay, number of stops, and split failures. These measures can be aggregated for operational performance measures such as arrival on green (AOG) and level of service (LOS).

Both researchers and practitioners have been building new tools to facilitate the integration of these new traffic signal performance measures into practice. Recent work by Saldivar-Carranza et al. (2023) and Wang et al. (2023) has significantly advanced the state-of-the-practice in performance analysis using vehicle trajectory data, inspiring the development of commercial analytics platforms such as *Signal Analytics* by INRIX and *ClearGuide Signals* by Iteris. However, current solutions rely solely on vehicle trajectory data and do not incorporate signal timing information, specifically green splits and cycle lengths. While this approach offers valuable insights without needing any data integration with local traffic management agencies, the absence of signal timing limits the ability of these tools to deliver more detailed or diagnostic performance analyses. For instance, tools like the Purdue Probe Diagram (PPD), can identify if a vehicle stops before clearing an intersection (Saldivar-Carranza et al., 2023). They can not, however, differentiate between a vehicle stopping because of a red light or because of some downstream blockage. This is particularly a limitation in permissive left-turn scenarios where vehicles stop before the stop bar while waiting for an acceptable gap.

Vehicle trajectory data is particularly advantageous for the identification of split failures because the entire vehicle path through the intersection is available. The state-of-the-practice for split failure identification with vehicle trajectory data is dependent upon the number of stops during a vehicle's approach to an intersection and minimum thresholds of control delay (Wang et al., 2023; Saldivar-Carranza et al., 2023; INRIX, 2024; Wolf et al., 2019). Using the PPD, Saldivar-Carranza et al. compared split failure identification from high-resolution controller data and vehicle trajectory data. They recommended using trajectories for identifying locations requiring retiming, maintenance, or upgrade activities due to the scalability of the method (Saldivar-Carranza et al., 2024a). Because the current practice can not differentiate stops caused by red lights from those caused by downstream blockage, one limitation to using pure stop numbers for split-failure identification is that sometimes vehicle can stop twice within the same cycle. For instance, permissive left-turning vehicle may stop twice during a single permissive phase while waiting for an acceptable gap.

Another limitation of the current state-of-the-practice in signal performance analysis with

vehicle trajectory data is techniques for quantifying the impact of downstream blockage on delay. This downstream blockage could be the result of spillover from queues forming at downstream intersections or conflicting traffic under a permissive phase preventing vehicles to clear the intersection during the green phase. Saldivar-Carranza et al. proposed a method for identifying downstream blockage from spillover in Saldivar-Carranza et al. (2023), but the method only provides the percentage of vehicles that experience downstream blockage and does not quantify the portion of control delay that can be attributed to such blockage. It also only identifies downstream blockage after a trajectory has passed the intersection, which will miss blockage caused by conflicting traffic in permissive control. By incorporating signal timing information, this chapter presents a new method for quantifying downstream blockage through a SIPD that segments the time-space diagram based on the normal dynamics of the formation and dissipation of queues under traffic signal control.

Stephanopoulos et al. (1979) investigated such dynamics by analyzing queue lengths given signal control variables and system parameters. The work examined the dynamics of the shock waves formed from intermittent traffic service of traffic signal control. They showed that signal control and traffic parameters can be used to model the growth of congestion. By using shock wave analysis on the time-space diagram, we can estimate control delay using methods such as what has been demonstrated in Dion et al. (2004) and in the Highway Capacity Manual (HCM) (Transportation Research Board, 2022). Liu et al. (2009) also proposed a method for real time queue estimation using Lighthill-Whitham-Richards (LWR) shockwave theory. The work was later extended to model arterial traffic flow dynamices (Wu and Liu, 2011). Ponlathep (2010)used time-space diagrams to model traffic dynamics at signalized intersection using shockwave theory for an adaptive signal control algorithm.

Vehicle trajectory data has been used in the literature to estimate shockwaves and queue dynamics (Izadpanah et al., 2009; Ban et al., 2011; Cetin, 2012; Zhao et al., 2019b; Fourati and Friedrich, 2019). These works provide valuable insights into how we can use vehicle trajectory data to estimate and predict the expected formation and dissipation of queues at signalized intersection. This chapter will build upon these techniques to incorporate traffic signal timing information into a framework for analyzing vehicle trajectories to identify and quantify the impacts of blockage on traffic signal performance measures.

3.1.2 Contributions and organization of this chapter

This chapter builds on the established state-of-the-practice in signalized intersection performance analysis with vehicle trajectory data by incorporating signal timing information. The contributions are as follows:

1. A Signalized Intersection Performance Diagram (SIPD): a time-space diagram segmented according to the dynamics of queue formation and dissipation in response to traffic signal control. With green split and cycle length information, this diagram is generalizable for any signalized intersection, providing a uniform method for evaluating overall intersection congestion from trajectory observations.

2. New performance measures that determine if the control delay, number of stops, and split failures are caused by blockage or queues formed during the red light phase. The ability to differentiate between these two types of scenarios will provide new diagnostic capabilities when attempting to mitigate congestion at intersections.

This chapter is organized as follows: Section 3.2 discusses the analytical derivation of the SIPD. Red light and blockage performance measures are introduced in Section 3.3. Section 3.4 explains how the SIPD can be constructed from vehicle trajectory observations. The proposed methods are demonstrated through case studies discussed in Section 3.5. Finally, we conclude by summarizing the advantages and applications of our approach in Section 3.6.

3.2 Analytical derivation of the SIPD

This section presents the derivation and construction of the SIPD. To facilitate our explanation of the analytical foundations of the SIPD, we will construct the diagram using the recently proposed Newellian Coordinates. The properties of this coordinate system allow us to easily construct and visualize the derivation of the necessary boundaries of the SIPD.

3.2.1 Newellian Coordinates

Newellian Coordinates assume that all vehicles follow a homogeneous deterministic Newell's car-following model in order to encode trajectories according to their intersection arrival time and stop position in relation to the stop bar (Newell, 2002; Wang et al., 2024a). These coordinates are based on a distorted grid where the slope of the vertical axis is the free-flow speed v_f (Figure 3.1a). Therefore, vehicle trajectories are encoded in either a stop or free-flow state according to their intersection arrival time and stop position in relation to the stop bar. This allows us to ignore the free-flow travel time and easily quantify delay resulting from traffic signal control, thus making it much more intuitive to derive and visualize the boundaries derived in the SIPD. The horizontal axis t (in units of time interval Δt) represents the free-flow stop bar arrival time, and the vertical axis n indicates the number of unit traffic flows (in units of Δu, where Δu indicates the number of vehicles traveling within time interval

Δt according to the saturation flow rate q_s). In this chapter, we let Δu equal one vehicle so that the vertical axis directly represents the stop position n of each vehicle in the queue. If we assume a saturation flow rate of 1800 vph, then $\Delta t = 2s$. Figure 3.1a also illustrates an example trajectory and how the Newellian Coordinates can be used to easily identify its free-flow arrival time t_a and departure time t_b, where the control delay is $t_b - t_a$. The discharge shockwave can also be drawn on the distorted grid and indicates where on the time-space diagram we expect to observe stops (anywhere to the left of it as shown in Figure 3.1b). The shockwave speed w_d is equal to $n/\Delta t$.

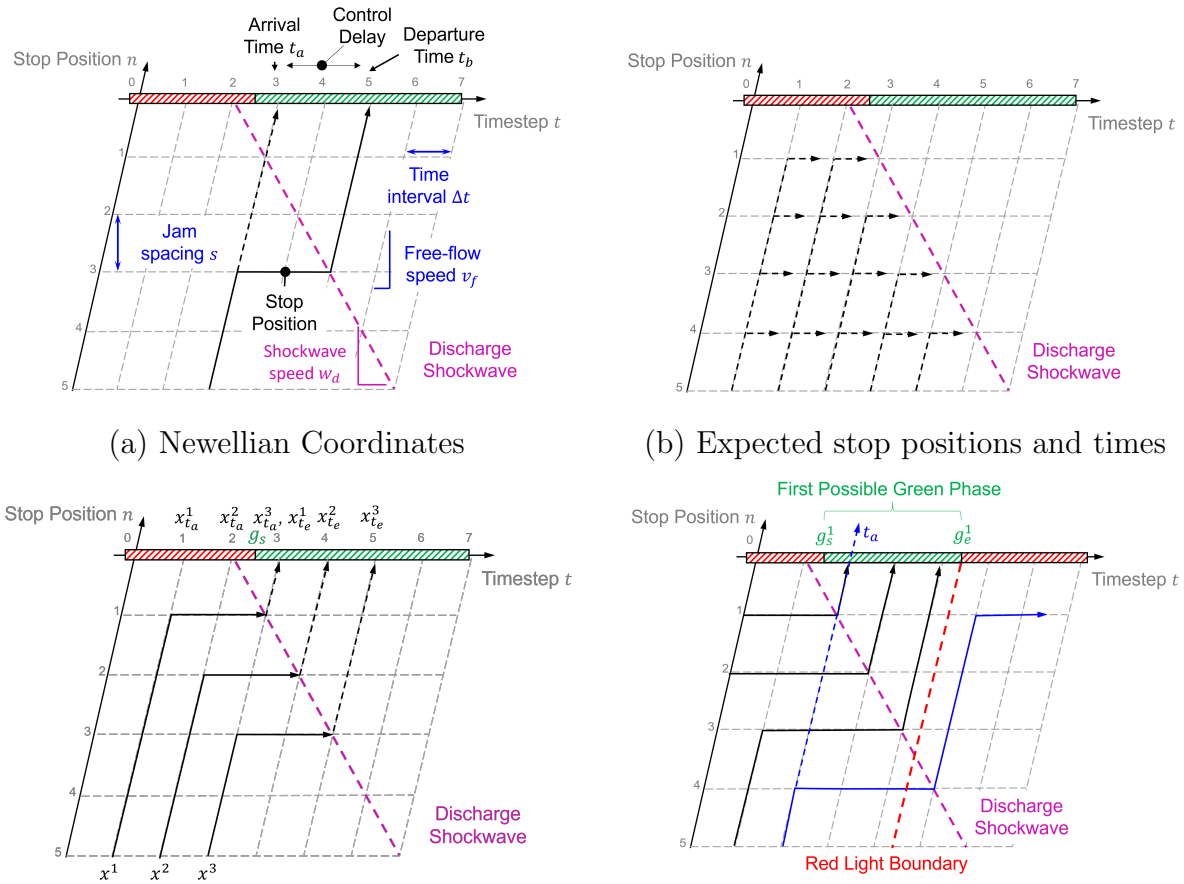

(a) Newellian Coordinates

(b) Expected stop positions and times

(c) Expected departure based on n

(d) Split failure illustration

Figure 3.1: Demonstrations of Newellian Coordinates

For each trajectory x^i, its first stop position n (left of the discharge shockwave) can be used to calculate the expected departure time t_e (Figure 3.1c):

$$t_e = g_s + n \cdot \Delta t \tag{3.1}$$

where g_s is the green phase start time. For example, trajectory x^1 is stopped at $n = 1$, so we expect it to depart at the first timestep after the green start which in this case is $t = 3$. Trajectory x^2 is stopped at $n = 2$, so it is expected to depart at the second timestep after the green start time ($t = 4$). Likewise, trajectory x^3, which is stopped at $n = 3$ is expected to depart at $t = 5$. We can also use the Newellian Coordinates to identify when a vehicle trajectory exhibits a split failure (Figure 3.1d). Each trajectory should be able to depart in the first available departure green split (g^1), which is defined as the first green split where the end g_e is greater than t_a. If the departure time t_b is in a later green split, than a split failure has occurred. Figure 3.1d demonstrates a split failure exhibited by the trajectory outlined in blue because it fails to depart before g_e^1. This figure also introduces the "red light boundary", which extends from the beginning of the red interval along the distorted vertical axis, dividing trajectories that will arrive before the green interval ends and after the red interval begins. Any trajectory that crosses this boundary exhibits a split failure.

3.2.2 SIPD boundaries and zones

In this section, we derive the boundaries of the SIPD using the Newellian Coordinates. The SIPD is a time-space diagram segmented based on the expected growth and decay of congestion in response to traffic signal control under protected operation. In addition to the discharge shockwave and the red light boundary, these zones are also partitioned according to the compression shockwave and capacity boundary (Figure 3.2a). The compression shockwave is the boundary where vehicles traveling at saturated conditions stop as they join the end of the queue after the green split ends and has the same velocity as the discharge shockwave. A "capacity boundary" indicates the point at which trajectories with stops begin to exhibit split failures as their expected arrival time t_e based on their stop position n exceeds the green interval. For instance, trajectory x^5 in Figure 3.2a exhibits a split failure because $x^5_{t_a} < g_e^1 < x^5_{t_b}$, causing it to cross the red light boundary. Since its stop position is beyond the capacity boundary, the split failure is the direct result of insufficient green time and oversaturation in the approach lane. Trajectory x^6, despite stopping twice, does not exhibit a split failure because its arrival time is greater than g_e^1, so it would not have been able to depart within the green interval g^1 anyway. You can also tell that it does not exhibit a split failure by noticing that it does not cross the red light boundary. The capacity boundary n_c is found by determining the number of vehicles that can pass through the green split g:

$$n_c = \frac{g}{\Delta t} \tag{3.2}$$

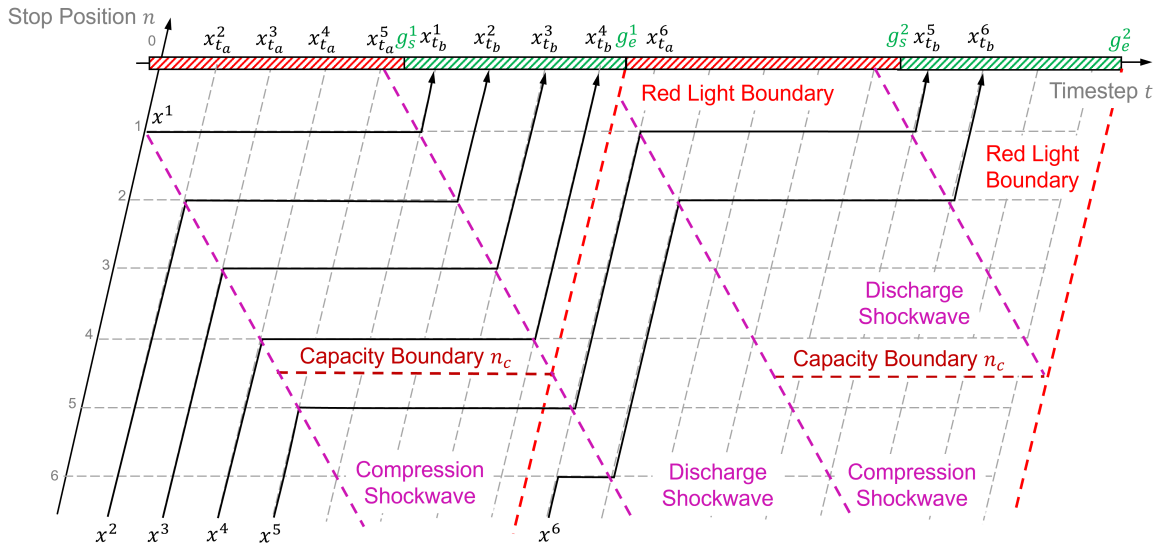

(a) Boundaries

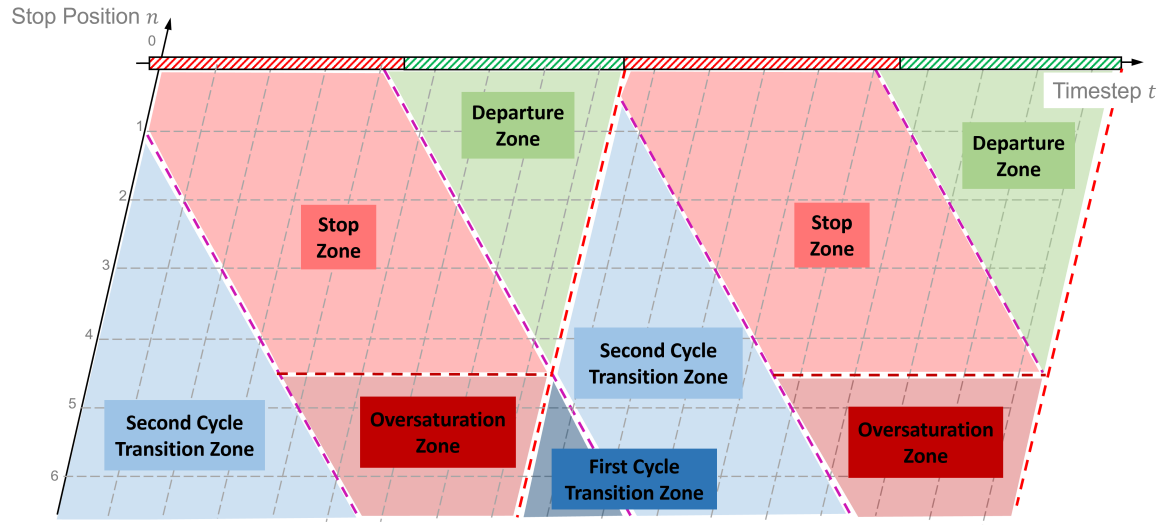

(b) Zones

Figure 3.2: Signalized Intersection Performance Code (SIPD)

These four boundaries create five zones (Figure 3.2b): 1.) the departure zone, bounded by the discharge shockwave and the red light boundary (shaded in green), 2.) the stop zone, bounded by the compression shockwave, the discharge shockwave, and the capacity boundary (shaded in red); 3.) the oversaturation zone, bounded by compression shockwave, the capacity boundary, and the red light boundary (shaded in dark red); 4.) the first cycle transition zone, bounded by the discharge shockwave and the red light boundary (shaded in dark blue); and 5.) the second cycle transition zone, bounded by the compression shockwave, the discharge shockwave, and the red light boundary (shaded in blue). The last two zones are called "cycle transition" zones because trajectories traveling through these zones

are ultimately heading to the next stop or oversaturation zone in preparation for the next green split. They are also located at the beginning of each cycle (right after the red light boundaries).

All five of these zones allow us to identify different traffic congestion states for particular intersection movements based on a limited number of vehicle trajectory observations. Table 3.1 outlines how where trajectory is in a stop state on the SIPD can help us diagnose different intersection movement congestion conditions. For trajectories under protected traffic signal operations, trajectories are expected to stop inside the stop zone and can indicate normal undersaturated traffic conditions at the point where the trajectory comes to the stop. These trajectories will be serviced by the upcoming green split. However, as the name implies, once trajectories start coming to stops within the oversaturation zone this indicates oversaturation in the current cycle. These trajectories will not be serviced by the cycle's green split. If a trajectory is in the stop state in the first cycle transition zone (such as x^6 in Figure 3.2), then this can indicate that the previous cycle will not be able to service all of the existing queued trajectories who stopped in the oversaturation zone.

Table 3.1: Diagnosing intersection movement congestion conditions using the SIPD

Zone where Trajectory is in Stop State	Movement Congestion Condition
Stop Zone	Undersaturated when trajectory stopped
Oversaturation Zone	Oversaturated in current cycle
First Cycle Transition Zone	Oversaturated in previous cycle
Departure Zone	Experiencing blockage in current green split
Second Cycle Transition Zone	Experienced blockage in previous green split

Stops inside the other two zones (departure and second transition) can indicate abnormal traffic congestion because they do not follow the conventions of protected traffic signal control. Under such control, all stops should end at the discharge shockwave. However, blockage preventing the normal queue dissipation could extend such stops into the departure zone or force other trajectories to stop in the departure zone. In normal conditions, trajectories would not be in the stop state at any point in the departure zone as trajectories traveling in this zone should be traveling at free-flow speed (ignoring start-up acceleration). The same is expected in the second cycle transition zone. The only difference is that stops inside this zone indicate blockage in the previous cycle's green split. The next section will describe how we can quantify such blockage using the SIPD.

3.3 Red light and blockage performance measures

The SIPD allows us to quantify the delay caused by abnormal congestion patterns at signalized intersections such as blockage preventing queue dissipation. Table 3.2 presents each of the proposed measures and how they relate to the state-of-the-practice. State-of-the-practice refers to the baseline methods established in previous studies. As described earlier, the these do not include signal timing data so they can not differentiate metrics influenced by blockage. In the proposed measures, the traditional measures of control delay, number of stops, and split failures are each divided into red light and blockage subcategories. Red light delay, stops, and split failures can be considered performance measures that are the direct result of red light traffic signal control. Blockage delay, stops, and split failure are the result of blockage that is preventing queue dissipation during the green phase. Delay is differentiated by the expected arrival time t_e according to the stop position n. Stops are differentiated based on if they occur before or after a trajectory enters the departure zone. Split Failures are differentiated based on how many departure zones the trajectory enters. Note that these measures are heavily based on the trajectory behavior after entering the departure zone because trajectories are expected to clear the intersection once they enter that zone given normal queue dissipation.

Table 3.2: Proposed performance measure comparison with state-of-the-practice

Performance Measures	State-of-the-Practice (SotP)	Proposed Measures	Proposed Method
No. of Stops	all observed stops	RL Stops	stops that occur before entering Departure Zone
		Blockage (Blkg) Stops	stops that occur after entering Departure Zone
Control Delay (CD)	$t_b - t_a$	Red Light (RL) Delay	$t_e - t_a$
		Blkg Delay	$t_b - t_e$
Split Failure (SF)	more than one stop and CD > threshold	RL SF	$t_b > g_e^1$ (enters 1 Departure Zone)
		Blkg SF	$t_b > g_e^1$ (enters more than 1 Departure Zone)

Figure 3.3 illustrates how these measures can be calculated for each vehicle trajectory plotted on the SIPD. The flow chart is segmented by each performance measure (number of stops, delay, and split failures). Blue boxes are conditions, green boxes are the performance measures, and purple boxes are variables that must be determined through the process to

help calculate the performance measures. The following paragraphs will discuss different examples of how to use this chart based on the plots in Figure 3.4.

The tables embedded in each plot in Figure 3.4 report the performance measures for both x^1 and x^2. Visually we can see that trajectory x^1 is not able to end its stop at the discharge shockwave and the stop extends into the departure zone due to some blockage (indicated by the red bar overlaid on top of the green light bar), but the performance measures can be quantified according to Figure 3.3. First, there is an arrival time t_a of 1 and a departure time t_b of 8. Therefore, the control delay experienced by this trajectory is 7. The first green end time g_e^1 based on t_a is between timesteps 8 and 9. The trajectory has one stop which occurs in the stop zone before the trajectory enters the departure zone, so it is a red light stop. We

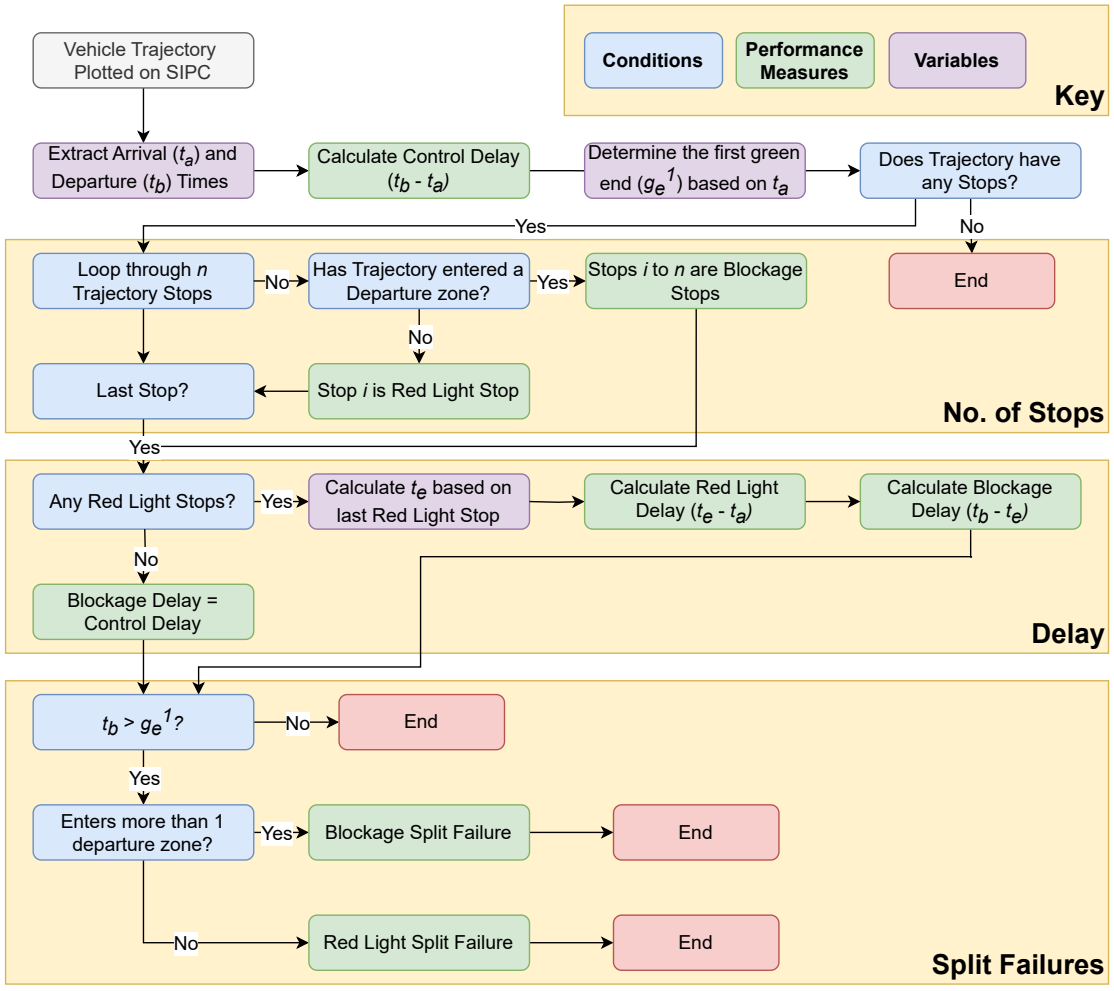

Figure 3.3: Flow chart for calculating proposed performance measures from trajectories plotted on the SIPD

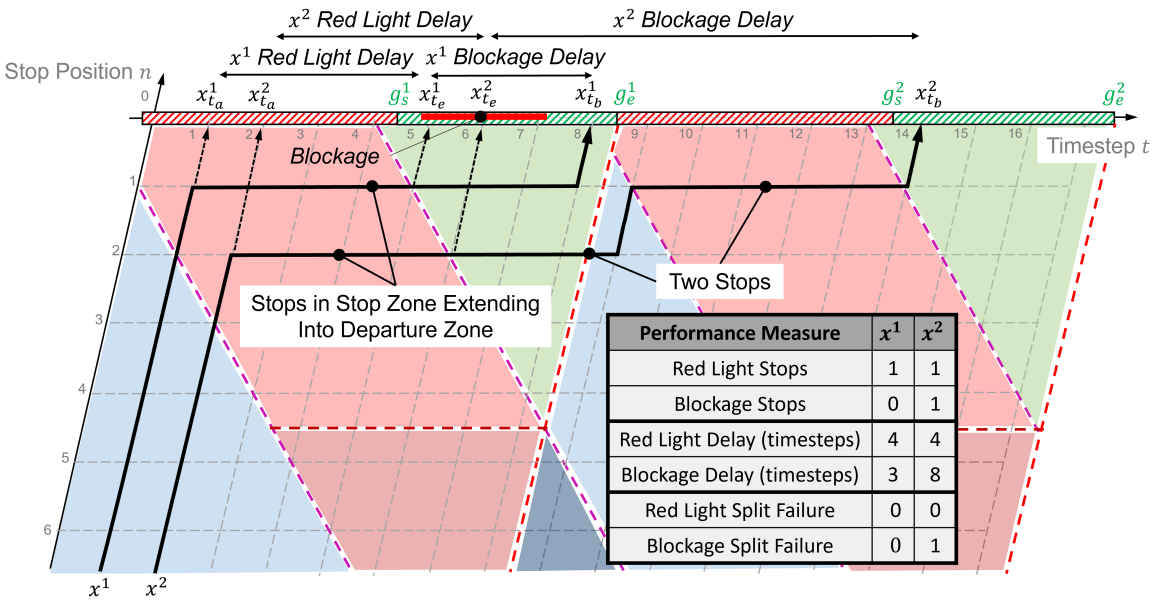

Performance Measure	x^1	x^2
Red Light Stops	1	1
Blockage Stops	0	1
Red Light Delay (timesteps)	4	4
Blockage Delay (timesteps)	3	8
Red Light Split Failure	0	0
Blockage Split Failure	0	1

(a) Example 1

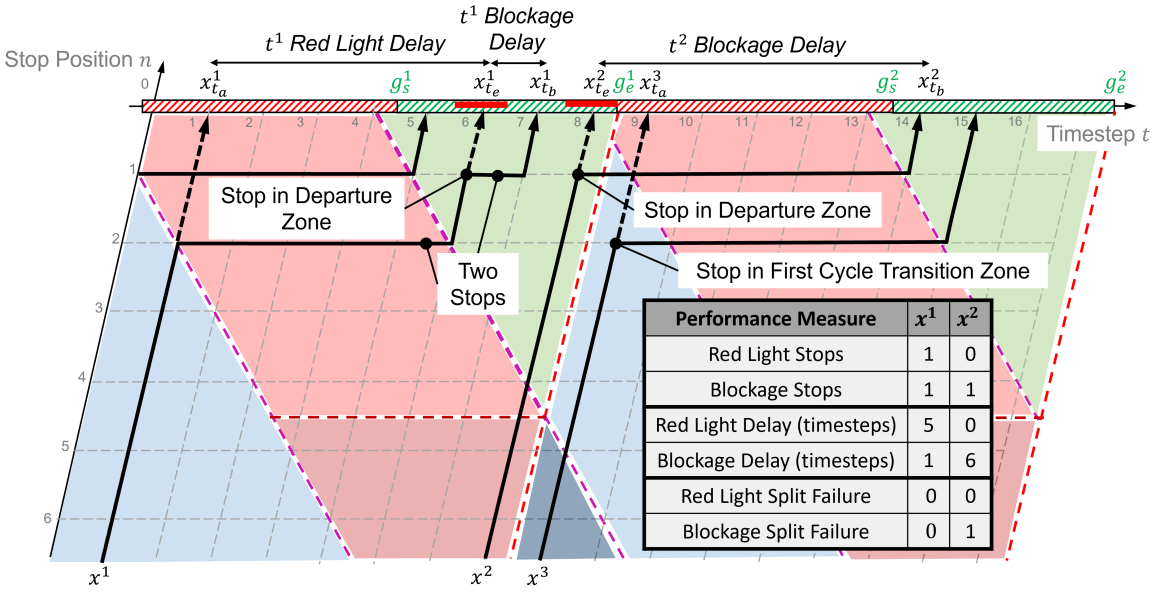

Performance Measure	x^1	x^2
Red Light Stops	1	0
Blockage Stops	1	1
Red Light Delay (timesteps)	5	0
Blockage Delay (timesteps)	1	6
Red Light Split Failure	0	0
Blockage Split Failure	0	1

(b) Example 2

Figure 3.4: Example trajectories plotted on the SIPD

can then calculate t_e to be 5 according to the stop position $n = 1$. Therefore, the trajectory departs 3 timesteps after its expected departure time $x^1_{t_e}$. We call this delay "blockage delay" and it is calculated by subtracting t_e from t_b. The other portion of the control delay is termed "red light delay" and is calculated by subtracting t_a from t_e. Therefore, control delay is the summation of both red light and blockage delay. Blockage delay is still considered to be

control delay because in most cases it will be caused by permissive phasing or oversaturation at the downstream intersection. In some other cases it could be the result of obstructions in the roadway such as an accident, and future work will look in to how to differentiate control blockage delay from non-control blockage delay.

Trajectory x^2 in Figure 3.4a shows how the blockage delay experienced by x^1 can impact other trajectories in the queue. While the figure helps illustrate this relationship, it is important to note that the performance measurements could be extracted using the flow chart in Figure 3.3 regardless if x^1 is observed. First, x^2 has an arrival time t_a of 2 and a departure time t_b of 14, so the control delay is 12. he first green end time g_e^1 based on t_a is between timesteps 8 and 9, just like x^1. The first stop occurs in the stop zone before the trajectory enters the departure zone, so it is a red light stop just like x^1. However, the blockage delay of x^1 prevents x^2 from departing at the expected departure time $x_{t_e}^2$. The second stop experienced by x^2 occurs after it travels through the departure zone so it is called a "blockage stop" because the stop occurred after experiencing blockage delay. The expected departure t_e is calculated according to the last red light stop position $n = 2$. Therefore $t_e = 6$ and the resulting red light blockage delays are 4 and 8, respectively.

Finally, since x^2 crosses the red light boundary and $t_b > g_e^1$, this trajectory exhibits a split failure. However, this split failure occurs because of the blockage delay experienced by x^1 which prevented x^2 from departing within its first green split. Since x^2 traveled through the departure zone, we know that it could have departed within the first green split had there not been any blockage. Therefore, we call this split failure a "blockage split failure." This is covered in the flow chart in Figure 3.3 by the condition of the trajectory entering more than 1 departure zone, which is clearly shown by the SIPD plot. A "red light split failure" would have occurred if x^1 had first stopped in the oversaturation zone and not crossed the red light boundary.

The state-of-the-practice for split failure identification with vehicle trajectory data is based on two criteria: more than one stop (Saldivar-Carranza et al., 2023; INRIX, 2024). The trajectories shown in Figure 3.4b demonstrate some of the shortcomings of this method. Trajectory x^1 has two stops, one red light stop and one blockage stop, and significant delay relative to the cycle but does not exhibit a split failure. Trajectory x^2 only has one blockage stop but does exhibit a split failure. This blockage split failure occurs despite only having one stop because some blockage forces x^2 to stop at $n = 1$ and prevents it from departing within the first available green split. These examples illustrate how identifying split failures according to the number of stops with some control delay threshold may lead to inaccuracies when blockage is present. Wang et al. (2023) attempted to mitigate this issue by adding a control delay threshold, but variability in arrival times and red light lengths make it

impossible to create a threshold that can apply to every case. As reported in Table 3.2, we use a delay threshold for the state-of-the-practice comparison in this chapter, as a modest threshold value can eliminate obvious false positives.

Trajectories that stop inside the second cycle transition zone can also indicate that trajectories ahead in the queue experienced blockage split failures (x^3 in Figure 3.4b). Because x^2 does not clear the intersection before g_e^1, this causes the queue to extend into the second cycle transition zone forcing x^3 to come to a stop before the stop zone. Even if we did not observe x^2, we could still infer that the trajectory in front of x^3 experienced blockage split failures based on the stop in the second cycle transition zone.

3.4 SIPD construction using vehicle trajectory data

While the Newellian Coordinates are useful for visualizing the derivations of the necessary boundaries of the SIPD, an important limitation when analyzing real-world scenarios is that vehicles do not travel at free-flow speeds during queue discharge. Therefore, this section describes how we can estimate the boundaries of the SIPD from trajectory data observations using Lagrangian Coordinates (time in cycle t vs. distance to the intersection x). In this chapter, t is set to zero at the start time of the green split for which the trajectory departs the intersection. To demonstrate the estimation process, we use a two-lane approach from an intersection running a two-phase signal timing operation under permissive only left-turn phasing. The approach does not have a protected left turn lane, so the inside lane is shared between the straight and left-turn movements. As a result, blockage delay is exhibited in both movements. This intersection is controlled by a fixed-time operation, but it is important to note that the necessary measurements could be determined by using signal timing data logged by the controller in actuated, traffic-responsive, or adaptive control settings.

First, the expected departure time t_e for the straight movement is estimated by plotting the stopping distance of each trajectory's last stop (x-axis) against its departure time after the green start time t_b (y-axis) (Figure 3.5). The stopping position is reported as the raw distance in meters x to the center of the intersection. Vehicles traveling in the inside lane straight through the intersection may experience blockage delay from the permissive movements in the lane waiting for an acceptable gap. These vehicles are associated with the plot points in the upper left half of the figure. Therefore, a regression line is drawn using the RANSAC regression algorithm to eliminate these outliers (Derpanis, 2010). The blue regression line represents the expected departure time for each stop distance and is defined by the equation embedded in the figure. The y-intercept can be interpreted as drivers' green start reaction time ($1.81s$).

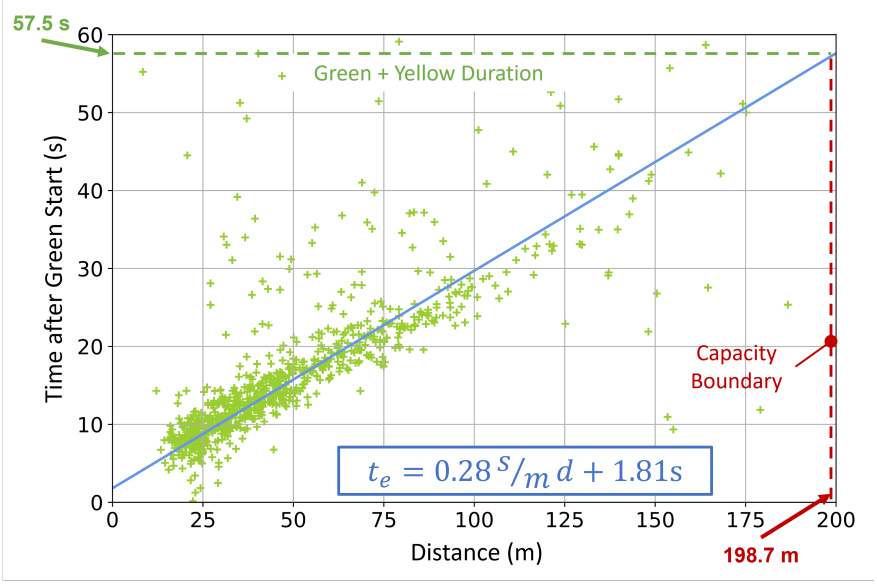

Figure 3.5: Departure time t_b after green start vs. stop position plot for stopped vehicles with expected departure regression line for a straight movement sharing a lane with a left-turn movement

Using the expected departure equation, we can determine the capacity boundary's distance by setting t_e to the green interval g and solving for x. As shown in Figure 3.5, the green interval is 57.5 seconds and the capacity boundary's distance is 198.7 meters. The time coordinates of the capacity boundary are found after estimating the discharge shockwave.

To estimate the discharge shockwave, the stopping distance x from before is now plotted against the stop end time t_{se} on the time-space diagram (Figure 3.6). The example trajectory on the right shows how these parameters are defined. The stop end time is found using the methods presented in (Wang et al., 2023). The respective plot point on the time-space diagram for this trajectory is circled in red. From these points, another RANSAC regression is performed in order to determine the discharge shockwave boundary while accounting for outliers experiencing blockage (purple dashed line in Figure 3.6). The discharge shockwave is define by the equation embedded in the figure. The end of the capacity boundary can now be found by setting this equation equal to the capacity boundary's distance ($33.8s$). The red light boundary can then be determined by connecting this point with the end of the green interval (the yellow change interval is included in the green interval in this chapter). Finally, the compression shockwave is plotted by shifting the discharge shockwave so that it starts at the end of the yellow change interval. With these boundaries, the SIPD is constructed.

Since the plot points in Figure 3.6 indicate where a trajectory's stop ends, points inside the departure zone of this constructed SIPD are considered to experience "blockage delay".

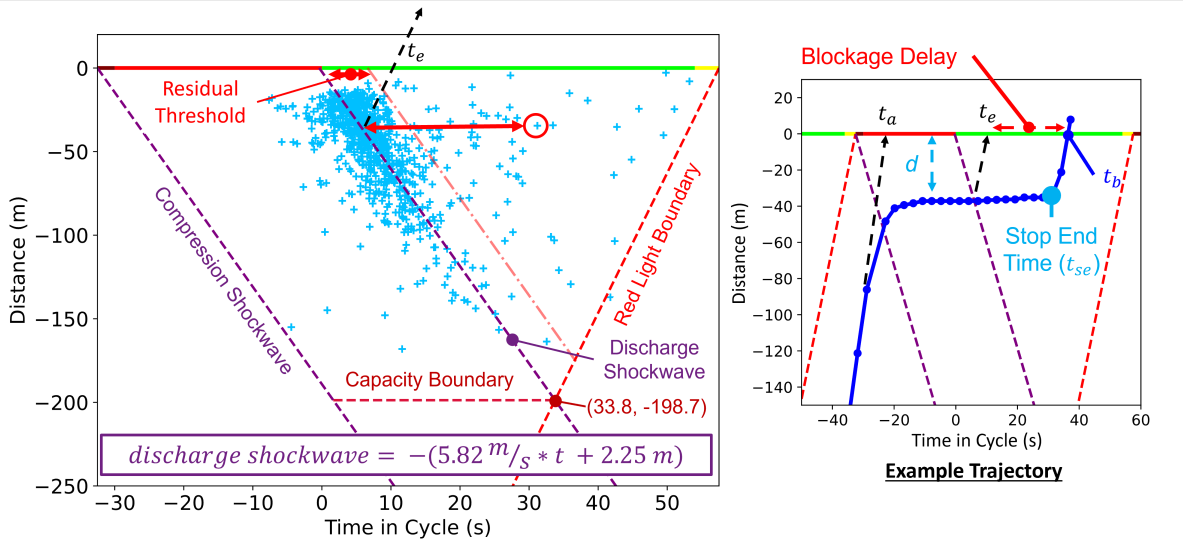

Figure 3.6: Stop end time (t_{se}) scatter plot on SIPD with example trajectory for a straight movement sharing a lane with a left-turn movement

A residual threshold between the discharge shockwave boundary and this zone accounts for trajectories in slower departing queues. In this study we assume a residual threshold of 7 seconds. The example trajectory exhibits a stop that extends into the departure zone, indicating some blockage delay. This delay can be calculated according to Table 3.2 by estimating t_e given x from the equation if Figure 3.5.

The blockage delay for this straight movement is the result of left-turning vehicles in the shared lane not being able to find an acceptable gap acceptance in the permissive phase. Figure 3.7 is the same SIPD time-space diagram plotted in Figure 3.6 for the left-turn movement constructed from the expected departure regression line and discharge shockwave calculated for the straight movement. The same regression lines are used because a large portion of the trajectories in this movement experiences some blockage delay, as shown in the figure, making it difficult to plot a regression line. Since the movements share a lane it is reasonable to expect the same expected departure and discharge shockwave. This is supported by the number of plot points along the discharge shockwave. Most of the plot points inside the departure zone for the left-turn movement are located closer to the center of the intersection as opposed to the more scattered distribution for the straight movement. This makes sense as left-turning vehicles usually must wait for an acceptable gap at the front of the queue in the permissive setting, whereas the last stop of a vehicle traveling straight through the intersection could be located at various distances since these vehicles do not have to wait for an acceptable gap when they reach the front of the queue.

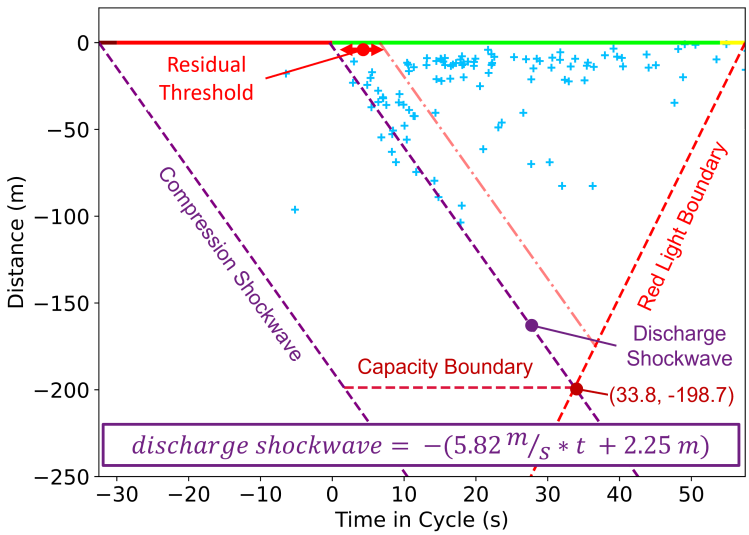

Figure 3.7: Stop end time (t_{se}) scatter plot on SIPD for the left-Turn movement that shares a lane with the straight movement in Figure 3.5

3.4.1 Modifications for real-time systems

This scenario specifically addresses fixed-time operations where the SIPD only needs to be plotted once because of the constant cycle length, green split, and offset. In cases where the green duration is not fixed on a cycle-by-cycle basis because it is not under maximum recall or is controlled by a traffic-responsive or adaptive operations, the capacity and red light boundaries should be adjusted for each cycle. The green duration for each cycle can be extracted using historical signal timing data logged by the controller. The discharge and compression shockwaves should remain consistent across each cycle.

3.5 Case studies

Case studies were conducted at five signalized intersections in Birmingham, MI and another in Pontiac, MI. Data is taken from AM, MD, and PM periods on weekdays between March 7th, 2022 and March 25th, 2022 in Birmingham and the weekdays between October 1st, 2023 and November 20th, 2023 in Pontiac. The SIPD for each respective intersection movement was constructed using fixed-time traffic signal parameters provided by the Road Commission for Oakland County (RCOC). These case studies demonstrate how plotting vehicle trajectories on the SIPD can give greater insight into the performance of signalized intersections compared with the state-of-the-practice. Blockage delay, stops, and split failures were collected from SIPDs plotted at six intersections with different intersection geometries and phase operations for both permissive movement and spillover scenarios.

3.5.1 Evaluating blockage impacts of permissive movements

In left-turn permissive movement settings, vehicles must wait for an acceptable gap in oncoming conflicting traffic before executing a turning movement and clearing the intersection. These vehicles will also impact the travel times for vehicles queued up behind them, including vehicles traveling straight the intersection when there are shared lanes present. The results presented in this section demonstrate how the SIPD can be used to quantify the impacts of conflicting traffic on the performance of permissive movements. Results were collected at three intersections with different intersection geometry and phase operations (Figure 3.8): 1.) one-lane approaches under permissive only left-turn phasing (Lincoln St. and Pierce St. in Figure 3.8a), 2.) two-lane approaches on the main street under permissive only left-turn phasing (Adams Rd. and Derby Rd. in Figure 3.8b), and 3.) three-lane approaches under protected-permissive left-turn phasing (Telegraph Rd. and Elizabeth Lake Rd. in Figure 3.8c). The variety of scenarios demonstrates the flexibility of the SIPD and the derived performance measures. Figure 3.8 also gives the traffic control phase sequences for each intersection, where the unfilled arrows indicate permissive movements. Spillover was ruled out as the cause of blockage at these intersections by examining the downstream behavior of each trajectory.

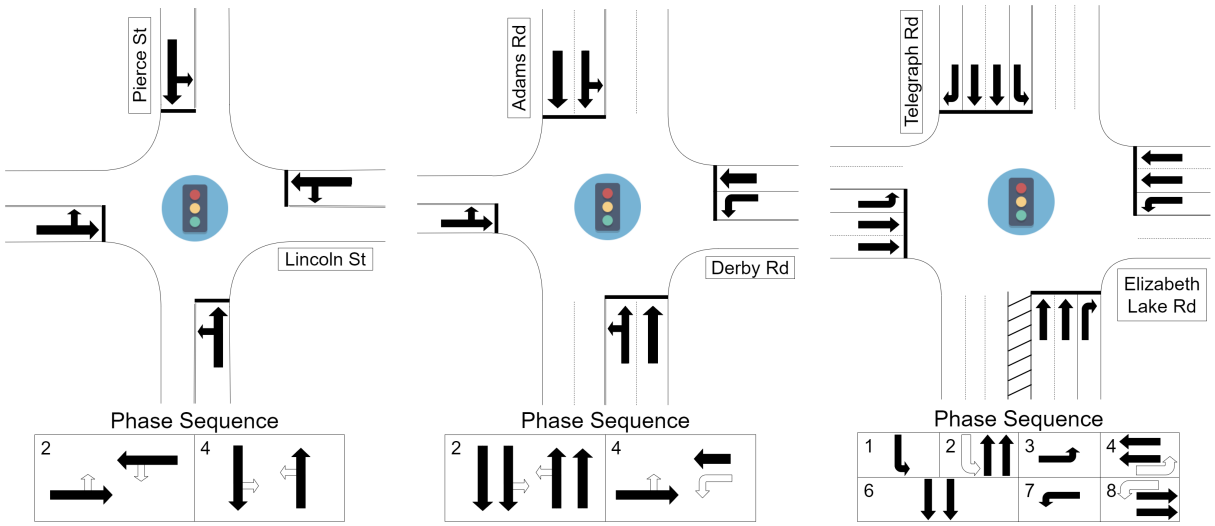

(a) Lincoln St. and Pierce St.

(b) Adams Rd. and Derby Rd.

(c) Telegraph Rd. and Elizabeth Lake Rd.

Figure 3.8: Intersection geometries and traffic control phase sequences for case studies examining blockage impacts from permissive movements

3.5.1.1 One-lane intersection approaches with permissive only left-turn phasing

The intersection of Lincoln St and Pierce St (Figure 3.8a) in Birmingham, MI has four one-lane approaches under permissive only left-turn phasing. Therefore, both the straight and left-turn movements for each approach are subject to blockage delay either from directly waiting for an acceptable gap or being stuck behind a left-turning vehicle waiting for an acceptable gap. Figure 3.9 plots some example trajectories on the SIPD, and Table 3.3 reports their respective performance measures, including red light delay, blockage delay, blockage stops, split failure identification according to the state-of-the-practice (with a 60 control delay threshold), red light split failure, and blockage split failure. These results show how the SIPD can be used to easily analyze trajectories and the mobility performance of the movement. Examples A-C are left-turning trajectories. Example A has a stop inside the departure zone, indicating a blockage stop where the control delay is entirely blockage delay. The red light stop exhibited in Example B extends into the departure zone, indicating blockage delay in addition to red light delay. The state-of-the-practice would have identified a split failure in Example C because of the multiple stops and control delay greater than the threshold, but the SIPD plot clearly shows that this trajectory does not cross the red light boundary and is not a split failure. Examples D and E are both through movements that experience blockage split failures as they have stops in the departure zone and they

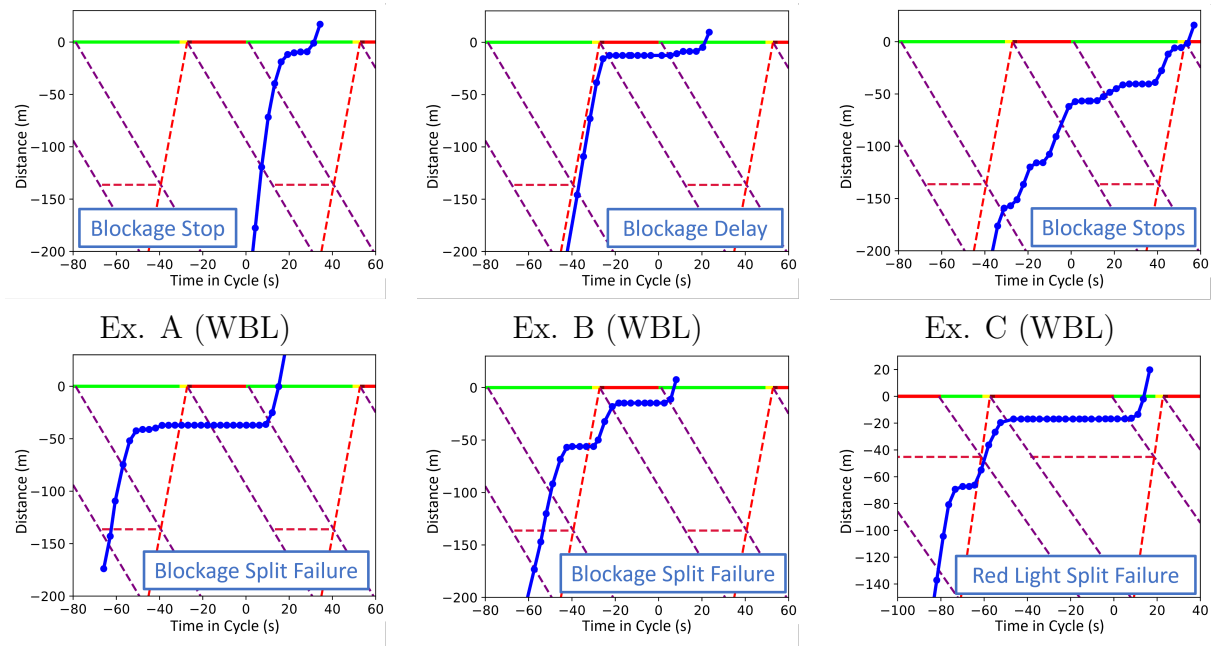

Ex. A (WBL) Ex. B (WBL) Ex. C (WBL)

Ex. D (WB) Ex. E (WB) Ex. F (NBL)

Figure 3.9: Example trajectories from Lincoln St and Pierce St

Table 3.3: Performance measures from trajectories in Figure 3.9

Ex.	t_a	t_e	t_b	RL Dly	Blkg Dly	Blkg Stops	SotP SF	RL SF	Blkg SF
A	13.5	13.5	31.5	0.0	18.0	1	0	0	0
B	-25.4	5.9	21.4	31.3	15.5	0	0	0	0
C	-18.2	22.9	54.2	41.1	31.3	2	1	0	0
D	-50.7	16.7	15.2	0.0	65.8	1	0	0	1
E	-40.3	-57.6	7.1	0.0	47.4	1	0	0	1
F	-71.0	7.9	13.9	84.9	0.0	0	1	1	0

cross the red light boundary. These split failures would not have been identified with the state-of-the-practice either because they did not have enough stops or their control delay did not surpass the threshold. The blockage stops in the departure zone also give insight as to the behavior of the unobserved trajectories at this point in time. With just one observation we can see that there is some blockage preventing queue discharge. Finally, the left-turning trajectory in Example F has a red light split failure because it stops in the oversaturation zone.

The results from each observed trajectory can be aggregated to gain insights into how blockage is influencing the performance measures at each signalized intersection movement. The results in Table 3.4 are from the PM peak period (3 - 7 PM). The blockage delay and stops are reported as a percentage of the control delay and number of stops, respectively. Lincoln St., which runs in the east/west direction, exhibits less control delay and number of stops but has a higher percentage of blockage delay and stops with the westbound left (WBL) movement having the highest percentages at 45.05% and 37.88%, respectively. This means that about half of the delay experienced by vehicles performing this movement is caused by waiting for an acceptable gap acceptance or being stuck behind other vehicles

Table 3.4: Aggregated delay and stop performance measures for Lincoln St and Pierce St in the PM peak period (3 - 7 PM)

Movement	Obs.	Avg. Control Delay (s)	Blkg Delay (% of CD)	Avg. No. of Stops	Blkg Stops (% of Stops)
WBL	102	19.17	45.05%	0.65	37.88%
WB	1862	10.23	10.74%	0.39	9.27%
EBL	87	14.58	31.33%	0.51	20.45%
EB	2151	10.35	5.87%	0.40	5.26%
SBL	55	33.51	13.88%	0.82	8.89%
SB	296	28.12	0.76%	0.76	1.33%
NBL	145	29.78	5.74%	0.72	2.86%
NB	298	27.97	0.45%	0.71	1.88%

waiting for this gap acceptance. The higher vehicle volumes in the westbound (WB) and eastbound (EB) movements account for the higher percentage of blockage in the respective left turning movements under permissive only phasing. As a result of the shared lane with the permissive left-turn movement, the westbound (WB) straight movement has around 11% blockage delay and 9% blockage stops. The interpretation is that this movement's delay and number of stops would decrease by these percentages if the straight movement did not share a lane with the left-turning movement, thus allowing us to quantify the direct impacts of a geometric design change to the intersection.

Table 3.5 compares the state-of-the-practice split failure identification results with the proposed method that includes red light and blockage distinctions. The state-of-the-practice method is particularly deficient in identifying split failures caused by blockage, most likely because these trajectories usually only exhibit one stop. For example, the westbound (WB) movement has 15 split failures in the proposed method, including 11 blockage split failures. The state-of-the-practice only identified 1. While these split failures only accounted for less than 1% of the observed trajectories, these results show how the state-of-the-practice might miss a significant amount of split failures.

Table 3.5: Aggregated split failure performance measures for Lincoln St and Pierce St in the PM peak period (3 - 7 PM)

Movement	No. of SFs (%) (SotP)	No. of SFs (%) (Proposed Method)	Red Light SFs	Blkg SFs
WBL	2 (1.96%)	4 (3.92%)	0	4
WB	1 (0.05%)	15 (0.81%)	4	11
EBL	0 (0.00%)	1 (1.15%)	0	1
EB	2 (0.09%)	6 (0.28%)	2	4
SBL	1 (1.82%)	3 (5.45%)	2	1
SB	5 (1.69%)	7 (2.36%)	7	0
NBL	4 (2.76%)	4 (2.76%)	4	0
NB	1 (0.34%)	2 (0.67%)	2	0

The proposed method can also account for sensitivities in stop identification. Trajectories arriving at the back of the queue might not come to a complete stop before being able to accelerate forward, so algorithms such as what is proposed in (Wang et al., 2023; Saldivar-Carranza et al., 2023) might not identify the split failures in these trajectories because they don't observe two stops. Figure 3.10 plots example trajectories that slow down in the oversaturation zone but a complete stop is not observed. However, these trajectories cross the red light boundary and do not travel through the g^1 departure zone, so it is easy to identify red light split failures despite not observing two stops.

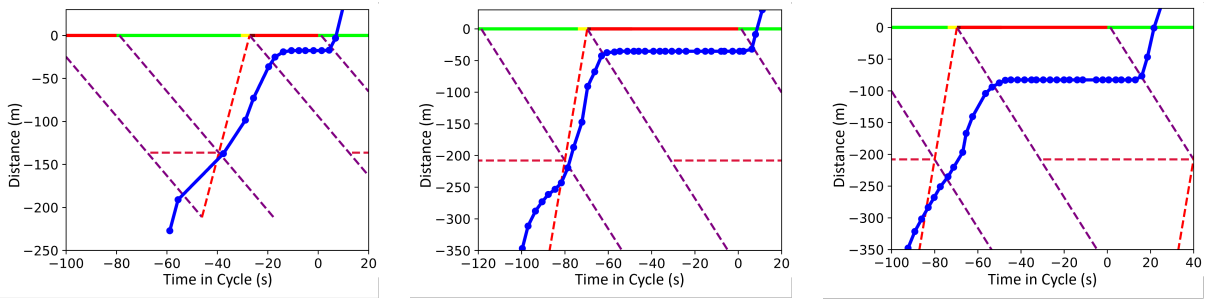

Ex. G (SBL) Ex. H (SBL) Ex. I (EBL)

Figure 3.10: Example trajectories with ted light split failures missed by state-of-the-practice

3.5.1.2 Two-lane intersection approaches with permissive only left-turn phasing (no dedicated left-turn lane)

The intersection of Adams Rd and Derby Rd in Birmingham, MI has two-lane approaches on the main street (Adams Rd) under permissive only left-turn phasing. The inside lane is shared between the straight and left-turn movements and subject to blockage delay. There is a school at the southeast corner of this intersection that starts in the morning between 7:00 AM and 10:00 AM (AM peak period) and lets out between 3:15 PM and 3:40 PM ("PM2" peak period). Therefore, there is more SBL traffic at these times of the day that causes blockage delay for the SBL and SB movements. Table 3.6 reports the aggregate delay and stop measures for this intersection. In the PM2 peak period, 51.97% of the control delay and 40.63% of the stops is caused by blockage in the SBL movement. This impacts the SB movement where 9.62% of its delay and 7.69% of its stops are caused by the permissive waiting time in the SB movement. The results in the AM period are a little lower, but this period covers a 3 hour period of the day and 42.78% of the SBL control delay is still the result of blockage from conflicting movements.

Table 3.6: Aggregated delay and stop measures for Adams Rd and Derby Rd in the AM (7 - 10 AM) and PM2 (3:15 - 3:40 PM) peak periods

Period	Movement	Obs.	Avg. Control Delay (s)	Blkg Delay (% of CD)	Avg. No. of Stops	Blkg Stops (% of Stops)
AM	SB	2308	11.09	6.02%	0.37	5.50%
	NB	1113	12.12	3.55%	0.55	2.11%
	SBL	210	25.55	42.78%	0.56	28.33%
PM2	SB	232	16.79	9.62%	0.50	7.69%
	NB	296	15.70	8.08%	0.60	6.78%
	SBL	36	40.76	51.97%	0.89	40.63%

3.5.1.3 Three-lane intersection approach with protected-permissive left-turn phasing (dedicated left-turn lane)

The intersection of Telegraph Rd and Elizabeth Lake Rd in Pontiac, MI has three-lane approaches with dedicated left-turn lanes and protected-permissive left-turn phasing. Therefore, the left-turn movements may be subject to blockage delay during the permissive portion of the phase. Figure 3.11 plots some example left-turning trajectories at this intersection on the SIPD where dark green at the signal bar indicates protected phase and the light green indicates permissive phase. Table 3.7 reports their respective performance measures. In this setting, we include one more performance measure call "protected green split failure" which indicates if a trajectory was not able to clear the intersection within the first available green split (including the permissive phase) but had an arrival time before the end of the protected phase, as shown in Example H. Protected green split failures could either be a red light or blockage split failure, but will in most cases by a blockage split failure with higher control delays than a regular blockage split failure. This measures gives some insight into the performance of the protected phase. Both Example G and H are not able to clear the intersection during the protected phase, but Example G was able to clear during the permissive phase. Example G was classified as a split failure in the state-of-the-practice but was not classified that way in the proposed method. Note that the red light boundary in our figures starts at the beginning of the yellow change interval and vehicles might still clear the intersection during the yellow or all red period. Examples H and I both exhibit blockage split failures while only Example H would have been classified as a split failure in the state-of-the-practice.

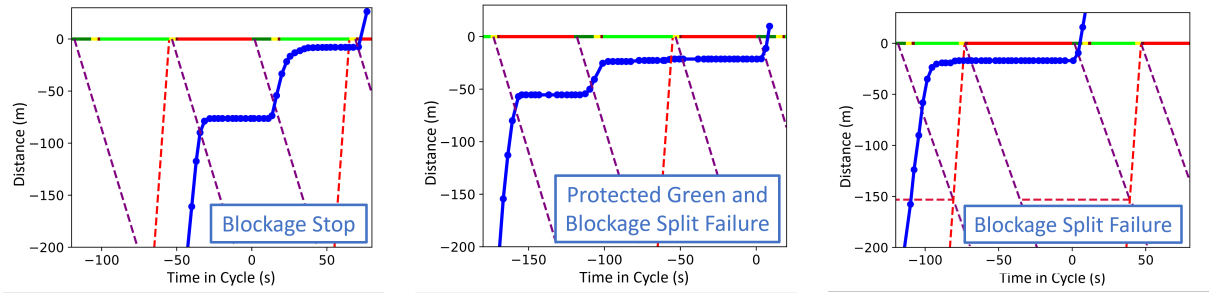

Ex. G (SBL) Ex. H (SBL) Ex. I (EBL)

Figure 3.11: Example trajectories from Telegraph Rd and Elizabeth Lake Rd

The aggregated performance measures for delay and stops are reported for the AM and PM peak periods in Table 3.8. The NBL movement is prohibited at this intersection. The SBL movement experiences the highest percentage of blockage delay at 51.68% and 57.42%

Table 3.7: Performance measures from trajectories in Figure 3.11

Ex.	t_a	t_e	t_b	RL Delay	Blkge Delay	Blkg Stops	SF (SotP)	RL SF	Blkg SF	Protected Green SF
G	-31.0	21.7	72.3	52.7	50.6	1	1	0	0	0
H	-157.0	-103.8	7.7	53.2	111.4	1	1	0	1	1
I	-100.8	-100.8	5.3	0.0	106.1	1	0	0	1	0

and blockage stops at 57.24% and 45.59%. Despite having a protected phase, the percentage of blockage delay and stops is pretty high for all left-turn movements. However, because these movements have dedicated lanes, the straight movements have almost no blockage delay and blockage stops. The small percentages reported in the table could be the result of spillover or in variations in the boundaries of the SIPD. For instance, there is variation in the discharge shockwave speed on a cycle-by-cycle basis, which would cause different capacity boundary locations as well.

Table 3.8: Aggregated delay and stop performance measures for Telegraph Rd and Elizabeth Lake Rd in the AM (6 - 10 AM) and PM (3 - 7 PM) peak periods

Period	Movement	Obs.	Avg. Control Delay (s)	Blkg Delay (% of CD)	Avg. No. of Stops	Blkg Stops (% of Stops)
AM	SBL	1091	18.65	51.68%	0.54	57.74%
	SB	10856	5.12	0.60%	0.12	0.84%
	NB	5361	7.97	0.45%	0.12	0.94%
	WBL	1514	17.75	38.59%	0.34	36.22%
	WB	1673	33.22	0.84%	0.67	0.35%
	EBL	1061	35.59	14.34%	0.77	17.52%
	EB	5150	47.18	0.17%	0.84	0.19%
PM	SBL	1259	39.36	57.42%	0.62	45.59%
	SB	7345	28.65	0.11%	0.58	0.38%
	NB	11973	17.06	2.71%	0.23	2.59%
	WBL	907	34.03	23.94%	0.69	36.84%
	WB	6738	46.22	0.27%	0.83	0.41%
	EBL	1045	55.42	31.54%	0.99	39.75%
	EB	1993	40.74	1.18%	0.73	0.55%

Table 3.9 reports the split failure measurements for this intersection at the PM peak period. These results also show the advantages of the proposed method when identifying split failures. For instance, the NB movement has almost twice as many split failures as what was identified with the state-of-the-practice. This is the result of the inaccurate stop identification mentioned in a previous section. In addition, the SBL movement has almost

14 times more split failures than what was identified by the state-of-the-practice. Almost 18% of the trajectories in the SBL movement experienced blockage split failures that are easily missed by the state-of-the-practice because they usually only have one stop. The EBL and WBL movements also have a lot of protected green split failures, indicating that many vehicles are experiencing split failures despite having arrival times before the end of the protected green portion of the green split. The identification of split failures as red light, blockage, and protected green split failures gives traffic engineers more insights into how signal retiming decisions might impact these measures. For instance, in the protected-permissive setting, blockage split failures that are not also protected green split failure might be more acceptable than protected green and red light split failures.

Table 3.9: Aggregated split failure performance measures for Telegraph Rd and Elizabeth Lake Rd in the PM (3 - 7 PM) peak period

Movement	No. of SFs (%) (SotP)	No. of SFs (%) (Proposed Method)	Red Light SFs	Blkg SFs	Protected Green SFs
SBL	16 (1.27%)	225 (17.87%)	0	225	10
SB	1 (0.01%)	0 (0.00%)	0	0	0
NB	136 (1.14%)	261 (2.18%)	186	75	0
WBL	52 (5.73%)	63 (6.95%)	18	45	24
WB	241 (3.58%)	229 (3.40%)	226	3	0
EBL	128 (12.25%)	182 (17.42%)	40	142	86
EB	26 (1.30%)	18 (0.90%)	16	2	0

3.5.2 Evaluating blockage impacts of spillover

This section demonstrates how the SIPD can also quantify the impacts of spillover on intersection congestion. Spillover occurs when a queue at an intersection extends into the next intersection upstream and prevents vehicles from clearing that upstream intersection even during the green interval. As a case study, we examine the West Maple Rd corridor from Bates St. to Old Woodward Ave. in downtown Birmingham, MI (Figure 3.12). This segment contains three signalized intersections and one unsignalized intersection. All of the signalized intersections on this corridor run a two phase operation with permissive left turn movements. Both Bates St. and Henrietta St. have single lane approaches while Old Woodward Ave. has dedicated left-turn lanes.

Figure 3.13 is an aggregated time-space diagram for this corridor segment in the eastbound direction for this corridor segment with the SIPD plotted for each intersection. The aggregated time-space diagram is built by aggregating each trajectory observation to one cy-

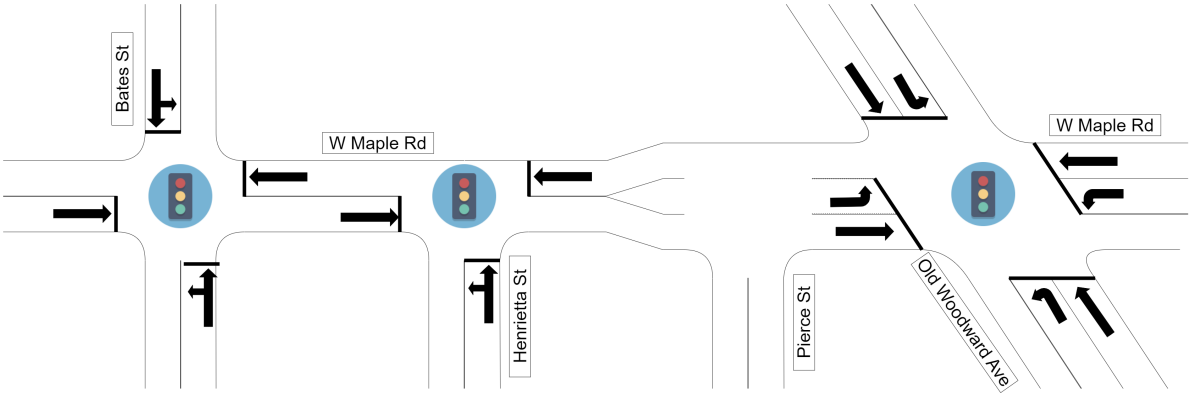

Figure 3.12: Geometric Layout for Corridor Case Study Examining Blockage Impacts from Spillover (West Maple Road from Bates St. to Old Woodward Ave)

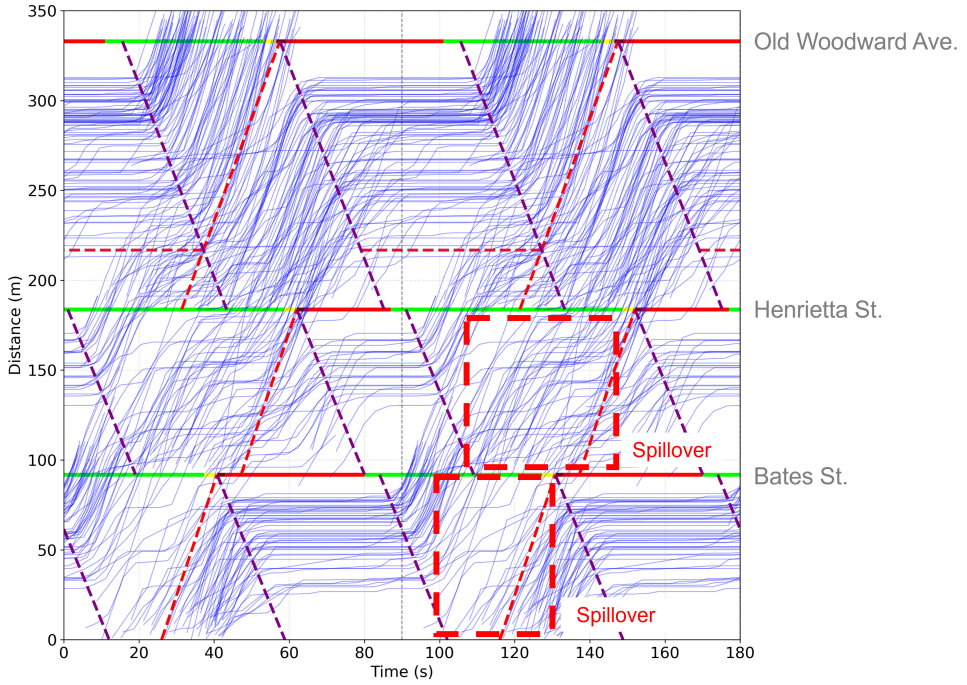

Figure 3.13: SIPD Aggregated time-space Diagram for Old Woodward Ave

cle. Refer to (Wang et al., 2023) and (Wang et al., 2024a) for more details on this procedure. For visualization purposes, data is only taken from two days from 11:00 AM to 1:00 PM. In addition, the aggregated time-space diagram is repeated once. There are a lot of blockage stops and trajectories stopped in the departure zones of both Henrietta St. and Bates St.. These intersections are also so closely spaced together that there is no oversaturation zone at Henrietta St, meaning that it is impossible for there to be any red light split failures. Therefore, the split failures observed at this intersection are always the result of blockage. If

you examine the observations at Old Woodward Ave., you can see that the queues sometimes build up to reach Henrietta St. This causes trajectories approaching Henrietta St. to stop in the departure zone. Similar behaviors can be observed at Bates St. as the queues from Henrietta St. extend into that intersection. It is important to note that there are no left turns permitted at Bates St and they are not possible at Henrietta St, which also supports the idea that these blockages shown by the SIPDs are the result of spillover.

Figure 3.14 illustrates the SIPD aggregated time-space diagrams for each individual intersection of Henrietta St. and Bates St. At Henrietta St. in Figure 3.14a, the downstream discharge shockwave from Old Woodward Ave is visible from the trajectories stopped in the departure zone and even extends into the second cycle transition zone. This clearly shows how the traffic control parameters of the downstream intersection are impacting the discharge behavior at Henrietta St. as the result of spillover. Figure 3.13b also gives a clearer picture of the behavior at Bates St.

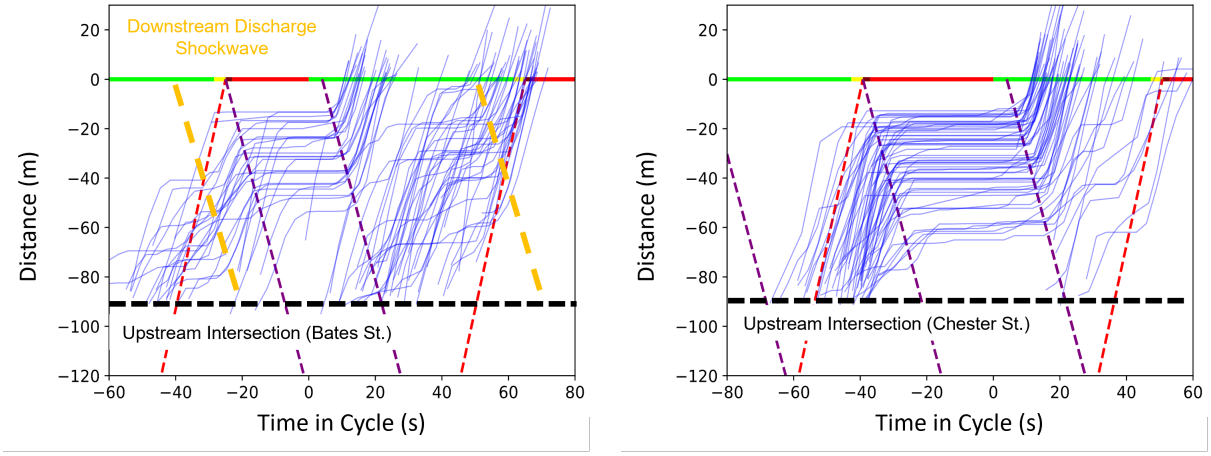

(a) Henrietta St (b) Bates St

Figure 3.14: SIPD Aggregated time-space Diagrams for Henrietta St and Bates St

The SIPD allows us to quantify the impact of such spillover. Table 3.10 reports the aggregated performance measures for the mid-day (10:00 AM - 3:00 PM) and PM (3:00 PM - 7:00 PM) periods at each intersection for the eastbound direction. Old Woodward Ave experiences very little blockage as it is the intersection causing the spillover and there is a protected left-turn lane for the permissive left-turn operation. However, Henrietta St, the immediate upstream intersection, carries the brunt of the spillover impacts with around 62% of the control delay and 83% of the stops being the result of blockage in both periods. The next intersection, Bates St., also experiences blockage impacts just not to the same degree as Henrietta St (around 20% blockage delay and 25-31% blockage stops).

Table 3.10: Aggregated delay and stop performance measures for Maple Rd eastbound in the MD (10 AM - 3 PM) and PM (3 - 7 PM) peak periods

Period	Intersection	Obs.	Avg. Control Delay (s)	Blkg Delay (% of CD)	Avg. No. of Stops	Blkg Stops (% of Stops)
MD	OWA*	2614	39.66	4.45	0.90	14.28
	Henrietta St.	3018	14.50	62.31	0.38	83.49
	Bates St.	2944	18.47	22.26	0.36	31.42
PM	OWA*	2230	34.19	4.75	0.80	13.66
	Henrietta St.	2372	14.25	62.18	0.37	82.13
	Bates St.	2342	21.21	18.09	0.41	24.74

*OWA: Old Woodward Ave

Table 3.11 reports the split failure performance measures. Around 13% of the trajectories traveling through Old Woodward Ave. experience a split-failure (this can be observed in Figure 3.13), contributing to the spillover issues as the capacity boundary is very close to Henrietta St. Around 25% of the trajectories traveling through Henrietta St. experienced a blockage split failure as a result of the spillover causing them to stop in the departure zone. As noted before, it is impossible for trajectories to experience a red light split failure at this intersection because Bates St. is closer than the capacity boundary. It can also be noted that the state-of-the-practice method for identifying split failures only observed around a third of the split failures that the proposed method observed. This is plausible because many blockage split failures will not exhibit two stops. Similar observations can be made for Bates St., whose trajectories felt the impacts of the spillover from Old Wooward Ave. extending through Henrietta St. with around 11-13% observing split failures.

Table 3.11: Aggregated split failure performance measures for Maple Rd eastbound in the MD (10 AM - 3 PM) and PM (3 - 7 PM) peak periods

Period	Intersection	No. of SFs (%) (SotP)	No. of SFs (%) (Proposed Method)	Red Light SFs	Blkg SFs
MD	OWA*	336 (14.28%)	294 (13.20%)	255	39
	Henrietta St	81 (7.11%)	268 (23.53%)	0	268
	Bates St	76 (7.26%)	141 (13.47%)	0	141
PM	OWA*	243 (14.28%)	196 (13.20%)	166	30
	Henrietta St	75 (8.48%)	225 (25.45%)	0	225
	Bates St	74 (7.66%)	106 (10.97%	0	106

*OWA: Old Woodward Ave

3.6 Conclusion

3.6.1 Summary

This chapter presents the Signalized Intersection Performance Diagram (SIPD) which provides a framework for quantifying the impacts of blockage on traffic signal performance measures using vehicle trajectory data. The SIPD is a segmented time-space diagram based on the formation and dissipation of queues under traffic signal control. The boundaries of this time-space diagram are the discharge shockwave, the compression shockwave, the capacity boundary, and the red light boundary, which can all be estimated using vehicle trajectory data. An individual trajectory's behavior through the SIPD can inform the overall traffic state based on the behaviors it exhibits through each zones. For instance, if a trajectory stops in, or has a stop extend into, the departure zone (bounded by the discharge shockwave and the red light boundary), this could indicate spillover in the downstream intersection in non-permissive scenarios. Another example is a trajectory stopping in the oversaturation zone could imply oversaturation of that particular intersection movement.

We present new signalized intersection performance measures to quantify the impacts of blockage: blockage delay, blockage stops, and blockage split failures. These measures were evaluated at six signalized intersections in Southeast, MI with both permissive only and protected-permissive left-turn phasing. The results from these intersections can provide site-specific insights to develop strategies for reducing delay. Blockage accounted for up to around 58% of the control delay and around 57% of the stops experienced by left-turning vehicle trajectories. This blockage delay contributed to up to around 10% of the control delay and stops experienced by straight movements sharing lanes with these permissive movements. The method was also tested on an oversaturated corridor where queues formed at downstream intersections "spilled over" to the upstream intersections. Blockage resulting from spillover accounted for up to 62% of control delay and 83% of stops. We also show how the method can account for split failures that might not always exhibit two stops on account of blockage delay preventing them from clearing the intersection. The SIPD provides a more robust method for identifying split failures by relying directly on the intersection arrival time of the trajectory. This allows us to avoid missing blockage split failures that usually only exhibit one stop. In some cases, the number of identified split failures was around 14 times higher than the state-of-the-practice.

Due to the large-scale coverage of vehicle trajectory data and the generalizability of the SIPD under different types of control, the methods demonstrated in this chapter are scalable across large networks. The methodology is also versatile. While this chapter covers blockage caused by permissive movements and spillover, we envision that the this method could be

extended to other blockage scenarios such as stopped transit vehicles or permissive right turns where pedestrians and bicycles have the right-of-way. In addition, the SIPD can be extended for other analysis techniques of vehicle trajectory data. Despite the incomplete observations provided by current penetration rates, the SIPD allows transportation engineers to easily visualize how these limited observations can give insight into the complete traffic state. Therefore, we anticipate many more applications of the SIPD beyond the blockage analysis presented in this chapter.

3.6.2 Integration into the traffic signal timing management system)

The SIPD provides the blockage analysis microservice in the diagnostic module of the overall signal timing management system (Figure 1.6). While the blockage and red light measures could be considered performance measures, they can not be calculated without the signal timing data, so they are not included in the traffic performance calculation service in the pre-processing module. In addition, the SIPD analysis provides more diagnostic insights into the causes of delay than traditional signal performance measuress (SPMs) by identifying inefficient right-of-way allocation through geometric design and left-turn operations. Therefore, it is included as a diagnostic microservice supporting the right-of-way diagnostic application.

CHAPTER 4

Detecting Opportunities for Improving Signal Coordination without Signal Timing Data

4.1 Introduction

This chapter presents methods for scanning large-scale traffic networks to identify opportunities to improve traffic signal coordination. It is currently very difficult to identify and capitalize on optimization opportunities across the more than 330,000 signalized intersections across the United States. Due to the high costs of installing and maintaining permanent detection infrastructure, agencies often rely on temporary detection methods to support signal optimization projects. These efforts are typically conducted on a 3- to 5-year fixed cycle where intersections are chosen before any meaningful analysis has determined potential benefits. As a result, agencies may miss key opportunities to retime signals where optimization could have the greatest impact—or may direct resources toward locations that are not in urgent need of adjustment.

The methods proposed in this chapter do not require any data from the managing agency (such as ground truth signal timing plans) and can cross jurisdictional boundaries, providing previously unavailable opportunities to identify coordination improvement opportunities between cities, counties, and even states. We first introduce a cycle-length estimator that determines whether an intersection is operating under a fixed cycle length, and if so, identifies the actual cycle length. This estimator is used to estimate the cycle lengths at over 1,400 intersections in Oakland County. A corridor of four intersections was identified for coordination optimization opportunities based on inconsistent cycle lengths. Next, this chapter investigates how roadway snow depths impact free-flow travel times between intersections and how these changes influence the performance of signal timing plans. The study area included 129 intersections in southeast Oakland County, MI.

4.1.1 Background

The goal of traffic signal coordination is to facilitate uninterrupted vehicle progression along a corridor by synchronizing the signal timing across intersections. The two key parameters in designing coordination are the cycle length and the free-flow travel speed. Consistency in cycle length is essential so that the designed arrival pattern of vehicles released from an upstream intersection during its green interval aligns with each successive cycle downstream. While half-cycle operation may be appropriate in certain cases, corridors are generally designed with a fixed cycle length at all intersections. The free-flow speed determines the arrival time of vehicles at the downstream intersection after departing upstream. Vehicle trajectory data can be used to evaluate whether implemented timing plans and traffic flow are performing as designed, as well as to identify opportunities to improve coordination based on the current state of these parameters.

4.1.2 Contributions and organization of the chapter

This chapter presents rule-based approaches for diagnosing signal coordination deficiencies from vehicle trajectory data without requiring signal timing data from the agency. First, we develop a cycle-length estimator that determines the duration of the cycle in fixed-time and coordinated-actuated operations, enabling us to check for inconsistent cycle lengths across corridors. Second, we observe changes in free-flow travel times between intersections during winter weather predicted by the High-Resolution Rapid-Refresh (HRRR) model.

Section 4.2 presents methods for estimating intersection cycle lengths, including a discussion of the relevant literature and real-world examples verified through ground truth data. Section 4.3 reports a large scale speed study during a snowstorm in southeast Oakland County, MI and the resulting impacts on signal coordination. Finally, a summary of the chapter is provided in Section 4.4

4.2 Estimating intersection cycle lengths

Traffic signals are a crucial component of urban traffic networks, and signal timing information serves as an essential input for various urban traffic operational applications. Obtaining signal timing information on a large scale is challenging due to the diversity of traffic signal controllers from different manufacturers and jurisdictions. In addition, remote access to traffic signal controllers can be difficult. Vehicle trajectories can be leveraged to estimate signal timing information since they provide temporal-spatial information about vehicles' movements through intersections in response to traffic signal control. By aggregating trajec-

tory crossing times into a predetermined duration, the cycle length can be identified as the duration with the most densely distributed crossing times. This searching-based approach to identifying cycle length is low-efficient and more suitable for traffic signals with fixed cycle lengths in a certain time period. The proposed method is validated through case studies at over 1,400 real-world intersections. The results from this method are then used to diagnose and opportunity to improve traffic signal coordination.

4.2.1 Background and related works

Most urban traffic state estimation approaches are dependent on this information (Li et al., 2017; Zhao et al., 2019b; Maripini et al., 2023; Wang et al., 2024b). As a result, signal timing information is necessary for the diagnosis and optimization of traffic signal timing (Akcelik, 1994; Li et al., 2023a; Wang et al., 2024a). Since a significant portion of urban traffic flow is regulated by traffic signals, signal timing also lays the foundation for developing large-scale network models. From the vehicle perspective, signal timing information can be used to optimize the speed profile when the vehicle approaches the intersection to improve energy consumption (Katsaros et al., 2011; Jiang et al., 2017; Hao et al., 2018). It can also be used to warn the driver when traffic lights turn green to mitigate the green start-up loss (Grumert and Pereira, 2022). Some mobile navigation applications have also shown traffic light countdowns to improve drivers' experience (Li et al., 2023b; ReturnZeroBeing, 2024).

However, obtaining signal timing information on a large scale is challenging due to the diversity of traffic signal controllers. Traffic signal controllers from different manufacturers have different application programming interfaces (APIs), and some intersections have limited remote access. Additionally, traffic signal controllers are operated by different traffic operation agencies, making it difficult to access their configurations across various jurisdictions.

Researchers have long noticed the potential of using vehicle trajectories, even at low penetration ratea, to estimate signal timing parameters (Hao et al., 2012; Fayazi et al., 2014; Yu and Lu, 2016; Axer and Friedrich, 2017; Mahmud et al., 2023; Li et al., 2023b). Hao et al. (2012) demonstrated the feasibility of estimating signal timing information of a single movement with sampled travel time from partially observable vehicles. Yu and Lu (2016) utilized the low penetration rate taxi GPS trajectories to estimate signal timing information of fixed-time traffic signals. The cycle length, as the most important parameter, was estimated through a general approximate greatest common divisor (AGCD) formulation. Du et al. (2019) also focused on the estimation of fixed-time traffic signal timing information, which was mainly featured by a time period breakpoint identification approach. Mahmud

et al. (2023) proposed an approach to identify the cycle length, timing plan schedules, and distributions of green times of coordinated phases in signalized arterial corridors.

Although these methods have been tested to successfully infer signal timing information, most have a limited scope and can only be applied to certain types of traffic signal controllers, particularly fixed-time traffic signals (Yu and Lu, 2016; Du et al., 2019). Most of them rely on at least a fixed cycle length as well as constant synchronization between a central clock and the signal controller (Axer and Friedrich, 2017). Both Du et al. (2019) and Mahmud et al. (2023) estimated the cycle length through a searching-based approach. By aggregating trajectory crossing times into a predetermined duration, the cycle length can be identified as the duration with the most densely distributed crossing times. This searching-based approach to identifying cycle length is low-efficient and more suitable for traffic signals with fixed cycle lengths in a certain time period.

4.2.2 Contributions

To address these limitations, this section proposes a cycle length estimator capable of estimating cycle lengths for almost all types of traffic controllers. This iterative cycle length estimation algorithm estimates both the mean value and the variation of the cycle length. The variation can indicate whether the traffic signal has a fixed cycle length or not. This algorithm is used to estimate the cycle length at more than 1,400 intersections in Oakland County. Using these estimations, we are able to identify opportunities to improve traffic signal coordination where cycle lengths may be inconsistent between consecutive intersections.

4.2.3 Vehicle trajectory preprocessing for cycle length estimation

Figure 4.1 illustrates an example trajectory passing through a signalized intersection in a time-space diagram. Each black circle denotes an observed trajectory point. Two critical points are labeled with blue crosses: $(g^*_{s,i}, x^*_i)$ represents the point where trajectory i starts to move and $t_{b,i}$ represents the departure time. Both $g^*_{s,i}$ and $t_{b,i}$ are epoch times, while x^*_i is the distance to the stop bar. Essential interpolation should be applied to obtain more accurate critical points, particularly for raw trajectories with a large temporal resolution. By assuming a fixed departure shockwave speed w_d as shown in Figure 4.1, the green start time of this specific cycle can be estimated as:

$$g'_{s,i} = g^*_{s,i} - \frac{x^*_i}{w_d}. \tag{4.1}$$

We assume a deterministic departure shockwave speed w_d for each intersection movement, which can be calculated according to the methods described in Section 3.4. The start-up loss time caused by vehicle acceleration and perception-reaction time is neglected based on the assumption that all movements are equally influenced. Only the estimated green start time $g_{s,i}$, stop location pair $\{(g_{s,i}, x_i), \forall i\}$ $(x_i \equiv x_i^*)$, and the the crossing time $t_{b,i}$ for each observed trajectory i will be utilized in the cycle length estimator. The raw vehicle trajectory points are no longer needed. Please also note that we can only collect $g'_{s,i}$ for trajectories that have at least one stop before the intersection while $t_{b,i}$ for all trajectories that pass through the intersection. Therefore, we will have more observed crossing times than estimated green start times and observed stop locations.

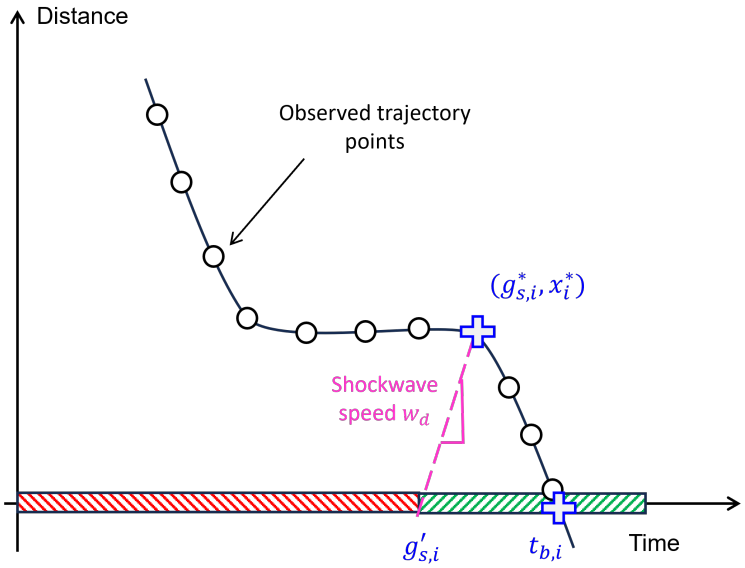

Figure 4.1: Green start estimation from vehicle trajectory

4.2.4 Cycle length estimation

This section introduces a complete cycle length estimation algorithm, including the estimation of both mean and variance. Compared with existing methods, the newly developed method has two main advantages: 1) As an iterative method, it is much more efficient than those methods that rely on searching (Du et al., 2019; Mahmud et al., 2023); 2) It can work for traffic signals with both fixed and variable cycle lengths by directly estimating the variance of the cycle length.

4.2.4.1 Histogram of the green start time differences

Cycle length estimation is developed based on the histogram of green start time differences between trajectory pairs. Figure 4.2 illustrates how to extract the green start time difference from observed vehicle trajectories. There are four steps in total:

1. Get the estimated green start time and the distance to the stop bar for each observed stopped trajectory $\{(g_{s,i}, x_i), \forall i\}$ for each movement m. The superscript m denotes a movement's index. The estimated green start time $g_{s,i}^m$ can be calculated by assuming a constant shockwave speed as shown by blue dashed lines in Figure 4.2.

2. Merge $g_{s,i}^m$ that are within the same cycle to get $\{\tau_j^m, \forall j\}$ for each movement m, where j is the cycle index for observed cycles. For the practical implementation, we first take the difference for every two adjacent $g_{s,i}^m$ of the same movement m; if the difference is less than a pre-determined threshold (e.g., 10 seconds), we then put these two trajectories in the same cycle. We combine $g_{s,i}^m$ of the same cycle to get τ_j^m by taking the average of $g_{s,i}^m$ weighted by $1/x_j^m$, as vehicles stopped closer to the stop bar will have smaller errors.

3. Get the temporal difference for every two adjacent τ_j^m: $\Delta\tau_j^m = \tau_{j+1}^m - \tau_j^m$ for each movement m.

4. Collect $\Delta\tau_j^m$ for each movement m of the intersection and plot the histogram.

Please note that Steps 1-3 are performed for each movement independently, and we obtain the set of $\{\Delta\tau_j^m\}$ for each movement m. We ignore the superscript m in Figure 4.2 for simplification. In Step 4, we combine all $\{\Delta\tau_j^m\}$ from different movements to obtain $\{\Delta\tau_j^m, \forall j, m\}$. Since each $\Delta\tau_j^m$ is the temporal difference of the green start time in different cycles of the same movement, it is expected to be an integer number of cycle length. Consequently, except for some outliers, $\Delta\tau_j^m$ will be centered around a certain number of cycle lengths as shown by red dashed lines in Figure 4.2.

4.2.4.2 Estimation of the mean cycle length

Using the green start time differences $\{\Delta\tau_j^m, \forall j, m\}$ obtained in the previous subsection as the input, we develop an iterative algorithm to estimate the mean cycle length. This algorithm is inspired by the K-means algorithm (Krishna and Murty, 1999) or the application of the EM (expectation-maximization) algorithm to solve a mixture Gaussian model (Bilmes et al., 1998). Starting from an initial cycle length $C^{(0)}$, the iterative cycle length estimation has two steps:

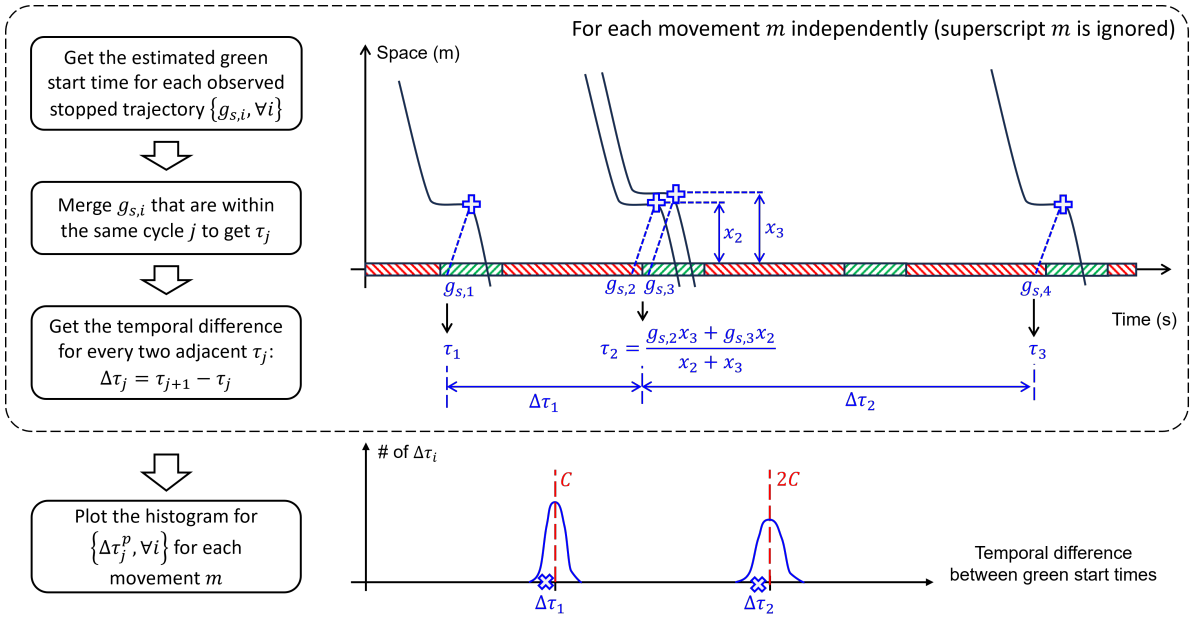

Figure 4.2: Extract green start time difference $\Delta\tau_j^m$ from observed vehicle trajectories

1. Given cycle length $C^{(i)}$ of the previous iteration i, assign each $\Delta\tau_j^m$ to the closest cycle according to:

$$h_j^m = \underset{h\in\mathbb{N}}{\operatorname{argmin}} \left|\Delta\tau_j^m - h \cdot C^{(i)}\right| \quad \forall j, \forall m \tag{4.2}$$

   where $h_j^m \in \{1, 2, \dots\}$ means that $\Delta\tau_j^m$ contains h_j^m cycles.

2. Calculate the new cycle length according to the new cycle assignment of the previous step:

$$C^{(i+1)} = \frac{\sum_{j,m,h_j^m<M} \Delta\tau_j^m}{\sum_{j,m,h_j^m<M} h_j^m}. \tag{4.3}$$

   Those $\{\tau_j^m, \forall j, m\}$ with a $h_j^m \geq M$ are ignored since they are much less useful when there are too many cycles between two adjacent observed trajectories. M is a predetermined integer, empirically $4 - 8$.

This iterative program ends whenever there is only a small change of $C^{(k)}$ between two iterations or it reaches the maximum number of iterations. In most cases, it will converge after a few iterations. However, it is widely known that such an EM-like iterative algorithm is easily trapped into undesired local minimums. This iterative algorithm essentially finds the cycle length according to the following formulation:

$$C^* = \underset{C}{\operatorname{argmin}} \sum_{j,m} \left(\min_{h_j^m<M} \left|\Delta\tau_j^p - h_j^m \cdot C\right| \right)^2 = \underset{C}{\operatorname{argmin}}\, J(C) \tag{4.4}$$

which is to minimize the mean square error of $\Delta\tau_j^m$ to the closest integer number of cycle C. Let C_0 represent the true cycle length. It is easy to verify that integer numbers (e.g., $1C_0, 2C_0, \dots$) or integer fractions (e.g., $C_0/2, C_0/3, \dots$) of the true cycle length are all local minimums. Moreover, what makes it worse is that integer fractions of true cycle length will yield even less objective function $J(C)$, i.e., $J(C_0) \geq J(C_0/2) \geq \cdots \geq J(C_0/z)$.

To address this issue, we add another regularization term such that the true cycle length tends to be the global optimum. Figure 4.3 illustrates how we can avoid the estimated results to be fractions of true cycle length. Figure 4.3 (a) and (c) shows the histograms of green start time difference, i.e., histograms of $\Delta\tau_j^m$, for a specific movement m. The estimated cycle length C is C_0 and $C_0/2$ for Figure 4.3 (a)-(b) and Figure 4.3 (c)-(d), respectively. Let us focus on Figure 4.3 (a) and (b) first. As shown in Figure 4.3 (a), each of $\Delta\tau_j^m$ can be assigned to the closest integer number of cycle lengths annotated by red dashed lines according to the following equation:

$$h_j^m = \underset{h \in \mathbb{N}}{\operatorname{argmin}} \left| \Delta\tau_j^m - h \cdot C^{(i)} \right| \quad \forall j \tag{4.5}$$

which is the same as Equation (4.2). h_j^m denotes the number of cycles in $\Delta\tau_j^m$. Here we want to show that h_j^m roughly follows a geometric distribution, for any movement m. Assuming a stationary arrival rate (i.e., traffic volume) and penetration rate, the number of observed stopped trajectories for each movement m in a cycle follows an i.i.d. distribution. Let α^m represent the probability of observing at least one stopped trajectory in a cycle for movement m. As shown in previous Figure 4.2, a $h_j^m = k$ means that, for movement m, given the current cycle with at least one observed stopped vehicle trajectory, we do not observe any stopped trajectory until the next kth cycle. By definition, h_j^m follows a geometric distribution with parameter α^m:

$$p(h_j^m = k) = \alpha^m \cdot (1 - \alpha^m)^{k-1} \quad \forall m. \tag{4.6}$$

This parameter α^m can be directly calculated beforehand given the total number of observed stopped trajectories of movement m and the total duration of the data collection period.

As shown in Figure 4.3 (a) and (b), for each movement m, we can count the number of $\Delta\tau_j^m$ that is assigned to cycle k, denoted by $n^m(k)$. Figure 4.3 (b) shows the frequency of each k. Based on the analysis before, if the cycle length is estimated correctly, the frequency curve in Figure 4.3 (b) will correspond to a geometric distribution with known parameter α^m. If the cycle length is not estimated correctly, for example, as shown in Figure 4.3 (c), the resulting frequency curve in Figure 4.3 (d) could be far from a geometric distribution. Guided by this intuition, we use the difference between the frequency curve (e.g., Figure 4.3 (b) and (d)) and the corresponding geometric distribution as a regularization term. Both

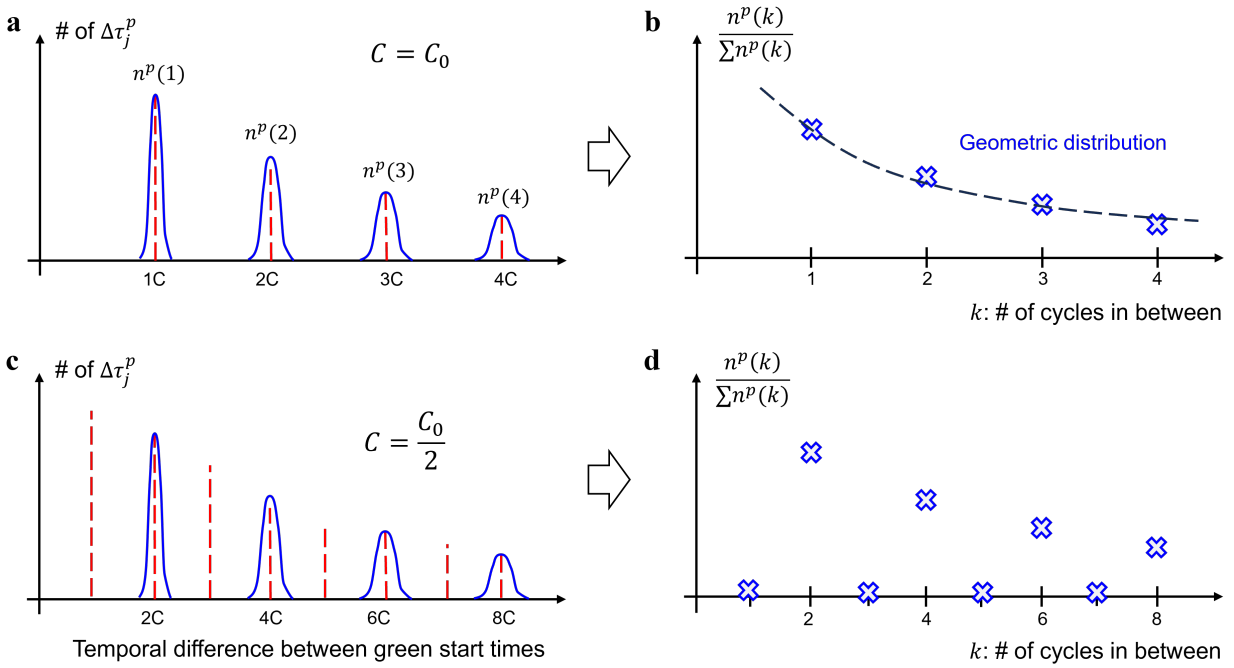

Figure 4.3: For each movement m, $n^m(k)$ is the frequency of h_j^m, which is expected to follow a geometric distribution

are also truncated by a maximum number of cycles M. Let $(q^m)'(k)$ and $q(k)$ represent the frequency of k and the corresponding geometric distribution, respectively, we have:

$$(q^m)'(k) = \frac{n^m(k)}{\sum_{k=1}^{M} n^m(k)}, \quad q^m(k) = \frac{(1-\alpha^m)^{k-1}\alpha^m}{\sum_{k=1}^{M}(1-\alpha^m)^{k-1}\alpha^m}, \quad \forall k \in \{1, 2, \dots M\}, \ \forall m. \quad (4.7)$$

The KL-divergence is used to quantify their difference:

$$\mathrm{KL}((q^m)'(k) \| q^m(k)) \equiv G^m(C), \quad \forall p \quad (4.8)$$

which is a function of the cycle C, denoted by $G^m(C)$. By summing up $G^m(C)$ for all movements m, we have $G(C) \equiv \sum_m G^m(C)$ that can be used as a regularization term to penalize results that are integer fractions of the true cycle lengths.

The final complete cycle length estimation algorithm combines the iterative algorithm and the regularization term. It has two main steps:

1. Starting from different initial points $\{C_1^{(0)}, C_2^{(0)}, C_3^{(0)}, \dots, \}$, perform the iterative algorithm given by Equation (4.2-4.3). The output estimated cycle lengths are given by $\{C_1, C_2, C_3, \dots, \}$.

2. Choose the optimal cycle length from the output in the previous step, according to the

following criteria:

$$C^* = \underset{C \in \{C_1, C_2, C_3, \ldots,\}}{\operatorname{argmin}} \quad J(C) + \beta \cdot G(C) \tag{4.9}$$

which is a weighted sum of the original objective function and the regularization term. β is a constant coefficient.

This modified algorithm improves upon the original simple iterative algorithm in two key aspects. First, starting from different initial points helps avoid being trapped in a local minimum. Second, the additional regularization term ensures that the true cycle length is identified as the global optimum, instead of either integer numbers or fractions of the true cycle length.

4.2.4.3 Estimation of the variance in cycle length

The previous subsection introduces an algorithm for estimating the mean of the cycle length. This subsection will explain how to estimate the variation of the cycle length in a further step. Assuming that the cycle length of each cycle is i.i.d. and follows a Gaussian distribution:

$$C \sim \mathcal{N}(C_0, \sigma_c^2) \tag{4.10}$$

where σ_c^2 is the variance of the cycle length. We have $\sigma_c^2 = 0$ for traffic signals with a fixed-cycle length while $\sigma_c^2 > 0$ for traffic signals with a variable cycle length. The estimation of the green start time τ_j given by previous Figure 4.2 is also assumed to have a Gaussian error:

$$\epsilon \sim \mathcal{N}(0, \sigma_g^2) \tag{4.11}$$

where σ_g^2 is the variance of the green start estimation error.

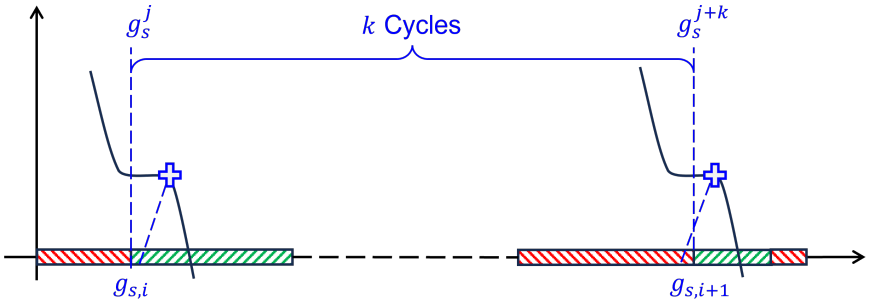

Figure 4.4: Probabilistic model of the green start difference.

As shown in Figure 4.4, we have two observed trajectories with k cycles in between. τ_j and τ_{j+1} denote the estimated green start time given observed trajectories while g_s^j and g_s^{j+k}

denote the ground truth of the green start time of cycle j and cycle $j+k$, respectively. According to the assumption in Equation (4.11), we have:

$$\tau_j \sim g_s^j + \mathcal{N}(0, \sigma_g^2), \quad \tau_{j+1} \sim g_s^{j+k} + \mathcal{N}(0, \sigma_g^2). \tag{4.12}$$

Let $\Delta\tau(k)$ denote the difference between τ_{i+1} and τ_i, which is the green start time difference with k cycles in between, we have:

$$\begin{aligned}
\Delta\tau(k) &= \tau_{i+1} - \tau_i && \text{(4.13a)}\\
&= (g_s^{j+k} - g_s^j) + (\mathcal{N}(0, \sigma_g^2) - \mathcal{N}(0, \sigma_g^2)) && \text{(4.13b)}\\
&\sim k\mathcal{N}(C_0, \sigma_c^2) + 2\mathcal{N}(0, \sigma_g^2) && \text{(4.13c)}\\
&\sim \mathcal{N}(kC_0, k\sigma_c^2 + 2\sigma_g^2). && \text{(4.13d)}
\end{aligned}$$

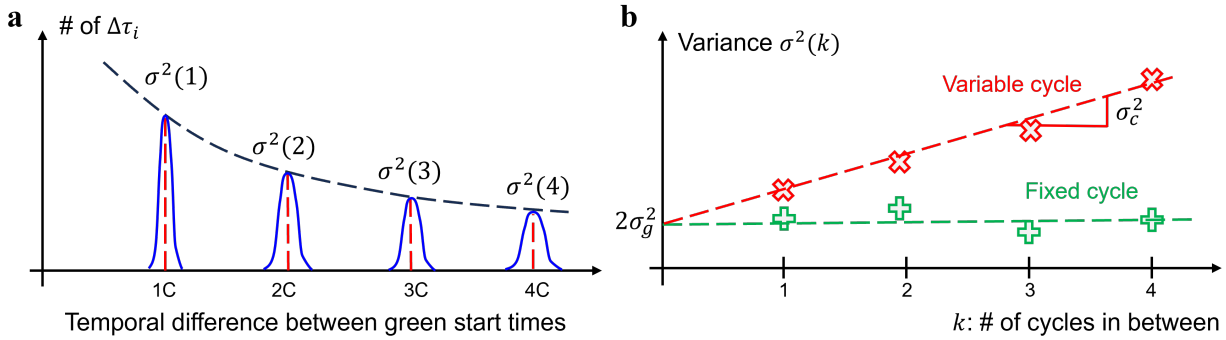

Figure 4.5: Identification of cycle length variation

Based on this probabilistic model, Figure 4.5 illustrates how we can estimate the variance of the cycle length σ_c^2. Figure 4.5 (a) shows the histogram of green start difference time $\Delta\tau_i$. Each $\Delta\tau_i$ is assigned to the closest integer number of cycle length. For each cycle k, the variance of $\Delta\tau_i$ is calculated as $\sigma^2(k)$. Figure 4.5 (b) shows how $\sigma^2(k)$ change with k. According to Equation (4.13), we have:

$$\sigma^2(k) = k\sigma_c^2 + 2\sigma_g^2. \tag{4.14}$$

This means that we can perform a linear regression regarding $\sigma^2(k) - k$; the slope and intercept will be σ_c^2 and $2\sigma_g^2$, respectively. As shown in Figure 4.5b, if the cycle is time-varying, we will get a monotonically increasing curve for $\sigma^2(k)$. On the contrary, if the cycle is fixed, $\sigma^2(k)$ will be roughly flat. In practice, if the estimated σ_c^2 is less than a pre-determined threshold, we will regard this cycle length as fixed.

4.2.5 Case studies

This section presents case studies of the cycle length estimator. First, we demonstrate the accuracy of the proposed method using two intersections: one operating with a fixed cycle length and the other without. Next, we demonstrate how a network-wide cycle length estimation can be used to diagnose opportunities to improve traffic signal coordination.

4.2.5.1 Cycle length estimation example

Figure 4.6 shows two examples of cycle length estimation including both fixed and variable cycle lengths. Figure 4.6 (a)-(b) are results from Telegraph Rd and Huron St in Pontiac, MI, which operates under coordinated-actuated control with a fixed cycle length while Figure 4.6 (c)-(d) are results from the Fuller St and Maiden Ln in Ann Arbor, MI, which operates under actuated control with variable cycle lengths. Both are based on the data from the same hour over a month.

Figures 4.6 (a) and (c) are the histograms of the green start time difference, which are generated according to Figure 4.2 and used to estimate the mean value of the cycle length. The estimated cycle lengths are reported in the title of each figure, and the vertical dashed blue lines illustrate integer numbers of estimated cycle lengths. As we expected, most green start time differences are distributed centering by these dashed blue lines. The difference between Figure 4.6 (a) and (c) is also quite obvious: we get much more dense distributions centering by dashed blue lines for Figure 4.6 (a) while relatively more flat distributions for Figure 4.6 (c). The fixed cycle lengths of $100s$ was confirmed through a comparison of the ground truth in signal work orders provided by the Road Commission for Oakland County (RCOC).

Figures 4.6 (b) and (d) show how the variance of the cycle length is estimated, which is generated according to Figure 4.5 in the previous methodology section. After applying the linear regression for these scatters, the slope can be directly used as an estimation of the variance of the cycle length. In these two specific cases, the standard deviations of the cycle length are estimated as 0.81 sec and 14.85 sec in Figure 4.6 (b) and (d), respectively. Consequently, Telegraph Rd and Huron St (Figure 4.6 (a)-(b)) is identified with a fixed cycle while Fuller St and Maiden Ln (Figure 4.6 (c)-(d)) has a time-varying cycle.

Figure 4.7 uses the same data as Telegraph Rd and Huron St to further validate that the h_j^m for each movement m follows a geometric distribution. The physical meaning of h_j^m is the number of cycles between cycles with at least one observed stopped trajectory. For example, if we observe stopped trajectories in cycle k and cycle $k+2$, with no observations in between, we will have $h_j^m = 2$. As aforementioned in Section 4.2.4.2, h_j^m is expected to

follow a geometric distribution. Figure 4.7 provides a validation for this argument, where the frequency of h_j^m (denoted by yellow bars) aligns well with the corresponding geometric distributions (blue lines with dots), for all through movements.

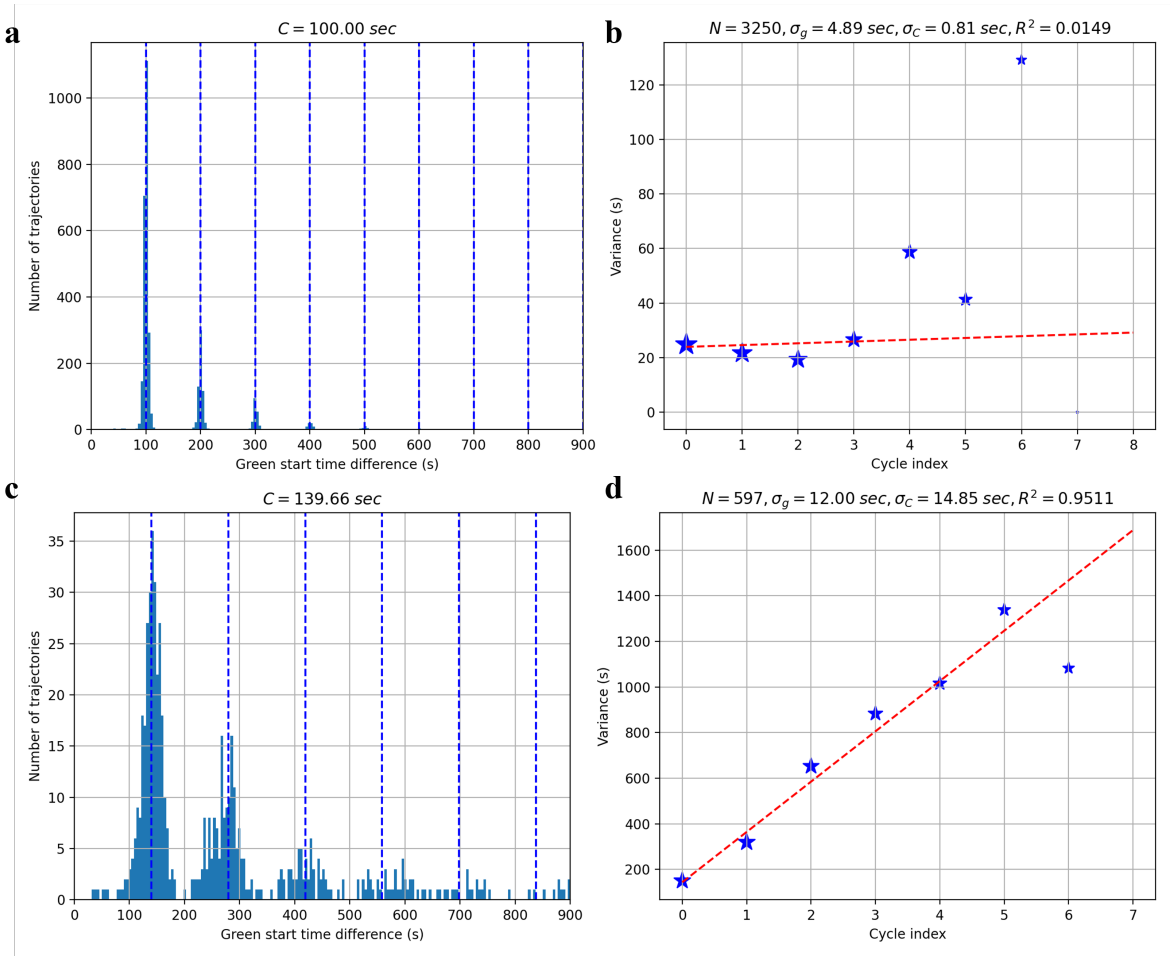

Figure 4.6: Examples of cycle length estimation: fixed (Telegraph Rd and Huron St) vs. variable (Fuller St and Maiden Ln).

4.2.5.2 Diagnosing coordination improvement opportunities

The cycle length estimator was used to estimate the cycle length at all of the signalized intersections in Oakland County (over 1,400). Using these estimation, we analyzed corridors in the county to see if any were operating at inconsistent cycle lengths. Figure 4.8 illustrates an example of a corridor where the cycle length is inconsistent among intersections displayed on the diagnostic user interface tool developed by research group. As a result, the coordination improvement score, which calculates potential coordination improvement opportunities (not covered in this dissertation), is very high between each intersection. These three intersec-

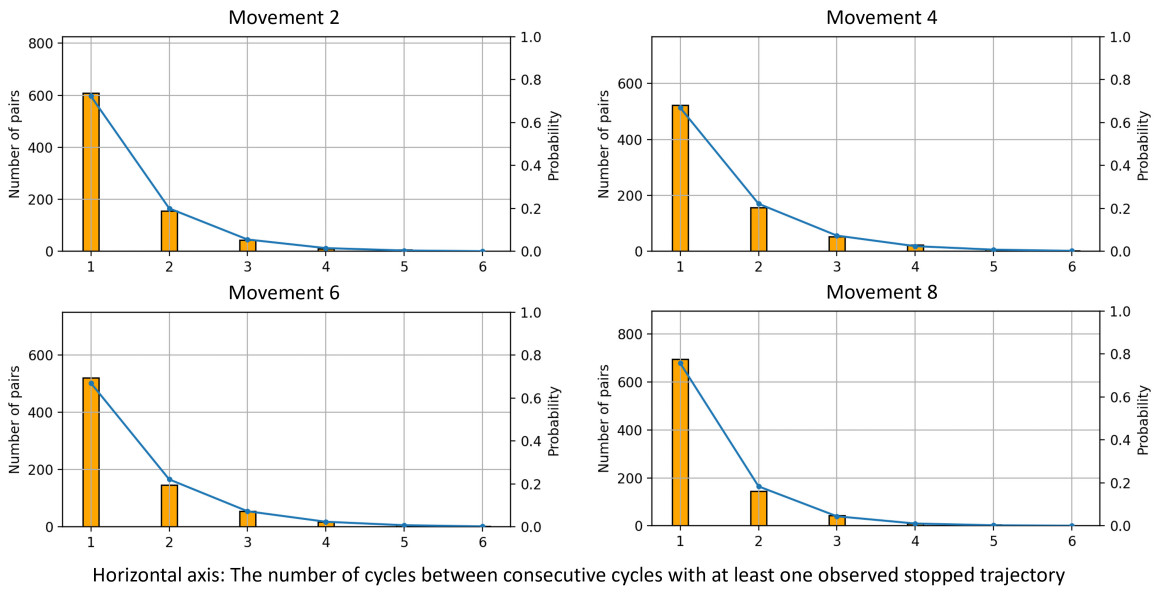

Figure 4.7: Validation of the geometric distribution of h_j^m in Section 4.2.4.2 (Telegraph Rd and Huron St).

tions on 8 Mile Rd in Farmington Hills were selected for new optimized signal timing plans. Upon review of the existing signal work order, it was determined that controller ID 1024 was designed for a 90 second cycle length but the controller had been programmed incorrectly. Without this diagnostic tool, RCOC would have only discovered this error through a routine field visit, which usually only takes place every two years, or in response to a citizen complaint.

New signal timing plans were developed for this corridor that not only fixed the inconsistent cycle length issue but also optimized the offsets. Before and after analysis using signal performance measuress (SPMs) from the vehicle trajectory data reported up to 30% decreases in delay and 40% decreases in number of stops. Figure 4.9 compares the aggregated time–space diagrams before and after the new timing plans were applied. The purple arrows in the "before" diagram reveal the negative effects of inconsistent cycle lengths on coordination. The "after" diagram highlights the improvement achieved by synchronizing cycle lengths, resulting in more consistent progression. As a result, the average control delay per intersection was reduced from 23.0 seconds to 15.7 seconds for a 7.3 second reduction in delay. While not provided here, similar results were found for the opposing direction.

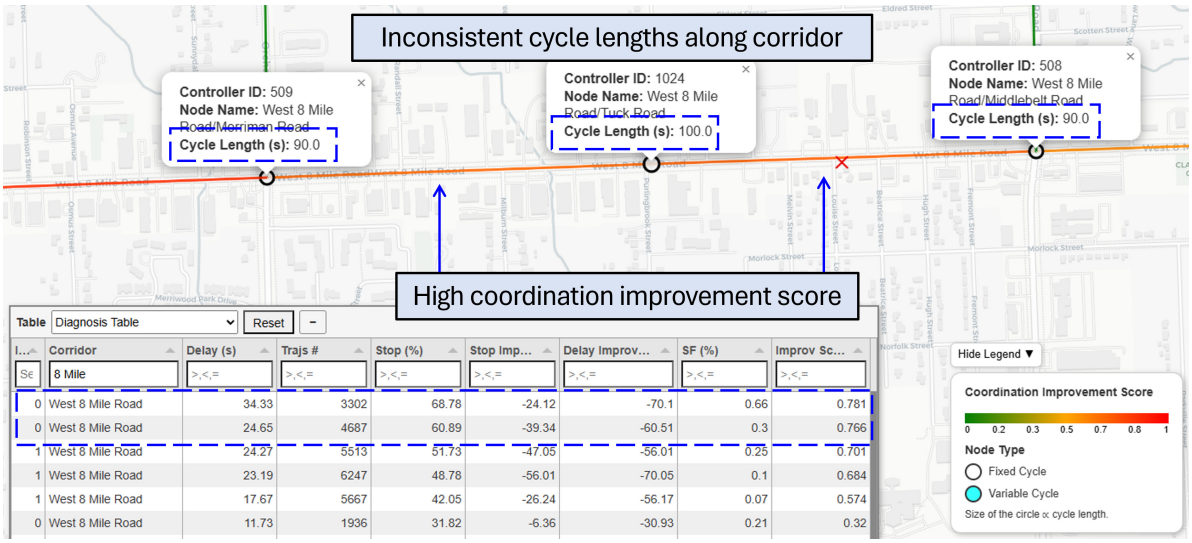

I...	Corridor	Delay (s)	Trajs #	Stop (%)	Stop Imp...	Delay Improv...	SF (%)	Improv Sc...
Se	8 Mile	>,<,=	>,<,=	>,<,=	>,<,=	>,<,=	>,<,=	>,<,=
0	West 8 Mile Road	34.33	3302	68.78	-24.12	-70.1	0.66	0.781
0	West 8 Mile Road	24.65	4687	60.89	-39.34	-60.51	0.3	0.766
1	West 8 Mile Road	24.27	5513	51.73	-47.05	-56.01	0.25	0.701
1	West 8 Mile Road	23.19	6247	48.78	-56.01	-70.05	0.1	0.684
1	West 8 Mile Road	17.67	5667	42.05	-26.24	-56.17	0.07	0.574
0	West 8 Mile Road	11.73	1936	31.82	-6.36	-30.93	0.21	0.32

Figure 4.8: Detected suboptimal coordination caused by inconsistent cycle length

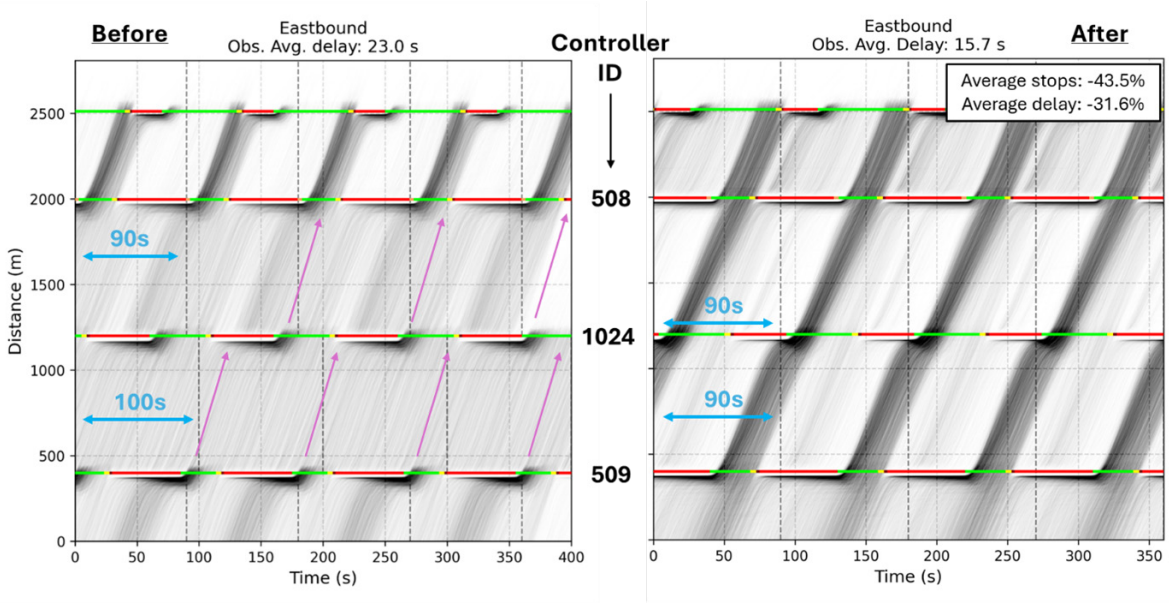

Figure 4.9: Before and after time-space diagrams for 8 Mile Rd

4.3 Winter conditions

Inclement weather such as snowstorms can be detrimental to traffic signal performance as it can impact important traffic parameters. However, pervious studies were limited to a small number of intersections. Using vehicle trajectory data and the HRRR weather prediction model from the National Oceanic Atmospheric Administration (NOAA), this section measures free-flow travel times between intersections on a large-scale urban network in southeast Oakland County, MI (70 square kilometers with 129 signalized intersections). To the best of our knowledge, this is the largest study of speed reductions in a winter storm on roadways that exhibit speeds under 55 mph in normal conditions. Changes in this parameter were investigated from a snowstorm on January 1st, 2022 at snow depths less than 2 inches. While the literature usually reports constant percentage reductions in speed, the percentages in this study are higher at faster speeds (22.8% at 50 mph) than slower speeds (5.9% at 20 mph). The number of stops increased by 11.2% and the control delay increased by 20.9%. Signal coordination was particularly impacted. One corridor direction experienced a 435.0% increase in the number of stops and a 311.6% increase in control delay. Another corridor's signal performance measures improved because free-flow speeds were reduced closer to the apparent design speed, demonstrating the importance of accurately calibrating the free-flow travel time parameter. The findings of this study demonstrate the potential to use vehicle trajectory data to calibrate traffic signal parameters across large-scale networks in a variety of environments, enabling traffic engineers to design targeted signal coordination plans in preparation for different conditions.

4.3.1 Background

Free-flow travel time between each intersection is a key parameter in signal coordination that indicates when arrivals from downstream intersections should be expected. Many studies have noted how winter conditions can change important traffic parameters such as saturation flow rate, headway, and free-flow speed (FFS), and are therefore detrimental to signal performance (Bernardin, Lochmueller, and Associates, Inc., 1995; Maki, 1999; Perrin et al., 2001; Goodwin, 2002; Goodwin and Pisano, 2004; Agbolosu-Amison et al., 2004, 2005; Al-Kaisy and Freedman, 2006; Strong et al., 2010; Brennan Jr et al., 2011; Balke et al., 2013; Chen et al., 2015; Lu et al., 2019). These studies promote implementing specific signal control plans based on adjusted signal parameters during these weather events. However, the scope of these projects was limited to a couple intersections or one corridor of 11 intersections at most. Because of the infrastructure needed to collect the required data, it is difficult to calibrate these signal parameters for even normal conditions at large scales, let alone for

inclement weather. Free-flow travel time, for example, requires detection capability and current fixed-point detection methods don't cover the entire travel path. Travel times can also be measured by pairing detector data with signal timing data, but this information is not always available and is not applicable if vehicles aren't queued at the upstream intersection (Brennan Jr et al., 2011). In addition, it can be hard to pair accurate weather data at a large scale with traffic flow data. These factors make it difficult to calibrate traffic parameters for inclement weather across traffic networks and have therefore impeded the wide spread implementation of weather-type-specific traffic signal timing plans.

Vehicle trajectory data can address these limitations by 1.) providing individual vehicle free-flow travel times (not a fixed point FFS) and 2.) enabling us, through 24/7 coverage, to analyze changes in these travel times during uncommon situations such as weather and construction. Because of the increasing availability of such data, measurements are available for any pair of intersections and do not rely on any physical detection systems. Vehicle trajectory data is not as susceptible to malfunctions as compared to detection systems, which could make it more reliable in inclement weather. This data can be paired with weather prediction models to show how travel times change in winter conditions. The NOAA HRRR weather prediction model provides real time high resolution weather predictions for the entire continental United State. Therefore, previous travel time measurements based on historical weather predictions could be used to proactively adjust signal timing coordination when these conditions are predicted again.

4.3.2 Related works

4.3.2.1 Impacts on traffic parameters

Inclement weather, especially snowy and icy conditions, has a negative effect on traffic flow by reducing visibility, pavement friction, vehicle performance, and infrastructure stability (Goodwin, 2002). These factors cause drivers to increase headways, decrease acceleration rates, and reduce speeds, which influences critical traffic operation parameters such as saturation flow rate, start-up loss time, and speed. Researchers at the Federal Highway Administration (FHWA) found that interstate vehicle speeds decreased at higher percentages with increasing degrees of inclement weather (McBride et al., 1977). Perrin et al. (2001) found similar results in their study in Salt Lake City. Speeds decreased by up to 30%, saturation flow rates decreased by 20%, and start-up lost times increased by 23% when snow and slush accumulated on the road at two intersections. Several studies have established the relationship between snowy conditions and decreasing vehicle speeds on freeways, with an average reduction of 9-12% during snowfall and 22-24% on icy pavement (Agarwal et al.,

2005; Hranac et al., 2006; Strong et al., 2010; Zegeer et al., 2014). These studies informed the development of Exhibit 11-21 in the 2016 Highway Capacity Manual (HCM), which gives default speed adjustment factors for different weather conditions (Transportation Research Board, 2016). Depending on the snowfall rate, the recommended speed percentage decrease can range from 6-12% for 55 mph in normal conditions to 16-19% for 75 mph in normal conditions.

Many studies have identified changes in important signal parameters during winter conditions in urban environments at signalized intersections with speeds less than 55 mph, but there is a lack of any uniform guidelines. In a study conducted by Asamer and Van Zuylen (2011) that used video recordings, saturation flow rates were reduced by 20% in snow slush and 30% when the road was fully covered in snow. Hirose et al. (2022) also used video recordings and reported that saturation headways can increase by up to 38.7% in adverse road-weather conditions at two signalized intersections in Winnipeg, Canada. Other researchers in Canada found saturation flow rates that were 17% and 25% lower than normal road surfaces on slushy and snow road surfaces, respectively (Lu et al., 2019). They also found FFSs to be 16.9% and 23.3% lower for those respective pavement conditions.

Saturation flow rate, start-up loss time, and FFS are important parameters when generating signal timing plans (Transportation Research Board and National Academies of Sciences, Engineering, and Medicine, 2015). Therefore, any variations in these parameters could impact the performance of the implemented plans. During winter conditions, one study found in a model that travel time travel time increased by 50% and average stops by 14% when normal signal timing plans were run during inclement conditions (Goodwin and Pisano, 2004). Brennan Jr et al. (2011) investigated a corridor in Noblesville, IN using Bluetooth probe vehicles and found an 83-second increase in travel time through a four-intersection signalized arterial during winter conditions. Using detector and signal data, researchers were able to notice increases in headway, platoon shifts, and link speeds. The arterial had a posted speed of 55 mph and experienced approximate reductions of 23% to 33% in effective link speed. Increases in link travel times extracted from the platoon shifts range from 15 - 30 s. Purdue Coordination Diagrams (PCDs) were used to show how these changes in travel times were detrimental to arrival on green efficiency and revealed opportunities to adjust the coordinated signal offset.

4.3.2.2 Simulation and modeling of weather-specific timing plans

Other works have used simulation and modeling to estimate how new parameters may improve signal performance. Work by Agbolosu-Amison et al. (2004) created new signal timing plans based on observed saturation flow rates and headways from video recordings and FFS

adjustments based on the work in Perrin et al. (2001). They were also able to show the benefits of implementing special signal plans for inclement weather, including reducing the control delay by 36% (Agbolosu-Amison et al., 2005). Brennan Jr et al. (2011) also predicted an overall system delay reduction of 23.1% for an updated signal timing plan designed to minimize delay for traffic behavior observed during the snow events. Another study by Lieu et al. used simulation to assess the benefits of retiming signals under adverse weather conditions by changing the start-up loss time, saturation headway, and reducing the traffic demand and found that operational benefits can only be realized in moderately high traffic flows and not when flow is low or oversaturated. Al-Kaisy and Freedman (2006) found potential travel time savings of 16.5%-21.5% in high-density town and city centers. However, they also noted, along with Lu et al. (2019) and Perrin et al. (2001), that new signal timing benefits are much more significant for coordinated segments than for isolated intersections.

4.3.2.3 Implementations of weather-specific signal-timing plans

Other studies have investigated the potential benefits of implementing new signal timing plans specifically for inclement weather. In Anchorage, AK, Bernardin, Lochmueller, and Associates, Inc. (1995) generated new signal timing plans specifically designed for winter and extreme conditions by adjusting these parameters and were able to decrease travel time by 13% and average delay by 23% on a 24 intersection signal network. Maki (1999) examined a highway during snow storms of at least 3 in. accumulation and found that speeds were about 40% slower, the start-up delay increase by 2-3s, and the saturation flow rate reduce by 11%. New signal timing plans were able to reduce delay and the average number of stops by 13% and 6%, respectively. Chen et al. (2015) has also implemented weather-responsive coordinated signal plans in Salt Lake City, Utah and facilitated smoother traffic progression.

Weather Responsive Traffic Management (WRTM) is a key FHWA strategy under the Roadway Weather Management Program (RWMP) for proactive management of traffic operations during weather events (Gopalakrishna et al., 2011, 2018). Under this component, traffic signal control is recognized for offering many opportunities for improving traffic flow during inclement weather. Specifically, in 2011, several states including Connecticut, Delaware, and Utah had implemented systems for deploying specific coordination plans during snow events, while some cities including Clearwater, Florida; Minneapolis, Minnesota; and Charlotte, North Carolina had discontinued this practice due to system upgrades, changes in intersection geometries, or staff reductions (Gopalakrishna et al., 2011). Utah has reported strong success with their program, noting that their engineers were able to maintain similar levels of progression during snow events as compared to normal conditions in terms of Arrivals on Green and Platoon Ratios (according to the PCDs) (Balke et al., 2013).

One of key obstacles to implementing signal timing plans specifically for inclement weather is knowing when to deploy them in real time. Perrin et al. (2001) and Martin et al. (2000) have recommended activating these plans based on engineering judgment according to four general areas: severity of the event (needs to at least be slush), duration of the event, area of influence, and current traffic flows. These guidelines have seemed to be the general principles the states previously listed have followed (Gopalakrishna et al., 2011). These processes are not automatic and require a lot of effort and judgment from engineers and meteorologists when determining and verifying upcoming snow events. Traffic operation centers already have many other responsibilities during snow events like fleet management of their snow removal operations (Desai et al., 2021). To our knowledge, very few if any traffic management agencies are using the HRRR weather prediction model, which has been shown to offer distinct advantages for observing traffic changes in response to weather events (Sakhare et al., 2023). The limitations of current methods for observing and predicting snow events have prevented the large-scale implementation of inclement weather specific signal timing plans. Despite their advantages, all implementations of these plans so far have included at most one corridor with 11 intersections (Balke et al., 2013).

4.3.2.4 Data collection limitations

The heavy data collection requirements have contributed to the limited scope of the previous studies that have investigated this topic. For instance, the implementation in Utah required advanced detection systems in addition to the existing detectors and a signal performance metrics system in order to extract the necessary traffic parameters (Balke et al., 2013). Many studies relied on detectors for these traffic parameters as well (Perrin et al., 2001; Martin et al., 2000; Maki, 1999; Rakha et al., 2008; Brennan Jr et al., 2011). Others utilized video detection (Agbolosu-Amison et al., 2004; Lu et al., 2019). Such fixed-location detection methods are limited in their observation ranges and it is therefore difficult to get accurate travel times between intersections even with signal timing data. Heavy implementation and maintenance costs have also limited their widespread implementation.

Vehicle trajectory data offers many advantages over fixed-location detectors, but very few studies have utilized this data to measure travel times between specific intersection during winter conditions. One study by Munehiro et al. (2006) in Japan in 2006 used data from 115 GPS-equipped taxi vehicles to investigate average travel speeds in compacted snow conditions, finding speed reductions of 40-44%. The study established the advantages of vehicle probe data for investigating vehicle behavior in snowy conditions, but very few studies have done so since, possibly because of the need for high quality weather data to complement it.

4.3.3 Contributions

This section uses vehicle trajectory data for the follow contributions:

1. Observe, at a large scale, changes in free-flow travel times between intersections during winter weather predicted by the HRRR model. To the best of our knowledge, this is the largest study of speed reductions in a winter storm on roadways that exhibit speeds under 55 mph in normal conditions.

2. Demonstrate how these speed reductions can impact traffic signal performance as reflect through vehicle trajectory SPMs.

The following study was conducted completely remotely and required no physical infrastructure, besides that used for the HRRR prediction model and some signal timing data for optional visualization purposes, demonstrating its efficiency and cost effectiveness. We highlight the advantages of vehicle trajectory data for inclement weather signal control diagnostics and reveal the potential for large-scale implementation. While this study shows how traffic management agencies can utilize vehicle trajectory data to measure travel times between intersections under winter conditions, the process can be applied to any conditions in which travel times change between intersections.

4.3.4 Data and study area

The case study harnesses the power of three critical data sources: 1.) road network, 2.) historical weather prediction data, and 3.) vehicle trajectory data. To the best of our knowledge, no one is pairing large-scale vehicle trajectory data with high resolution weather prediction models to evaluate fluctuations in free-flow travel times between intersections as weather conditions change. The availability of these data sources presents an unprecedented opportunity to perform this evaluation without additional sensor instrumentation on the physical road infrastructure.

4.3.4.1 Road network

The study took place in southeast Oakland County, Michigan and included 10 cities and townships (Bloomfield Township, Bloomfield Hills, Troy, Birmingham, Bingham Farms, Beverly Hills, Royal Oak, Clawson, Franklin, and Southfield). The 70 square kilometer study area contains 129 signalized intersections located on either urban arterials or major and minor collectors (Figure 4.10 (a)). Note that some signalized intersections on the north side of the study area were not included because of data sufficiency issues. Roads highlighted in

blue in Figure 4.10 (a) depict identified arterials and collectors. Among the 129 signalized intersection, 232 intersection pairs were identified with travel distances ranging from 65 to 1900 meters.

4.3.4.2 Weather prediction model

The HRRR model is a weather prediction model provided by the NOAA. A prediction model is preferable to historical data for analysis because the goal of this research is to provide FFS parameters for proactively adjusting the signal coordination in preparation for changes in weather conditions. HRRR assimilates radar data ever 15 minutes over a grid of 3-by-3 km cells and predicts a variety of weather parameter information for each cell every hour. The intersections in this study are found in 13 of the HRRR grid cells, illustrated in Figure 4.10 (b). HRRR includes hundreds of weather parameters including temperature, humidity, precipitation, wind speed, total snowfall, and snow depth. This study focuses on snowy conditions, but future work might explore others. Model data is stored in Grib2 file formats by the NOAA. These files were downloaded and processed with the help of the open-source *Herbie* python package (Blaylock, 2023).

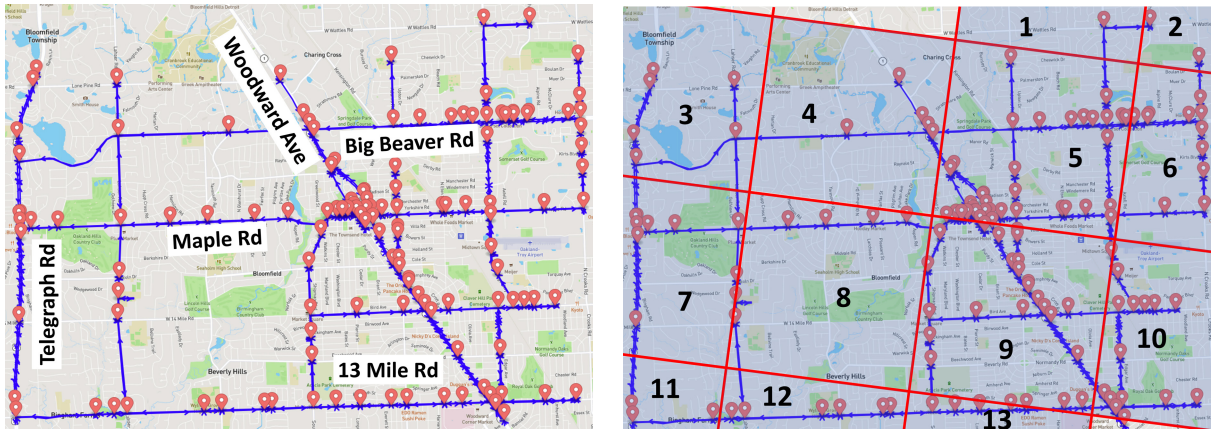

(a) Intersection locations (b) HRRR prediction grid

Figure 4.10: Study area in southeast Oakland County, MI

Based on vehicle trajectory data availability and HRRR analysis, a 2022 snowstorm on Saturday, January 1st to Sunday, January 2nd was chosen for this study. Figure 4.11 reports the predicted hourly snowfall (Grib2 parameter "ASNOW") in dashed lines and the predicted snow depth (Grib2 parameter "SNOD") in solid lines. Between 6 PM on Saturday to 4 AM on Sunday, each cell consistently experienced a half an inch of snowfall each hour. By 7 AM Sunday, the predicted snow depth was over 4.5 inches in each cell. Hourly snowfall alone might not indicate road conditions as ground temperatures will affect snow accumulation.

In addition, less than half an inch of snowfall per hour is generally considered a "low" rate (NOAA's National Weather Service, 2018) and might not impact driver behavior. Therefore, most of the analysis in this study focuses on the impact of snow depth on FFS. However, future studies should investigate how snowfall rates impact driving behavior and how it might differentiate from that of snow depth. It is also important to note that this study does not have any access to road treatment behavior. It is assumed, based on anecdotal observations and vehicle trajectory measurements, that this did not occur until early Sunday morning. However, no analysis was done after midnight due to trajectory data sufficiency issues (more in next section), so the authors are confident that no post snowfall treatment influenced the results.

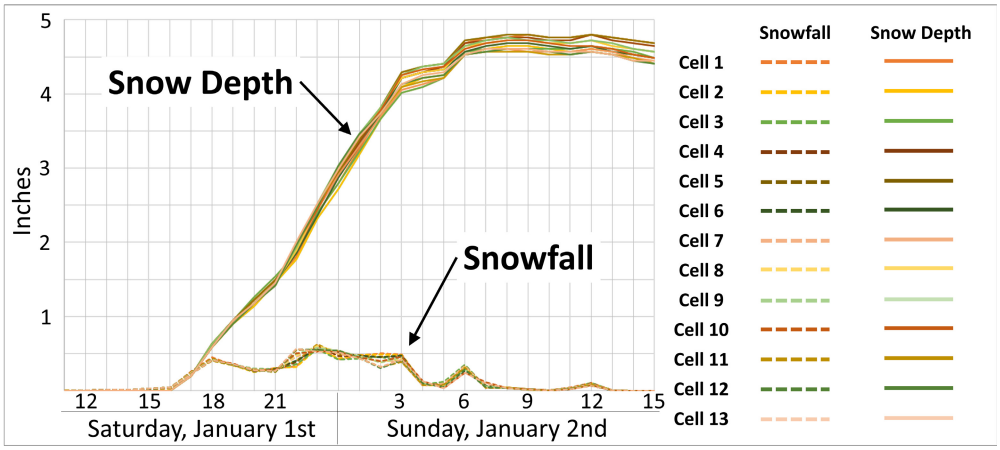

Figure 4.11: Hourly snowfall and snow depth prediction in each HRRR prediction cell

4.3.4.3 Vehicle trajectory data

Because the literature indicates that the potential benefits of weather-specific signal plans are much more beneficial for corridors than isolated intersections, this study is primarily interested in how we can adjust offsets between intersections during winter events. Therefore, we are interested in measuring free-flow travel time between intersections as this is the primary parameter that informs offset choice. Vehicle trajectory data allows us to extract travel times between intersections directly from individual vehicles rather than by pairing the detector data with the signal timing data. Measurements are available for any pair of intersections as trajectory data covers the entire spatial-temporal space. While detector data can only provide traffic counts and estimated speeds at certain locations, vehicle trajectory data provides more enriched information such as delay, number of stops, and travel times between any two points along its travel path (Figure 4.12).

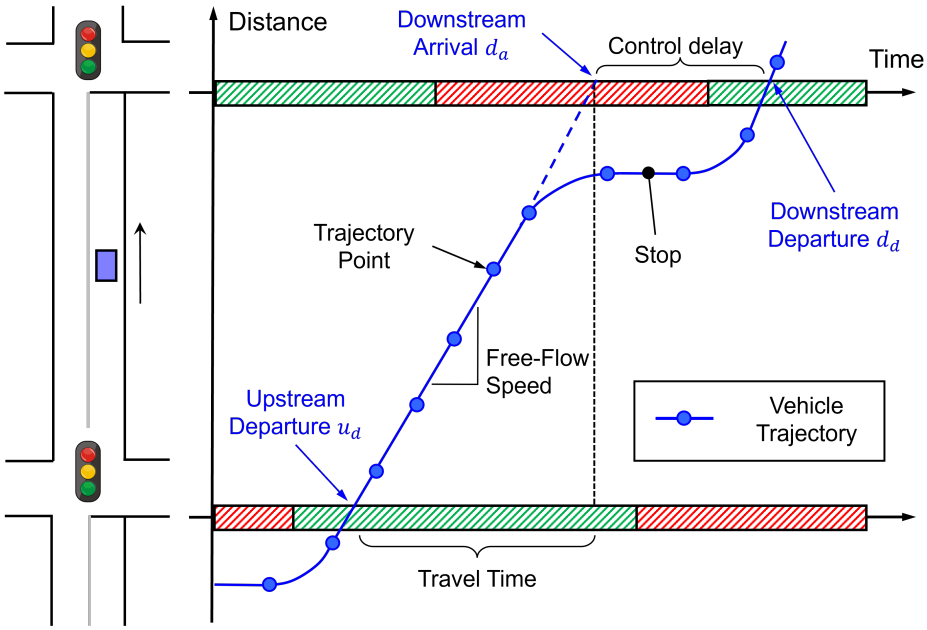

Figure 4.12: Performance calculations for vehicle traveling between two intersections

Each intersection pair has a downstream and upstream movement. Here we define the downstream arrival d_a as time the vehicle would have arrived at the intersection if did not have to stop or slow because of an existing queue or the traffic signal (Figure 4.12). Upstream departure u_d is the time at which the vehicle left the intersection. The free-flow travel time t_{ud} between these intersections can be calculated by taking the difference between the downstream arrival and upstream departure ($t_{ud} = d_a - u_d$). The performance of the signal coordination can be evaluated by the control delay and number of stops. For more details about the trajectory processing and how to calculate the performance indices, refer to (Wang et al., 2020). Note that while Figure 4.12 provides the signal timing information for illustration purposes, it is not required to calculate any of these measures.

This study utilized the original equipment manufacturer (OEM) dataset introudced in Section 1.2.2. Figure 4.13 illustrates the hourly number of intersection pair observations (one vehicle traversing between two intersections) during the 2022 snowstorm on January 1st at 3 PM to January 2nd at 7 AM. For comparison to "normal" road conditions, the same time frame from Sunday, January 2nd to Monday, January 3rd was used as a baseline. This time frame is also on the weekend and is close to the New Year's Day Holiday, making it the best choice for comparison based on trajectory data availability. There was no predicted precipitation during the baseline time frame according to the HRRR model. From Figure 4.13, it is easy to see that there was more observations during the no snow time period (32,118) than the snow period (23,680). This is probably a combination of the snowstorm

discouraging travel and January 1st being a holiday. In addition, Monday is a normal workday hence the increase in morning traffic starting at 5 AM on the 3rd.

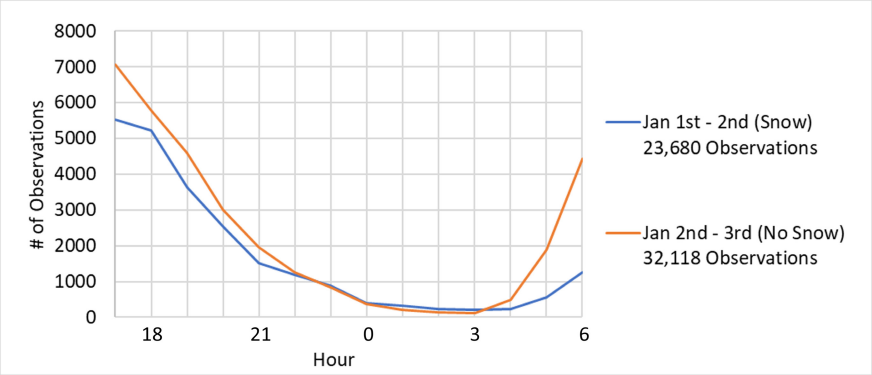

Figure 4.13: Hourly number of intersection pair observations during snow and no snow conditions

Table 4.1 reports the average number of observations per intersection pair for different ranges of snow depths based on Figure 4.11 and their respective baseline hour range. The average number of observations is insufficient for any meaningful analysis during the hour ranges with snow depth ranges between 2 and 4 inches (11 PM - 3 AM) because they occur late in the night. The large difference in observations during the hour ranges for snow depths larger than 4 inches (3 AM - 7 AM) make them unsuitable for analysis as well. Therefore, this study focus exclusively on snow depths less than 2 inches from 5 to 11 PM on Saturday, January 1st with the baseline "normal" conditions comparison being at the same time on Sunday, January 2nd.

Table 4.1: Average number of observations per intersection pair for different snow depths

Date Range	Time Range	Snow Depth (in.)	No. of Obs.
Jan. 1st - 2nd	17-20	<1	62.0
	20-23	1-2	22.5
	23-1	2-3	5.5
	1-3	3-4	2.4
	3-7	3-7	9.7
Jan. 2nd - 3rd	17-20	0	75.2
	20-23	0	26.7
	23-1	0	5.3
	1-3	0	1.5
	3-7	0	29.8

4.3.5 Results and discussion

Snowy conditions with a depth of less than 2 inches occurred on Saturday, January 1st, 2022 from hour 17 to 23 (Figure 4.13 and Table 4.1). Sunday, January 2nd, 2022 from hour 17 to 23 is used as a baseline comparison for "normal" conditions. Figure 4.14 reports the travel time distributions for an example intersection pair that is 505 meters apart (E Lincoln St. to Bowers St on Woodward Ave NB). There is an average travel time difference of around 6 seconds between the normal (27.1s) and snowy (33.4s) conditions. The space mean speed was 42 mph and 34 mph for normal and snowy conditions, respectively, a 18.8% decrease in speed. Not only does the distribution shift as a result of the increase in travel times, but it becomes flatter and wider. As a result, the standard deviation increases, which may indicate that drivers' speed choices become less consistent during snowy conditions. A Welch's t-test, which does not assume equal population variance, is used to compare the two distributions (Welch, 1947). The t statistic is 15.0 and the m value is 8.00×10^{-39}, indicating that the difference between these two distributions is statistically significant.

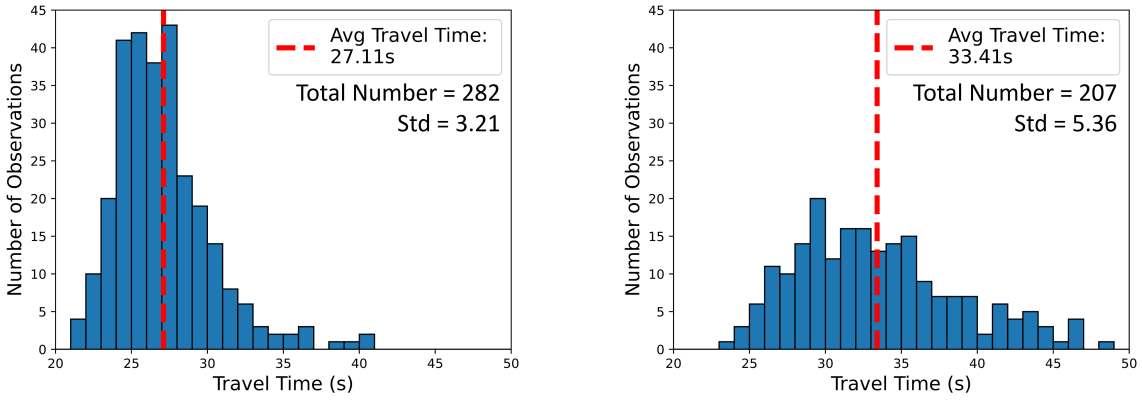

(a) Normal conditions

(b) Snowy conditions (< 2 in. depth)

Figure 4.14: Travel time distributions for E. Lincoln St. to Bowers St on Woodward Ave NB

4.3.5.1 Large-Scale urban traffic network speed study

The speed study looked at how average intersection pair travel times changed during snowy conditions compared to the normal baseline. The FFS (intersection pair distance divided by the average travel time) was calculated to compare these changes across all 232 intersection pairs. We analyzed the results in three groups to see if there was any difference across snow depths: 1.) all snow depths less than 2 inches, 2.) 0 to 1 inches, and 3.) 1 to 2

inches. Each intersection pair has a different number of observations, space mean speed, and distance. The descriptive statistics of these variables are shown in Table 4.2. Based on the mean and median measurements, the number of observations and intersection distances for all time periods are more heavily distributed below the mean (right skewed). The speed measurements are more normally (symmetrically) distributed.

Table 4.2: Descriptive statistics of key variables at different snow depths and time ranges for each intersection pair

Variable	Time Range	Date	Snow Depth (in.)	Min	Max	Mean	Median	Std.
No. of Obs.	17-20	Jan. 1st	0-1	2	248	62.8	46.5	50.4
		Jan. 2nd	0	2	301	76.1	57.0	62.1
	20-23	Jan. 1st	1-2	0	87	23.0	16.0	19.8
		Jan. 2nd	0	0	134	27.2	19.0	26.6
	17-23	Jan. 1st	0-2	7	332	86.1	61.5	69.5
		Jan. 2nd	0	8	409	103.7	77.0	87.9
FFS (mph)	17-20	Jan. 1st	0-1	15.7	42.0	29.4	30.3	5.2
		Jan. 2nd	0	16.7	55.8	36.0	37.4	7.6
	20-23	Jan. 1st	1-2	15.3	44.3	30.4	31.5	5.1
		Jan. 2nd	0	16.9	55.7	37.2	38.7	7.4
	17-23	Jan. 1st	0-2	15.8	42.5	29.6	30.6	5.1
		Jan. 2nd	0	17.0	55.7	36.3	37.8	7.5
Distance between intersections (m)				65	1900	518.2	392.5	384.9
Number of intersection pairs = 232								

Figure 4.15 (a)-(c) reports the regression lines for each analysis group, where the independent variable is the FFS during normal conditions and the dependent variable is the FFS during snowy conditions. Each point in these figures represents these measurements for one intersection pair. The regression models (dashed lines) for 0-2 in. and 0-1 in. fit fairly well with R^2 values of 0.9323 and 0.9244, respectively. The R^2 value for the 1-2 in. snow depth does not fit as well at 0.8415, which is likely due to the reduction in the number of observations shown in Table 4.2. In terms of difference among the three study areas, Figure 4.15 (d) illustrates that these three regression lines across the range of interest for normal conditions (20-55 mph) are very similar. Therefore, the rest of this section will discuss the results from Figure 4.15 (b) because most of the observations took place at a snow depth less than one inch.

The fitted lines show how there are larger speed reductions at higher speeds, rather than a constant percent reduction. For instance, from the regression line for 0-1 in. snow depth in Figure 4.15 (b), a 50 mph speed in normal conditions would result in a predicted snow

speed of 38.6 mph, a 22.8% reduction. However, a 20 mph speed in normal conditions would result in a predicted snow speed of 18.8 mph, a 5.9% reduction. It is important to note that this regression line is only valid across the range of FFSs in normal conditions available from the data (16.9-55.7 mph). The positive y-intercept and slope less than 1 means that, for some values (in this case those less than 16.5 mph), the regression line will output a speed that is faster than normal conditions. It is more reasonable to assume that speeds less than 16.5 mph in normal conditions are not impacted that much by snowy conditions and remain the same, but future work should investigate this. However, most coordinated arterials will have speeds higher than this value, so this is not a concern in this study.

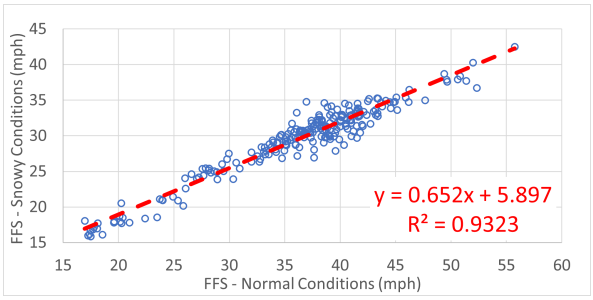

(a) Regression for 0-2 in. Snow Depth

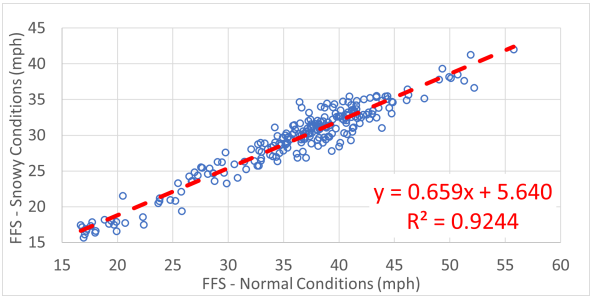

(b) Regression for 0-1 in. Snow Depth

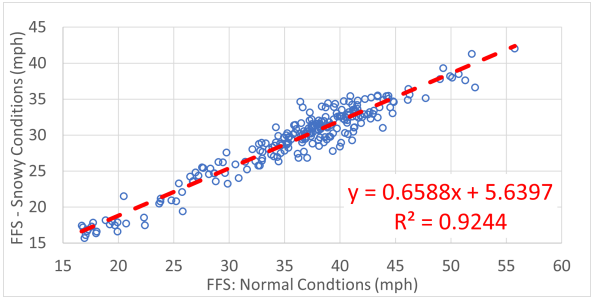

(c) Regression for 1-2 in. Snow Depth

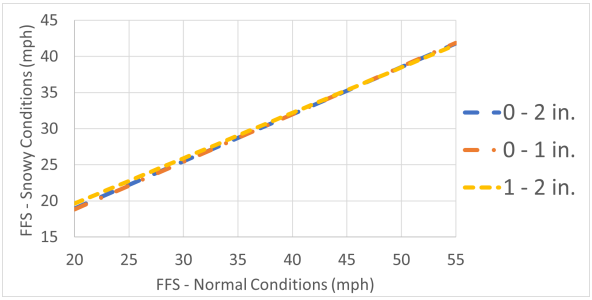

(d) Comparison of Each Regression Line

Figure 4.15: Regression lines at different snow depths

4.3.5.2 Impacts on Signal Timing Performance

Across the entire network of 129 signalized intersections, there was an 11.23% increase in the average number of stops per intersection per vehicle and a 20.93% increase in control delay per intersection per vehicle during the snowy conditions among the observed vehicles. Control delay is delay caused directly by the traffic signals. It does not reflect increases in travel time from slower traveling speeds in snowy conditions (Figure 4.12). The increases in the average number of stops and control delay indicate that the signal timing plans do not work as well in snowy conditions. One possible explanation is that the coordination was not

as effective due to the reductions in FFSs reported in Figure 4.15.

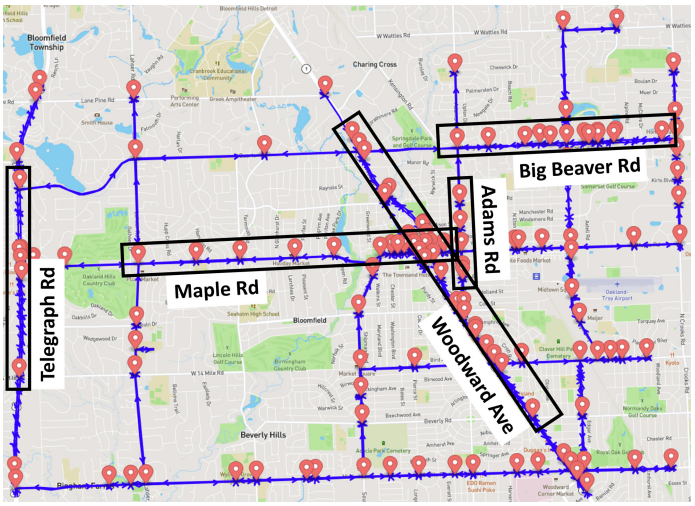

Figure 4.16: Selected arterial and collector sections

Table 4.3: Percent changes in average number of stops and control delay (per intersection per vehicle) for selected corridors

Corridor	Direction	Avg No. of Stops			Avg Control Delay (s)		
		Norm.	Snow	% Change	Norm.	Snow	% Change
Woodward Ave	NB	0.03	0.11	259.2	1.20	3.95	230.7
	SB	0.06	0.12	107.9	1.77	4.14	134.4
	Both	0.05	0.12	157.1	1.49	4.05	171.7
Maple Rd	WB	0.19	0.23	25.8	6.66	8.61	29.3
	EB	0.11	0.18	63.8	4.26	7.86	84.6
	Both	0.15	0.21	35.2	5.65	8.25	46.1
Telegraph Rd	NB	0.02	0.10	435.0	0.78	3.22	311.6
	SB	0.11	0.13	23.7	3.33	4.50	35.9
	Both	0.05	0.11	107.2	1.80	3.71	106.0
Big Beaver Rd	WB	0.10	0.16	60.4	5.21	9.73	86.6
	EB	0.15	0.13	-8.5	5.87	6.70	14.0
	Both	0.13	0.15	16.5	5.57	8.04	44.5
Adams Rd	NB	0.33	0.19	-43.5	7.57	7.66	1.2
	SB	0.25	0.12	-53.5	7.98	6.24	-21.8
	Both	0.29	0.15	-49.11	7.79	6.86	-12.0

To investigate this further, we identified 5 arterial and collector sections of roadway that exhibited good coordination during normal conditions. Figure 4.16 shows their locations while the signal performance results are in Table 4.3. Woodward Ave and Telegraph Rd have the highest percent increase in average number of stops (157.1% and 107.2%) and

control delay (171.7% and 106.0%). Their posted speed limit is 45 mph and they experience very good coordination during normal conditions, with average number of stops of 0.05 and average control delay between 1.49-1.80s. These are both heavily trafficked collector roads. Maple Rd is a local arterial that travels through a downtown area with posted speed limits between 25 and 35 mph with closer spacing between the signals. In general, we see that corridor directions that have very good coordination during normal conditions have higher percentages of worse performance during snow conditions. For instance, Telegraph Rd NB had an average of 0.02 stops per vehicle per intersection and an average control delay of 0.78s per vehicle per intersection, the lowest for both metrics for all corridor directions. This direction experienced the highest percent increase in average number of stops (435.0%) and control delay (311.6%). In contrast, the worst performing corridor direction in normal conditions (besides Adams Rd, which is a special circumstance that will be explored later) was Maple Rd WB with an average of 0.19 number of stops and control delay of 6.66s. The stops for this direction only went up by 25.8% and the control delay only went up by 29.3%, which were some of the lowest percent increases in Table 4.3. It is also interesting to note that, for each corridor, the more coordinated side was much more heavily impacted by the snowy conditions than the other, further indicating how the snowy conditions were particularly harmful for traffic signal coordination.

For detailed analysis of a specific corridor direction, we now explore the Woodward Ave. NB results. Figure 4.17 includes the aggregated time-space diagrams for both normal and snowy conditions. These diagrams are drawn by aggregating the trajectory data which is possible because of common cycle length of 90s (Du et al., 2019). The corridor experienced great coordination in normal conditions as shown in the time-space diagram. There is a distinct green band that smoothly covers the entire corridor. In snowy conditions, the coordination suffers because of reduced FFS, shown by the slope of the lines representing the trajectories. More trajectories have to stop at each intersection. The dashed red lines in Figure 4.17 point to the same location on the time-space diagram. In the normal conditions, all the vehicles are able to pass through the intersection without stopping whereas in the snowy conditions vehicles at the end of the platoon are not able to make it. The histograms in Figure 4.18 also record the travel times of vehicles that travel the entire corridor. They illustrate how the vehicles that travel the entire corridor in snowy conditions are not able to travel the corridor within the green band and instead arrive in 3 distinct platoons. Finally, the results in Table 4.4 provide individual results for each intersection pair. Of particular note is the increases in standard deviation for each intersection pair during snowy conditions, indicating that drivers are more variant in their speeds during snowy weather which may also impact signal performance. In general, the standard deviations are also larger for pairs

that are farther apart.

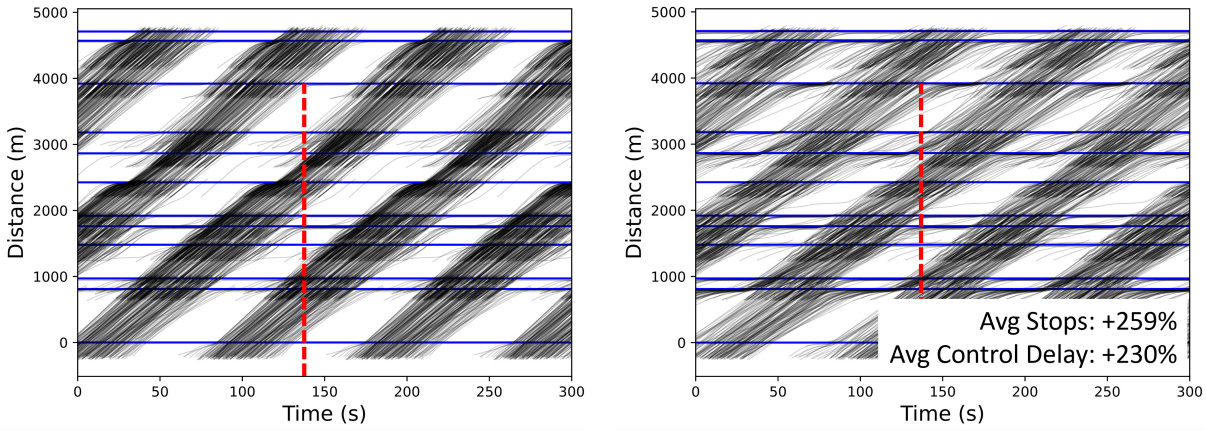

(a) Normal conditions (b) Snowy conditions

Figure 4.17: Aggregated time space diagrams for NB Woodward Ave. in normal and snowy conditions

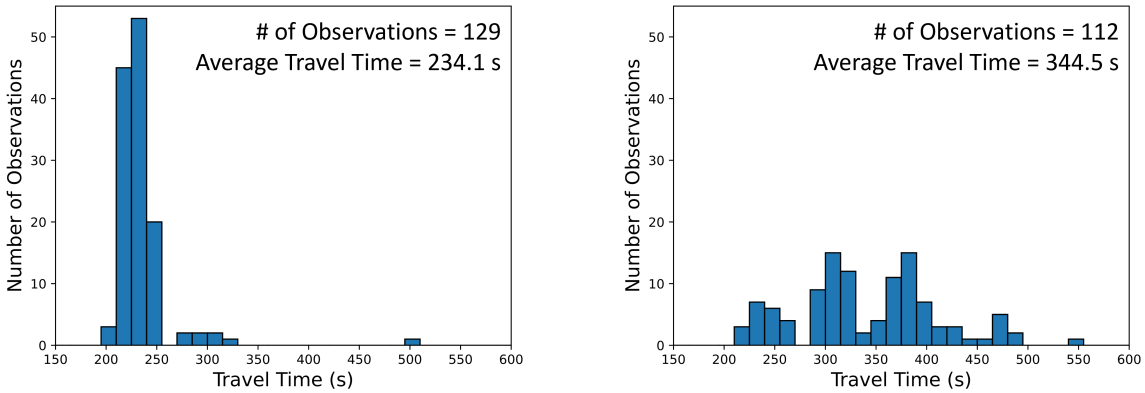

(a) Normal (b) Snow

Figure 4.18: Histograms of travel times for vehicles traveling the entire NB Woodward Corridor section in normal and snow conditions

From Table 4.3, the Adams Rd corridor unexpectedly experiences decreases in the performance metrics. To explain this phenomena, we again plot the aggregated time-space diagrams in Figure 4.19. For this corridor, the existing Signal Phase and Timing (SPaT) data was available from signal work orders provided by RCOC. The boxed areas depict how the vehicles arrive at the intersection earlier than in snowy conditions, resulting in more stops and longer wait times. It seems the coordination might assume travel times that are too long as performance is better when vehicle speeds are slower. As shown in Table 4.5,

particularly for the first three intersections, the FFSs are closer to the posted 25 mph speed limit during snowy conditions and the signal performance in terms of the average number of stops is better. This example highlights how accurately calibrating the free-flow travel time is important in signal coordination, and changing it to more accurate levels during snowy conditions could benefit traffic flow.

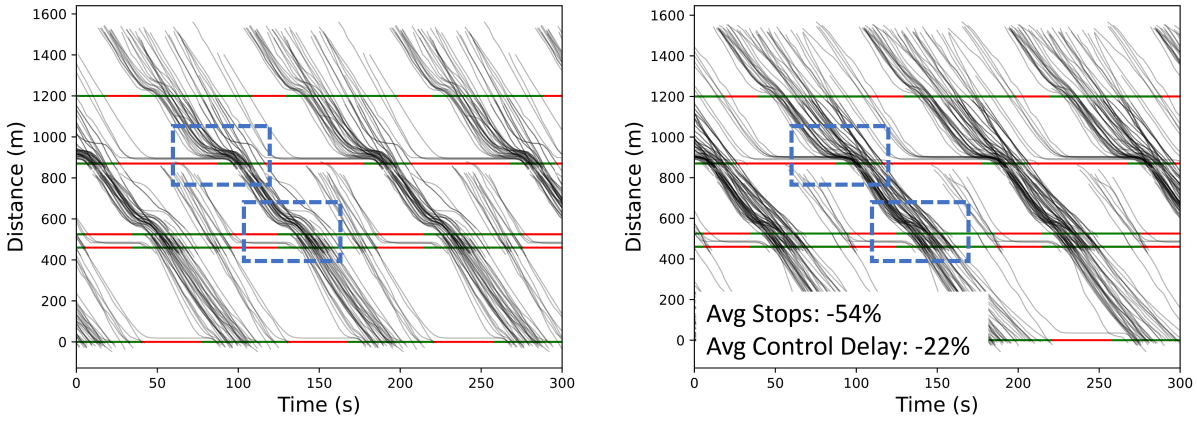

(a) Normal (b) Snow

Figure 4.19: Aggregated time-space diagrams for Adams Rd. in normal and snow conditions

4.3.6 Summary

Using vehicle trajectory data and historical data from the HRRR weather prediction model, this section investigates how roadway snow depths impact free-flow travel times between intersections and how these changes influence the performance of signal timing plans. The study area included 70 square kilometers in southeast Oakland County, MI containing 129 signalized intersections. We examined a snowstorm from January 1st - 2nd, 2022 that exhibited snow depths of up to 4.5 inches and hourly snowfall rates of 0.5 in/hr from hours 18 to 4. Due to the lack of trajectory data for certain snow depths, we only report results for snow depths less than 2 inches. The study contains two parts: 1.) a large-scale urban study on FFS reductions during snow depths predicted by HRRR and 2.) an analysis of how these reductions can influence the effectiveness of signal performance, specifically coordination.

To the best of our knowledge, this is the largest study of speed reductions in a winter storm on roadways that exhibit speeds of under 55 mph in snowy conditions using vehicle trajectory data. The findings provide a clear trend line for FFS in normal conditions between 20-55 mph. Speeds in normal conditions of 50 mph are reduced by 22.8%. The reduction percentage slowly decreases to 5.9% for speeds in normal conditions of 20 mph. This finding

Table 4.4: Woodward Ave. NB results at each intersection

Downstream Intersection	Upstream Dis. (m)	No. of Obs.		Avg Travel Time (s)			Travel Time Std.		Avg No. of Stops		
		Norm.	Snow	Norm.	Snow	% Change	Norm.	Snow	Norm.	Snow	% Change
Big Beaver Rd	140	314	231	7.5	10.0	34.0	1.48	2.63	0.00	0.06	1667.1
Big Beaver Rd LT	650	305	221	30.5	41.6	36.2	3.03	7.52	0.04	0.16	271.6
Oak Ave	740	304	225	33.4	43.7	31.0	3.03	7.74	0.02	0.16	710.7
Oakland Ave	315	268	215	15.7	20.3	29.3	2.08	3.88	0.01	0.06	274.0
E Maple Rd	440	235	203	23.1	28.0	21.2	2.33	4.52	0.03	0.19	652.5
Bowers St	505	282	207	27.1	33.4	23.2	3.21	5.36	0.04	0.02	-54.6
E Lincoln St	160	315	236	8.6	10.7	24.3	1.32	2.19	0.02	0.06	166.9
S Adams Rd	280	317	237	14.5	17.8	22.8	1.90	3.14	0.07	0.11	58.1
Chapin Ave	510	348	269	26.1	33.5	28.4	3.22	5.89	0.01	0.03	107.0
14 Mile Rd	160	335	253	8.7	12.0	36.9	1.75	3.26	0.03	0.07	116.7
14 Mile Rd LT	810	308	237	40.7	52.2	28.2	5.59	10.56	0.05	0.30	559.1
Total	4710	3331	2534	235.8	303.0	28.5	N/A		0.03	0.11	259.2

Table 4.5: Adams Rd. SB results at each intersection

Downstream Intersection	Upstream Dis. (m)	No. of Obs.		FFS (mph)			Avg No. of Stops		
		Norm.	Snow	Norm.	Snow	% Change	Norm.	Snow	% Change
Buckingham Rd	160	92	87	30.6	26.2	-14.4	0.25	0.06	-77.0
Maple Rd	280	62	61	28.6	25.0	-12.6	0.66	0.46	-30.6
Bowers St E	510	57	60	27.1	23.9	-11.5	0.39	0.03	-91.4
Bowers St W	160	88	74	24.0	20.9	-12.8	0.03	0.04	18.9
Lincoln St	810	58	51	28.3	24.8	-12.4	0.02	0.02	13.7
Total	1920	357	333	N/A			0.25	0.12	-53.5

is new to the existing literature which usually reports constant percent speed reductions for all speeds below 55 mph. It was also noted that the distributions of travel times were wider when there was snow on the road, indicating that driving behavior is more variant in these conditions.

For the entire study area, the number of stops increased by 11.2% and the control delay increased by 20.9%. Signal coordination was particularly impacted: one corridor direction experienced a 435.0% increase in the number of stops and a 311.6% increase in control delay. These increases were much larger than what had been previously reported in the literature. In general, corridors with very good coordination during normal conditions were more effected by snowy conditions (higher percentages of increases in number of stops and delay). Another corridor's signal performance measures improved because FFSs were reduced closer to the apparent design speed, demonstrating the importance of accurately calibrating the free-flow travel time parameter.

The findings of this study demonstrate the potential to use vehicle trajectory data for real-time measurements of the free-flow travel time parameter across large-scale networks in a variety of weather conditions, allowing traffic engineers to design signal coordination plans (offsets) in preparation for winter conditions as predicted by HRRR. This process, which requires no physical infrastructure and can be conducted remotely, can also be applied to any conditions in which travel times change between intersections such as construction or roadway maintenance. Future studies will investigate other weather (snowfall rates, ice, visibility, rain, etc.) and environmental conditions and address limitations of this work. Namely, we do not investigate changes in saturation flow rates and start up loss times, which have been shown to impact signal timing performance in previous works. We would also like to continue studying these impacts at a larger scale and perform a real-world implementation of weather-specific signal timing plans.

4.4 Conclusion

4.4.1 Summary

This chapter presents methods for detecting signal coordination improvement opportunities without ground-truth signal timing data. First, we present a cycle length estimator using only vehicle trajectory data to identify corridors that have inconsistent cycle lengths among their intersections. As consistent cycle lengths (or in some cases multiples of the same duration) are a staple of traffic signal coordination, inconsistent cycle lengths indicate potential signal coordination improvement opportunities. A real-world example is provided demon-

strating the applications of this estimator. Second, we show how weather prediction models can be used to diagnose poor coordination performance during winter weather. A large scale speed study was performed at 129 intersections in southeast Oakland County, MI that analyzed increases in travel times between 232 intersection pairs during a snowstorm. Then we explored how these travel time increases impact traffic signal performance by degrading traffic signal coordination. Both of these methods provide key a diagnostic application that can help traffic agencies proactively identify signal retiming opportunities across large traffic networks.

4.4.2 Integration into the traffic signal timing management system

The cycle length estimator presented in Section 4.2 serves as a diagnostic microservice in the overall traffic signal timing management system presented in Figure 1.6. The HRRR weather prediction tool presented in Section 4.3 is also included as a module in the traffic signal timing management system. The coordination diagnostic application can call either one of this tools when identifying opportunities to improve signal coordination. Notably, neither of these tools require ground-truth signal timing data. The cycle length estimator measures the cycle length using only vehicle trajectory data, and the evaluation of coordination during winter weather simply evaluates travel-times between intersections and SPMs during predicted snowfall events.

CHAPTER 5

Iterative Traffic Signal Timing Optimization to Alleviate Traffic Congestion

5.1 Introduction

This chapter presents procedures for alleviating traffic congestion caused by evolving traffic patterns at intersections controlled by fixed-time or coordinated-actuated signal control. These procedures optimize timing plan schedules, cycle lengths, offsets, and green splits from just a small percentage of vehicle trajectory data as the only input. Together they form a complete online closed-loop traffic signal optimization system without requiring any input from roadside detection systems. The system utilizes a new model for designing signal timing plans that leverages the temporal-spatial information of trajectory data as opposed to traditional software such as Synchro which relies on turning movement counts (Wang et al., 2024a). This model allows us to accurately reconstruct average recurrent traffic states by aggregating sufficient historical data, even at low penetration rates. The system's technical readiness for deployment is demonstrated through multiple real-world implementations, including a direct comparison with a traditional optimization. In that deployment, the proposed system outperformed the conventional approach, reducing overall control delay by 17.4% and the number of stops by 20.4%, compared to 13.7% and 14.9% reductions, respectively, from the traditional method. By leveraging trajectory data as the sole input and requiring no additional infrastructure, this system offers a scalable and cost-effective solution that can be applied to signalized intersections around the world.

5.1.1 Background and related works

While many existing studies have investigated traffic signal control with vehicle trajectory data (Chen and Englund, 2015; Li et al., 2023a; Li and Ban, 2018; Guo et al., 2019; Lin et al., 2017; Feng et al., 2015), they assume a high penetration rate, which is not realistic in the

current practice. Some studies have developed statistical methods to estimate certain traffic flow parameters such as traffic volumes or queue lengths (Zhao et al., 2019a; Comert and Cetin, 2009; Comert, 2013; Zheng and Liu, 2017; Zhao et al., 2021), but they can only be used for traffic monitoring purposes due to the lack of an explicit traffic flow model. Therefore, real-world signal optimization efforts using vehicle trajectory data have relied on heuristic methods that analyze split failure percentages across all phases to reallocate green time. In 2024, Purdue University worked with the Indiana Department of Transportation (INDOT) to scan their more than 2,000 traffic signals using vehicle data and prioritize signal retiming activities (Saldivar-Carranza et al., 2024b). Eleven timing plans were adjusted at nine traffic signals based on identifying "critical movements" and "donor movements" according to split failure ratios, reducing average control delay and split failures by up to 53 seconds and 30%, respectively. Other optimization implementations have been limited to coordinating only pairs of intersections rather than entire corridors. A team from Project Green Light with Google Research used probe data for traffic signal coordination and performed an experimental study of such a method in Jakarta, Indonesia, where the average travel time dropped from 14.6 seconds to 9.5 seconds (Haddad et al., 2024). While the implementations from Purdue and Google demonstrate the potential for using trajectory data for traffic signal optimization, the lack of a traffic flow model limits the capabilities of their methods.

For traffic signal optimization, it is important to have the capability to predict traffic flow performance under different traffic signal parameters. However, most existing traffic flow models do not fit with vehicle trajectory observations, so only a handful of studies have used such data to attempt traffic signal optimization heuristically with a very limited scope for implementation (Day et al., 2017; Ma et al., 2020; Yan et al., 2019). In this chapter, we aim at optimizing traffic signals utilizing vehicle trajectories at the currently available market penetration rate. We overcome the sparse and incomplete observation of the overall traffic state provided by low penetration rate vehicle trajectory data by leveraging the probabilistic time-space (PTS) model developed by this group in Wang et al. (2024a). By aggregating sufficient historical vehicle trajectory data, the PTS model can accurately reconstruct average, recurrent traffic conditions even with limited trajectory availability, enabling us to predict future traffic flow performance under different traffic signal timing plans. Building on these capabilities, this dissertation creates methods for optimizing timing plan schedules, cycle lengths, offsets, and green splits from just the currently available vehicle trajectory data.

5.1.2 Contributions and organization of this chapter

This chapter presents procedures for leveraging cloud and cellular communications with vehicles to iteratively optimizing timing plan schedules, cycle lengths, offsets, and green splits every few weeks in response to evolving traffic demand patterns, as opposed to the typical 3-5 year timelines executed in the practice. Together these procedures represent a complete deployable optimization system with the flexibility to alleviate traffic congestion by adjusting four of the major traffic signal timing parameters. This system utilizes the PTS model, which leverages the temporal-spatial information of vehicle trajectory data as opposed to traditional software such as Synchro which relies on turning movement counts. The technical readiness for deployment of this system is demonstrated through multiple real-world implementations, including a direct comparison with a traditional optimization project.

Section 5.2 establishes the theoretical foundations of the system through a summary of the PTS model. It also describes upgrades made to the model to accommodate coordinated-actuated control. Section 5.3 explores an implementation case study to demonstrate how we use the PTS model to perform the vehicle trajectory-based optimization. This section also compares the real-world implementation with the traditional optimization through before and after studies of both methods. Other implementations are presented in **??**. Finally, we conclude by summarizing the advantages of the vehicle trajectory-based optimizations and next steps in 5.4.

5.2 Theoretical foundations

Vehicle trajectory data has been used widely in the literature and in practice to evaluate traffic performance at signalized intersection through signal performance measuress (SPMs). Despite limited vehicle trajectory penetration rates, the aggregated time-space diagram (Figure 5.1) has been used in the past to overcome this limitation. Figure 5.1 illustrates our own variation that leverages the cyclical nature of traffic signal parameters and traffic demand to depict an average (recurrent) traffic state of a particular movement. Other variations, such as the Purdue Probe Diagram (PPD), exist that do not include signal timing information (Saldivar-Carranza et al., 2023). These diagrams serve very similar functions to commercial solutions such as the percent arrival on green (AOG) graphs provided in the *Signal Analytics* platform provided by INRIX and the *ClearGuide Signals* platform provided by Iteris. While aggregating the observations is very useful for evaluating the performance of traffic signals, and in some cases can be used to adjust green splits (Saldivar-Carranza et al., 2024b), it has

its limitations when used to optimize offsets and cycle lengths.

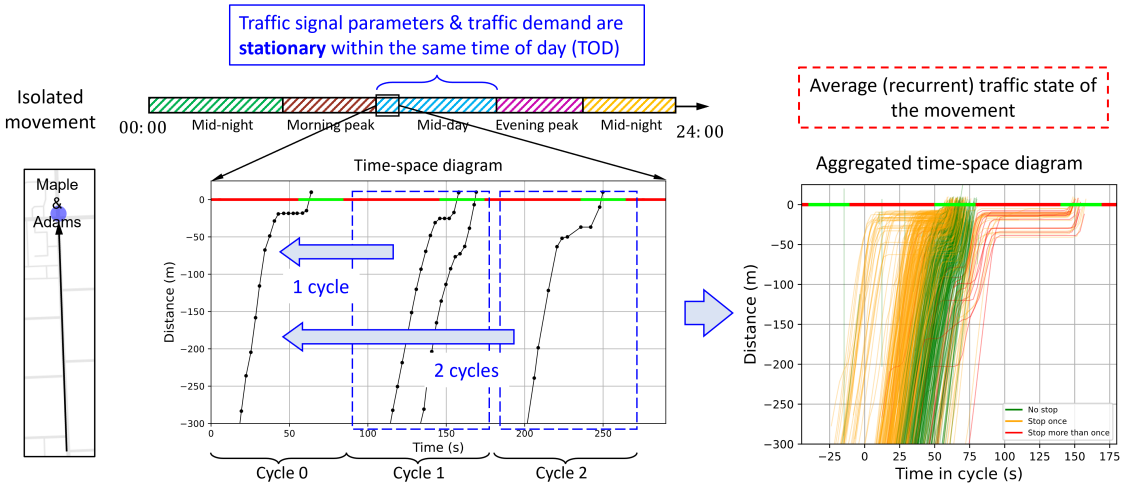

Figure 5.1: Building the aggregated time-space diagram

In order to optimize these crucial traffic signal parameters, we need a model that not only captures the current traffic state, but also predict future states under alternative signal timing plans. Traditional models (e.g., Synchro) require inputs such as speed, density, or volume measurements taken from detector data or turning movement counts, and are not compatible with low penetration rate vehicle trajectory data (Figure 5.2). A prediction model for vehicle trajectory-based optimization needs to leverage the temporal-spatial advantages of vehicle trajectory data rather than simply the number of observations. A basic introduction to this concept is provided in Figure 1.4 in Section 1.1.2.

5.2.1 The probabilistic time-space PTS model

The PTS model introduced in our previous work was designed to fill this gap (Wang et al., 2024a). Figure 5.3 provides an overview of the model's technical details. It is a stochastic traffic flow model built using a new coordinate system, the Newellian Coordinates, that can encode trajectories in a way that harnesses their temporal-spatial advantages (Figure 5.3 (a)). Newellian Coordinates assume that all vehicles follow a homogeneous deterministic Newell's car-following model in order to encode their trajectories according to their intersection arrival time and stop position in relation to the stop bar (Newell, 2002; Wang et al., 2024a). These coordinates are based on a distorted grid where the slope of the vertical axis is the free-flow speed v_f (Figure 5.3 (a)). Therefore, vehicle trajectories are encoded in either a stop or

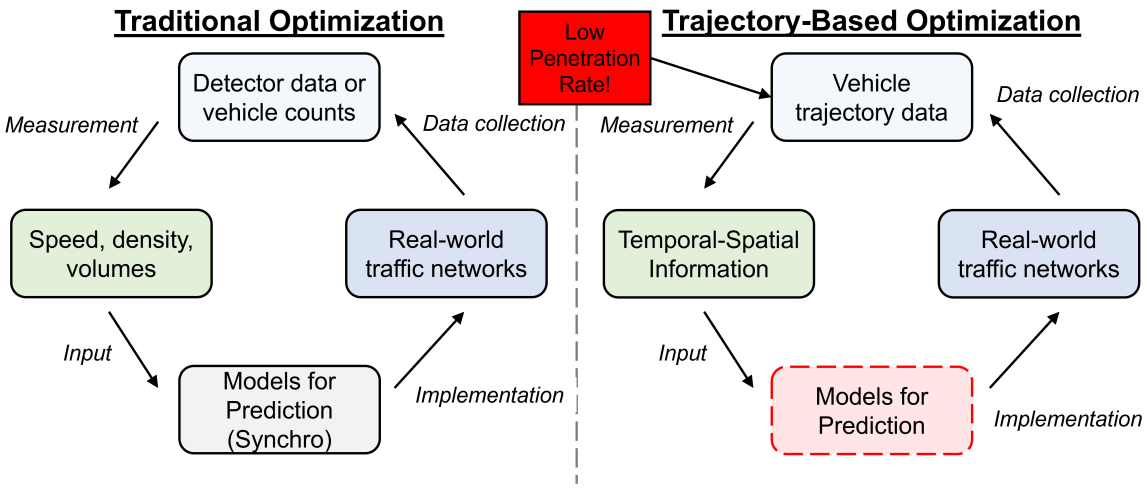

Figure 5.2: Difference Between the current practice and the proposed vehicle trajectory-based method

free-flow state. This allows us to ignore the free-flow travel time and easily quantify delay resulting from traffic signal control.

We have demonstrated that a simple point-queue model under the proposed Newellian coordinates can sufficiently capture spatial-temporal traffic state through the probabilistic time-space (PTS) diagram. The main advantage of the model is that it is a stochastic model with low dimensions and can be directly calibrated by taking the vehicle trajectory data as the input. It enables us to apply different estimation algorithms to estimate unknown traffic states and parameters. Even at a low penetration rate, recurrent traffic states can be accurately reconstructed by aggregating sufficient historical data.

The PTS model accepts two primary inputs: the arrival rates $A(t)$ and the state of the traffic signal $S(t)$ within a cycle (Figures 5.3 (b) and (c)). As shown in Figure 5.3 (d), the PTS model can be visualized as the PTS diagram, which looks like the time-space diagram. However, unlike the time-space diagram, where each line represents a trajectory, the opacity of the line in the PTS diagram represents the probability of there being a vehicle. The model can be calibrated by scaling the arrival rate distribution (determined by the observed aggregated time space diagram in Figure 5.1) in way where the observed delay is equal to the delay predicted by the model. Once the model is calibrated, it can determine an optimal signal timing plan through delay predictions under a range of feasible alternatives.

The model's ability to improve coordination through offset adjustments for fixed-time control was tested through a manual implementation on Adams Rd in Birmingham, MI. None of the signalized intersections on this corridor are equipped with any vehicle detectors,

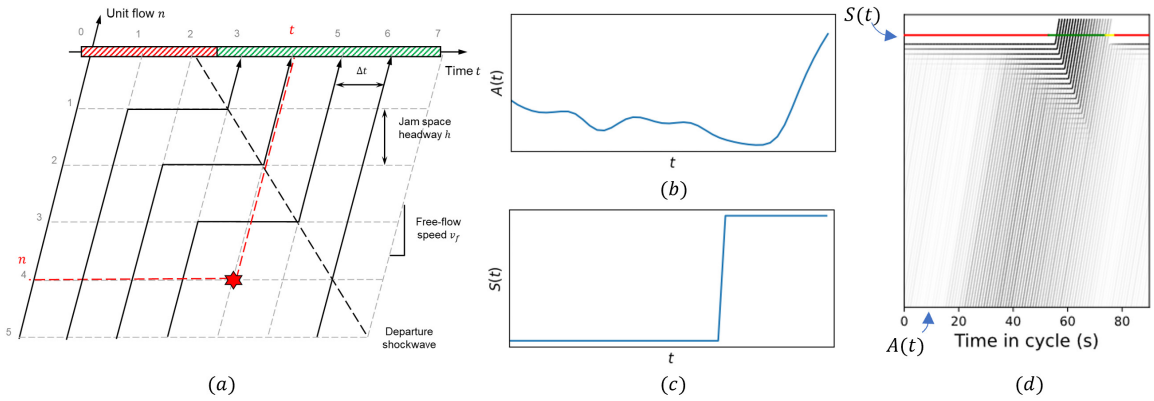

Figure 5.3: Demonstration of PTS model. (a) Newellian coordinate system; (b) Arrival rate profile $A(t)$; (c) Signal state $S(t)$; (c) PTS diagram given arrival rate and signal state, drawn in the Newellian coordinates;

so the proposed system provided previously unavailable opportunities. New optimized signal timing plans were deployed in April 2022, and three weeks' data both before and after the implementation were used to evaluate before-and-after performance. Figure 5.4 illustrates the results of the field implementation during the morning peak period (northbound). Left and right figures show the aggregated time-space diagram of the corridor using vehicle trajectories before and after the offsets were adjusted, respectively. The aggregated time-space diagram is directly generated from the observed vehicle trajectory by aggregating trajectories within the same time of day interval into one cycle. It clearly shows how vehicles pass

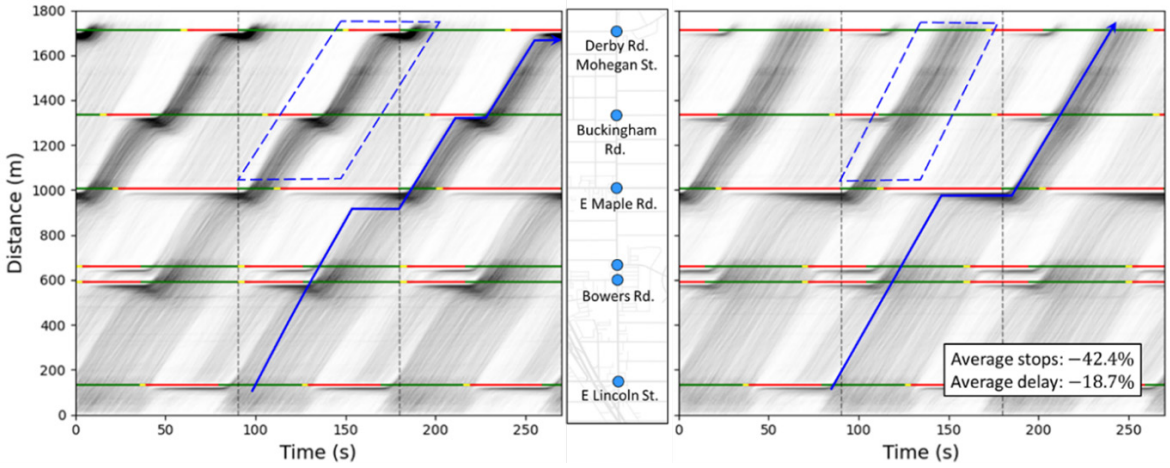

Figure 5.4: Before (left) and after (right) comparison of implemented offsets in morning peak of northbound Adams Rd corridor

the whole corridor across multiple signalized intersections. The dashed outlined box highlights how the stopping behavior improved for two specific intersections, and the blue lines are hypothetical trajectories that traverse the whole corridor and demonstrate how these trajectories have less delay and stops after the optimization. In the northbound direction, the number of stops and average control delay decreased by over 40% and 20% accordingly. The other direction of this corridor which is not shown also performed better than before by roughly 10%.

5.2.2 Modifications for coordinated-actuated control

Since the original study only considered fixed-time signal control, this section presents upgrades to the PTS model in order to accommodate coordinated-actuated control. This type of control maintains coordination by operating actuated control only on the non coordinated movements since the coordinated major phases must be serviced at the same fixed point in each cycle. In this case, when all the non-coordinated phases gap out, early return to green (ERG) occurs where the coordinated major phase starts earlier than the offset value. While ERG can increase the green time for the main direction, it can have a negative impact on coordination as it can alter the intended green bands (Transportation Research Board and National Academies of Sciences, Engineering, and Medicine, 2015). Vehicles that benefit from ERG might face additional stops and delays downstream due to premature departures. Therefore, it is crucial to incorporate ERG considerations into the modeling and optimization of traffic coordination. However, it can be difficult to model the variations in ERG start times.

Various methods have been proposed to mitigate this issue in vehicle count-based optimization, but they hold a variety of limitations. Some approaches coordinate based on the end of green (Jovanis and Gregor, 1986), which can compromise efficiency because the densest departures typically occur at the green start, especially under high traffic volumes. Others solely focus on the mean value of the green start (Skabardonis, 1996), which does not adequately address extreme scenarios, such as when there is no ERG or ERG occurs very early, both of which are critical to the transportation system. Additionally, some methods encounter implementation challenges due to shortcomings of the algorithm itself, such as stability issues of the algorithm in oscillatory traffic patterns (Abbas et al., 2001), or due to reliance on strong assumptions. For instance, arrival patterns or arrival rates of all phases are assumed to be known (Zhang and Lou, 2015; Ma et al., 2016). Moreover, other methods rely on archived traffic signal data (Yin et al., 2007; Hu and Liu, 2013; Mathew et al., 2019), which can be difficult to obtain and may vary across different types of controllers.

We can leverage the temporal-spatial advantages of vehicle trajectory data to estimate the green start time of the coordination phase for each cycle. As shown in Figure 5.5 (a), suppose the cycle length is known for this movement. The designated green split is also known and is shown in green. The actual green start time is unknown, but we know it is somewhere in the blue diagonal-hatching area. The dashed black lines depict the unobserved trajectories, while the solid orange lines represent the observed trajectories. To estimate the actual green start in this cycle, we can find the first observed stopped trajectory and its point of departure. Draw a line through this point with a slope corresponding to the shockwave speed. The intersection of this line with the stop bar represents the estimated green start time (Figure 5.5 (b)). So, the blue diagonal-hatching area in Figure 5.5 turns into red and green back-diagonal-hatching areas, which represent the red light and the extra green due to ERG, respectively. The shockwave speed can be estimated by aggregating trajectories in the fixed-time intersection into one cycle and fitting all the departure points with a robust linear regression algorithm.

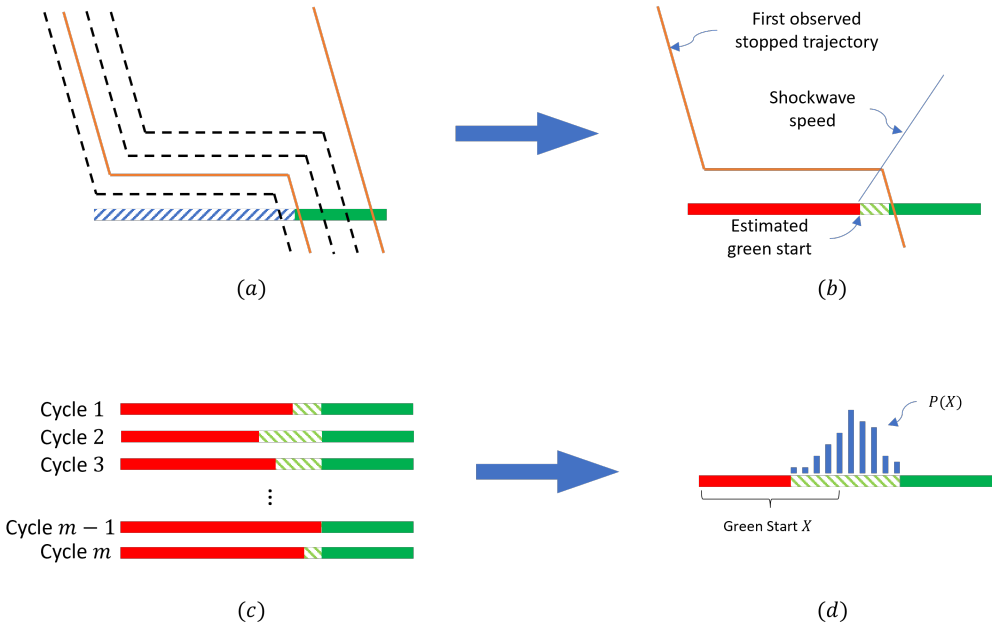

Figure 5.5: Estimating green start time distribution in coordinated actuated settings.

In this way, we can obtain the green start distribution by aggregating the estimated green start time from multiple cycles. This process is illustrated by Figure 5.5 (c)-(d). We can then reflect the green start probability in the signal state $S(t)$ depicted in Figure 5.3 (c).

5.3 Case study

This section presents a real-world implementation of the procedures for optimizing the timing plan schedules, cycle lengths, offsets, and green splits in the vehicle trajectory-based optimization method. In the real-world deployment conducted in coordination with the Michigan Department of Transportation (MDOT) and the Road Commission for Oakland County (RCOC), we used trajectory data from an estimated 7% of vehicles in the traffic network to update cycle lengths, splits, offsets, and timing schedules at seven intersections along a 2.5-mile stretch of a coordinated-actuated arterial in Pontiac, MI. This corridor recently went through a traditional signal optimization based on vehicle count data, providing a unique opportunity to directly compare the performance of the new trajectory-based system against conventional methods. The trajectory-based system outperformed the traditional approach, reducing the overall control delay by 17.4% and the number of stops by 20.4%, compared to reductions of 13.7% and 14.9%, respectively, achieved by traditional optimization.

5.3.1 Study area and data

The study was carried out at seven intersections along a 2.5-mile stretch of Telegraph Rd from County Center Dr to Voorheis St in Pontiac, MI (Figure 5.6 (a)). Both MDOT and RCOC were involved in the project as these seven intersections are owned by MDOT, but maintained and managed by RCOC. The segment operates under coordinated-actuated control. The northbound and southbound directions each have two lanes in the northern half of the segment from County Center Dr to Elizabeth Lake Rd, where they then each convert to three lanes. Figure 5.6 (b) depicts the spacing (in meters) between each intersection. The street names in red font indicate intersections where at least one of the non coordinated movements is operating on minimum or no recall, meaning that an ERG scenario is possible for the coordinated movements. Figure 5.6 (c) shows an aerial view of the intersection with the side street that has the highest volume (Huron St).

Figure 5.7 outlines the implementation schedule and data used for both the traditional and vehicle trajectory-based signal optimizations. All new timing plans for both optimizations were reviewed and implemented by RCOC. The traditional optimization was executed by a hired consultant using Synchro/SimTraffic version 11 from 24-hour approach counts and turning-movement counts during the three peak periods for a typical weekday (7 AM to 9 AM, 11 AM to 1 PM, and 2 PM to 6 PM) on a Tuesday, Wednesday, or Thursday. It included timing plan schedules, flash schedules, vehicle and pedestrian clearance interval calculations, cycle lengths, splits, and offsets. The initial optimization plans occurred on November 21st,

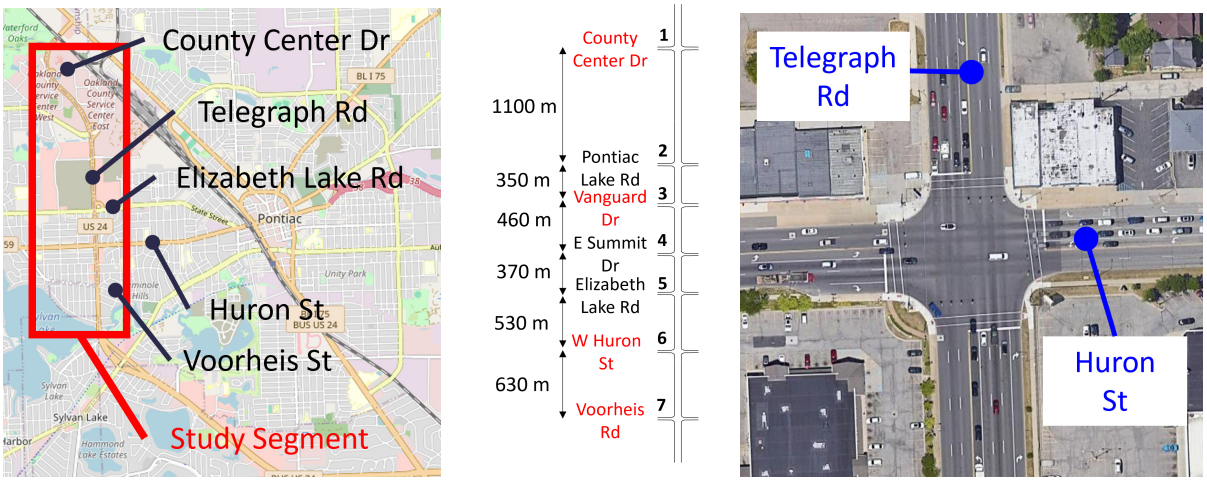

(a) Study segment (b) Intersections (c) Intersection with Huron St

Figure 5.6: Telegraph road study segment in Pontiac, MI

2023, with some final adjustments taking place before a final implementation on February 21st, 2024.

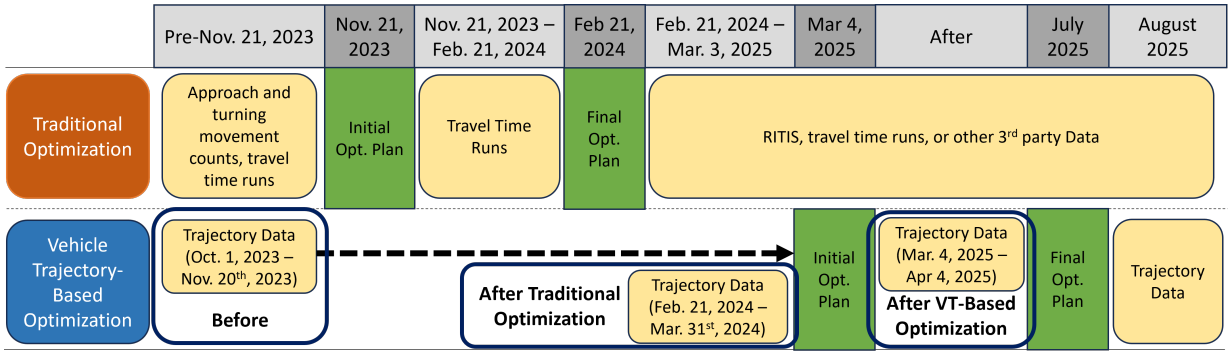

Figure 5.7: Implementation schedule

To structure a comparison that was as fair as possible, the vehicle trajectory-based optimization utilized data from before the initial traditional optimization implementation on November 21st, 2023 to create optimized plans that were implemented on March 4th, 2025. This study included everything from the traditional study except flash schedules and clearance interval calculations (vehicle and pedestrian). Neither study considered left-turn phasing analysis.

5.3.2 Procedures for before and after studies

To conduct the before and after analysis for both the traditional and vehicle trajectory-based optimizations, this study utilized 24-hour weekday vehicle trajectory data from the following dates:

- Before: October 2nd, 2023 to October 27th, 2023
- After traditional optimization: March 4th, 2024 to March 28th, 2024
- After vehicle trajectory-based optimization: March 10th, 2025 to March 28th, 2025

The review schedule includes a significant time gap between the before and after study for the vehicle trajectory-based optimization. We believe that using data collected prior to the traditional optimization—both to generate and evaluate the vehicle trajectory-based optimization—was a necessary decision to ensure a fair comparison between the two signal timing plans. The extended duration between the before and after periods reflects a practical trade-off inherent in conducting real-world implementations.

To evaluate the performance of each movement at each intersection along the corridor, we utilize three common SPMs: control delay, number of stops, and split failures (Figure 1.5). These measures are extracted from individual vehicle trajectories and then averaged by movement, intersection, and across the entire corridor. While this method is effective for assessing movement-level performance, traffic agencies often rely on Global Navigation Satellite System (GNSS) travel time runs to evaluate signal coordination. Traditionally, this involves manual data collection, with a driver conducting 5–10 runs along the corridor using an onboard GNSS receiver. In contrast, crowdsourced vehicle trajectory data enables the extraction of hundreds of travel time runs with minimal effort. For example, Figure 5.8shows 403 observations collected between 7 AM and 9 AM over the course of a week. This not only simplifies data collection but also yields more statistically robust travel time averages. Note that the orange color on the signal bar indicates the range of possibility for an ERG scenario based on the minimum service times of the other movements.

5.3.3 Optimization procedures

5.3.3.1 Timing plan schedules

The first step in the signal timing optimization process is to evaluate the timing plan schedules. For this study, we were limited to the standard three time periods (AM, MD, and PM), so we only investigated the placement of their boundaries. Figure 5.9 depicts the

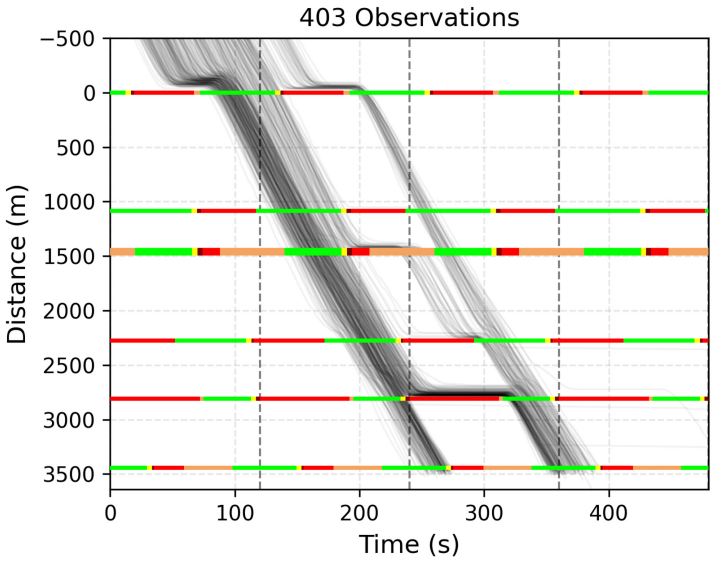

Figure 5.8: Corridor travel times using crowdsourced vehicle trajectory Data

trajectory histograms for the northbound and southbound movements along the corridor segment across the 24-hour period (aggregated from October 2nd, 2023 to October 20th, 2023). The black dashed line indicates the boundaries that did not change as part of the vehicle trajectory-based optimization. The red dashed lines indicate the original boundaries

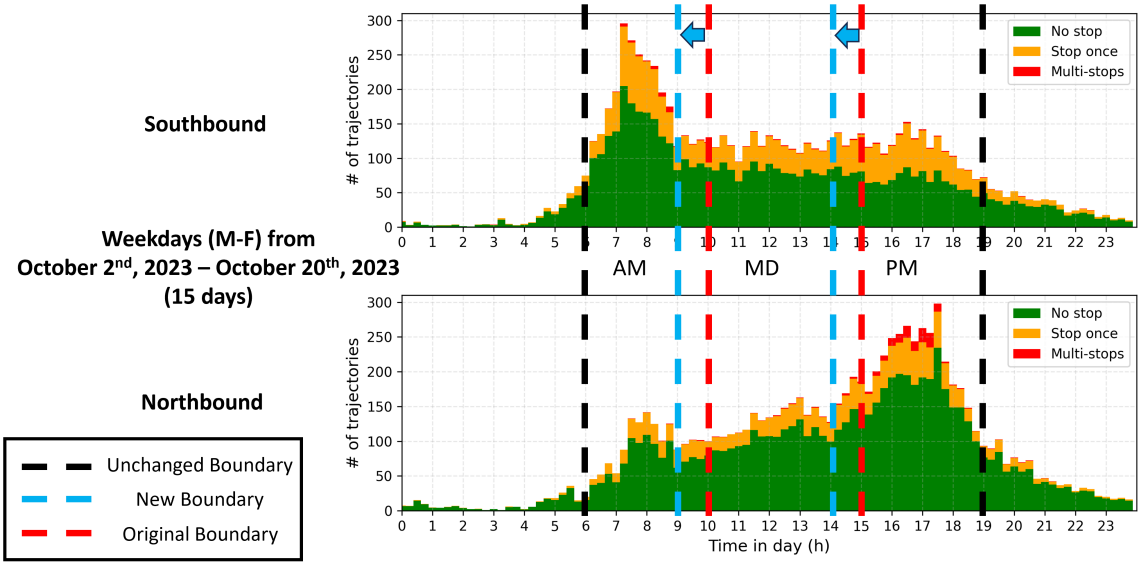

Figure 5.9: Trajectory histograms for northbound and southbound movements along corridor segment across 24-hour period with timing plan schedule changes

and the blue dashed line indicate new boundaries. The major changes included shifting the end of AM/beginning of MD from 10 to 9 and shifting the end of MD/beginning of PM from 15 to 14. The 10 to 9 shift was chosen because the observations in the middle of the the day start to level out starting at 9. The 15 to 14 shift was chosen because the PM peak pattern seems to start building at 14 in the northbound direction.

5.3.3.2 Offsets

The offsets are optimized using the PTS model. In order to not overlap with any of the timing plan schedule changes, the aggregation time periods (time ranges where trajectories were extracted to build model for each time period) was limited to 7-9, 10-14, and 15-18 for the AM, MD, and PM time periods, respectively. A demonstration of how this works is shown in Figure 5.10. The top left figure illustrates the aggregated time-space diagram for the entire corridor, which is built by stacking the aggregated time-space diagram for each intersection. The corridor is depicted through the PTS diagram in Figure 5.10b. Note how the ERG is accounted for in the model through departures during the orange band, particularly at Vanguard Dr. The model for this particular direction is calibrated by matching the observed average delay with the model estimated average delay. In general, a match within 1-2 seconds is sufficient. Next, the bottom right figure (d) illustrated the predicted performance after the optimization. This optimization provides the new offsets. It is easy to see how coordination is improved in the optimized PTS diagram. In this case, the model predicts a reduction in delay from 15.5 seconds to 8.8 seconds (43.2%). To complete the visualization of this process, we have gone ahead and included the observation after the optimization of the vehicle trajectory-based implementation in this figure in the bottom left (c).

5.3.3.3 Cycle length

The PTS model can also be used to model changes in cycle length. Table 5.1 reports the predicted average control delay per coordinated movement considering different cycle lengths in the MD time period. This particular time period is of interest because the traditional optimization chose to increase the cycle length from 100 seconds (current) to 120 seconds. The green split ratios in relation to the cycle were kept constant for each cycle length evaluation. According to the PTS model, the 100 second cycle length was determined to still be the optimal cycle length for the MD time period.

A comparison of the timing plan schedules and optimized cycle lengths for both optimizations are provided in Table 5.2. Plan 2 is associate with the AM period, Plan 1 is associated with the MD period, and Plan 3 is associated with the PM period. While the

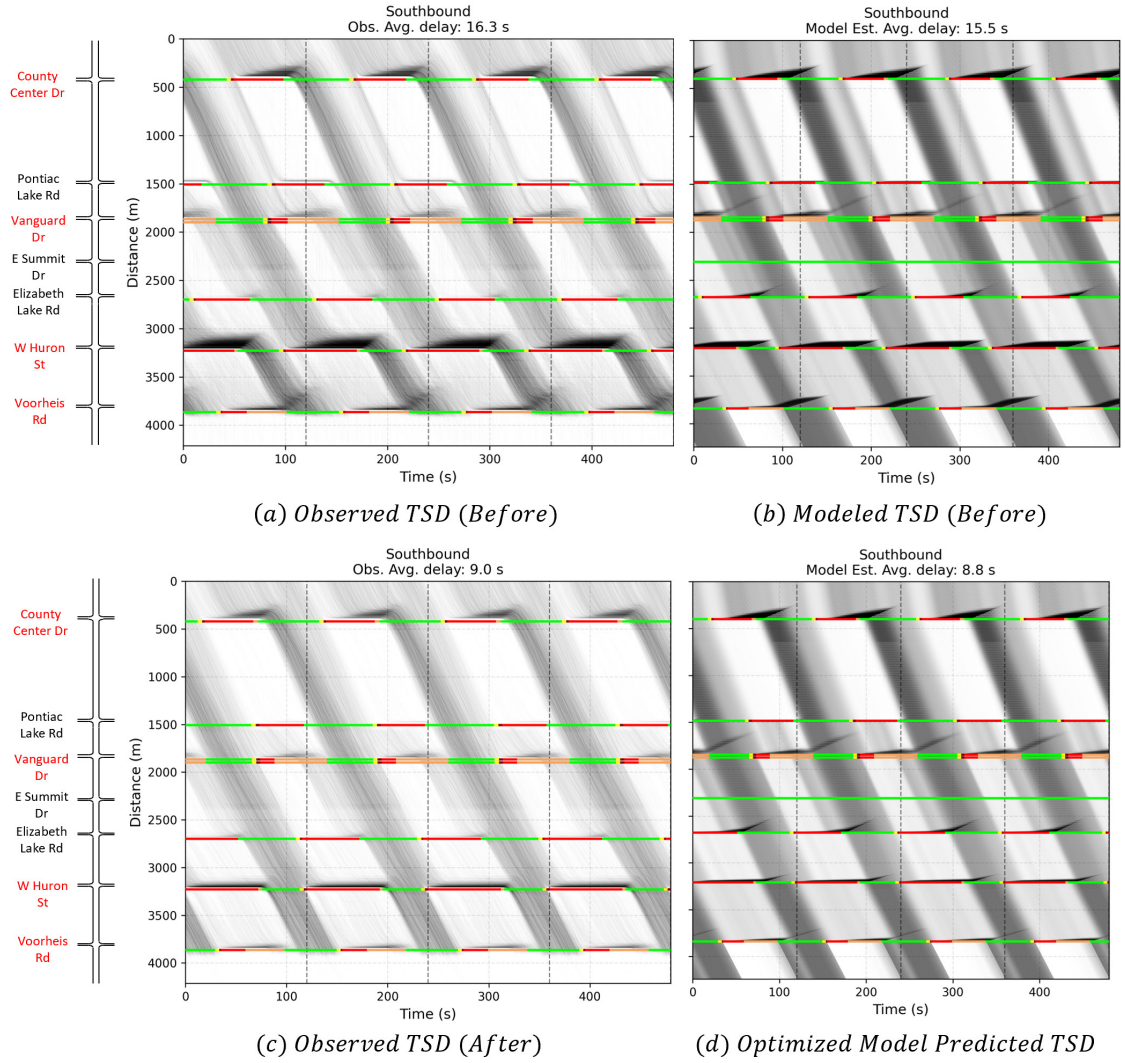

Figure 5.10: Observed and modeled time-space diagrams (TSDs) of Telegraph Road during the AM time period before and after vehicle trajectory-based optimization

vehicle trajectory-based optimization changed the timing plan schedules, the cycle lengths were kept constant for their respective period names. The traditional optimization also decided to change the end of MD/beginning of PM from 15 to 14, but did not pursue the 10 to 9 change.

5.3.3.4 Green splits

Green splits were adjusted heuristically by identifying oversaturated movements according to high split failure ratios (Figure 5.11a). "Donor" movements were identified by isolating

Table 5.1: Prediction of average control delay per movement (s) along coordinated movements for different cycle lengths during the MD time period

Cycle	Northbound	Southbound	Both
80	6.6	10.6	8.5
90	7.5	10.0	8.7
100	7.0	9.7	8.3
110	8.3	10.3	9.3
120	7.4	13.9	10.4

Table 5.2: Summary of timing plan schedule changes and cycle lengths

Time Range	Orig. Plan	Orig. Cycle	Trajectory-Based Plan	Trajectory-Based Cycle	Traditional Plan	Traditional Cycle
6-9	Plan 2 (AM)	120s	Plan 2 (AM)	120s	Plan 2 (AM)	120s
9-10	Plan 2 (AM)	120s	Plan 1 (MD)	100s	Plan 2 (AM)	120s
10-14	Plan 1 (MD)	100s	Plan 1 (MD)	100s	Plan 1 (MD)	120s
14-15	Plan 1 (MD)	100s	Plan 3 (PM)	120s	Plan 3 (PM)	120s
15-19	Plan 3 (PM)	120s	Plan 3 (PM)	120s	Plan 3 (PM)	120s

trajectories that only stop once (orange) and the available green time before these vehicles start to experience split failures (Figure 5.11 (b)). The limitation to this method is that as we reduce the green time the number of one stop vehicles will increase. Therefore, green split adjustments were limited to 4 seconds. This project plans to execute a second round of optimization (Figure 5.7), so the green splits can be adjusted again if the 4 second maximum is too restrictive. Intersections with no oversaturated movements were rebalanced to give more green time to Telegraph Rd based on available "donor" movements. Pedestrian minimums were used as a constraint where required.

5.3.4 Results and discussion

Table 5.3 reports the average corridor travel times before and after each optimization. Overall, the vehicle trajectory-based optimization reduced average corridor travel times by around a half a minute (9.9%), slightly better that the traditional optimization, which reduced travel times by around 7.6%. Both optimizations performed relatively the same for the northbound direction, reducing travel times from 263 seconds to 242 and 240 seconds. However, the vehicle trajectory-based optimization outperformed the traditional optimization in the

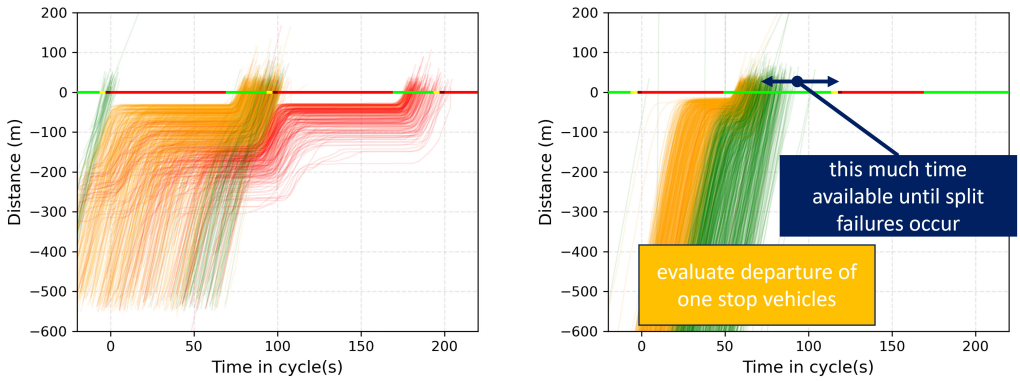

(a) Oversaturated movement (b) "Donor" movement

Figure 5.11: Green split adjustment methodology

southbound direction, where the average travel times were reduced from 293 seconds to 258 seconds (11.8%) compared to the traditional optimization reduction to 275 seconds (6.3%). Table 5.3 also breaks down the results by time period, isolating hours 9-10 and 14-15 because of the timing plan schedule changes executed by both optimizations. While the magnitude varies, the vehicle trajectory-based optimization performed better than the traditional optimization in every time period. The biggest difference was during the AM time period, where the vehicle trajectory-based optimization reduced travel times by 47 seconds compared to a 32 reduction by the traditional optimization. Another comparison point of interest is the 9-10 hour because the vehicle trajectory-based optimization changes the timing plan schedule by starting the MD timing plan at 9. The vehicle trajectory-based optimization reduced travel time by 30 seconds during this hour, compared to a 22 second reduction by the traditional optimization.

While travel time runs are great for analyzing the experience of vehicles that traverse the entire corridor, it is possible that traffic volumes may not be evenly distributed at each intersection along the segment of interest as vehicles may turn off the corridor at various points. Therefore, Table 5.4 presents the average control delay per movement for the northbound and southbound directions along the study segment. The reported values are weighted averages, accounting for the number of observations at each movement, to more accurately represent the delay experienced along each coordinated direction. For the 24-hour period, the vehicle trajectory-based optimization reduced the control delay by 17.2% from 13.5 seconds to 11.2 seconds, as opposed to a 14.5% decrease by the traditional optimization. The vehicle trajectory-based optimization again performed better than the traditional optimization in every time period except the 14-15 hour. There was a minimal difference during the 9-10 hour between the two optimizations, indicating no real advantage for shifting the MD

Table 5.3: Average corridor travel time (s) by time range before and after trajectory-based and traditional optimizations (weekdays)

Time Range	Direction	Before	After Trajectory-Based Opt. (% Change)	After Traditional Opt. (% Change)
24-hours	NB	263	242 (-8.2%)	240 (-8.7%)
	SB	293	258 (-11.8%)	275 (-6.3%)
	Both	277	250 (-9.9%)	256 (-7.6%)
6-9 (AM)	Both	288	241 (-16.3%)	256 (-11.3%)
9-10	Both	276	246 (-11.0%)	254 (-8.0%)
10-14 (MD)	Both	257	252 (-1.8%)	256 (-0.2%)
14-15	Both	264	258 (-2.1%)	262 (-0.7%)
15-19 (PM)	Both	309	263 (-14.8%)	264 (-14.3%)

time period start time to 9. The MD period (10-14) is also of particular note because each optimization strategies chose different cycle lengths. The traditional optimization, which increased the cycle length from 100 seconds to 120 seconds, resulted in a 6.6% increase in the average control delay, while the vehicle trajectory-based optimization, which kept the cycle length at 100 seconds, resulted in a slight decrease (2.7%) in the average control delay. This result demonstrates the vehicle trajectory-based optimization's ability to evaluate different cycle lengths during the optimization process, as the decision to not increase the cycle length proved to be more beneficial for coordination.

Table 5.4: Average control delay per movements (s) along coordinated movements by time range before and after trajectory-based and traditional optimizations (weekdays)

Time Range	Direction	Before	After Trajectory-Based Opt. (% Change)	After Traditional Opt. (% Change)
24-hours	NB	11.3	9.6 (-15.0%)	9.3 (-17.7%)
	SB	15.9	12.8 (-19.5%)	13.9 (-12.6%)
	Both	13.5	11.2 (-17.2%)	11.5 (-14.5%)
6-9 (AM)	Both	14.9	10.8 (-27.3%)	11.4 (-23.1%)
9-10	Both	13.9	10.5 (-24.4%)	10.6 (-23.5%)
10-14 (MD)	Both	11.3	11.0 (-2.7%)	12.1 (+6.6%)
14-15	Both	12.7	12.3 (-3.3%)	12.3 (-3.1%)
15-19 (PM)	Both	16.8	12.9 (-23.2%)	12.5 (-25.5%)

Another method for evaluating the performance of the vehicle trajectory-based optimiza-

Table 5.5: Average control delay per movement along coordinated movements for different time periods: observations vs. model calibration and optimization

Time Period (Plan)	Observed (Before)	Observed (After)	Model (Calibrated)	Model (Optimized)
AM (Plan 2)	14.9	10.8 (-27.5%)	13.1s	9.0 (-31.8%)
MD (Plan 1)	11.3	11.0 (-2.7%)	9.6s	8.3 (-13.3%)
PM (Plan 3)	16.8	12.9 (-23.2%)	15.1s	13.2 (-12.6%)

tion method is to see how well the model predicted the resulting performance after the optimization. This was already demonstrated in Figure 5.10 in the Methodology section for the southbound direction in the AM period. Table 5.5 reports the observed control delay per coordinated movement before and after the implementation and compares it to the calibrated and optimized model for the both directions in the AM, MD, and PM time periods. Again, as noted in the methodology section, it is common for the observation and the calibrated model to be within 1-2 seconds of each other. The AM model predicted a 31.8% reduction in control delay for both directions, closely aligning with the observed 27.5% decrease. For the MD time period, the observed performance followed the same general trend but was not directly comparable in magnitude to the model's predictions. In contrast, the PM time period outperformed the expectations set by the model. We attribute the discrepancies between predicted and observed performance to several factors, including the extended time gap between the data used for optimization and the actual implementation. Nevertheless, based on its ability to accurately predict the direction of the improvement and its strong performance relative to the traditional optimization, we conclude that the vehicle trajectory-based optimization model offers substantial benefits for traffic signal retiming.

Finally, we report the changes in average control delay and number of stops per movement for all movements (including left turns and side street movements) in Table 5.6. The vehicle trajectory-based system outperformed the traditional approach for the 24-hr time range, reducing the overall control delay by 17.4% and the number of stops by 20.4%, compared to reductions of 13.7% and 14.9%, respectively, achieved by the traditional optimization. Again, we draw special attention to the 9-10 period because of the timing plan schedule change. While the reduction in control delay is slightly larger in the vehicle trajectory-based optimization, the traditional optimization achieved a greater reduction in number of stops. This is not completely surprising because the traditional optimization has a 120 second cycle length during the AM timing plan while the MD timing plan had a 100 second cycle length, and increases in cycle length generally result in decreases in the number of stops. For the

Table 5.6: Average control delay and number of stops per movement for all movements by time range before and after trajectory-based and traditional optimizations (weekdays)

Time Range	Performance Measure	Before	After Trajectory-Based Opt. (% Change)	After Traditional Opt. (% Change)
24-hours	Control Delay (s)	21.8	18.0 (-17.4%)	18.8 (-13.7%)
	No. of Stops	0.44	0.35 (-20.4%)	0.38 (-14.9%)
6-9 (AM)	Control Delay (s)	24.2	18.9 (-21.7%)	19.7 (-18.5%)
	No. of Stops	0.47	0.35 (-20.8%)	0.39 (-16.8%)
9-10	Control Delay (s)	21.1	17.2 (-18.5%)	17.2 (-18.7%)
	No. of Stops	0.43	0.37 (-15.1%)	0.35 (-18.8%)
10-14 (MD)	Control Delay (s)	18.4	15.4 (-16.7%)	18.2 (-1.2%)
	No. of Stops	0.41	0.34 (-17.8%)	0.37 (-11.5%)
14-15	Control Delay (s)	21.4	18.6 (-12.9%)	18.9 (-11.3%)
	No. of Stops	0.48	0.36 (-25.2%)	0.40 (-17.2%)
15-19 (PM)	Control Delay (s)	26.6	22.6 (-15.14%)	21.1 (-20.9%)
	No. of Stops	0.50	0.41 (-18.9%)	0.42 (-16.5%)

MD period from 10-14, the vehicle trajectory-based optimization reduced control delay by a full 3 seconds compared to only 0.2 seconds in the traditional. It also reduced the number of stops by 0.07 compared to 0.04. The greater reduction in stops by the vehicle trajectory-based optimization was unexpected because of the shorter cycle length. However, a closer look at one intersection not only provides an explanation for the decrease in number of stops, but also why the vehicle trajectory-based optimization performed much better in terms of control delay as well.

Figure 5.12 illustrates aggregated time-space diagrams for all movements at the intersection of Telegraph Rd and Huron St (depicted in Figure 5.6c) for the MD time period before and after the vehicle trajectory-based optimizations. The diagrams are arrayed according to the intersection's dual-ring phase diagram sequencing. The numbers in the bottom right hand corner of each diagram indicate the green split changes implemented by the optimization. Additionally, while not reflected in these diagrams, the offset was increased by 50 seconds (or -50 seconds given 100 cycle length). The bottom left hand corner of phases 4 and 8 (far right of each dual-phase diagram) report the changes in delay and split failures (SFs) as a result of the green split increase. Visually, it is very easy to notice the reduction in red, indicating trajectories that stopped twice before clearing the intersection. While the green split changes alone resulted in split failure reductions (phase 8 dropped from 23.6% split failures to 8.5%), it is also interesting to note how the offset change, designed for improving coordination on

the Telegraph Rd, resulted in improved coordination for the westbound movement (phase 4) on Huron St. The call outs on the diagrams note how, because of the 50 second increase in the offset, the upstream platoon is not arriving during the green band but rather at the beginning of the red interval. This is also shown by there being more trajectories colored green, indicating those that did not have to stop before clearing the intersection. As a result, not only did the number of stops greatly reduce, but the delay reduced by almost 40 seconds (73.6%). This result would not have been possible if the cycle length had increased to 120 seconds, because the coordination would have gone out of sync with the 100 second cycle lengths set on Huron St. This example highlights the power of using vehicle trajectory data to evaluate the network implications of signal coordination optimization.

5.3.5 Summary

This section compares real-world implementations of our vehicle trajectory-based traffic signal optimization system and a traditional optimization. The implementation took place on a 2.5-mile stretch of a coordinated-actuated arterial with seven intersection in Pontiac, MI. Both optimizations retimed signal timing plan schedules, cycle lengths, offsets, green splits. However, the traditional optimization used vehicle count data while the vehicle trajectory-based optimization used a small percentage of vehicle trajectory data as the only input.

Besides different offsets and green split decisions between the vehicle trajectory-based and traditional optimizations, the optimizations differed in two key aspects. First, the vehicle trajectory-based optimization chose to move the end of the AM/beginning of the PM from hour 10 to 9. Both optimizations moved the end of MD/beginning of PM from hour 15 to 14. Second, the vehicle trajectory-based optimization chose to maintain a 100 second cycle length for the MD time period while the traditional optimization increase it to 120 seconds.

Overall, the vehicle trajectory-based system outperformed the traditional approach, reducing the overall control delay by 17.4% and the number of stops by 20.4%, compared to reductions of 13.7% and 14.9%, respectively, achieved by the traditional optimization. Large improvements in coordination were observed in the AM time period, where the vehicle trajectory-based optimization reduced average delay at each coordinate movement by 4.1 seconds, compared to the 3.5 seconds achieved by the traditional. For the coordinated movements, the vehicle trajectory-based optimization outperformed the traditional in every time period except PM (15-19).

It was unclear if the time period border change chosen by the vehicle trajectory-based optimization from 10 to 9 yielded any superior benefits than the traditional optimization's choice to maintain the time period border at 10. While the coordination seemed to be slightly

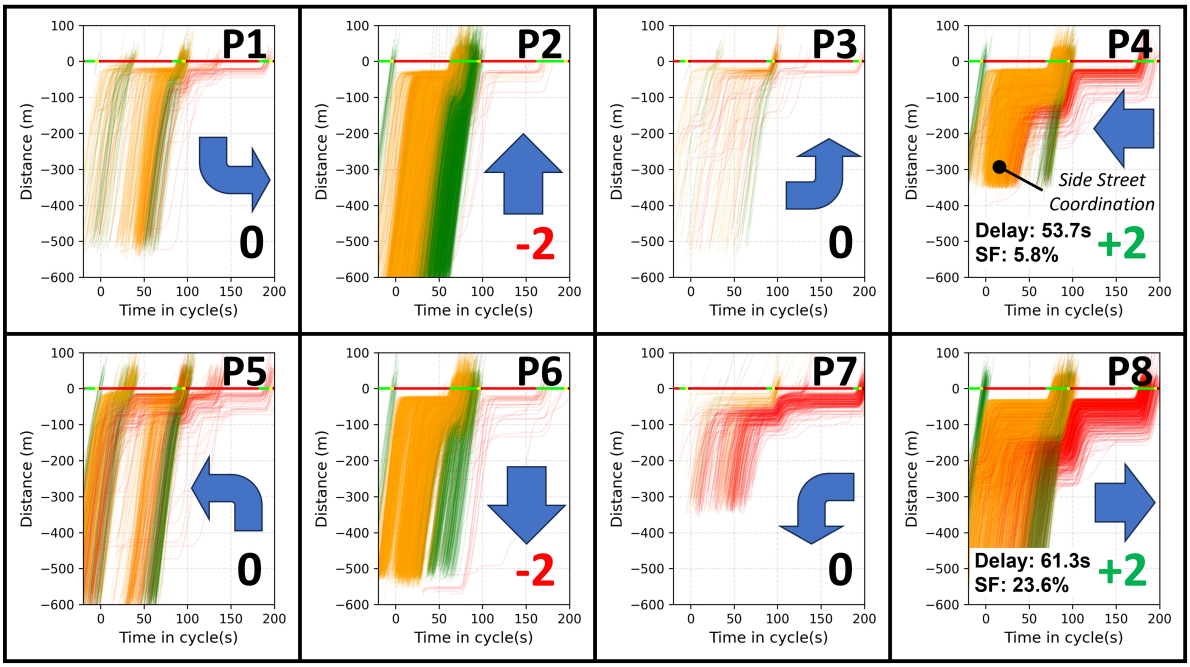

(a) Before

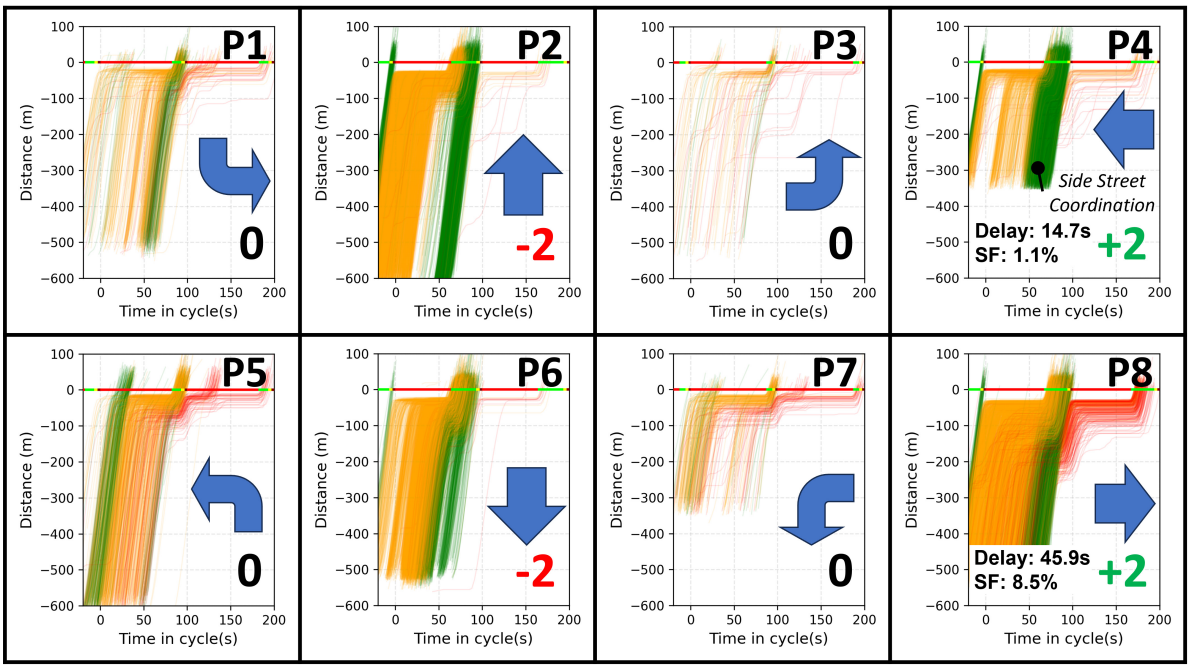

(b) After

Figure 5.12: Time-space diagrams before and after trajectory-based optimizations for each movement at Telegraph Rd and Huron St for the MD time period

better (0.1 second), the overall average control delay and number of stop improvements were not as significant as the traditional optimization for hour 9 to 10. These results make sense based on the method used for the timing plan schedule changes, which was based on the

travel patterns along the corridor. Future work will develop other methods for timing plan schedule optimization that considers the entire network.

The decision to maintain the 100 second cycle length for the MD time period yielded much better performance than the traditional optimization's increase to 120 seconds. Not only did the vehicle trajectory-based optimization perform 1.1 seconds better in average delay along the coordinated movements, but the average control delay and number of stops per movement dropped by 16.7% and 17.8%, respectively, compared to only 1.2% and 11.5%, respectively, in the traditional optimization. A huge reason for these reductions was the improvement in coordination along a side street, which was made possible by maintaining the 100 second cycle length.

The results of this study offer a valuable case study for directly comparing the implementation of two distinct optimization methods. Although the vehicle trajectory-based optimization demonstrated overall superior performance, a single study is insufficient to draw definitive conclusions about which method is categorically better—especially given that the traditional optimization outperformed the vehicle trajectory-based approach during certain time periods. Nonetheless, the findings highlight the promise of using vehicle trajectory data as a practical and effective tool for traffic signal optimization in real-world applications. As shown in Figure 5.7, the project will include a second round of optimization using the vehicle trajectory-based system that will also include analysis of new timing plans for the weekends. Additionally, we are in the process of comparing the two methods using other evaluation criteria, including cost, time, and resource requirements.

5.4 Conclusion

5.4.1 Summary

This chapter presents procedures for optimizing four traffic signal timing parameters from just the currently available vehicle trajectory data penetration rates: timing plan schedules, offsets, cycle lengths, and green splits. By utilizing the PTS model developed in this research group, we are able to estimate recurrent traffic state and predict future states under alternative signal timing plans. This chapter introduces upgrades to this model that allow it to accommodate coordinate-actuated signal control. The model serves as the foundation to develop the retiming procedures for the four traffic parameters. Together they form a complete online closed-loop traffic signal optimization system without requiring any input from roadside detection systems.

We demonstrate the system's technical readiness for deployment through multiple real-

world implementations, including a direct comparison with a traditional optimization. In that deployment, the proposed system outperformed the conventional approach, reducing overall control delay by 17.4% and the number of stops by 20.4%, compared to 13.7% and 14.9% reductions, respectively, from the traditional method. By leveraging trajectory data as the sole input and requiring no additional infrastructure, this system offers a scalable and cost-effective solution that can be applied to signalized intersections around the world.

5.4.2 Integration into the traffic signal timing management system)

The procedures presented in this chapter serve as retiming microservices in the signal timing management system presented in Figure 1.6. The parameter optimization for evolving traffic flow application utilizes these microservices when called to alleviate traffic congestion by optimizing traffic signal timing parameters in fixed-time and coordinated-actuated control. Through widespread 24/7 vehicle trajectory data coverage, this application can be called to iteratively optimize traffic signal timing every few weeks rather than every the 3 to 5 year timelines typically used in practice.

CHAPTER 6

Summary and Future Directions

6.1 Summary

This dissertation presents a traffic signal timing management system that relies solely on currently available vehicle trajectory data, even at low penetration rates. The goal of this system is to provide performance monitoring, diagnoses, and optimization capabilities across large scale networks without the need for any roadside detection technology. This is enabled by increasingly available vehicle trajectory data that provides widespread 24/7 coverage across traffic networks through cloud or cellular communications. Not only does this data provide more detailed insights into travel paths-such as delays, stops, and travel time-previously unavailable from traditional roadside detection systems, but online communication from vehicles enables efficient cloud-based calibration of a traffic flow model that can provide more responsive signal retiming.

In traditional signal timing management, the need to collect information about the traffic dynamics from fixed-detection systems usually limits signal retiming efforts to about once every 3 to 5 years. Without reliable, continuous, and widespread data coverage, the process can resemble performing surgery without first understanding the symptoms or confirming the diagnosis, where traffic agencies must first select intersections to optimize without having any reliable monitoring capabilities on site. As a result, agencies may miss key opportunities to retime signals where optimization could have the greatest impact—or may direct resources toward locations that are not in urgent need of adjustment. Improved data sources would also facilitate a transition from infrequent, periodic adjustments to more continuous and responsive optimization as traffic patterns evolve. While vehicle trajectory data is promising, few comprehensive solutions currently exist that fully leverage the advantages this data to detect performance issues at signalized intersections, diagnose their root causes, and implement the targeted interventions needed to improve their operation.

The traffic signal retiming system proposed in this dissertation fills this gap through

closed-loop framework that offers a comprehensive, systematic solution. Key technical contributions of this dissertation include a method for determining minimum yellow change and all-red clearance intervals that reduce the risk of red-light running by eliminating dilemma zones; the development of the Signalized Intersection Performance Diagram (SIPD), which integrates signal timing data with advanced performance analytics to identify the root causes of congestion by diagnosing inefficient right-of-way control; and rule-based approaches for diagnosing signal coordination deficiencies without requiring signal timing data from the agency. In addition, the system includes procedures for iteratively optimizing timing plan schedules, cycle lengths, offsets, and green splits every few weeks to alleviate traffic congestion caused by evolving traffic demand patterns.

Each of these four contributions serve as an application to the traffic signal retiming system, illustrated in Figure 1.6. Each application has access to process vehicle trajectory data, a weather prediction module, and diagnostic and retiming microservices. The system architecture has been deliberately structured to support future applications with minimal modification.

This dissertation demonstrates the technical readiness for deployment of this system through multiple real-world implementations, including a direct comparison with a traditional optimization. It represents a major milestone in this research group's ten years of groundbreaking theoretical work—culminating in a deployable system with demonstrated impact in real-world transportation engineering practice. By leveraging trajectory data as the sole input and requiring no additional infrastructure, this system offers a scalable, systematic, and cost-effective solution that can be applied to signalized intersections around the world.

6.2 Future Directions

As mentioned in the introduction, the system presented in Figure 1.6 has been designed to enable the incorporation of new applications with minimal modification. Below are some future directions including both research problems and practical issues in real-world implementation that could foster the development of future applications.

Optimization techniques for left-turn operations. The right-of-way diagnostics application presented in this dissertation provides insights into the performance of left-turn permissive movements. However, no methods for optimizing traffic signal control by adjusting left turn operations were proposed. As a segmented time-space diagram, the SIPD provides new performance measures that could be used to calibrate future models that are

designed to optimize these operations. In these models, many competing factors will need to be considered such as the trade-offs between protected and permissive left-turns and the required designated lane requirements. There is also an opportunity to include the safety considerations of change intervals for left-turn movements. As explored in Chapter 2, left-turns may require longer yellow change intervals that through movements. However, many intersections control these movements through one phase/signal head. These considerations should be included in future optimization models looking at left-turn operations.

Traffic responsive signal control. Vehicle trajectory streaming could enable more responsive dynamic control strategies that react to the time-varying traffic conditions. While previous work has explored this possibility in China, future research should investigate the practical issues surrounding implementation of such as a system in the United States (Wang et al., 2024c). The temporal-spatial qualities of vehicle trajectory data in addition to the enhanced monitoring capabilities provided by the SIPD proposed in this dissertation will allow the signal timing management system to easily identify congestion in the form of split failures caused by oversaturation and spillovers. For instance, cycle failures and spillovers can be easily identified by plotting the trajectories on the SIPD, especially compared to fixed-point detectors. We can locate, with a high level of confidence, congested movements in real-time at an intersection if we observe multiple trajectories exhibiting these characteristics in a short time frame (3-5 minutes). Therefore, future research should develop algorithms for incrementally adjusting the green splits in real-time to alleviate these oversaturated conditions.

Virtual actuation. Cellular Vehicle-to-Everything (CV2X) technology has the potential to enable real-time signal control strategies by transmitting vehicle trajectory information through cellular infrastructure. Leveraging this data to develop real-time traffic signal control strategies that remain compatible with existing controllers would be highly beneficial. In traditional systems, physical detection devices send a "call" for service whenever a vehicle is detected. This approach, known as actuated signal control, follows well-established logic implemented in current signal controllers. Future research could implement methods for replicated vehicle actuation to enable more large-scale actuated signal control through real-time vehicle trajectory data. One major challenge would be to provide all vehicles equal benefits, not just those that are equipped with technology. One potential solution could be based on the probabilistic methods established in this dissertation and in Wang (2023).

BIBLIOGRAPHY

Abbas, M., Bullock, D., and Head, L. (2001). Real-time offset transitioning algorithm for coordinating traffic signals. *Transportation Research Record*, 1748(1):26–39.

Agarwal, M., Maze, T. H., and Souleyrette, R. (2005). Impacts of weather on urban freeway traffic flow characteristics and facility capacity. In *Proceedings of the 2005 mid-continent transportation research symposium*, volume 9.

Agbolosu-Amison, S. J., Sadek, A. W., and ElDessouki, W. (2004). Inclement weather and traffic flow at signalized intersections: case study from northern new england. *Transportation research record*, 1867(1):163–171.

Agbolosu-Amison, S. J., Sadek, A. W., and Henry, B. (2005). Factors affecting benefits of implementing special signal timing plans for inclement weather conditions. *Transportation research record*, 1925(1):146–155.

Akcelik, R. (1994). Estimation of green times and cycle time for vehicle-actuated signals. *Transportation Research Record*, 1457:63–72.

Al-Kaisy, A. and Freedman, Z. (2006). Weather-responsive signal timing: practical guidelines. *Transportation research record*, 1978(1):49–60.

Asamer, J. and Van Zuylen, H. J. (2011). Saturation flow under adverse weather conditions. *Transportation research record*, 2258(1):103–109.

Axer, S. and Friedrich, B. (2017). Signal timing estimation based on low frequency floating car data. *Transportation research procedia*, 25:1645–1661.

Baerwald, J. (1965). *Traffic Engineering Handbook*. Institute of Transportation Engineers (ITE).

Balke, K., Gopalakrishna, D., et al. (2013). Utah DOT weather responsive traffic signal timing. Technical Report FHWA-JPO-13-088, Road Weather Management Program, Federal Highway Administration, Office of Operations.

Ban, X. J., Hao, P., and Sun, Z. (2011). Real time queue length estimation for signalized intersections using travel times from mobile sensors. *Transportation Research Part C: Emerging Technologies*, 19(6):1133–1156.

Beeber, J. (2020). An explanation of mats järlström's extended kinematic equation. *ITE journal*, 90(4):34–38.

Benioff, B., Dock, F., and Carson, C. (1980). Carson. a study of clearance intervals, flashing operation, and left-turn phasing at traffic signals. report fhwa-rd-78-47. *FHWA, U.S. Department of Transportation*.

Bennett, J. (2010). *OpenStreetMap*. Packt Publishing Ltd.

Bernardin, Lochmueller, and Associates, Inc. (1995). Anchorage signal system upgrade—final report. *Municipality of Anchorage, Alaska*.

Bilmes, J. A. et al. (1998). A gentle tutorial of the em algorithm and its application to parameter estimation for gaussian mixture and hidden markov models. *International computer science institute*, 4(510):126.

Blaylock, B. K. (2023). *Herbie: Retrieve Numerical Weather Prediction Model Data v2023.3.0*. Zenodo.

Boston Transportation Department and Howard/Stein-Hudson Associates, Inc (2010). The benefits of retiming/rephasing traffic signals in the back bay, benefit cost evaluation of signal improvements. Technical report, Boston Transportation Department and Howard/Stein-Hudson Associates, Inc.

Brennan Jr, T. M., Day, C. M., Wasson, J. S., Sturdevant, J. R., and Bullock, D. M. (2011). Assessing signal timing plans for winter conditions. *Journal of Transportation of the Institute of Transportation Engineers*, 1(1):59–76.

Cesme, B., Stevanovic, A., Day, C., Schroeder, B., Bonneson, J., Hale, D., et al. (2023). Traffic signal change and clearance interval pooled fund study: Synthesis report. Technical Report FHWA-HOP-23-037, United States. Department of Transportation. Federal Highway Administration.

Cetin, M. (2012). Estimating queue dynamics at signalized intersections from probe vehicle data: Methodology based on kinematic wave model. *Transportation research record*, 2315(1):164–172.

Chang, M.-S., Messer, C. J., and Santiago, A. J. (1985). Timing traffic signal change intervals based on driver behavior. *Transportation Research Record*, 1027:20–30.

Chen, L. and Englund, C. (2015). Cooperative intersection management: A survey. *IEEE transactions on intelligent transportation systems*, 17(2):570–586.

Chen, Y., Mahmassani, H. S., Hong, Z., Hou, T., Kim, J., Halat, H., and Alfelor, R. M. (2015). Online implementation and evaluation of weather-responsive coordinated signal timing operations. *Transportation research record*, 2488(1):71–86.

Chien, S. I., Kim, K., and Daniel, J. (2006). Cost and benefit analysis for optimized signal timing-case study: New jersey route 23. *Institute of Transportation Engineers. ITE Journal*, 76(10):37.

Choupani, A.-A. (2020). Assessing drivers' compliance with restrictive yellow traffic lights in a developing country. *Transportation Research Record*, page 0361198120973659.

Comert, G. (2013). Simple analytical models for estimating the queue lengths from probe vehicles at traffic signals. *Transportation Research Part B: Methodological*, 55:59–74.

Comert, G. and Cetin, M. (2009). Queue length estimation from probe vehicle location and the impacts of sample size. *European Journal of Operational Research*, 197(1):196–202.

Day, C. M., Li, H., Richardson, L. M., Howard, J., Platte, T., Sturdevant, J. R., and Bullock, D. M. (2017). Detector-free optimization of traffic signal offsets with connected vehicle data. *Transportation Research Record*, 2620(1):54–68.

Day, C. M., Sturdevant, J. R., and Bullock, D. M. (2010). Outcome-oriented performance measures for management of signalized arterial capacity. *Transportation Research Record*, 2192(1):24–36.

Denney Jr, R. W., Curtis, E., and Olson, P. (2012). The national traffic signal report card. *ITE Journal*, 82(6):22–26.

Derpanis, K. G. (2010). Overview of the ransac algorithm. *Image Rochester NY*, 4(1):2–3.

Desai, J., Mahlberg, J., Kim, W., Sakhare, R., Li, H., McGuffey, J., and Bullock, D. M. (2021). Leveraging telematics for winter operations performance measures and tactical adjustment. *Journal of Transportation Technologies*, 11(4):611–627.

Dion, F., Rakha, H., and Kang, Y.-S. (2004). Comparison of delay estimates at under-saturated and over-saturated pre-timed signalized intersections. *Transportation Research Part B: Methodological*, 38(2):99–122.

Dobrota, N., Stevanovic, A., and Mitrovic, N. (2020). Development of assessment tool and overview of adaptive traffic control deployments in the us. *Transportation research record*, 2674(12):464–480.

Dobrota, N., Stevanovic, A., and Mitrovic, N. (2022). Modifying signal retiming procedures and policies by utilizing high-fidelity modeling with medium-resolution traffic data. *Transportation research record*, 2676(3):660–684.

Du, Z., Yan, X., Zhu, J., and Sun, W. (2019). Signal timing parameters estimation for intersections using floating car data. *Transportation research record*, 2673(6):189–201.

Eccles, K. A. and McGee, H. W. (2001). *A history of the yellow and all-red intervals for traffic signals*. Number IR-113. Institue of Transportation Engineers.

Fayazi, S. A., Vahidi, A., Mahler, G., and Winckler, A. (2014). Traffic signal phase and timing estimation from low-frequency transit bus data. *IEEE Transactions on Intelligent Transportation Systems*, 16(1):19–28.

Feng, Y., Head, K. L., Khoshmagham, S., and Zamanipour, M. (2015). A real-time adaptive signal control in a connected vehicle environment. *Transportation Research Part C: Emerging Technologies*, 55:460–473.

FHWA (2023). *Manual on Uniform Traffic Control Devices for Streets and Highways 11th Edition*. Federal Highway Administration, U.S. Department of Transportation.

FHWA (2023). *Manual on Uniform Traffic Control Devices for Streets and Highways, 11th edition*. United States Federal Highway Administration.

Fourati, W. and Friedrich, B. (2019). Trajectory-based measurement of signalized intersection capacity. *Transportation research record*, 2673(10):370–380.

Gazis, D., Herman, R., and Maradudin, A. (1960). The problem of the amber signal light in traffic flow. *Operations research*, 8(1):112–132.

Goodwin, L. C. (2002). Weather impacts on arterial traffic flow. *Mitretek systems inc*, 24:4–8.

Goodwin, L. C. and Pisano, P. A. (2004). Weather-responsive traffic signal control. *Institute of Transportation Engineers. ITE Journal*, 74(6):28.

Gopalakrishna, D., Cluett, C., Kitchener, F., Balke, K., et al. (2011). Developments in weather responsive traffic management strategies. Technical report, United States. Joint Program Office for Intelligent Transportation Systems.

Gopalakrishna, D., Kitchener, F., Serulle, N. U., Neuner, M., Schmit, J., Donaldson, G., and Duvall, J. (2018). Connected vehicle-enabled weather responsive traffic management–final report. Technical report, Federal Highway Administration.

Grumert, E. F. and Pereira, I. (2022). Heads-up green in connected traffic signals. *IEEE Transactions on Intelligent Transportation Systems*, 23(12):23334–23345.

Guo, Q., Li, L., and Ban, X. J. (2019). Urban traffic signal control with connected and automated vehicles: A survey. *Transportation research part C: emerging technologies*, 101:313–334.

Haddad, J., Tur, N., Veikherman, D., Buchnik, E., Ferster, S., Kalvari, T., Karliner, D., Litov, O., Zagoury, A., Rottenstreich, O., et al. (2024). Quantitative approach for coordination, at scale, of signalized intersection pairs. In *2024 European Control Conference (ECC)*, pages 1881–1888. IEEE.

Hao, P., Ban, X., Bennett, K. P., Ji, Q., and Sun, Z. (2012). Signal timing estimation using sample intersection travel times. *IEEE Transactions on Intelligent Transportation Systems*, 13(2):792–804.

Hao, P., Wu, G., Boriboonsomsin, K., and Barth, M. J. (2018). Eco-approach and departure (ead) application for actuated signals in real-world traffic. *IEEE Transactions on Intelligent Transportation Systems*, 20(1):30–40.

Hirose, R., Mehran, B., and Pani, A. (2022). Investigating combined impact of adverse road-weather conditions and heavy vehicles on saturation headway. *Transportation research record*, 2676(10):303–314.

Hranac, R., Sterzin, E., Krechmer, D., Rakha, H. A., Farzaneh, M., et al. (2006). Empirical studies on traffic flow in inclement weather. Technical report, Federal Highway Administration.

Hu, H. and Liu, H. X. (2013). Arterial offset optimization using archived high-resolution traffic signal data. *Transportation Research Part C: Emerging Technologies*, 37:131–144.

INRIX (2024). Inrix documentation: Metrics. inrix iq documentation. https://docs.inrix.com/signals/metrics/. Accessed: 2024-07-30.

ITE (2020). Guidelines for determining traffic signal change and clearance intervals. Technical Report RP-040B, Institute of Transportation Engineers, Washington, DC.

Izadpanah, P., Hellinga, B., and Fu, L. (2009). Automatic traffic shockwave identification using vehicles' trajectories. In *Proceedings of the 88th Annual Meeting of the Transportation Research Board (CD-ROM)*.

Järlström, M. (2014). An investigation of the ite formula and its use. *Beaverton, Oregon, USA*.

Järlström, M. (2020). An extended kinematic equation. *Beaverton, Oregon, USA*.

Järlström, M. (2021). Precise yellow traffic signal solutions. *Beaverton, Oregon, USA*.

Jerome, Z., Wang, X., Shen, S., and Liu, H. X. (2022). Determining yellow change and clearance intervals for left-turning phases: evaluation of the current guidelines with connected vehicle data. *Transportation research record*, 2676(11):1–14.

Jiang, H., Hu, J., An, S., Wang, M., and Park, B. B. (2017). Eco approaching at an isolated signalized intersection under partially connected and automated vehicles environment. *Transportation Research Part C: Emerging Technologies*, 79:290–307.

Jovanis, P. P. and Gregor, J. A. (1986). Coordination of actuated arterial traffic signal systems. *Journal of Transportation Engineering*, 112(4):416–432.

Katsaros, K., Kernchen, R., Dianati, M., and Rieck, D. (2011). Performance study of a green light optimized speed advisory (glosa) application using an integrated cooperative its simulation platform. In *2011 7th International Wireless Communications and Mobile Computing Conference*, pages 918–923. IEEE.

Koonce, P. (2008). Traffic signal timing manual. Technical Report FHWA-HOP-08-024, United States Federal Highway Administration.

Krishna, K. and Murty, M. N. (1999). Genetic k-means algorithm. *IEEE Transactions on Systems, Man, and Cybernetics, Part B (Cybernetics)*, 29(3):433–439.

Li, F., Tang, K., Yao, J., and Li, K. (2017). Real-time queue length estimation for signalized intersections using vehicle trajectory data. *Transportation Research Record*, 2623(1):49–59.

Li, J., Yu, C., Shen, Z., Su, Z., and Ma, W. (2023a). A survey on urban traffic control under mixed traffic environment with connected automated vehicles. *Transportation research part C: emerging technologies*, 154:104258.

Li, W. and Ban, X. (2018). Connected vehicles based traffic signal timing optimization. *IEEE Transactions on Intelligent Transportation Systems*, 20(12):4354–4366.

Li, Y., Liu, Y., Wang, D., Zuo, F., and Zhou, H. (2023b). Mining method for traffic light cycle duration, electronic equipment and computer program product. Patent No. CN114463969B.

Lin, P., Liu, J., Jin, P. J., and Ran, B. (2017). Autonomous vehicle-intersection coordination method in a connected vehicle environment. *IEEE Intelligent Transportation Systems Magazine*, 9(4):37–47.

Liu, C., Herman, R., and Gazis, D. C. (1996). A review of the yellow interval dilemma. *Transportation Research Part A: Policy and Practice*, 30(5):333–348.

Liu, C., Yu, L., Saksit, K., and Oey, H. S. (2002). Determination of left-turn yellow change and red clearance interval. *Journal of transportation engineering*, 128(5):452–457.

Liu, H. X., Wu, X., Ma, W., and Hu, H. (2009). Real-time queue length estimation for congested signalized intersections. *Transportation research part C: emerging technologies*, 17(4):412–427.

Lu, Z., Kwon, T. J., and Fu, L. (2019). Effects of winter weather on traffic operations and optimization of signalized intersections. *Journal of traffic and transportation engineering (English edition)*, 6(2):196–208.

Ma, W., An, K., and Lo, H. K. (2016). Multi-stage stochastic program to optimize signal timings under coordinated adaptive control. *Transportation Research Part C: Emerging Technologies*, 72:342–359.

Ma, W., Wan, L., Yu, C., Zou, L., and Zheng, J. (2020). Multi-objective optimization of traffic signals based on vehicle trajectory data at isolated intersections. *Transportation research part C: emerging technologies*, 120:102821.

Mahmud, S., Huang, T., Sharma, A., and Day, C. M. (2023). Use of connected vehicle data to identify signal timing plans on signalized arterial corridors. In *2023 IEEE International Automated Vehicle Validation Conference (IAVVC)*, pages 1–6. IEEE.

Maki, P. J. (1999). Adverse weather traffic signal timing. In *Transportation Frontiers for the Next Millennium: 69th Annual Meeting of the Institute of Transportation EngineersInstitute of Transportation Engineers (ITE)*.

Maradudin, A. A. (2015). A. a. maradudin to the institute of transportation engineers.

Maripini, H., Khadhir, A., and Vanajakshi, L. (2023). Traffic state estimation near signalized intersections. *Journal of Transportation Engineering, Part A: Systems*, 149(5):03123002.

Martin, P. T., Perrin, J., Hansen, B., Quintana, I., et al. (2000). Inclement weather signal timings. *Upper Great Plains Transportation Institute*.

Mathew, J. K., Li, H., and Bullock, D. M. (2019). Signal green time estimation method for connected vehicle-to-infrastructure applications. In *2019 IEEE International Conference on Connected Vehicles and Expo (ICCVE)*, pages 1–6. IEEE.

McBride, J. C. et al. (1977). Economic impact of highway snow and ice control. Technical report, Federal Highway Administration.

McGee Sr, H., Moriarty, K., and Gates, T. J. (2012). Guidelines for timing yellow and red intervals at signalized intersections. *Transportation research record*, 2298(1):1–8.

Mohammed, H. A. (2019)). *Evaluating Driver Response to the Onset of Circular Yellow Indication in the Presence of a Following Vehicle at Isolated High-Speed Signalized Intersections*. PhD thesis, Oregon State University.

Munehiro, K., Takahashi, N., and Asano, M. (2006). Using probe-car data to analyze winter road traffic performance in the urban sapporo area. In *5th International Symposium on Highway Capacity and Quality of ServiceTransportation Research Board*.

National Association of City Transportation Officials (NACTO) (2012). Fixed vs. actuated signalization. urban street design guide. https://nacto.org/publication/urban-street-design-guide/intersection-design-elements/traffic-signals/fixed-vs-actuated-signalization/. Accessed: 2024-11-18.

National Center for Statistics and Analysis (2022). Traffic safety facts 2020: A compilation of motor vehicle crash data (report no. dot hs 813 375). *National Highway Traffic Safety Administration*.

National Operations Center of Excellence (2019). Traffic signal benchmarking and state of the practice report. Technical report, National Operations Center of Excellence.

Newell, G. F. (2002). A simplified car-following theory: a lower order model. *Transportation Research Part B: Methodological*, 36(3):195–205.

NOAA's National Weather Service (2018). Snowfall rate graphics loop. https://www.weather.gov/buf/Snowfall_Rate_Threat_Loop. Accessed: 2023-07-28.

Olson, P. L. and Rothery, R. W. (1972). Deceleration levels and clearance times associated with the amber phase of traffic signals. *Traffic Engineering, Inst Traffic Engr*, 42(7).

Perrin, H., Martin, P. T., and Hansen, B. G. (2001). Modifying signal timing during inclement weather. *Transportation Research Record*, 1748(1):66–71.

Ponlathep, L. (2010). A simple adaptive signal control algorithm for isolated intersections using time-space diagrams. In *13th International IEEE Conference on Intelligent Transportation Systems*, pages 273–278. IEEE.

Rakha, H., Farzaneh, M., Arafeh, M., and Sterzin, E. (2008). Inclement weather impacts on freeway traffic stream behavior. *Transportation Research Record*, 2071(1):8–18.

Remias, S., Waddell, J., Klawon, M., and Yang, K. (2018). Mdot signal performance measures pilot implementation. *Michigan Department of Transportation, SPR-1681*.

ReturnZeroBeing (2024). Traffic light countdown display on mobile navigation apps: The tech truth.

Rossow, M. (2020). Free speech vs. regulation of professional engineers. *PDH Star*.

Sakhare, R. S., Zhang, Y., Li, H., and Bullock, D. M. (2023). Impact of rain intensity on interstate traffic speeds using connected vehicle data. *Vehicles*, 5(1):133–155.

Saldivar-Carranza, E., Li, H., Mathew, J., Hunter, M., Sturdevant, J., and Bullock, D. M. (2021). Deriving operational traffic signal performance measures from vehicle trajectory data. *Transportation research record*, 2675(9):1250–1264.

Saldivar-Carranza, E. D., Gayen, S., Li, H., and Bullock, D. M. (2024a). Comparison at scale of traffic signal cycle split failure identification from high-resolution controller and connected vehicle trajectory data. *Future Transportation*, 4(1):236–256.

Saldivar-Carranza, E. D., Li, H., Mathew, J. K., Desai, J., Platte, T., Gayen, S., Sturdevant, J., Taylor, M., Fisher, C., and Bullock, D. M. (2023). Next generation traffic signal performance measures: Leveraging connected vehicle data. Technical report, Purdue University.

Saldivar-Carranza, E. D., Platte, T., Wills, T., Sturdevant, J. R., Bullock, D. M., et al. (2024b). Business processes to prioritize traffic signal retiming and assess the impact of retiming activities. Technical report, Purdue University. Joint Transportation Research Program.

Schuman, R. (2022). INRIX U.S. signal scorecard. https://inrix.com/signals-scorecard/. Accessed: 2024-11-18.

Skabardonis, A. (1996). Determination of timings in signal systems with traffic-actuated controllers. *Transportation Research Record*, 1554(1):18–26.

Smaglik, E. J., Sharma, A., Bullock, D. M., Sturdevant, J. R., and Duncan, G. (2007). Event-based data collection for generating actuated controller performance measures. *Transportation Research Record*, 2035(1):97–106.

Stephanopoulos, G., Michalopoulos, P. G., and Stephanopoulos, G. (1979). Modelling and analysis of traffic queue dynamics at signalized intersections. *Transportation Research Part A: General*, 13(5):295–307.

Strong, C. K., Ye, Z., and Shi, X. (2010). Safety effects of winter weather: the state of knowledge and remaining challenges. *Transport reviews*, 30(6):677–699.

Sunkari, S. (2004). The benefits of retiming traffic signals. *Institute of Transportation Engineers. ITE Journal*, 74(4):26.

Transportation Research Board (2012). *Guidelines for Timing Yellow and All-Red Intervals at Signalized Intersections*. The National Academies Press, Washington, DC.

Transportation Research Board (2016). *Highway Capacity Manual 6th Edition: A Guide for Multimodal Mobility Analysis*. The National Academies Press, Washington, DC.

Transportation Research Board (2022). *Highway Capacity Manual (7th Edition) - A Guide for Multimodal Mobility Analysis*. Transportation Research Board (TRB).

Transportation Research Board and National Academies of Sciences, Engineering, and Medicine (2010). *Traffic Signal Retiming Practices in the United States*. The National Academies Press, Washington, DC.

Transportation Research Board and National Academies of Sciences, Engineering, and Medicine (2015). *Signal Timing Manual - Second Edition*. The National Academies Press, Washington, DC.

Urbanik, T. and Koonce, P. (2007). The dilemma with dilemma zones. *Proceedings of ITE District*, 6.

U.S.DOT FHWA (2024). About intersection safety. https://highways.dot.gov/safety/intersection-safety/about. Accessed: 2024-11-18.

Waddell, J. M., Remias, S. M., Kirsch, J. N., and Young, S. E. (2020). Scalable and actionable performance measures for traffic signal systems using probe vehicle trajectory data. *Transportation Research Record*, 2674(11):304–316.

Wang, X. (2023). *Traffic Signal Optimization with Connected Vehicle Trajectories*. PhD thesis, University of Michigan, Ann Arbor, MI.

Wang, X., Jerome, Z., Wang, Z., Zhang, C., Shen, S., Kumar, V. V., Bai, F., Krajewski, P., Deneau, D., Jawad, A., et al. (2024a). Traffic light optimization with low penetration rate vehicle trajectory data. *Nature communications*, 15(1):1306.

Wang, X., Jerome, Z., Zhang, C., Shen, S., Kumar, V. V., and Liu, H. X. (2023). Trajectory data processing and mobility performance evaluation for urban traffic networks. *Transportation Research Record*, 2677(3):355–370.

Wang, X., Shen, S., Bezzina, D., Sayer, J. R., Liu, H. X., and Feng, Y. (2020). Data infrastructure for connected vehicle applications. *Transportation Research Record*, 2674(5):85–96.

Wang, X., Wang, Z., Jerome, Z., and Liu, H. X. (2024b). Traffic state estimation and uncertainty quantification at signalized intersections with low penetration rate vehicle trajectory data. *arXiv preprint arXiv:2404.08667*.

Wang, Z., Lloret-Batlle, R., Zheng, J., and Liu, H. X. (2024c). Adaptive green split optimization for traffic control with low penetration rate trajectory data. *Journal of Intelligent Transportation Systems*, 28(6):830–845.

Welch, B. L. (1947). The generalization of 'student's'problem when several different population varlances are involved. *Biometrika*, 34(1-2):28–35.

Wolf, J. C., Ma, J., Cisco, B., Neill, J., Moen, B., and Jarecki, C. (2019). Deriving signal performance metrics from large-scale connected vehicle system deployment. *Transportation research record*, 2673(4):36–46.

Wortman, R. H. and Fox, T. C. (1986). *A reassessment of the traffic signal change interval*. University of Arizona.

Wu, X. and Liu, H. X. (2011). A shockwave profile model for traffic flow on congested urban arterials. *Transportation Research Part B: Methodological*, 45(10):1768–1786.

Yan, H., He, F., Lin, X., Yu, J., Li, M., and Wang, Y. (2019). Network-level multiband signal coordination scheme based on vehicle trajectory data. *Transportation Research Part C: Emerging Technologies*, 107:266–286.

Yin, Y., Li, M., and Skabardonis, A. (2007). Offline offset refiner for coordinated actuated signal control systems1. *Journal of Transportation Engineering*, 133(7):423–432.

Yu, J. and Lu, P. (2016). Learning traffic signal phase and timing information from low-sampling rate taxi gps trajectories. *Knowledge-Based Systems*, 110:275–292.

Yu, L., Qiao, F., Zhang, Y., Tian, Z., and Chaudhary, N. (2003). Yellow and red intervals to improve signal timing plans for left-turn movement. Technical report, Texas Southern University, Department of Transportation Studies.

Zegeer, J., Bonneson, J. A., Dowling, R. G., Ryus, P., Vandehey, M., Kittelson, W., Rouphail, N. M., Schroeder, B. J., Hajbabaie, A., Aghdashi, B., et al. (2014). Incorporating travel time reliability into the highway capacity manual. Technical report, National Research Council (US). Transportation Research Board.

Zhang, L. and Lou, Y. (2015). Coordination of semi-actuated signals on arterials. *Journal of Advanced Transportation*, 49(2):228–246.

Zhao, Y., Shen, S., and Liu, H. X. (2021). A hidden markov model for the estimation of correlated queues in probe vehicle environments. *Transportation Research Part C: Emerging Technologies*, 128:103128.

Zhao, Y. and Tian, Z. (2012). An overview of the usage of adaptive signal control system in the united states of america. *Applied Mechanics and Materials*, 178:2591–2598.

Zhao, Y., Zheng, J., Wong, W., Wang, X., Meng, Y., and Liu, H. X. (2019a). Estimation of queue lengths, probe vehicle penetration rates, and traffic volumes at signalized intersections using probe vehicle trajectories. *Transportation Research Record*, 2673(11):660–670.

Zhao, Y., Zheng, J., Wong, W., Wang, X., Meng, Y., and Liu, H. X. (2019b). Various methods for queue length and traffic volume estimation using probe vehicle trajectories. *Transportation Research Part C: Emerging Technologies*, 107:70–91.

Zheng, J. and Liu, H. X. (2017). Estimating traffic volumes for signalized intersections using connected vehicle data. *Transportation Research Part C: Emerging Technologies*, 79:347–362.